SHEAR-WAVE POLARIZATIONS FROM LOCAL SEISMIC EVENTS

by

Graham Roberts
(BSc. University of Edinburgh)

Thesis submitted for degree of Ph.D
University of Edinburgh, Department of Geophysics
July 1985

I hereby declare that this thesis was composed by myself and that the work described in it is entirely my own unless explicitly stated otherwise.

ABSTRACT

Shear-wavetrains from three-component seismograms of local seismic events are analysed for diagnostic effects of wave propagation through effectively anisotropic media. There is recent evidence to suggest that cracks within the upper crust are differentially aligned by non-lithostatic stresses to produce effectively anisotropic structures to short period seismic waves. Shear-wave splitting - the propagation of two, or more, shear-waves with approximately orthogonal polarizations and different velocities along a single ray path - and the orientation of shear-wave polarizations can be used to identify effective seismic anisotropy. The effects of the shear-wave interaction at the free surface and the shear-wave radiation pattern from seismic sources are also considered.

Three data sets are available for shear-wave particle motion analysis. The data sets consist of three-component short period seismic records of (i) reservoir-induced seismic events from Monticello, South Carolina, USA; (ii) hydraulic-induced seismic events from a Hot Dry Rock site at Cornwall, UK, and (iii) natural seismic events associated with the San Andreas fault system in the Livermore Valley, California, USA. The shear-wave particle motion is displayed in polarization diagrams.

A few seismic records from Monticello display shear-wave splitting, but the presence of many transversely-polarized shear-waves recorded at angles of incidence beyond the critical angle suggests that shear-wave interaction at the free surface masked any anisotropic effects.

The data set from the HDR site, Cornwall, provides a demonstration of seismic wave propagation through in situ cracked rock as both sources and receivers are contained within a granite batholith. The acoustic events induced by the hydraulic injection were recorded on a surface network of single-component and three-component stations centred on the HDR site. The observation of shear-wave splitting, alignment of shear-wave polarizations,

and time delay patterns suggests that the in situ cracks and joints are effectively anisotropic to seismic waves. The shear-wave polarizations and time delays are displayed on equal-area projections of the focal sphere and show patterns characteristic of wave propagation through vertical parallel liquid filled cracks. The effective anisotropy appears to pervade the whole granite rock mass. Focal mechanisms are determined for the acoustic events using P-wave polarities. The source mechanism is shear as opposed to jacking. A comparison of theoretical shear-wave polarizations from the seismic sources to the observed polarizations supports the anisotropic interpretation of the data.

The Livermore data set was recorded on a permanent three-component seismic network operating in the Livermore Valley area. Shear-wave splitting and alignments of shear-wave polarizations at several stations suggests the presence of effective anisotropy in the upper crust. Random patterns of polarizations at other stations, and the reverberative nature of many seismograms suggests that much seismic energy is scattered. There is good correlation between theoretical shear-wave polarizations from seismic sources and observed shear-wave polarizations at several stations.

Acknowledgements

This work was undertaken at the Global Seismology Unit of the British Geological Survey and was supported by a research studentship grant from the Natural Enviroment Research Council. I would like to thank my supervisor Stuart Crampin for giving me the opportunity to carry out research in such a new and promising field. His encouragement, advice, and enthusiasm contributed significantly to the project.

I would also like to thank everyone at GSU who has helped particularly Russ Evans for help and advice during the early stages of this work and with computing; Chris Browitt, Terry Turbitt, and Alice Walker for access to and help with the Cornwall data; Charlie Fyfe for help with the computing facilities at GSU, and Bob McGonigle and David Booth for the use of some computer programs.

I am particularly in debted to fellow students at GSU - Andrew McDonald, Colin Macbeth, Ian Main, Jas Singh, Alan Logan, and Sheila Peacock for discussions, help, and keeping spirits up when things were not going as well as they might have been.

I also thank the Geophysics Department for supplying computing and giving me a solid background in Geophysics.

I would like to thank Jim Scheimer for access to data from Livermore, and for making my stay at Livermore very pleasant. Jon Fletcher is thanked for the data from Monticello.

Finally I thank my wife Joan who has had to put up with me 'doing my thesis' over the last three and a half years, and the arrival of my daughter Claire for ensuring a speedie finish.

CONTENTS

PAGE

CHAPTER ONE

INTRODUCTION: SHEAR-WAVES AND ANISOTROPIC PROPAGATION

1.1 Introduction

Seismology is a science based on records of the mechanical vibrations of the earth called seismograms (Aki & Richards 1980). A seismogram is dependent on three factors - source, medium, and receiver. Seismic energy is radiated from the source propagates through the medium and is detected at the receiver. Seismic sources can be caused by stress release within the crust or upper mantle, or they can be generated artificially, for example, by explosives. The medium is simply the part of the earth through which the seismic energy dissipates. Its composition, degree of homogeneity, the pressure and temperature conditions, and the dimensions of the seismic wavelength influence the behaviour of the seismic energy as it travels through the medium. The receiver records the mechanical vibrations of the earth at a single point. Ground vibrations can be recorded as variations of displacement, velocity, or acceleration with time. From the information contained in the seismogram an attempt is made to build up a picture of the mechanical and dynamical properties of the source and medium. In this way models of seismic source mechanisms and the earth's internal structure can be constructed. The main interest of the dissertation is the effective anisotropic elasticity of the medium, caused by aligned crack structures in the crust.

The object is to identify and assess effective seismic anisotropy in the upper crust from the analysis of shear-wave particle motion recorded on three-component seismograms. The motivation derives from work by Crampin (1978, 1981), which showed that structures of aligned cracks are effectively anisotropic

to seismic waves, and that the behaviour of shear-waves, particularly shear-wave splitting, offer the most diagnostic features indicative of wave propagation through an anisotropic medium.

On entry into an anisotropic zone a plane shear-wave splits into two orthogonally polarized phases which are not, in general, parallel to either the vertical or horizontal directions. The shear-waves travel with different velocities, hence become split, and result in shear-wave particle motion being resolvable into nearly orthogonal components. A schematic diagram illustrating shear-wave splitting is shown in Figure 1.1. The characteristic signature written into the polarization of the shear-wave will persist for any isotropic segment of the ray path. The time delay between the split shear-waves and the polarization of the first shear-wave can be used to evaluate the geometry and orientation of the anisotropy (Crampin & McGonigle 1981). This can convey information about, the mineralogy and internal structure of the anisotropic rock, and possibly the ambient or paleo stress field. In contrast, the behaviour of the P-wave is modified by anisotropic propagation in subtle ways which are difficult to recognise on seismograms (Crampin et al. 1981). Only when accurate velocity measurements can be made for propagation in many directions over a single plane will the effects of anisotropy be easily distinguished.

Shear-wave splitting is usually not observed on standard playouts of the three-components of ground vibration as linear traces with time. It is most easily identified by displaying the three-component records as polarization diagrams: three mutually perpendicular sections of particle motion for successive time intervals (Crampin et al. 1984a). An example of a three-component seismogram trace and the corresponding polarization diagrams recorded during the monitoring of hydrofracture-induced seismicity at a Hot Dry Rock site in Cornwall is shown in Figure 1.2. The shear-wave particle motion displays abrupt changes in direction expected for the arrival of split shear-waves, and the arrows

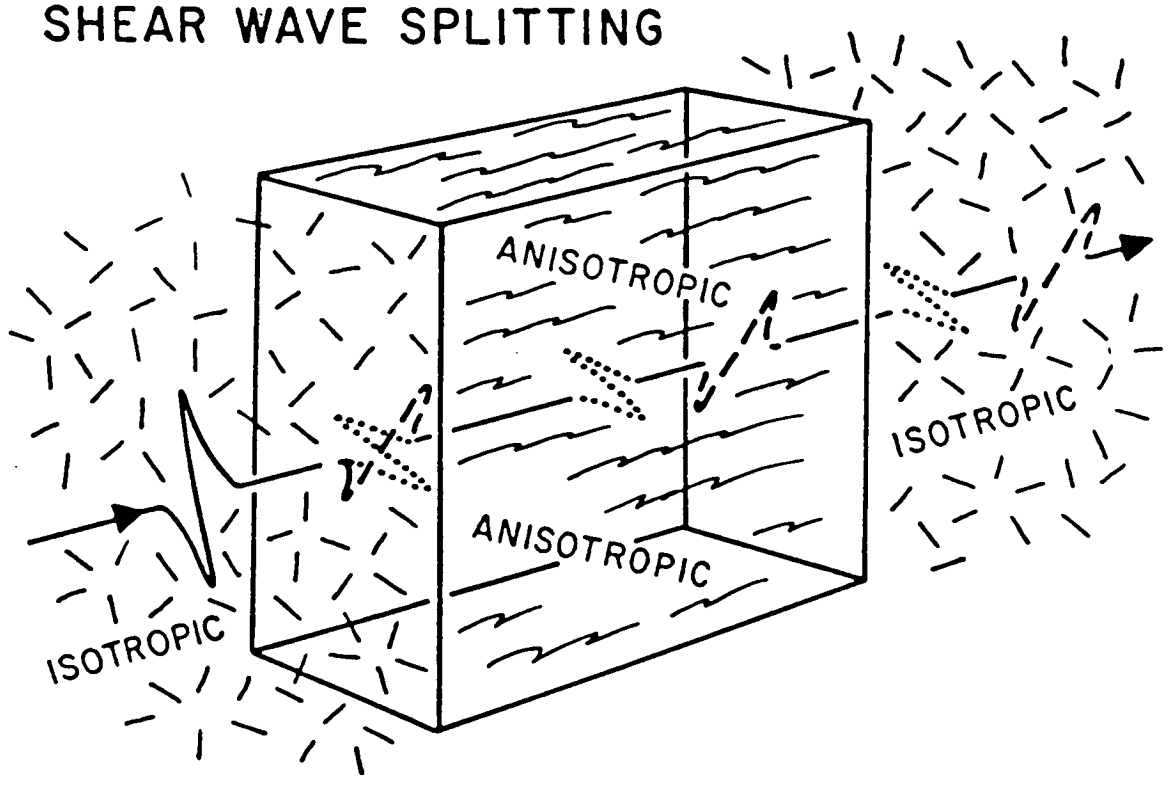
SHEAR WAVE SPLITTING
ANISOTROPIC
ANISOTROPIC
ISOTROPIC
ISOTROPIC

Figure 1.1

Figure 1.2

An example of a three-component seismogram and polarization diagrams for an acoustic event recorded at a Hot Dry Rock site, Cornwall on 20 November 1982, with epicentre 50° 10.24'N, 5° 10.54'W, and a depth of 2.34 km. The seismograms were recorded at station CTR at an epicentral distance of 1.06 km and an azimuth of N 116°E from the epicentre. The seismogram traces are unrotated with components orientated vertical (Z), north-south (NS), and east-west (EW). The polarization diagrams are three mutually orthogonal sections of particle motion. The upper polarization diagrams show particle motion in the vertical/north-south plane; the middle row of polarization diagrams show particle motion in the vertical/east-west plane, and the lower polarization diagrams show particle motion in the horizontal plane. The polarization diagrams are plotted at successive time intervals, corresponding to the time windows marked above each seismogram. Time window length is 0.07 seconds. Directions: U-up; D-down; N-north; S-south; E-east; W-west. Each set of three diagrams have been normalised and the relative multiplication factor is marked at the bottom of each diagram. Cross bars are marked on the polarization diagrams at every 0.0025 seconds. The heavy arrows on the horizontal projection of the shear-waves mark the first shear-wave arrival and a possible later arrival with a different polarization.

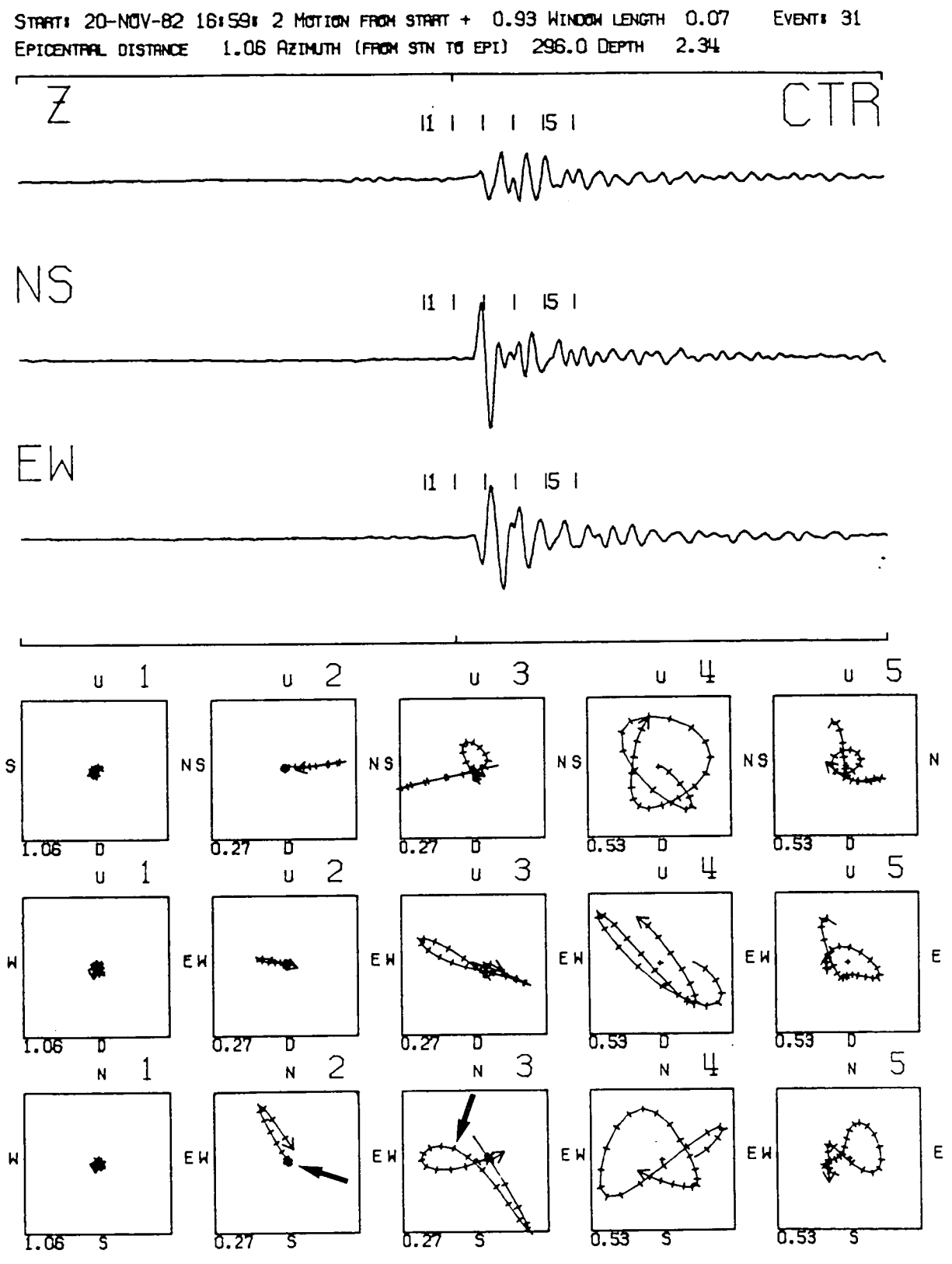
START: 20-NOV-82 16:59: 2 MOTION FROM START + 0.93 WINDOW LENGTH 0.07 EVENT: 31
EPICENTRAL DISTANCE 1.06 AZIMUTH (FROM STN TO EPI) 296.0 DEPTH 2.34
Z
CTR
NS
EW
U 1
U 2
U 3
U 4
U 5
S
NS
N
W
E
D
N 1
N 2
N 3
N 4
N 5
1.06
0.27
0.53
S

Figure 1.2

in the polarization diagrams indicate the probable shear-wave arrivals.

The analysis of the particle motion of shear-waves has been a relatively neglected topic in seismological research. Occasional studies, however, are present in the literature. The developing interest in earthquake focal mechanisms in the late 1950's and early 1960's led some seismologists (Hodgson 1959; Stauder 1960) to develop methods of utilising shear-wave particle motion in such studies. Observations of the complexity of shear-wave particle motion by Hodgson (1960) and Byerly (1960) initiated a study by Nuttli (1961) on the effect of the earth's surface on the shear-wave particle motion. Nuttli & Whitmore (1962) developed a method for determination of the polarization angle of the shear-wave, and Nuttli (1964) created a technique for polarization angle determination in an earth model with crustal layers. Subsequently Mendiguren (1969) used polarizations of the shear-wave to study focal mechanisms of deep earthquakes occurring in northern Argentina. In the last decade, primarily due to advances in computer technology, numerical experimentation with computer programs enabled studies of shear-wave propagation through various earth models to be modelled by synthetic seismograms (Kind & Müller 1973; Herrmann 1976; Crampin 1978; Booth & Crampin 1983). This was a significant step forward since synthetic seismograms generated from realistic sources and media could be compared to observations. However, studies of observed shear-wave particle motion were still sparse, primarily due to a lack of adequate three-component recording, and possibly because of the often complex nature of shear-wave particle motion. Over recent years several networks of three-component instruments have been deployed both on a permanent and temporary basis (Crampin et al. 1980; Taylor & Scheimer 1982; Fletcher 1982) thus allowing observational studies of shear-wave particle motion.

In this chapter I will discuss: the main features of body-wave propagation in anisotropic media; the likely causes and observations of crustal anisotropy; the

influences of the source, medium, and free surface on shear-waves, and finally the three data sets which are available for shear-wave particle motion analysis. The discussion in this chapter provides the necessary background for the interpretation of the shear-wave particle motion. The techniques used in shear-wave particle motion analysis are outlined in the next chapter and the results from the various data sets are discussed in the following four chapters.

1.2 Theory of anisotropic propagation for body-waves

The propagation of seismic waves in anisotropic media has been discussed by Crampin (1977) and Keith & Crampin (1977 a, b, c). The main differences in behaviour of body-wave propagation in homogeneous isotropic media to propagation in homogeneous anisotropic media are easily illustrated following Crampin (1981).

The elastodynamic equations of motion in a uniform homogeneous elastic anisotropic medium are:

$$p\ddot{u}_i = c_{ijpq}\, u_{p,qj} \qquad i = 1,2,3 \tag{1.1}$$

where p is density, u_i is displacement, and c_{ijpq} are the elements of the fourth order elastic tensor. The dot notation for differentiation and the repeated suffices notation for summation are used throughout.

For convenience the elastic tensor has been rotated into a coordinate system by the usual tensor transformation (Jeffreys 1965) so that the direction of phase propagation is along the x_1- coordinate direction with the x_3- coordinate direction vertically downwards. The general expression for the harmonic displacement of a homogeneous plane-wave propagating along the x_1- axis is:

$$u_i = a_i \exp\left(iw\,(t - q_j x_j)\right) \tag{1.2}$$

where a_i is the amplitude vector specifying the polarization of the particle motion, and q_j is the slowness vector, where $\mathbf{q}=(1/c,0,0)$ and c is the phase velocity.

Substituting the displacement (1.2) into the equation of motion (1.1) gives three simultaneous equations which can be solved for the phase velocity, c, as a linear eigenvalue problem for pc^2:

$$(T - pc^2 I)\,\mathbf{a} = 0 \qquad (1.3)$$

where T is the 3x3 matrix with elements c_{ijpl} and the time dependence, exp(iwt), is omitted for convenience.

The eigenvalue problem has real positive roots for pc^2 with orthogonal eigenvectors a_j. These roots refer to the phase velocities of a quasi P-wave and two quasi shear-waves with their polarizations defined by the eigenvectors a_j.

It is immediately recognisable that wave propagation in anisotropic media is fundamentally different from wave propagation in isotropic media. In every direction of phase propagation in an anisotropic medium there are three body-waves propagating with velocities varying with direction and with orthogonal polarizations fixed for the particular direction of phase propagation. The anisotropic symmetry is defined by the elements of the elastic tensor. Since, in general, two shear-waves travel with different velocities it is apparent that shear-wave splitting is characteristic of shear-wave propagation in anisotropic media. From extensive numerical experimentation (Crampin 1978; Crampin & McGonigle 1981) it has been recognised as the most diagnostic feature of anisotropy.

Further complications arise because the wave number, which is usually a scalar quantity for wave propagation in isotropic media, becomes a vector. As a result the expression for body-wave group velocity,

$$U = dw/dk \qquad (1.4)$$

where U is the body-wave group velocity, w is the angular frequency, and k is the wavenumber becomes:

$$\mathbf{U} = (dw/dk_1,\ dw/dk_2,\ dw/dk_3) \qquad (1.5)$$

Therefore the propagation of energy, in general, deviates both in velocity and

direction from the direction of the phase propagation. This means that the behaviour of waves from point sources with approximately spherical wavefronts is different from the behaviour of plane-waves. However, in weakly anisotropic media, the deviation of the group velocity from the phase velocity direction is, in general, negligible.

The significance of the techniques used to evaluate seismic anisotropy was realised when Crampin (1978) recognised that wave propagation through a two-phase material could be simulated by propagation through a homogeneous anisotropic material. Crampin (1978) modelled wave propagation through cracked isotropic solids, with properties theoretically determined by Garbin & Knopoff (1973, 1975a, 1975b), by approximating the inhomogeneous material to a homogeneous solid with effective elastic constants having the same variation of velocity with direction as the cracked solid. This showed that crack structures are effectively anisotropic to seismic waves provided the dimensions of the cracks are small in comparison to the seismic wavelength. Therefore, in theory, in situ crack structures in the crust can be modelled from seismic observations.

1.3 **Seismic anisotropy in the earth's crust**

1.3.1 Causes of crustal anisotropy

Various phenomena may cause rocks to display effective seismic anisotropy, for example alignments of grains or crystals, or the propagation of long seismic wavelengths through thin sedimentary layers (Backus 1962; Christensen 1984; Robertson & Corrigan 1983). However, probably the most common cause of effective seismic anisotropy in the crust derives from the propagation of seismic waves through aligned crack structures (Crampin et al. 1984a).

The presence of orientated crack structures within the crust is essentially dependant on two factors. First cracks must be ubiquitous in the crust, and secondly these cracks must align under the prevailing low magnitude deviatoric

stresses (Crampin et al. 1984b). Stress drop calculations (Fletcher 1982; Hanks & Wyss 1972) and in situ stress measurements (Zoback & Hickman 1982; Klein & Brown 1983) indicate that stress fields of about 10 MPa or so pervade the upper crust. Atkinson (1979) has shown that cracks can develop within a rock under such low magnitude stresses by the process of subcritical crack growth. Although it is often assumed that cracks are closed at depths below 1 or 2 km because of increased lithostatic pressures, there is experimental evidence (Stierman et al. 1979; Brace 1980) and observational evidence from deep boreholes (Kozlovsky 1984) which suggests that liquid filled cracks or pores will exist deeper in the crust. Also experimental observations on stressed rock samples suggest aligned cracks can be created from random existing crack structures subjected to fairly low magnitude deviatoric stresses. Nur & Simmons (1969) showed that in a sample of rock under uniaxial stress existing cracks normal to the stress axis closed preferentially to cracks parallel to the axis. This caused elastic wave velocity anisotropy, where the compressional waves travelled fastest in the direction of the applied stress, and two shear-waves travelled with different velocities in any direction, exhibiting shear-wave splitting. Other experimental work has shown orientated crack structures develop from random pre-existing crack distributions in stressed rock samples (Hadley 1975), and that shear-wave splitting occurs when shear-waves are propagated through cracked rock samples (Gupta 1973 a, b).

Hence the experimental work illustrates that cracks are likely to pervade the crust (Atkinson 1979; Brace 1980), that they will align under low magnitude deviatoric stresses (Hadley 1975; Nur & Simmons 1969) and that acoustic shear-wave splitting and velocity anisotropy result when shear-waves propagate through cracked rock (Nur & Simmons 1969; Soga et al. 1978).

If such an aligned system of cracks is present within the earth's crust and it exerts a major influence on wave propagation then recognition of the diagnostic

effects of wave propagation through effective anisotropic media is a useful tool in determining the density, geometry and orientation of the crack structure. Crampin & McGonigle (1981) have shown that shear-waves offer the most sensitive technique for evaluating anisotropic parameters. So by continuously monitoring shear-waves, the in situ stress field may be investigated since it is the stress field which gives rise to the anisotropic character of the crack distribution. The generation of effective seismic anisotropy from crack alingment by stress-induced processes is called extensive-dilatancy anisotropy (EDA). EDA has been put forward by Crampin et al. (1984b) as a new physical basis for earthquake prediction. In addition to assessing changes of stress another possible application is assessing crack distributions in geothermal heat or hydrocarbon reservoirs.

1.3.2 Observations of crustal anisotropy

Widespread velocity anisotropy in the crust is not observed, probably due to lateral and vertical inhomogeneties in the earth's crust which make azimuthal velocity variations on a large scale difficult to recognise. Some reports of crustal velocity anisotropy are present. For example, Dorman (1972) observed crustal seismic velocity anisotropy in northern Georgia and attributed it to aligned cracks. Bamford & Nunn (1976) carried out small scale azimuthal velocity determination experiments with explosive sources in fractured limestone which showed strong azimuthal velocity anisotropy. Seismic velocity anisotropy in underground mines in Khibiny, USSR, has been correlated with in situ stress measurements (Turchaninov et al. 1977).

After the experimental work of Nur & Simmons, Gupta, etc. interest was stimulated in field observations of shear-wave splitting. Gupta (1973c) claimed to observe variations in split shear-wave time delays prior to a M_L=0.4 earthquake in Nevada, which he attributed to a stress increase in the earthquake

source region. Ryall & Savage (1974) contested Gupta's criteria for shear-wave identification, but Crampin et al. (1981) point out that both reports are in error as a result of misunderstandings in the nature of wave propagation in anisotropic media. Shear-wave splitting has been observed in Armenia, USSR. Yegorkina et al. (1977) attribute velocity anisotropy to the stress state of the earth's crust in Armenia, and the spatial mapping of shear-wave time delays has been used for the same region to model the underlying crack distribution (Bezgodkov & Yegorkina 1984).

During the summer of 1979 and 1980 the Turkish Dilatancy Project (TDP) was set up to investigate shear-wave splitting above a swarm of small earthquakes near the North Anatolian fault in northern Turkey (Crampin et al. 1980; Crampin et al 1984c). Shear-wave splitting was a common feature on many seismograms, and the orientation of the shear-wave polarizations at most stations were aligned parallel to the axis of maximum compression (Booth et al. 1984). This shear-wave polarization distribution has been interpretated in terms of aligned crack structures in the crust by Crampin & Booth (1984).

1.4 **Shear-wave propagation: source, medium, and free surface**

The analysis of shear-waves is extremely complicated, particularly in the case of local seismic events where the plane-wave approximation does not apply. Many factors other than anisotropic effects must be considered in the interpretation of shear-waves and their coda. Shear-wave splitting is only one potential phenomeneon and cannot be treated in isolation from the other factors which influence shear-wave propagation. In the dissertation the object is to search for evidence of wave propagation in effective anisotropic media, therefore the main concern is the effect of the medium on shear-waves. However details of the influence of the source and the free surface on shear-waves are necessary in order to isolate the effects of the medium. Such non-

anisotropic influences on shear-wave propagation are outlined in this section.

1.4.1 Plane shear-waves at the free surface

Most seismic recordings are made at the free surface. The free surface interaction has a major effect on the waveform of the recorded shear-wave. The simplest shear-wave free surface interaction is that of a plane shear-wave of arbitrary polarization propagating through an isotropic half space and incident on a planar free surface at an arbitrary angle of incidence. The equations describing the resultant shear-wave particle motion are well known (Nuttli 1961; Aki & Richards 1980) and give an insight into the free surface interactions of teleseisms.

For an understanding of free surface effects resulting from an incident shear-wave in an isotropic half space, it is crucial to note that the event identified as the shear-wave onset on the seismogram is the resultant of the motion produced by the incident shear-wave and the reflected shear- and P-phases. Hence the motion of a particle on the earth's surface at the time of arrival of the shear-wave will, in general, not be transverse to the ray and for certain angles of incidence will not be linear but will describe a three dimensional figure. Nuttli (1961) analysed this problem and his results can be summarised simply. For angles of incidence less than $\arcsin(V_S/V_P)$, the critical angle, where V_P and V_S are the P-wave and shear-wave velocities respectively, at the earth's surface, all three components of ground motion (vertical, radial, and transverse) will be in phase and the resultant motion is linear for a linear incident polarization. For angles of incidence greater than the critical angle all three components of ground motion will, in general, be out of phase with resultant motion describing some three dimensional figure. The value of the critical angle at the earth's surface is usually between 30^{o} and 40^{o}.

The main effect of the free surface on plane shear-waves is the introduction

of ellipticity into the particle motion, and the domination of the transverse-component of displacement for angles of incidence much greater than the critical angle. For plane shear-waves incident at angles less than the critical angle a shear-wave window occurs where all the components of displacement of the incident shear-wave are approximately doubled at the free surface (Evans 1984). Hence the waveform of the incident shear-wave is preserved, and, within this shear-wave window, shear-waves are recorded with very little distortion due to the free surface.

1.4.2 Curved shear-waves at the free surface

At local and regional distances the shear-wave particle motion at the free surface is due to the interaction of curved wavefronts with the free surface. Using synthetic seismograms Booth & Crampin (1984) showed that curved shear-wavefronts exhibit similar behaviour to the plane shear-wave interactions at the free surface. However the critical angle is now also dependant on the seismic wavelength, the aperture of the effective shear-wave window is increased by the curvature of the wavefront, and the shift from linear to elliptical particle motion beyond the critical angle is less abrupt.

Probably the most significant consequence of curved wavefronts interacting with the free surface is the generation of the surface P- or SP-phase. This pulse originates at the source as a shear-wave, undergoes critical reflection at the surface, and subsequently propagates along the surface as a head wave with the P-wave velocity.

The SP-phase was originally described by Nakano (1925) but since then it has stimulated little attention, and has only been recognised in a few theoretical papers (eg. Lapwood 1949; Bouchon 1978). Bouchon (1978) showed that the SP-phase is most prominant in the horizontal seismogram and has very little impact on the vertical-component resulting in apparently uncorrelated horizontal and

vertical seismograms. Bouchon, however, presents his results as Green's functions. Only since Booth & Crampin (1983) modelled waveforms at the free surface using synthetic seismograms has the SP-phase been displayed in a form suitable for the interpretation of shear-wave observations. Their results show that at angles of incidence beyond the critical angle the SP-phase appears as a precursor to the direct shear-wave arrival, and that its amplitude is largest on the radial-component of a recorded seismogram. Outside the shear-wave window the SP-phase may be misidentified as the direct shear-wave particularly since a reduction of shear-wave amplitude in the radial direction occurs at angles of incidence beyond the critical angle. Also the uncorrelated seismogram may be interpreted as shear-wave splitting arising from wave propagation in anisotropic media.

A key feature in the identification of the SP-phase is the early radial onset. The vertical-component of the SP-phase is small so, in principal, the shear-wave onset could be identified in the vertical/transverse plane (Booth & Crampin 1983). A further complication can arise when topography, on occasion, results in the local angle of incidence exceeding the critical angle with the effect that the SP-phase can be recorded within the shear-wave window (Crampin 1983). Observations of the SP-phase have been identified, apparently for the first time, on three-component seismograms recording local seismicity in northern Turkey during the TDP projects (Evans 1984).

To summarize, recording shear-waves at the free surface places several constraints on our ability to reconstruct the incident shear-wave. Outside the shear-wave window the introduction of ellipticity, the domination of the transverse-component plus the interference of the locally generated SP-phases all contrive to alter the incident shear-wave polarization and significantly rewrite the original particle motion. Consequently, shear-wave particle motion analysis should be conducted within the shear-wave window to reliably recover

the effects of the source and medium on shear-wave propagation.

1.4.3 Source mechanism

Earthquake sources are a consequence of failure within the earth due to a temporary breakdown of the elastic stress-strain relation represented by Hooke's law (Doornbos 1981). Typically failure of material is caused by low magnitude forces acting for a long time period eventually resulting in energy release in the form of fracture and the radiation of seismic energy. Earthquake source mechanism is usually visualized as slip along a plane of fracture. This can be represented by a displacement discontinuity along an internal surface within a medium where Hooke's law holds. The seismic effect of the displacement discontinuity is equivalent to the excitation of the medium by a distribution of body-forces acting at a point within the medium. These body-forces have a spatial and temporal distribution. The spatial distribution is represented by the seismic moment tensor and the temporal distribution by the source-time function. These forces arise when substituting into the equations of motion the true physical stress by stress satisfying Hooke's law. They are called equivalent body-forces and offer the most effective technique to model any type of internal seismic source.

Earthquakes radiate shear-waves with polarizations which are fixed at the source by the geometry and orientation of the source mechanism, as defined by the seismic moment tensor. The initial shear-wave polarizations from a known source mechanism can be determined using the body-force representation of the seismic source. The alignments of these polarizations will be preserved from source to receiver for shear-waves propagating through a homogeneous isotropic structure. Therefore if the orientation of the shear-wave polarization differs from that predicted from the source mechanism the medium must, in some way, alter the initial shear-wave polarization. In which case the medium cannot be

assumed to be simply homogeneous and isotropic.

The energy distribution between split shear-waves depends upon the orientation of the shear-wave polarization with respect to the anisotropic vibration directions (the shear-wave polarization directions of the split shear-waves) prior to its entry into an anisotropic zone. Their orientation is dependent on the anisotropic symmetry and orientation of the ray path through the anisotropic region (see section 1.2). Therefore the alignment of the initial shear-wave polarization from the source is also a factor controlling the type of shear-wave splitting. For example shear-wave splitting will not occur if the source generates a shear-wave polarization parallel to one of the anisotropic shear-wave polarization directions.

1.4.4 The medium

An effectivey anisotropic medium affects shear-waves in a fundamental way with the propagation of two shear-waves (at least) in most directions. Inhomogeneous and/or layered isotropic media do not affect shear-waves so fundamentally, but the generation of converted phases, multiple reflections, head waves etc. introduces complexities to the interpretation of shear-wave particle motion. As an example consider converted phases from a near-source or near-surface interface.

A converted phase is seismic energy which has travelled partly as a shear-wave and partly as a P-wave. It derives from reflection or refraction at oblique incidence on an interface between two materials.

In isotropic media a shear-wave of arbitrary polarization is represented by an SV-phase and an SH-phase. The polarization of the SV-phase is perpendicular to the ray path and lies in the sagittal plane (the vertical plane through the direction of phase propagation). A P-phase or SV-phase incident at a planar interface generates reflected and refracted P-phases and SV-phases as their

excitations both lie in the sagittal plane. The P-wave polarization is of course parallel to the ray path. The SH-phase, however, is polarized at right angles to the sagittal plane. An incident SH-phase generates only reflected and refracted SH-phases as no motion is excited in the sagittal plane. Converted phases are only likely to be recorded in the vertical and radial directions since SH-excitation decouples from P/SV-excitation. Hence the true shear-wave arrival may be observed in the transverse direction.

However the orientation of the direct shear-wave polarization could be modified by the interference of a converted phase, generated at either a near-source or near-surface interface, with the direct shear-wave. Synthetic seismograms are often generated to ascertain the relative amplitudes of converted phases (Kennett 1980; Hron & Covey 1983; Kempner & Gettrust 1982ab). Usually many layers are modelled and depending on seismic wavelength, layer thickness, and velocity contrasts between layers, a host of phases can be generated. Synthetic seismograms from such models are complex. Synthetic seismograms are illustrated in Figure 1.3, from Booth & Crampin (1983), for a shear-wave travelling through an isotropic half space with a near-surface low velocity layer. This shows that even simple earth structures can generate complicated seismograms, with an S to P converted phase interfering with the direct shear-wave at close distances.

Consequently, an idea of the local geological structure is useful as it may indicate if such non-anisotropic medium effects on wave propagation are likely to dominate. In particular it is helpful to have knowledge of the size of structures with respect to the seismic wavelength.

1.5 **The data**

Three data sets are available for shear-wave particle motion analysis.

1. Jon Fletcher sent data recorded by a temporary network of three-component

Figure 1.3
Synthetic seismograms illustrating the interference of an S to P converted phase with the direct shear-wave on the vertical and radial components. A shear-wave polarized at SV45SH is radiated from a source at 1 km depth in a half space with a low velocity surface layer. Details in Crampin (1983).

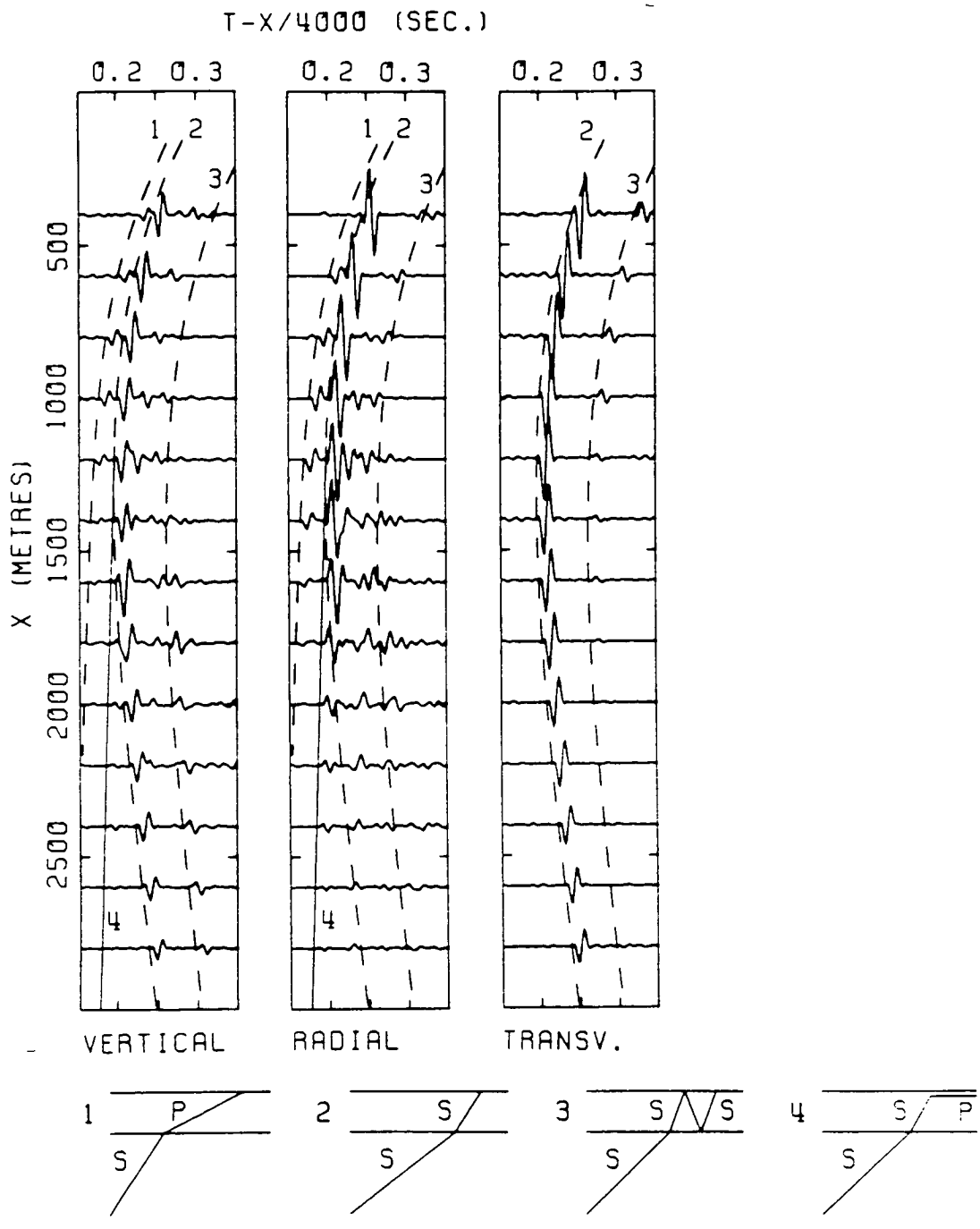
T-X/4000 (SEC.)
0.2 0.3
0.2 0.3
0.2 0.3
1 2
3
4
500
1000
1500
2000
2500
X (METRES)
VERTICAL
RADIAL
TRANSV.
1 P S
2 S S
3 S S S
4 S P S

Figure 1.3

stations monitoring reservoir-induced seismicity at Lake Monticello, South Carolina.

2. The second data set was recorded by the Global Seismology Research Group (GSRG) of the British Geological Survey (BGS) to monitor seismicity at a Hot Dry Rock Geothermal Energy Project site run by the Camborne School of Mines at Rosemanowes Quarry, Cornwall.

3. I visited the Lawrence Livermore National Laboratory (LLNL), Livermore, California where I selected data from their seismic network of three-component stations deployed to monitor the seismicity of the Livermore Valley.

Each data set consisted of three-component recordings of short period seismic records. The main objective is to search for shear-wave splitting and measure shear-wave polarizations for each data set to see if the results are consistent with shear-wave propagation through effectively anisotropic structures.

CHAPTER TWO

DATA PROCESSING AND ANALYSIS TECHNIQUES

2.1 Introduction

To avoid repetition in later chapters, the basic steps involved in data processing and the analysis of shear-wave particle motion are outlined in this chapter. In subsequent chapters the results for each data set are discussed.

Originally the seismic records are stored on magnetic tape. Each data set is written on the magnetic tape in different formats and has to be processed from its original to a format suitable for the generation of polarization diagrams. This stage in the analysis is described as data processing, and the end objective is to display the data from the magnetic tapes as three-component seismogram traces and polarization diagrams.

After data processing the particle motion of the shear-wave is analysed. This involves measuring shear-wave polarizations from the polarization diagrams, and utilising techniques to interpret the observations. This stage is primarily concerned with displaying, quantifying, and interpreting the particle motion of the shear-wave.

2.2 Data processing

An analogue to digital (A to D) processing system is used by the Global Seismology Research Group (GSRG) to digitize analogue magnetic tapes recorded on RACAL T81000 and Geostore systems. The A to D hardware consists of a PDP 11/50 minicomputer with an 11 bit A to D converter and associated peripherals (Evans 1980). The digitization software produces tapes in a standard format - a series of physical files with no volume, header, or

trailer labels (Evans 1980). Each file consists of a header block and many data blocks. The header block is 3200 bytes long and consists of forty ASCII encoded card images containing details of station location and instrumental response. The data blocks are of constant length throughout the file - in the range 4072 to 4096 bytes depending on the number of channels on the analogue magnetic tape which are digitized. The seismic records are stored in multiplex format. Each data block contains a fixed number of frames where a single frame contains a single sample from each channel. A suite of data handling computer programs is available, including the program PMPLOT which plots data in this format as three-component seismogram traces and polarization diagrams.

For each data set we are faced with the problem of either reformatting the original data to the GSRG standard format described above or adapting the available computer programs to generate seismogram traces and polarization diagrams. A different approach is used depending on the original format of the data.

2.2.1 The Monticello data set

Seismic records of the induced activity at Monticello reservoir are stored on two 1600 bpi magnetic tapes. Each magnetic tape consists of a series of logical files. Each logical file contains a header file with station and event information; a data file consisting of a single digitized seismic record in time sequential format and a trailer file. Note that each seismic record is a single-component recording of a three-component set. For this data set, the data on the original magnetic tapes is reformatted to the standard GSRG tape format. Primarily this is because the maximum number of input/output channels which can be opened simultaneously on the PDP 11/50 minicomputer was less than the maximum number of channels on the digital magnetic tape which required

to be multiplexed. Software for multiplexing is then easily written. However, complications arose during multiplexing of the data because different seismic stations were triggered at different times for a single event. Therefore it is necessary to correct for the relative time shifts between seismic record start times at different stations.

The reformatting of the Monticello data is tackled in two stages.

1. Data from selected events undergoes minor reformatting and is transferred from the original magnetic tape to an RK05 disk.
2. Major reformatting of the data is carried out on the RK05 disk. This includes multiplexing, and transfer of data from the RK05 disk to magnetic tape where the seismic records are stored in standard GSRG format.

Only events which are recorded by three or more stations are transferred from magnetic tape to RK05 disk since this is the minimum required to locate the hypocentre. The computer program F11TDK is written to achieve this, and to reduce the time length of the seismogram. The computer program FFTGSU completes the reformatting process by multiplexing the data on the disk, creating standard GSRG header blocks within data files, and transferring the reformatted data to magnetic tape. The end product is a magnetic tape of seismograms of selected events from the Monticello data set in standard GSRG format. The computer program PMPLOT is then used to generate three-component seismogram traces and polarization diagrams.

2.2.2 The Cornwall data set

The recordings from the GSRG seismic network in Cornwall are available on analogue magnetic tape at the British Geological Survey (BGS). Seismic records from the analogue magnetic tapes are digitized on the PDP 11/50 minicomputer and Store 14 RACAL T81000 replay system. The maximum number of channels which can be simultaneously digitized is 16 and the

maximum sampling rate which the computer can handle in real time is 12000 samples per second (sps).

The above figures set the following condition on the sampling rate of each seismogram (Houliston & Laughlin 1976; Evans 1981):

$$s < 12000\, r_0/n\, r_1 \qquad (2.1)$$

where s is the sampling rate, r_0 is the recording speed of the analogue magnetic tape on the Geostore, r_1 is the replay speed of the analogue magnetic tape on the Store 14, and n is the number of channels on the analogue magnetic tape which can be simultaneously digitized. Another restriction on the value of s, due to instrumental hardware, is that s must equal 2^N, where N is an integer.

The first approach is to digitize selected seismic records using the computer program ADC (Evans 1980). At one pass all relevant channels and all specified events on the analogue magnetic tape are digitized. The number of channels, n, simultaneously digitized is 12 (3 x three-component seismograms + strong motion seismogram + internal clock + MSF). The record speed, r_0, is 15/160 ins/sec and the analogue magnetic tapes are replayed at the minimum replay speed, r_1, of 15/16 ins/sec to give a maximum sampling rate, s, of 100 sps. The computer program PMPLOT generates polarization diagrams of the digitized data.

Figure 2.1a shows an example of a 100 sps digitized seismogram with the shear-wave particle motion illustrated in the corresponding polarization diagrams. The particle motion of the shear-wave is jagged because of coarse sampling with respect to the frequency content of the signal. Only four or five samples represent a single pulse. This makes determination of the initial shear-wave polarizations and time delays highly subjective and open to erroneous interpretation. To improve the representation of the shear-wave particle motion the records are digitized at a higher sampling rate of 400 sps.

Figure 2.1

Three-component seismogram traces and polarization diagrams for the acoustic event at Cornwall on 7 November 1982, with epicentre 50° 10.10'N, 5° 10.82'W, and depth 2.62 km. The seismograms were recorded at station CRA at an epicentral distance of 1.12 km and at an azimuth of N 244°E from the epicentre. Notation and format as in Figure 1.2.
(a) Seismogram sampled at 100 samples/second - cross bars at every 0.01 second. (b) Seismogram sampled at 400 samples/second - cross bars at every 0.0025 second.
This illustrates the difference in particle motion when the sampling rate is 100 samples/second and 400 samples/second.

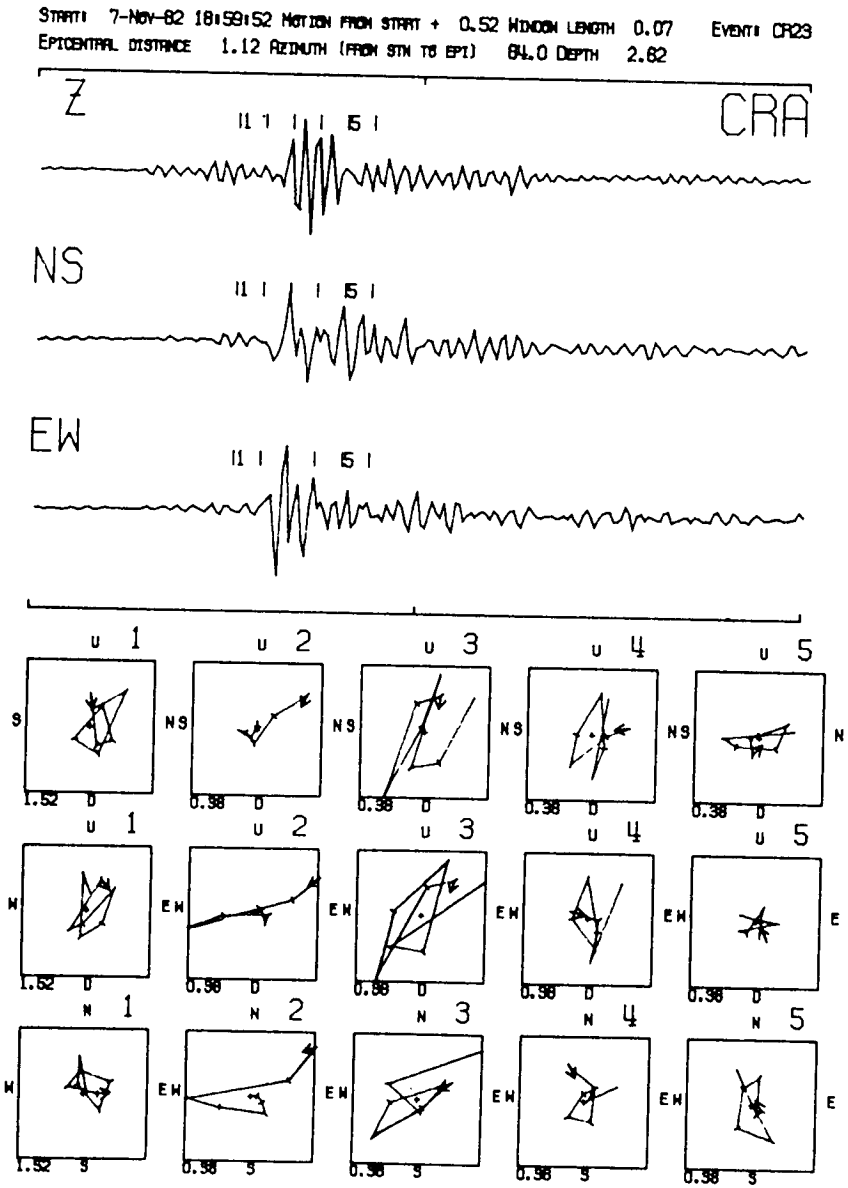

Figure 2.1a

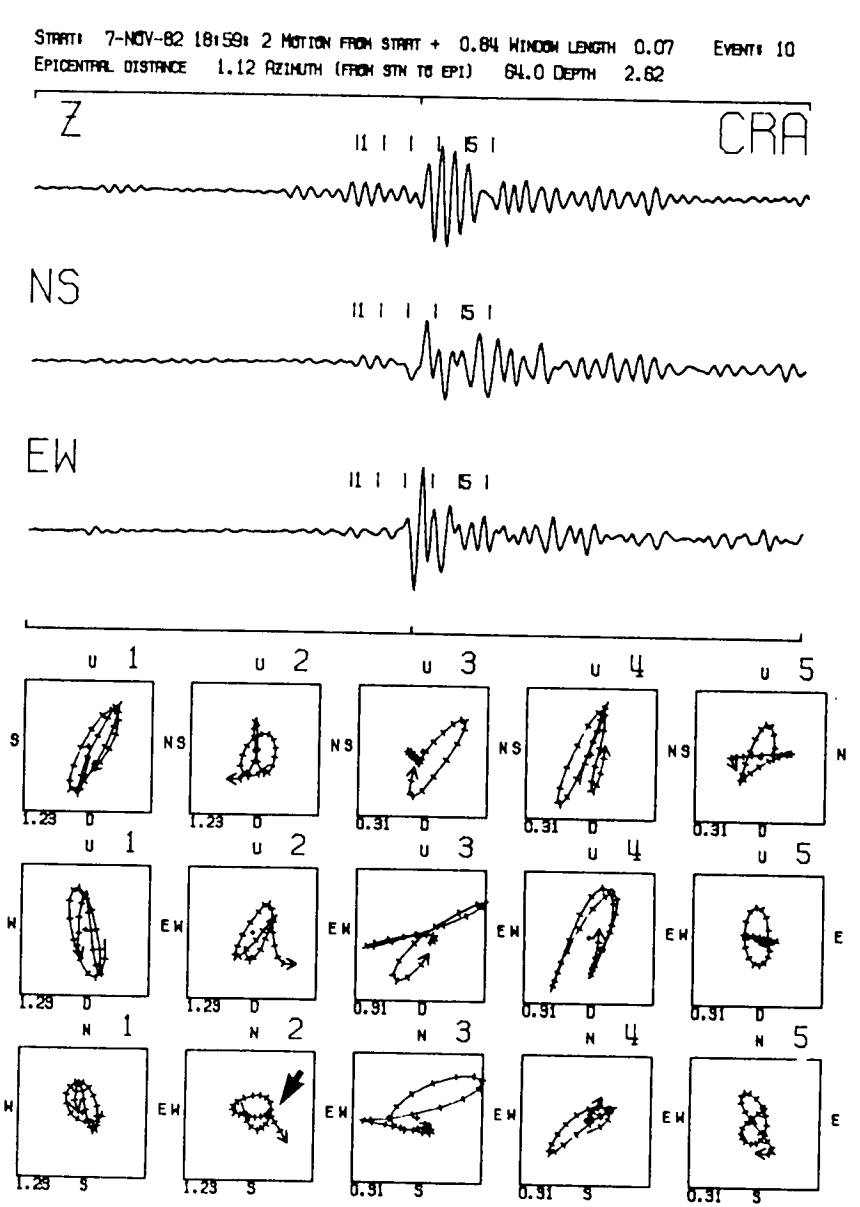

Figure 2.1b

Only three channels can be simultaneously digitized at 400 sps, so that one three-component seismogram is digitized at a single pass. Since the time clock is not digitized the more robust digitizing program MTDIG is used for digitization. ADC format header blocks are added after the digitized data is windowed to produce a 5 second seismic record. In this final format the computer program PMPLOT, with minor modifications, is used to generate three-component seismogram traces and polarization diagrams. The seismogram, now digitized at 400 sps, and the corresponding polarization diagrams are shown in Figure 2.1b. The waveforms on the digital seismic traces are identical to those on the original analogue record. Therefore the higher sampling rate significantly improves the representation of the digitized shear-wave particle motion.

The increased sampling rate of 400 sps does not increase the amount of information available in the seismic records. Instrumental filters in the Store 14 result in a frequency cut-off at 320 Hz real time. For the Cornish tapes the replay speed is ten times the record speed which results in a frequency cut-off at 32 Hz with respect to the recorded data. Therefore any signal with a frequency greater than 32 Hz on the analogue magnetic tape will be lost on replay. Hence a sampling rate of 100 sps is sufficiently large for spectral analysis since the Nyquist frequency of 50 Hz is greater than the 32 Hz cut-off. The higher sampling rate of 400 sps is required solely to improve the quality of the seismogram representation in the time domain. This shows that suitable interpolation between sampling points maybe necessary for particle motion analysis.

2.2.3 The Livermore data set

I collected seven 1600 bpi magnetic tapes of digitized seismic records from the Lawrence Livermore National Laboratory (LLNL) during the Spring of 1983

and another eleven tapes were sent from Livermore in January 1984. Data from about 130 earthquakes recorded by up to ten three-component stations are stored on the eighteen tapes. At the LLNL the seismic records were written to magnetic tape as alphanumeric files to ensure compatibility with the PDP 11/50 system at BGS. Each tape consists of a series of files, with each file containing a single digitized seismic record preceeded by a header block. The large number of magnetic tapes, the inability to easily multiplex the data, plus the possibility of creating informative header blocks with event location details resulted in only some degree of reformatting of the original data. Hence the existing particle motion plotting routines required some modification.

The original data files on magnetic tape are transferred to an RK05 disk until it is full. On transfer new header blocks are constructed and the original data files are cut from a time length of up to 5 minutes to the 18 seconds windowing the P-wave and shear-wave arrivals. The data files are more easily manipulated on the RK05 disk than on magnetic tape. Seismogram traces and polarization diagrams are generated a disk at a time by a modified version of the computer program PMPLOT.

2.3 **Analysis of the shear-wave particle motion**

The shear-wave particle motion analysis begins with a qualitative description of the three-component seismogram trace, noting such features as frequency content, length of coda, impulsiveness of onsets etc.. The seismogram traces are either rotated into vertical-, radial-, and transverse-components or are left in the original three-component recording configuration of vertical, north-south, and east-west components. Similarly polarization diagrams showing two-dimensional particle motion are rotated or unrotated. Orientation of the polarization of the shear-wave first motion,

time delays between split shear-waves and the general character of the particle motion are analysed from the polarization diagrams. This information provides the observational data base for interpretation. Similarity of the shear-wave particle motion at a given station from different earthquakes (doublets) is a useful aid, since repeatibility of particle motion instils a degree of confidence in the interpretation of the observations.

2.3.1 Orientation of the shear-wave polarization

Normally, estimates of the polarization direction of the shear-wave are made for all earthquakes with station-source geometries within the shear-wave window: the region where the shear-wave is recorded without distortion due to the free surface. For practical purposes the shear-wave window of any station is defined to include events with epicentral distances which are less than the product of source depth and tangent of the critical angle. The critical angle is usually taken to be 40°. The shear-wave polarization is defined by the "polarization angle". Here, it is the angle between the orientation of the incident shear-wave particle motion in the horizontal plane and geographic North. It ranges from N 0°E to N 180°E if an undirected lineation (non-vector polarization) is measured or N 0°E to N 360°E for a directed lineation (vector polarization).

The determination of the shear-wave polarization angle can often be ambiguous since it is difficult to decide a single direction from a complicated pattern of particle motion. Therefore the polarization angle determination involves interpretation of the shear-wave particle motion. The polarization direction could either be the average direction associated with the first cycle or so of the shear-wave particle motion, or the direction of the first motion of the shear-wave. In this study the shear-wave polarization is usually measured from the first motion of the shear-wave, unless linear or well defined elliptical

motion occurs for a complete cycle. In the latter situation the major axis of the ellipse defines the direction of the shear-wave polarization. As an example of the former, consider the shear-wave arrival indicated by the arrow in Figure 2.1. The shear-wave polarization angle is N 135°E, from the orientation of the first motion, and not N 83°W which defines the direction of the first half cycle. An example of the latter type of measurement is shown in Figure 2.2. The shear-wave onset is impulsive, and the particle motion of the shear-wave in the horizontal plane describes a well defined ellipse. The polarization angle is given by the major axis of the ellipse rather than the direction of first motion. Its value is N 11°W. The average error in such measurements is estimated to be about ±10° (Booth et al. 1984).

If effective seismic anisotropy is present then the distribution of shear-wave polarizations are dependant on the geometry and orientation of the anisotropy. Following Crampin & McGonigle (1981) and Booth et al. (1984), the spatial distribution of the shear-wave polarizations is displayed by plotting non-vector or vector polarizations on an equal-area projection of the focal sphere. Histograms illustrating the azimuthal distribution of the shear-wave polarization angle are plotted also, as in Booth et al. (1984). The observed distributions of shear-wave polarizations can then be compared to predicted patterns from anisotropic models.

The observed distribution of shear-wave polarizations are also compared when possible to theoretically determined shear-wave polarizations from the earthquake source mechanisms. Hence as part of the shear-wave analysis the determination of source mechanisms is required in order to define the source generated shear-wave polarizations. Appendix A explains the method used to determine earthquake focal mechanisms and Appendix B explains how theoretical body-wave radiation patterns are determined for shear dislocation and other source mechanisms.

Figure 2.2

The determination of the shear-wave polarization angle. A three-component seismogram and polarization diagrams for an acoustic event recorded at the HDR site, Cornwall on 9 November, with epicentre 50° 10.08'N, 5° 10.75'W, and a depth of 2.55 km. The seismograms were recorded at station CRQ at an epicentral distance of 0.62 km and at an azimuth of N 111°E from the epicentre. Notation and format as in Figure 1.2. The shear-wave onset is indicated by the heavy arrow in a polarization diagram of horizontal particle motion. The polarization angle of the shear-wave is measured from the major axis of the ellipse in the horizontal plane. The value is N 11°W.

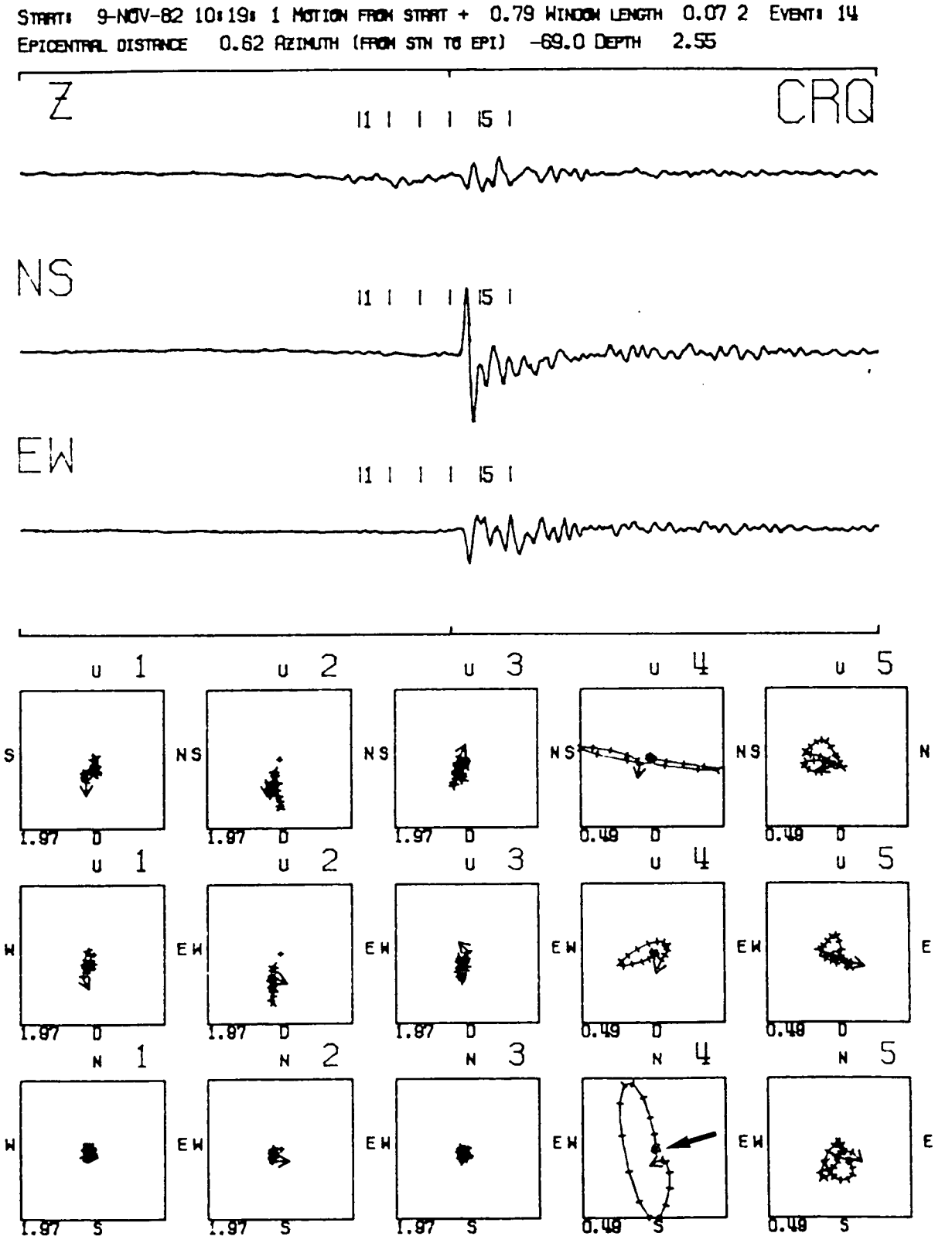
START: 9-NOV-82 10:19: 1 MOTION FROM START + 0.79 WINDOW LENGTH 0.07 2 EVENT: 14
EPICENTRAL DISTANCE 0.62 AZIMUTH (FROM STN TO EPI) -69.0 DEPTH 2.55
Z
CRQ
NS
EW
11 I I I 15 I
U 1
U 2
U 3
U 4
U 5
S
NS
N
W
E
EW
N 1
N 2
N 3
N 4
N 5
1.97
0.49
D

Figure 2.2

2.3.2 Time delays between split shear-waves

Most shear-wave seismograms are likely to show particle motion akin to shear-wave splitting, since at some stage in the shear-wave coda, a new phase introduces a change in the direction of the particle motion. Whether this is a result of anisotropic propagation is a matter of interpretation, since lateral heterogeneities, horizontal layering, or possibly, a combination of all these factors may be responsible. For the measurement of time delays, however, we assume that anisotropy is the cause.

The time delay is the time difference between the arrival of the faster shear-wave and the arrival of the slower shear-wave. It is measured directly from the polarization diagram. The arrival of the slower phase is usually marked by increased ellipticity or by a sharp change in direction of the shear-wave particle motion in the horizontal plane. For example see Figure 1.2 where the time delay is about 21/400 seconds. Time delays between split shear-waves are corrected for an equivalent time delay over a sphere of fixed radius to eliminate the time delay variations due to different ray path lengths. They are then plotted on an equal-area projection. Time delays consistent with a shear-wave polarization pattern fitting a realistic anisotropic model would lend support to wave propagation in an effectively anisotropic medium.

2.3.3 Summary

The shear-wave particle motion of each data set is analysed following the four steps outlined below.

1. Shear-wave polarization angle determination from the polarization diagram containing the shear-wave arrival.

2. Time delay determination from the polarization diagram containing the shear-wave arrival.

3. Equal-area plots of shear-wave polarizations and time delays, and histogram plots of shear-wave polarization angles are generated.

4. Interpretation of the shear-wave particle motion, and the pattern of shear-wave polarizations and time delays, in terms of underlying crack structures.

CHAPTER THREE

THE MONTICELLO DATA

The analysis of the shear-wave particle motion of the Monticello data set was undertaken at the start of this project early in 1982. Shear-wave particle motion characteristic of shear-wave splitting is evident but the limited number of seismic records available for analysis inhibited interpretation. In addition the full significance of the free surface on the recording of shear-waves was not recognised at this time. Most of the seismograms are recorded outside the shear-wave window therefore any shear-wave particle motion characteristic of anisotropy would be masked by the shear-wave interaction at the free surface. In fact, shear-wave free surface interaction is the most likely explanation for the predominance of transversely-polarized shear-waves in the data.

The results from this data set are only discussed briefly because of the unsuitability of the data for the purpose of the dissertation. However note that it was only during the analysis of the data that its limitations for examining anisotropy-induced effects upon shear-wave particle motion were recognised.

3.1 The seismic network

The Monticello data set was recorded on a temporary seismic network set up around Monticello reservoir in South Carolina. It was collected originally to determine stress parameters from the reservoir-induced seismicity (Fletcher 1982). Five three-component Sprengnether DR100 seismometers and a single-component vertical Ranger seismometer were deployed for 27 days during May

and June, 1979. Monticello reservoir was created one and a half years earlier between December 1977 and early February 1978. Low level earthquake activity (M_L<3.0) increased shortly after the filling of the reservoir was started. Seismic activity reached a peak in February 1978 and has continued through to the deployment of the temporary network.

The three-component seismometers are event triggered and recorded digitally at 200 sps. The eight different sites occupied during the deployment of the network are illustrated in Figure 3.1, and the site coordinates are given in Table 3.1. Both stations DUC and SNK had 70 Hz filters, and the other stations filtered at 50 Hz. Over 300 events were detected during the recording time of the network, all with M_L<1.7, but only 52 events were recorded at three or more stations. Three-component seismogram traces and polarization diagrams were generated for these 52 events.

3.2 **Hypocentral distribution of the reservoir-induced events**

Hypocentres were calculated by Fletcher (1982) using the computer program HYPOINVERSE (Klein 1978). Both P-wave and shear-wave arrival times from the temporary array of three-component seismometers were used, as well as some data from a more regional network (Talwani et al. 1980). The velocity model was derived from a well log velocity-depth profile to 1 km, and from a regional refraction survey (Talwani et al. 1980) for depths below 1 km. Of the events recorded at three or more stations only 32 could be located.

Only five of these events were detected by five stations, nine events were detected by four stations, and the majority, eighteen, were detected by three stations. Horizontal and depth errors of up to 3 km and 5 km respectively were generated when arrival times from the temporary network were used in hypocentral location. In an effort to improve the hypocentral solutions arrival times from the regional network were included also. However this resulted in

Table 3.1 Latitude and longitude of the sites of three-component stations deployed by Fletcher (1982) at Monticello reservoir, South Carolina, USA.

STATION	LATITUDE N	LONGITUDE W	ELEVATION (KM)
CEM	34.3127	81.3415	-
CPL	34.3327	81.2753	-
DON	34.3570	81.3533	-
DUC	34.3345	81.3510	-
JAB	34.3713	81.3245	-
LKS	34.3325	81.2948	-
SNK	34.3382	81.3257	-

Figure 3.1
Hypocentral distribution of the reservoir-induced seismicity at Monticello, South Carolina during May 1979. Hypocentral locations are by HYPO71 from the seismograms recorded by the temporary network set up by Fletcher (1982). (a) Map of epicentres (circles) and station positions (triangles). The outline of the reservoir is shown also. (b) East-west cross-section A-B. The vertical axis is depth marked in kilometres.

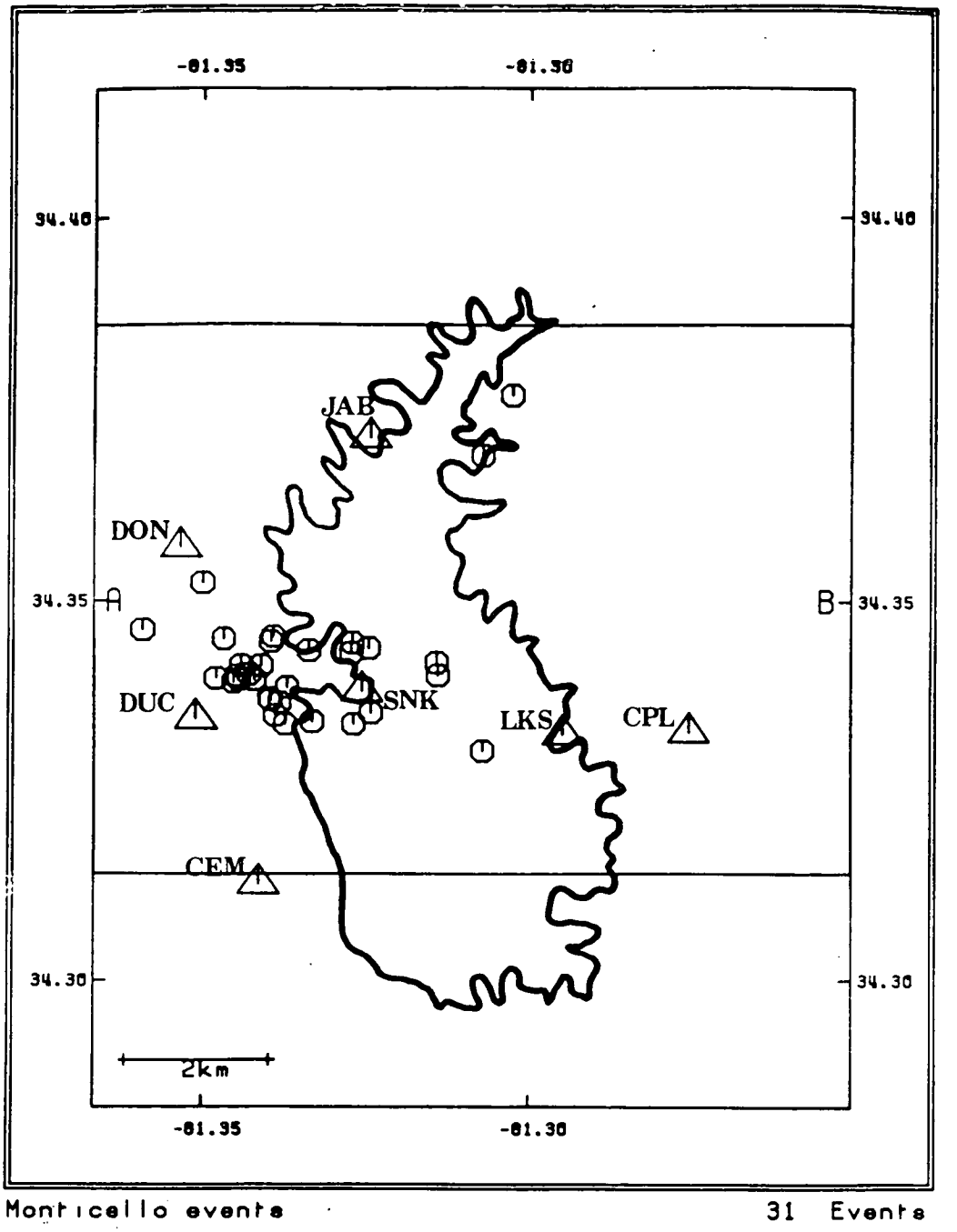

Figure 3.1a

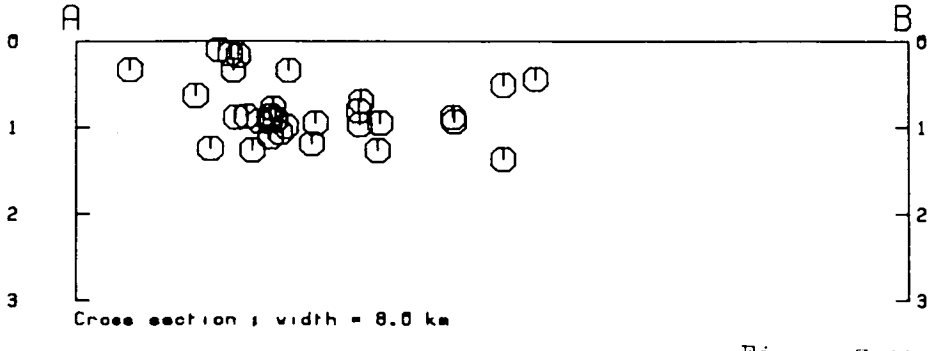

Figure 3.1b

an increase of the horizontal and depth errors to about 6 km and 10 km respectively. Fletcher (1982) found that only events recorded at a minimum of four stations gave reliable hypocentres.

The poor quality of the hypocentral solutions suggests that the data may not be suitable for anisotropic studies. Therefore to check the hypocentres calculated by Fletcher (1982) the P-wave and shear-wave arrival times are repicked. The events are relocated using the computer program HYPO71 (Lee & Lahr (1973) with a step-velocity model, given in Table 3.2, derived from the velocity-depth profile extracted from Fletcher (1982). The hypocentral distribution remains virtually unchanged upon relocation. Only one event is shifted significantly, so that its hypocentre coincides with an event which has a similar seismogram to the shifted earthquake. Another event is not located due to insufficient data. Therefore the earthquake locations seem stable to some extent despite the large values of the errors associated with the hypocentral location.

Figure 3.1 shows the epicentral distribution and an east-west cross-section of the events located by HYPO71. The hypocentral parameters are given in Table 3.3. Most of the activity is situated along the central-western edge of the reservoir between stations DUC and SNK. The cross-section shows that the focal depths extend from 0.1 km to 1.5 km.

3.3 Shear-wave particle motion

Of the 112 seismograms recorded at the three-component stations from the 32 located events only 76 are available for shear-wave particle motion analysis. The main reasons for omission are overloading at stations DUC and SNK, and dead components at stations JAB and CPS. The seismograms are recorded at close epicentral distances, usually less than 5 km, but the shallow focal depths means that most seismograms are recorded outside the shear-

Table 3.2 Monticello velocity model (derived from Fletcher (1982)) input into HYP071 for relocation of reservoir-induced events. V_p/V_s is 1.77.

P-wave velocity (km/sec)	Depth to upper interface (km)
5.19	0.0
5.41	0.069
5.64	0.138
5.86	0.208
6.07	0.387
6.21	0.567
6.24	1.000
6.25	9.000

Table 3.3 Date, origin time, epicentre, and depth of the events located at Monticello reservoir, South Carolina.

DATE	ORIGIN TIME	LATITUDE N	LONGITUDE W	DEPTH (KM)
790507	7 50.53	34-20.42	81-18.84	0.93
790507	1000 19.21	34-20.03	81-19.62	0.70
790507	1113 22.59	34-20.67	81-19.63	0.97
790508	1053 30.51	34-20.77	81-21.54	0.33
790508	1119 52.42	34-20.70	81-20.81	0.10
790508	1158 7.61	34-20.38	81-20.67	0.88
790508	1337 43.05	34-20.59	81-19.64	0.81
790508	1343 41.62	34-20.42	81-20.58	0.87
790510	214 58.60	34-20.68	81-20.38	1.11
790510	216 29.60	34-20.72	81-20.36	0.78
790510	958 8.25	34-20.23	81-20.39	0.91
790510	2028 48.80	34-20.36	81-20.72	0.15
790510	2328 41.82	34-20.49	81-20.65	0.17
790517	1411 56.60	34-20.32	81-20.23	0.34
790518	942 26.47	34-22.14	81-18.43	0.51
790518	1258 40.76	34-19.82	81-18.43	1.37
790518	1427 34.76	34-20.05	81-20.00	0.95
790518	1740 25.25	34-22.61	81-18.16	0.44
790521	26 19.52	34-21.14	81-21.00	0.63
790522	331 6.40	34-20.03	81-20.25	0.99
790525	1429 16.86	34-20.61	81-20.03	1.19
790529	0 3.88	34-20.41	81-20.69	0.34
790529	1028 54.83	34-20.39	81-20.88	1.24
790529	2347 42.62	34-20.52	81-18.85	0.88
790530	631 21.23	34-20.63	81-19.48	1.27
790530	714 45.67	34-20.10	81-20.34	0.91
790530	1531 18.67	34-20.22	81-20.38	0.87
790530	2352 32.44	34-20.20	81-20.30	1.06
790531	433 32.44	34-20.49	81-20.47	0.93
790531	841 30.11	34-20.38	81-20.53	1.26
790531	1619 38.26	34-20.12	81-19.46	0.95

Table 3.4 Number of records available for shear-wave particle motion analysis is 76. Thirty-six records are unusable due to instrumental problems.

Station	Records from located events	Unusable records
CEM	14	0
CPL	6	6 - overloaded
DON	1	0
DUC	28	5 - overloaded
JAB	25	10 - dead components
LKS	7	1 - overloaded
SNK	31	14 - overloaded

wave window.

However a few of the seismic records display sharp changes in direction of shear-wave particle motion expected for the onset of orthogonally polarized split shear-waves. A good example of shear-wave particle motion typical of shear-wave splitting in synthetic seismograms (Crampin 1978) is shown in Figure 3.2. The three-component seismogram trace and polarization diagrams were recorded at station DUC for an event at a depth of 1.11 km and epicentral distance of 1.5 km. Initially the shear-wave particle motion is linear and orientated N 125^{o}E. The onset of the slower shear-wave probably coincides with the abrupt change of direction 0.03 seconds after the onset. The shear-wave particle motion now becomes aligned at N 40^{o}E -approximately right angles to the first shear-wave polarization.

3.3.1 Orientation of the shear-wave polarizations

In Figure 3.3 the shear-wave polarizations are displayed on an equal-area projection of the lower focal hemisphere centred at the station site for stations CEM, DUC, JAB, LKS, and SNK. Measurements of the shear-wave polarizations could not be made at stations CPS and DON because of instrumental problems. An inner circle at 40^{o} incidence angle represents the shear-wave window. The corresponding histograms of the azimuthal distribution of the shear-wave polarization angles are shown below each equal-area plot. The polarity of the shear-wave first motion is neglected (non-vector polarizations are measured), so each histogram is repeatable over a range of 180^{o}.

The equal-area projections show that the azimuthal distribution of ray paths to each station is poor, and that most shear-wave polarizations plot outside the shear-wave window. At stations CEM, JAB, LKS, and DUC many of the shear-wave polarizations align within $\pm$20^{o} of N 120^{o}E, but they are distinctly

Figure 3.2

A three-component seismogram and polarization diagrams for a reservoir-induced event recorded at Monticello on 10 May 1979, with epicentre 34° 20.68'N, 81° 20.38'W, and a depth of 1.10 km. The seismogram was recorded at station DUC at an epicentral distance of 1.5 km and at an azimuth of N 223°E from the epicentre. Notation and format as in Figure 1.2 except cross bars are marked every 0.005 seconds. The heavy arrows in the horizontal polarization diagrams mark possible shear-wave arrivals.

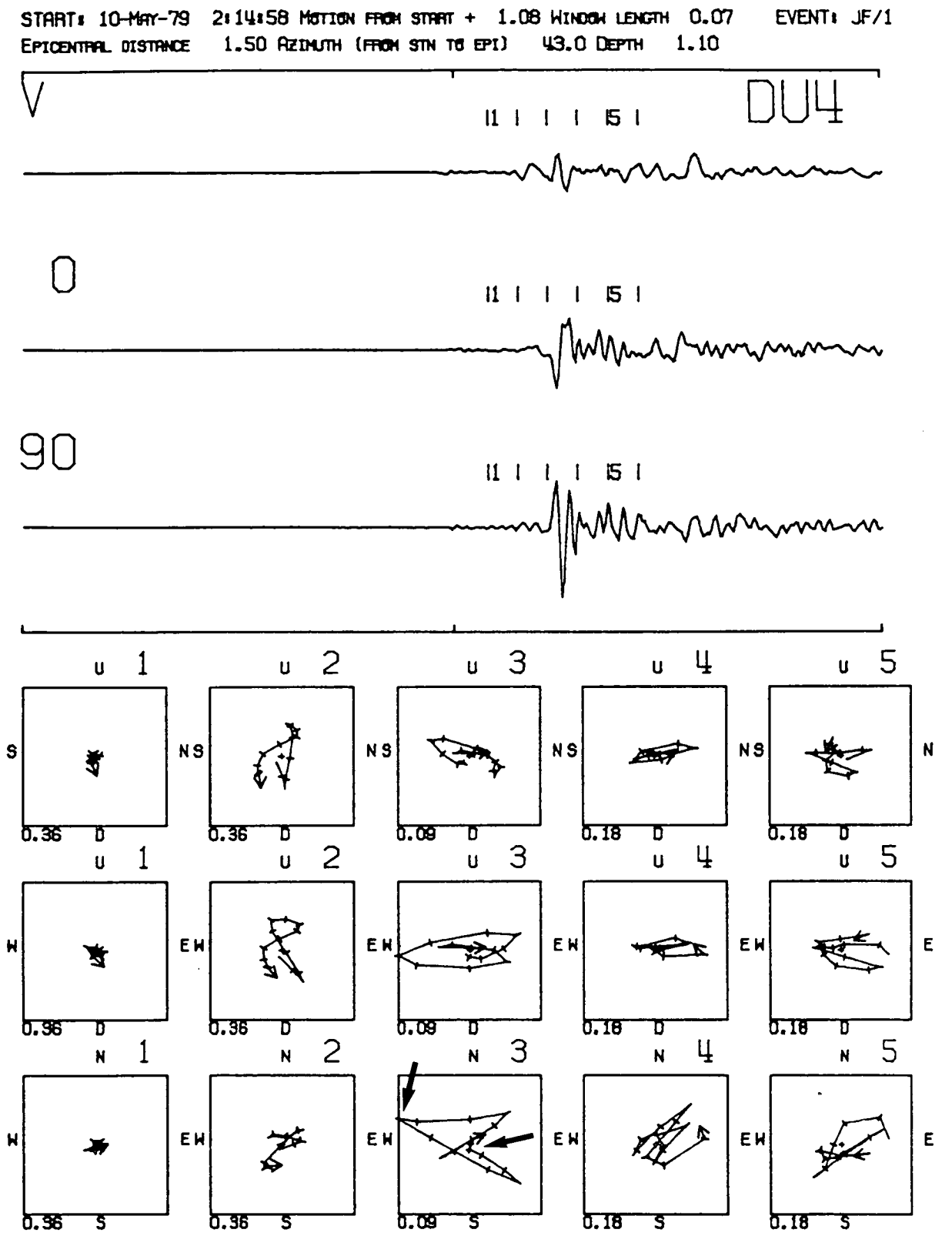
START: 10-MAY-79 2:14:58 MOTION FROM START + 1.08 WINDOW LENGTH 0.07 EVENT: JF/1
EPICENTRAL DISTANCE 1.50 AZIMUTH (FROM STN TO EPI) 43.0 DEPTH 1.10
V
DU4
0
90
U 1
U 2
U 3
U 4
U 5
S
NS
N
0.36
0.09
0.18
D
W
EW
E
N 1
N 2
N 3
N 4
N 5
S

Figure 3.2

Figure 3.3
Shear-wave polarizations from the reservoir-induced events, Monticello, measured at three-component stations - CEM, DUC, LKS, JAB, and SNK. The upper diagrams are lower equal-area projections out to incidence angles of 90° of the horizontal shear-wave polarizations. The inner circle on each projection defines an incidence angle of 40°. The lower diagrams are histograms showing the azimuthal distribution of the shear-wave polarization angles at each station. Non-vector shear-wave polarizations are displayed.

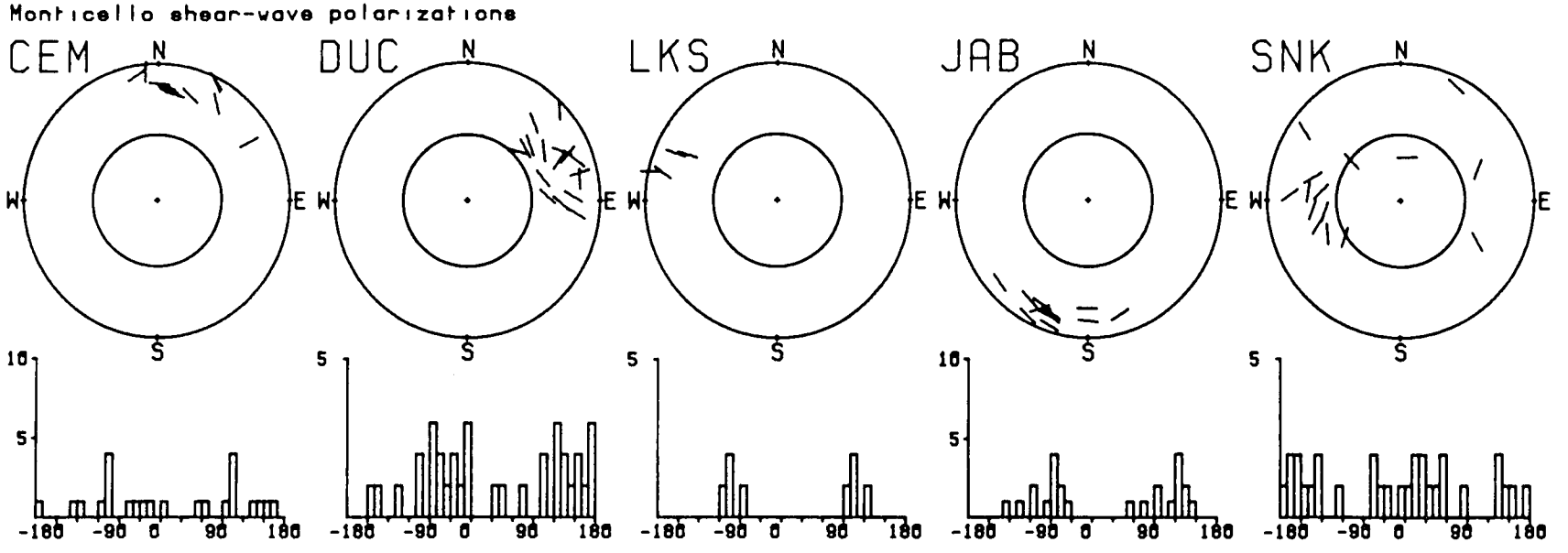
Monticello shear-wave polarizations
CEM
DUC
LKS
JAB
SNK
N
W
E
S
10
5
-180
-90
0
90
180

Figure 3.3

scattered at SNK. Composite fault plane solutions of the reservoir-induced activity indicate that the average direction of greatest horizontal compressive stress is N 71°E (Talwani et al. 1980), whereas an orientation of N 35°W to N 15°E is derived from in situ measurements by overcoring (Secor et al. 1982). However neither of the maximum compressive stress directions coincides with the N 120°E alignment of the shear-wave polarizations, in contrast to the observations of Booth et al. (1984) in northwest Turkey.

As most of the seismograms are recorded at incidence angles greater than the critical angle the SV-component of the shear-wave (radial polarization) would be expected to interfere destructively at the free surface leaving the SH-component (transverse polarization) predominant (Nuttli 1961; Evans 1984). Therefore the transverse polarization of many shear-waves, including those at stations CEM, DUC, and JAB, suggest that the free surface exerts the main influence on the shear-wave particle motion. Consequently any anisotropic effects on the shear-waves are probably masked by the interaction of the shear-wave at the free surface.

3.3.2 Time delays

The measurement of time delays is highly subjective. Even under the most suitable conditions it is difficult to objectively identify the onset of the slower shear-wave either at the point when the particle motion becomes more elliptical, or when there is a change in polarization direction (Booth et al. 1984). Consequently, for the Monticello data, time delays could only be measured on a few seismic records. Given the subjectivity involved in measurement, the lack of data, in addition to problems associated with the free surface it is not suprising that no coherent spatial or temporal pattern of time delays emerged.

3.4 Conclusions

For the following reasons the Monticello data set is unsuitable for the search for anisotropic-induced effects on the shear-waves.

1. Most of the seismograms are recorded outside the shear-wave window.
2. There are large errors associated with the position of the hypocentre.
3. There is an insufficient amount of data.

Most of the seismograms are recorded at incidence angles greater than the critical angle. Theoretical work by Nuttli (1961) has shown that when a linearly polarized shear-wave is recorded at the free surface at angles beyond the critical, the particle motion becomes elliptical and/or polarized transverse to the ray path. Therefore any anisotropic effects in the shear-wavetrain are likely to be modified at the free surface for most seismograms recorded by the temporary network at Monticello.

Both the lack of data and poor hypocentral locations limits the possibility of a realistic interpretation of the shear-wave polarizations. At best only a few general comments on the shear-waves could be made. Also there are an insufficient number of stations to obtain reliable fault plane solutions for the reservoir-induced events recorded during the operation of the temporary network. Consequently the source generated shear-wave polarizations cannot be estimated for comparison to the observed shear-wave polarization distribution.

CHAPTER FOUR

THE CORNWALL DATA 1: OBSERVED SHEAR-WAVE POLARIZATIONS

The following two chapters are concerned with the shear-wave particle motion from microseismic acoustic events induced during a Hot Dry Rock (HDR) Geothermal Energy Project in Cornwall. The seismograms from selected acoustic events are analysed for signs of shear-wave splitting. Shear-wave polarizations and time delays are measured from polarization diagrams and then displayed on equal-area projections of the focal sphere. In addition source mechanisms are determined from the P-wave first motion polarity patterns, and theoretical far-field radiation patterns of the shear-wave are generated. A comparison of the observed and predicted shear-wave radiation suggests that the medium influenced the wave propagation sufficiently to modify the orientation of the shear-wave polarization generated by the source. The cause of this deviation can be explained by wave propagation through a structure of cracks aligned by the in situ stress field.

This chapter presents an outline of the HDR experiment; describes the hypocentral distribution of the seismicity; discusses the shear-wave particle motion, and finishes with a preliminary interpretation of the data in terms of an aligned crack structure. In chapter five the source mechanisms are discussed; source generated shear-wave polarizations are compared with observed shear-wave polarizations, and final conclusions are drawn.

4.1 Camborne School of Mines Geothermal Energy Project

The Camborne School of Mines (CSM) is engaged in a Hot Dry Rock (HDR) Geothermal Energy Project at Rosemanowes quarry, Cornwall to develop a

method to extract heat from a hot low-permeability crystalline rock mass. The HDR site consists of two wells interconnected by a fracture system. Water is injected into the fractured rock via one well, the injection well, where it is heated at depth and emerges as hot water at the surface via the other well, the recovery well. Evidence from HDR projects (Fenton Hill at Los Alamos, New Mexico) and at other fluid injection sites suggests that hydraulic injection will induce acoustic emissions (Evans 1966; Pearson 1981; Aki et al. 1982). The fracture growth initiated by water diffusion can be mapped by monitoring the induced microseismicity. Therefore two independant seismic networks were deployed during the lifetime of the Cornwall HDR project. The CSM microseismic location sensor system consisted of four near surface accelerometer units and three hydrophones located below 1.8 km (Pine & Batchelor 1984). The Global Seismology Research Group (GSRG) of the British Geological Survey (BGS) deployed a surface network of both single-component vertical seismometers and three-component stations.

At Rosemanowes quarry two wells were drilled to depths of 2 km. The recovery well was drilled vertically to 0.38 km then drilled at an angle of 30° to the northwest. The injection well, to the southeast of the recovery well, was drilled a further 0.42 km vertically before drilling to the northwest. The wells were separated by 0.15 km at a depth of 2 km. During October and November 1982 about 10^5 m^3 of water was injected at wellhead pressures in excess of 10 MPa and flow rates typically of 30 litres/sec (Pine & Batchelor 1984).

4.2 The local geology

Rosemanowes quarry is centred on one of the outcrops of the Carnmenellis granite (see Figure 4.1), part of the major granite batholith underlying much of

Figure 4.1
The granites of southwest England. A solid triangle indicates the site of the HDR experiment at Rosemanowes quarry in the Carnmenellis granite. The line L-L is the seismic line of Brooks et al. (1984). Adapted from Turbitt et al. (1984).

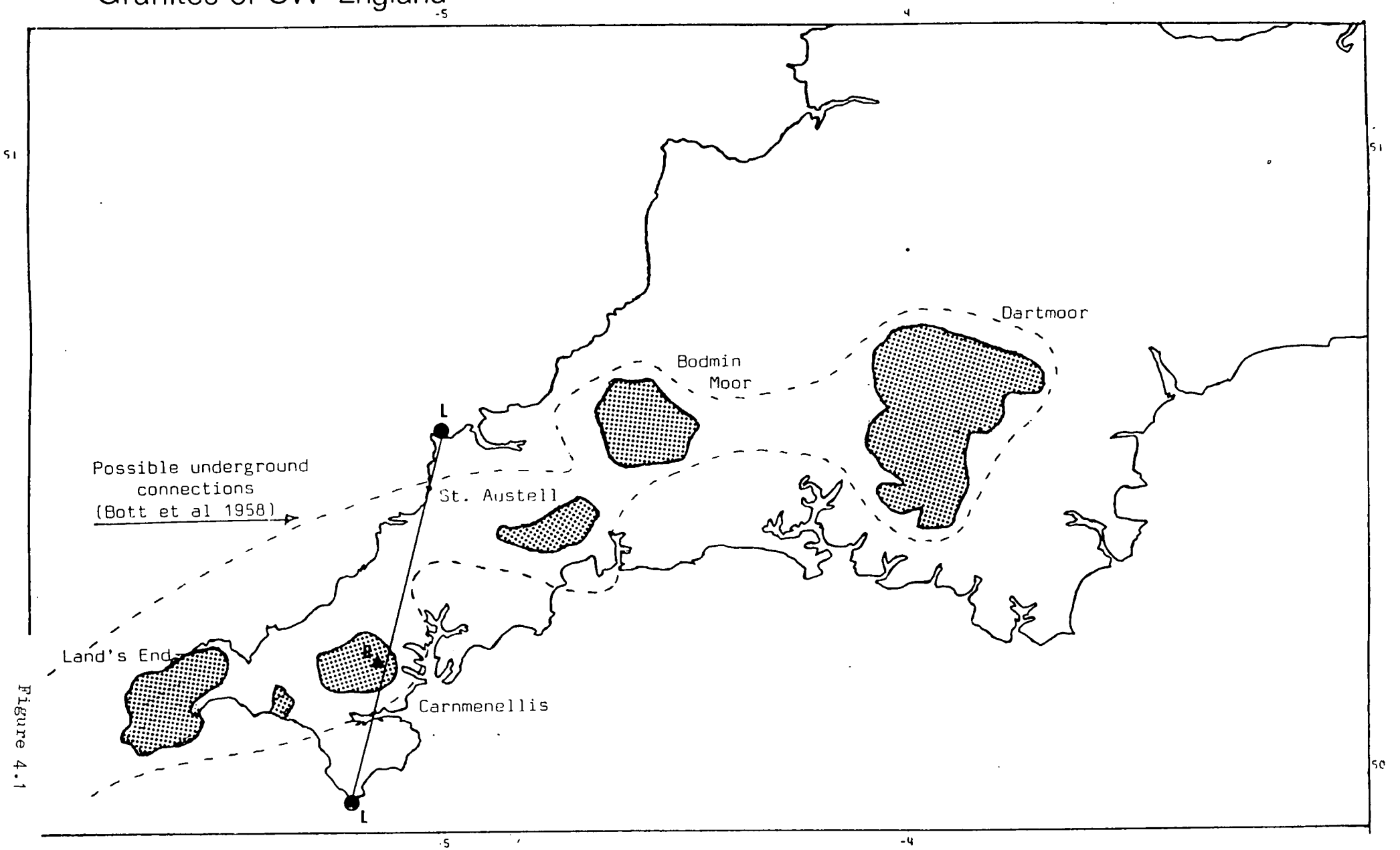
Granites of SW England
-5
-4
51
50
Dartmoor
Bodmin
Moor
L
Possible underground
connections
(Bott et al 1958)
St. Austell
Land's End
Carnmenellis
L

Figure 4.1

Cornwall (Tombs 1977). The mineralogy of the Carnmenellis granite is remarkably constant over a wide area and to a depth of at least 2 km (Pine & Batchelor 1984). It is typically made up of crystals of alkali feldspar set in a coarse groundmass of plagioclase, alkali feldspar, micas, and trace minerals. Grain size is usually 2-5 mm with the feldspar crystals up to 20 mm in length. The structure of the granite is dominated by two subvertical joint sets striking approximately N 155°E - N 335°E and N 75°E - N 255°E with a less important subvertical set trending N 30°E - N 210°E. There are also horizontal joint sets throughout (Pine & Batchelor 1984). At the ground surface the major subvertical joint spacings are about 1 to 5 m increasing to 3 to 10 m at a depth of about 0.8 km. The horizontal joints are typically more widely spaced. At the ground surface the size of the major joint sets can extend to several tens of metres, and in a few cases, hundreds of metres.

A reversed seismic refraction line of four shots was fired along a north-northwesterly direction from the Lizard across the Carnmenellis granite outcrop to Trevose Head on the northern Cornish coast. The seismic line is shown in Figure 4.1. Reflectors at 8 km, 12 to 15 km, and 27 to 30 km were detected with the 12 to 15 km reflector interpretated by Brooks et al. (1984) as the base of the granite.

The mineralogical homogeneity of the granite, and the fact that the receivers and sources are both contained in this homogeneous rock mass provide an excellent opportunity to study the influence of in situ cracked rock on shear-wave propagation. Of particular interest is the effect of the microcracks (or any cracks with dimensions significantly smaller than the seismic wavelength) on the shear-wave propagation.

4.3 The seismic network

The seismic records analysed in this study were recorded by the GSRG of

BGS. A surface network of four single-component and four three-component stations using Willmore MkIII seismometers was deployed to monitor the background and hydrofracture-induced seismicity. A map of the distribution of the stations is shown in Figure 4.2, and their coordinates are given in Table 4.1. Station CRQ is within 25 m of the wellhead at the HDR site.

During December 1980 the four single-component vertical seismometers were installed within a 4 km radius of the HDR site, and one three-component station, CRQ, was set up at Rosemanowes quarry. About one month before the main phase of hydraulic injection three additional three-component stations were installed within a 1 km radius of the HDR site to ensure good quality hypocentral locations and to allow the study of shear-waves generated by the induced seismicity. The seismic vibrations recorded by the network were telemetered to Rosemanowes quarry where they were recorded on 14 track analogue magnetic tape. The recording speed was 15/160 inches/second which resulted in a 3 db cut-off at 32 Hz because of the response of the Store 14 RACAL T81000 replay system. This combined with the low detection threshold of a surface network meant that only the higher magnitude acoustic events were detected and only the low frequency end of the body-wave spectrum was recorded.

The frequency range of interest is between 20 Hz and 30 Hz which contrasts sharply with the frequency range recorded during microseismic monitoring at the Los Alamos HDR site at Fenton Hill, New Mexico. At Fenton Hill acoustic signals were recorded with frequencies typically of 12 kHz (Fehler 1981) and very low magnitude microseismicity ($-2 > M_L > -4$) was analysed (Pearson 1981). The seismic experiments at Fenton Hill were concerned with how a fluid filled crack affects seismic wavelengths comparable to or shorter than the crack size (Aki et al. 1982). Consequently different structures are sampled in this study, since, at Cornwall, we are concerned with the affects of cracks on

Figure 4.2
The seismic network in Cornwall set up by the GSRG, BGS. Station CRQ marks the position of the HDR site. The strikes of the major joint sets are shown also. Adapted from Turbitt et al. (1984).

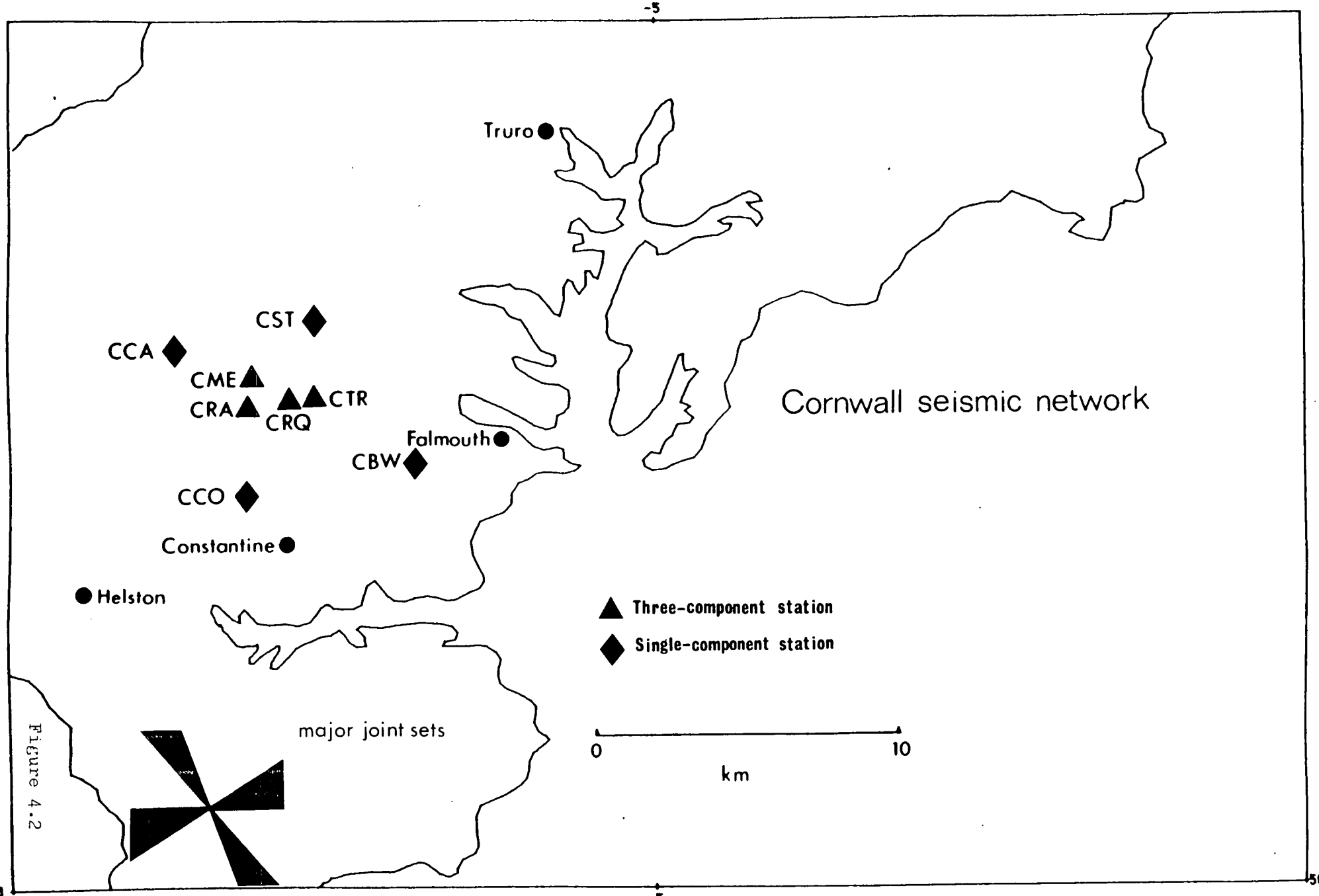
-5
Truro
CST
CCA
CME
CRA
CRQ
CTR
Falmouth
CBW
CCO
Constantine
Helston
Cornwall seismic network
Three-component station
Single-component station
major joint sets
0
10
km
50
-5

Figure 4.2

Table 4.1 Latitude, longitude, elevation and site rock of the seismic stations deployed by GSRG at the HDR site, Cornwall, UK. Stations CME, CTR, CRA & CRQ consist of three-component sets, and stations CBW, CST, CCO & CCA consist of single-component vertical seismometers.

STATION	LATITUDE N	LONGITUDE W	ELEVATION (KM)	SITE ROCK
CST	50.1952	5.1635	0.1390	granite
CCA	50.1863	5.2277	0.2130	granite
CCO	50.1358	5.1960	0.1830	granite
CBW	50.1482	5.1143	0.0980	granite
CME	50.1760	5.1903	0.1780	granite
CRA	50.1648	5.1920	0.1980	granite
CTR	50.1665	5.1625	0.1920	granite
CRQ	50.1672	5.1728	0.1650	granite

wavelengths significantly greater than the crack dimensions.

A downwell explosive source was used to check instrumental polarities of the vertical and horizontal components. P-wave arrivals were compressional at all detectors indicating correct setting of all the instrumental polarities.

4.4 Hypocentral locations of the hydrofracture-induced seismicity

Hypocentres are located using the computer program HYPO71 (Lee & Lahr 1975). The velocity model is averaged from velocity-depth profiles calculated from arrival time data from explosive sources recorded on the CSM seismometer network. The velocity model consists of an upper layer of 300 m, with a P-wave velocity of 5.5 km/sec, overlying a half space with a P-wave velocity of 5.73 km/sec. Poisson's ratio is 0.25 which gives a Vp/Vs ratio of 1.73. The 5.73 km/sec velocity is significantly lower than the average velocity of 5.9 km/sec calculated by Brooks et al. (1984) down to the 8 km reflector. However since seismic velocity generally increases with depth and the Brooks et al. (1984) average encompasses greater depths the discrepancy is not unexpected.

Only four acoustic events were detected at the site prior to the main phase of hydrofracturing. The largest occurred on the 19 October 1981, with M_L=0.3, about two weeks before the main pumping started. The other events - one on the 14 October and the other two on the 19 October - are detected only at the three-component stations CRQ, CME, CTR, and CRA. The events are located directly below the HDR site at depths of about 2 km. They were probably induced by the testing of the hydraulic equipment on 14 October 1982.

From 4 November 1982 induced seismicity is detected in association with the commencement of hydraulic injections. During the months November 1982 to February 1983 over 11,000 acoustic events are detected, and activity

continued at a high level well into 1983. Most activity is centred on the HDR site at depths between 1.5 km and 3.5 km, with a concentration of the microseismicity at a depth of 2.5 km just below the injection and recovery wells (see Figure 4.3). Evidence of fluid diffusion is illustrated by the migration of the seismicity to deeper depths with time, and an epicentral map of the events located by GSRG up to March 1983 clearly shows a NW-SE lineation of epicentres. The distribution of the seismicity indicates that the hydrofractured zone developed at depths between 2 km and 3 km directly below the HDR site.

Seventy-five acoustic events are selected for shear-wave particle motion analysis. The selected events are made up of all the acoustic events with M_L>0.3 recorded during the first three weeks after the initiation of pumping; one M_L>0.3 acoustic event detected on 19 October 1982 before hydrofracturing, and several acoustic events located away from the main concentration of hypocentres at the base of the wells. The criteria used for event selection is a combination of choosing records with good signal to noise ratios and varied source to station ray path orientations within the granite rock mass. The latter is only partially achieved since the recording sites are centred directly above the seismicity, which is clustered just below the injection and recovery wells. Events located away from this cluster often have poor quality locations. Figure 4.4 shows the epicentral distribution of the selected events, a time against depth plot, and an east-west cross section. The hypocentral parameters of the selected events are given in Table 4.2. A comparison of Figures 4.3 and 4.4 indicate that the hypocentral distribution of the selected events display all the features characteristic of all the events located by GSRS.

4.5 Shear-wave particle motion

Most of the three-component seismograms are recorded within the shear-

Figure 4.3

The hypocentral distribution of the HDR acoustic events, Cornwall, located by Turbitt et al. (1984) from the surface network between November 1982 to March 1983. Hydraulic injections started on 4 November 1982. (a) Map showing epicentres and three-component stations. (b) Time against depth section. The vertical axis is depth, marked in kilometres. The horizontal axis is time with dates written as year: month: day. (c) East-west cross-section, A-B. Vertical axis is depth, marked in kilometres. Note: a Poisson's ratio of 0.27 was used to locate the events in this diagram which resulted in a slight systematic decrease in hypocentral depths.

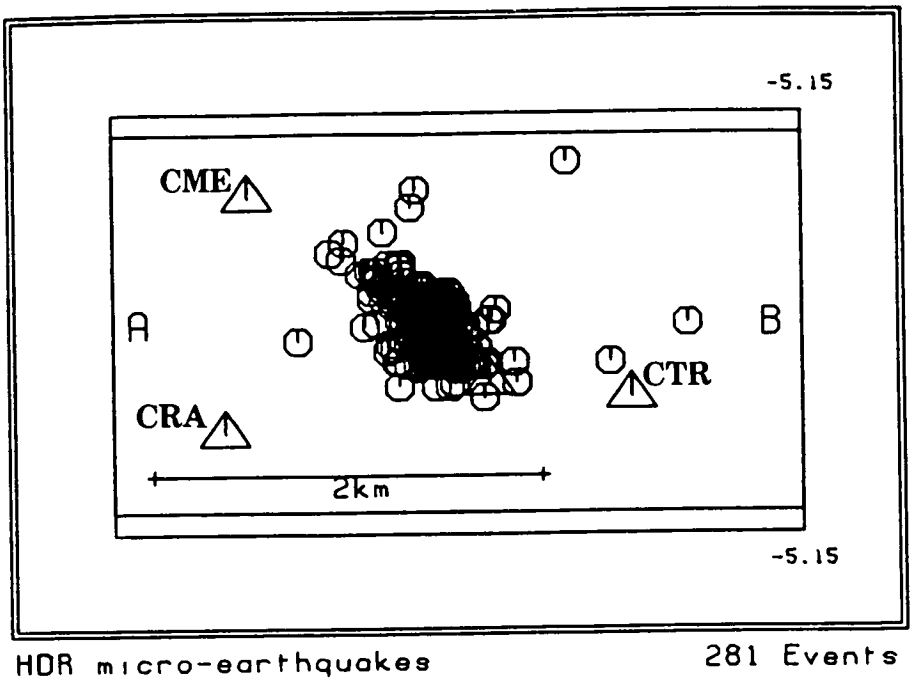

Figure 4.3a

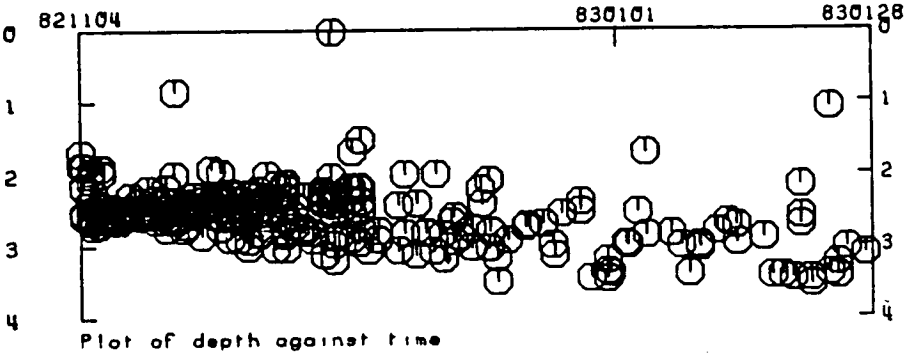

Figure 4.3b

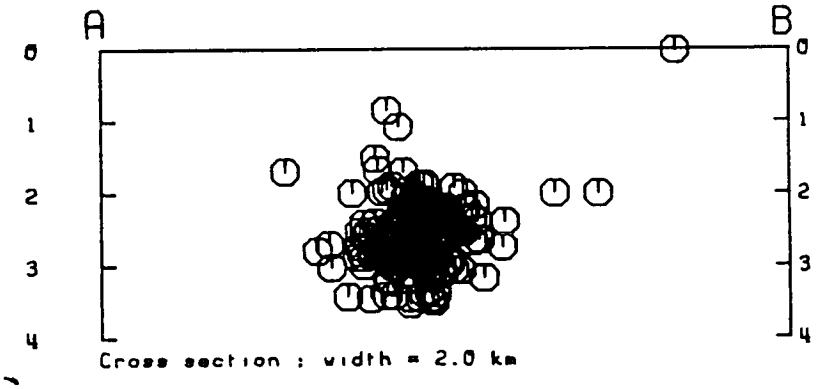

Figure 4.3c

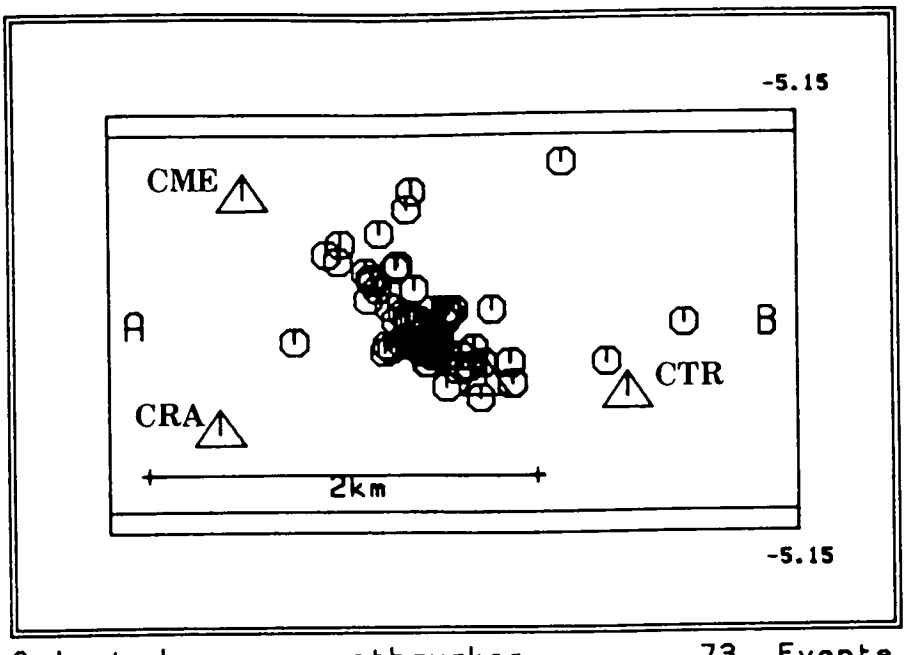

Figure 4.4a

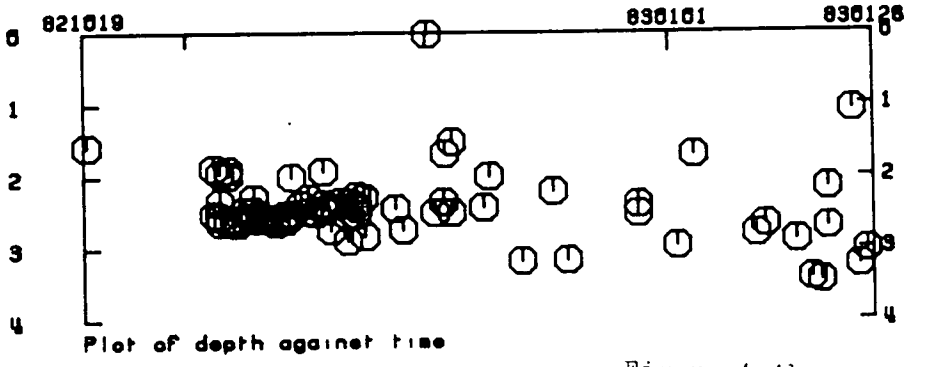

Figure 4.4b

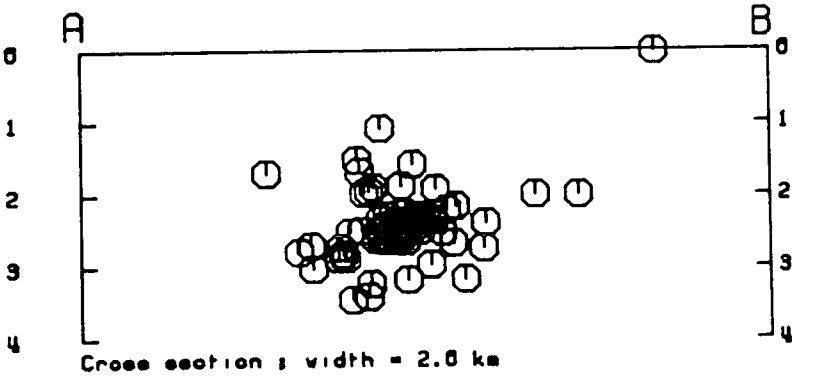

Figure 4.4c

Table 4.2 Date, origin time, epicentre, and depth of the selected HDR acoustic events, Cornwall.

	DATE	ORIGIN TIME	LATITUDE N	LONGITUDE W	DEPTH (KM)
S	821019	2323 39.08	50-10.12	5-10.57	1.58
	821104	1447 28.03	50- 9.77	5-13.04	0.29
S	821104	2159 5.71	50-10.12	5-10.62	1.88
D	821104	2353 0.24	50-10.30	5-10.84	2.52
	821105	349 14.90	50-10.21	5-10.66	2.55
	821105	5 3 23.54	50-10.11	5-10.48	2.35
S	821105	613 12.80	50-10.21	5-10.76	1.95
D	821105	1412 58.66	50-10.18	5-10.63	2.64
D	821106	426 44.63	50-10.23	5-10.73	2.62
S	821106	810 30.90	50-10.15	5-10.74	1.90
S	821106	1050 15.39	50-10.13	5-10.78	1.98
D	821107	836 16.54	50-10.21	5-10.70	2.59
	821107	1047 17.65	50-10.14	5-10.64	2.59
D	821107	1859 52.86	50-10.15	5-10.67	2.62
D	821107	2225 50.91	50-10.15	5-10.60	2.65
D	821108	1230 10.60	50-10.15	5-10.59	2.47
D	821109	232 24.05	50-10.13	5-10.62	2.55
D	821109	1019 22.30	50-10.13	5-10.61	2.55
D	821109	1213 20.48	50-10.09	5-10.62	2.47
D	821109	1830 34.58	50-10.13	5-10.62	2.57
	821109	2256 21.42	50-10.30	5-10.68	2.29
D	821110	612 28.92	50-10.11	5-10.60	2.54
D	821110	1018 26.61	50-10.21	5-10.68	2.59
D	821111	821 23.56	50-10.12	5-10.64	2.57
D	821112	542 48.22	50-10.14	5-10.70	2.64
D	821113	1323 36.40	50-10.15	5-10.62	2.53
D	821113	2211 24.77	50-10.16	5-10.62	2.60
	821114	3 1 39.74	50-10.66	5-10.03	2.00
D	821114	3 6 16.30	50-10.22	5-10.71	2.51
D	821115	1652 33.27	50-10.13	5-10.65	2.38
D	821116	1048 33.94	50-10.15	5-10.57	2.48
D	821116	1211 58.20	50-10.11	5-10.54	2.29
D	821117	514 9.20	50-10.13	5-10.64	2.50
D	821118	132 37.77	50-10.08	5-10.47	1.92
D	821118	7 7 57.35	50-10.15	5-10.61	2.37
D	821118	748 10.59	50-10.13	5-10.64	2.46
	821119	027 45.84	50-10.09	5-10.26	2.74
D	821120	1659 9.87	50-10.24	5-10.54	2.34
D	821121	444 19.26	50-10.14	5-10.66	2.54
	821121	522 53.97	50-10.32	5-10.86	2.89
D	821121	2257 24.81	50-10.16	5-10.71	2.35
D	821122	356 27.38	50-10.23	5-10.53	2.40
D	821122	812 29.76	50-10.09	5-10.63	2.52
D	821122	1416 46.97	50-10.24	5-10.60	2.26
D	821122	1751 57.30	50-10.14	5-10.61	2.43
	821123	857 15.77	50-10.21	5-10.55	2.29
	821123	1821 47.69	50-10.33	5-10.87	2.83
	821127	634 23.10	50-10.58	5-10.69	2.44
	821128	213 20.34	50-10.27	5-10.88	2.74
	821201	1226 43.84	50-10.20	5- 9.50	0.02
D	821202	419 30.74	50-10.02	5-10.54	2.50
D	821203	1058 21.18	50-10.24	5-10.51	2.35
	821203	2218 58.70	50-10.14	5-10.80	1.68
	821204	1611 4.07	50-10.25	5-10.79	2.50

Table 4.2 continued.

	DATE	ORIGIN TIME	LATITUDE N	LONGITUDE W	DEPTH (KM)
S	821204	1714 6.49	50-10.12	5-10.81	1.52
	821208	2024 25.96	50-10.12	5-10.65	2.43
D	821209	035 32.62	50-10.09	5- 9.84	2.00
D	821213	1317 37.76	50-10.17	5-10.59	3.18
D	821217	14 9 13.11	50-10.13	5-10.42	2.21
	821219	032 28.22	50-10.24	5-10.34	3.17
	821228	443 59.30	50-10.08	5-10.44	2.52
	821228	518 56.76	50-10.03	5-10.25	2.39
	830102	2 1 59.69	50-10.07	5-10.49	2.97
	830104	1232 26.73	50-10.15	5-11.20	1.70
	830112	227 2.54	50-10.40	5-11.06	2.80
	830113	1342 14.64	50- 9.99	5-10.39	2.67
	830117	757 41.73	50-10.35	5-10.89	2.89
	830119	929 10.85	50-10.36	5-10.76	3.42
	830120	1950 47.76	50-10.46	5-10.83	3.46
	830121	9 7 5.02	50-10.38	5-11.01	2.71
	830121	916 22.42	50-10.09	5-10.38	2.16
	830124	1958 39.43	50-10.99	5-11.71	5.68
	830124	2311 59.66	50-10.53	5-10.71	1.08
	830125	1242 40.35	50-10.37	5-10.75	3.24
	830126	12 5 51.75	50-10.43	5-11.00	3.03

wave window because of the proximity of the four three-component stations to the seismicity at the HDR site. Therefore the incident angle of the ray path is usually less than 40° at these stations, which means that the shear-wave is recorded without modification due to the free surface. Jet pen records of all the three-component traces from analogue magnetic tape are analysed to select records for shear-wave particle motion analysis. From a total of 300 analogue records 69 records from CTR and CRA, 63 records from CME, and 9 records from CRQ are digitized and seismogram traces and polarization diagrams are generated. Instrumental overloading and low signal to noise ratios are the chief reasons for omitting some records from CTR and CRA. The small number of records available for analysis from CRQ is due to a persistant instrumental problem. Station CME also failed for a short period, and there are less records available at this station than at CTR and CRA. Also the shear-wave particle motion is only analysed for reliably located events to reduce the likliehood of misinterpretation. For example the event at the surface shown in the cross section in Figure 4.4 is poorly located, and using such events will lead to erroneous conclusions. The poorly located events combined with events which overload the three-component stations reduces the number of events from 75 to 61. However 192 seismic records are available for shear-wave particle motion analysis. Examples of three-component seismograms and polarization diagrams recorded at stations CME, CTR, and CRA are shown in Figures 4.5 and 4.6. A three-component seismogram and polarization diagrams from CRQ is shown in Figure 2.2.

On almost all of the seismic records the shear-wave onset is impulsive and most of the energy is contained in the first cycle of the shear-wave coda. The shear-wave frequency is typically about 25 Hz which gives a wavelength of about 130 m for a shear-wave velocity of 3.3 km/sec. The P:S amplitude ratio ranges from 0.2 to 0.5, and the P-wave coda rarely extends into the shear-

Figure 4.5

Three-component seismograms and polarization diagrams for a selection of group D acoustic events recorded at stations CME, CTR, and CRA. Notation and format as in Figure 1.2.

	Origin time	Epicentre	Depth
(a-c)	821104 2353 0.24	50-10.30 N 5-10.84 W	2.52
(d-f)	821107 1859 52.86	50-10.15 N 5-10.67 W	2.62
(g-i)	821114 3 6 16.30	50-10.22 N 5-10.71 W	2.51
(j-l)	821120 1659 9.87	50-10.24 N 5-10.54 W	2.34
(m-o)	821122 1751 57.30	50-10.14 N 5-10.61 W	2.43

The heavy arrows in the horizontal polarization diagrams mark the shear-wave arrivals, and the heavy arrows below the polarization diagrams mark the 'away' radial direction.

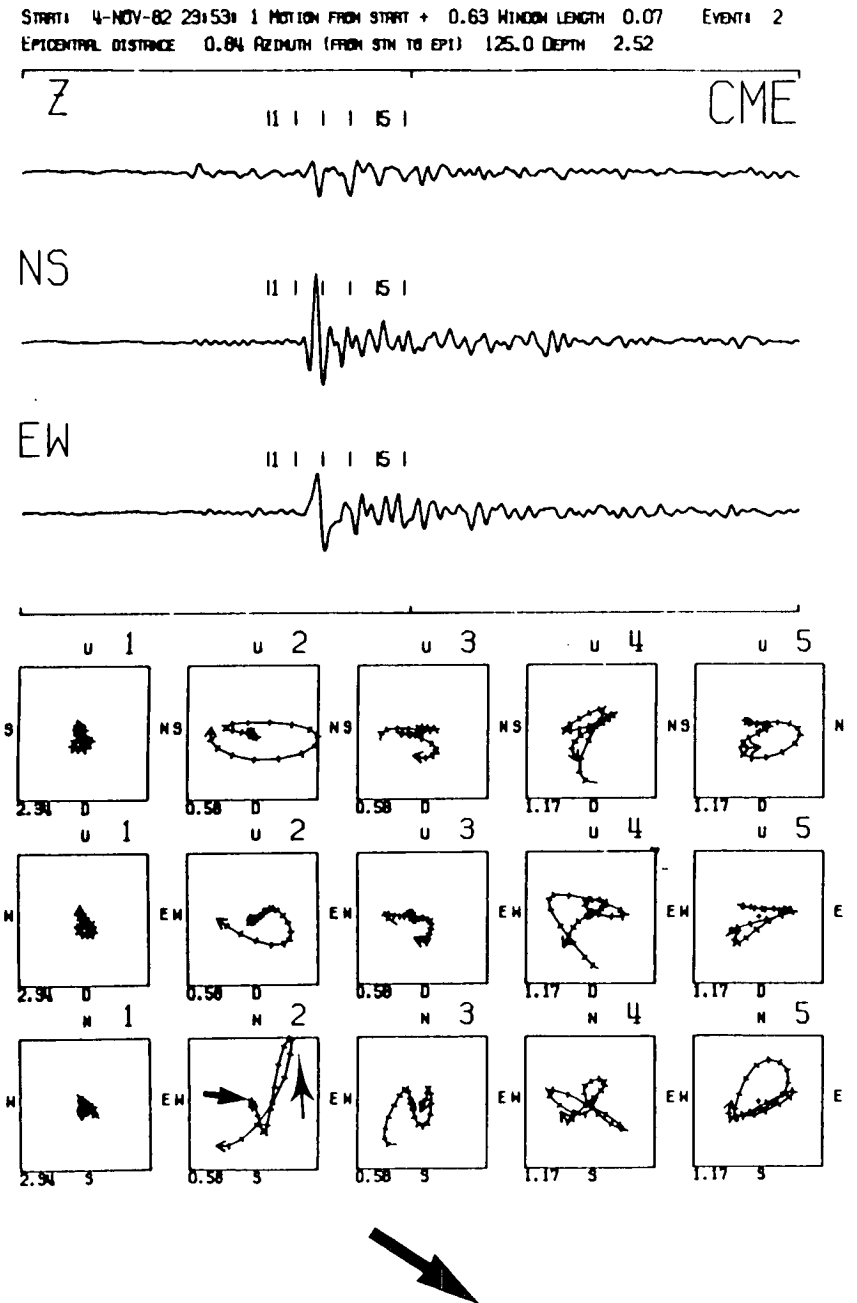

Figure 4.5a

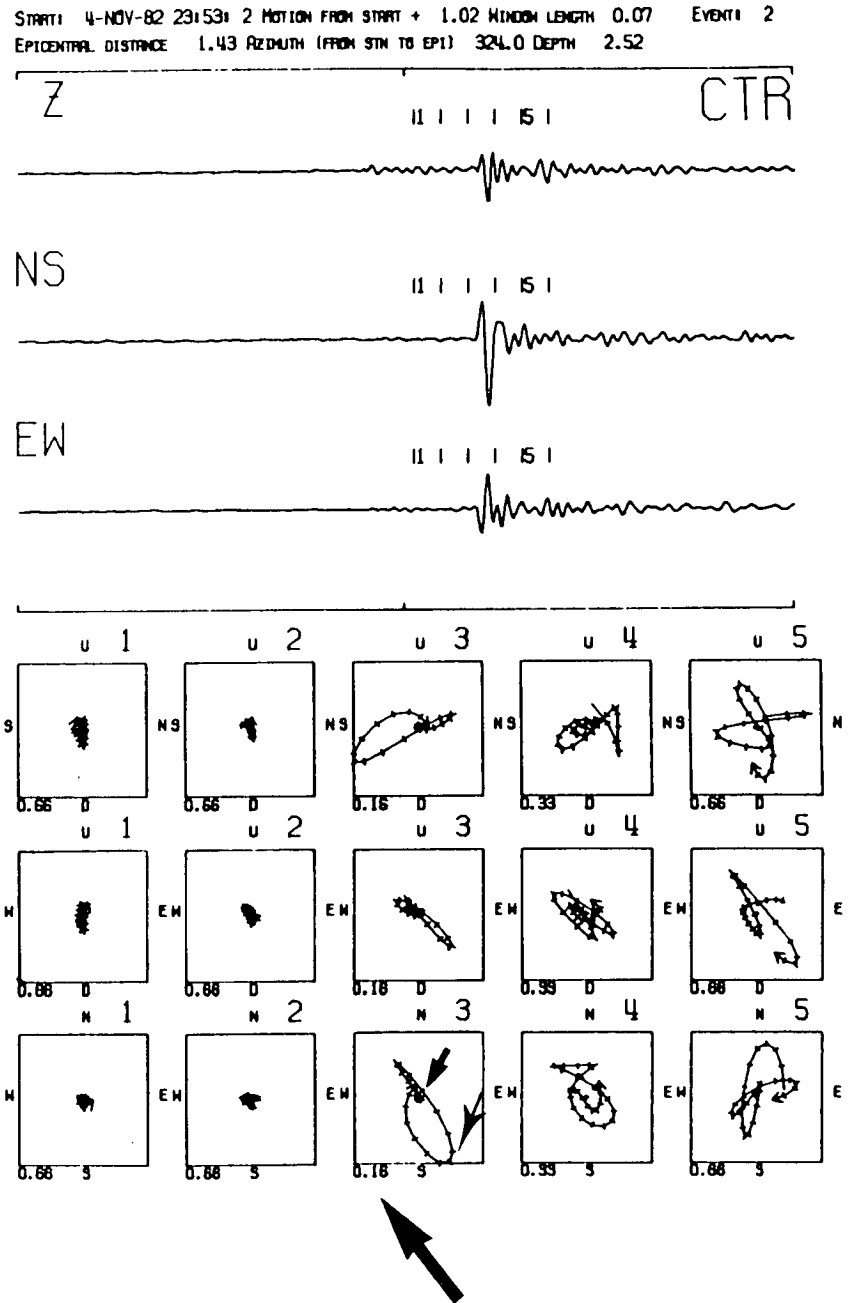

Figure 4.5b

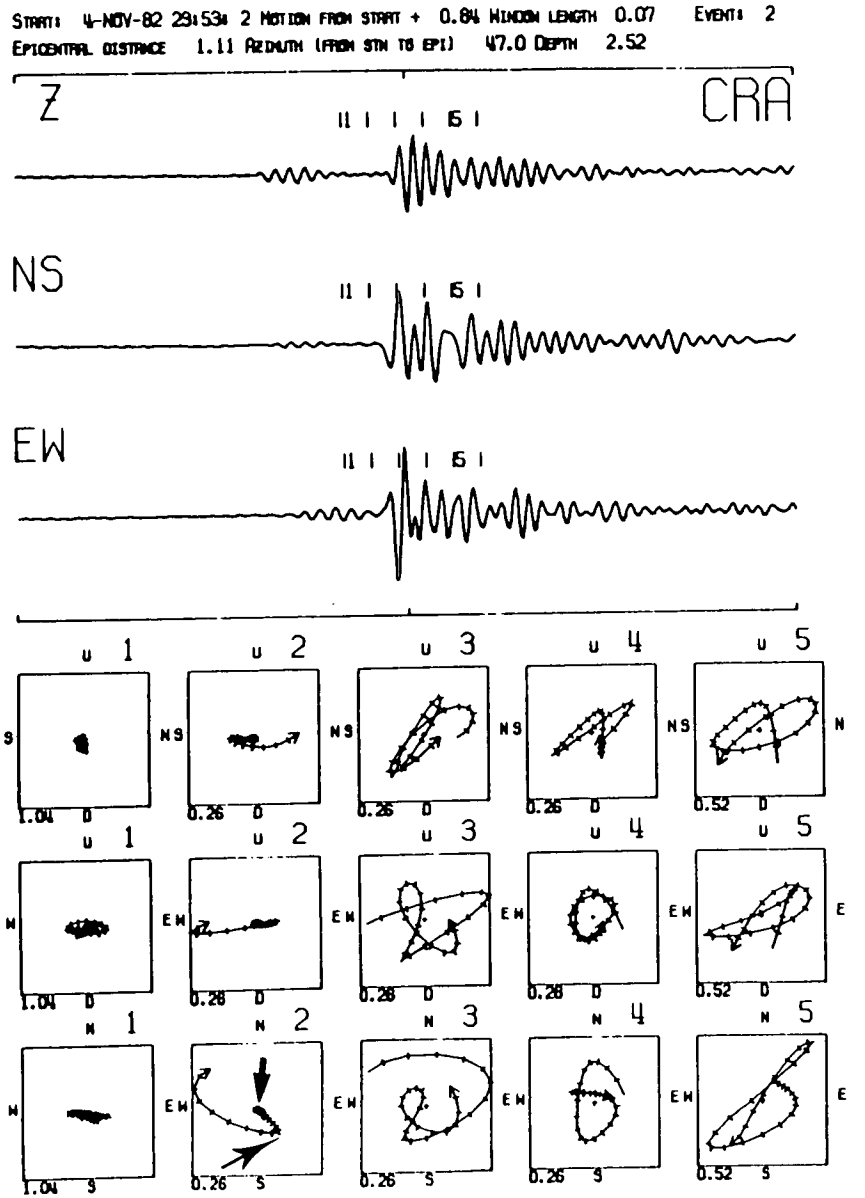

Figure 4.5c

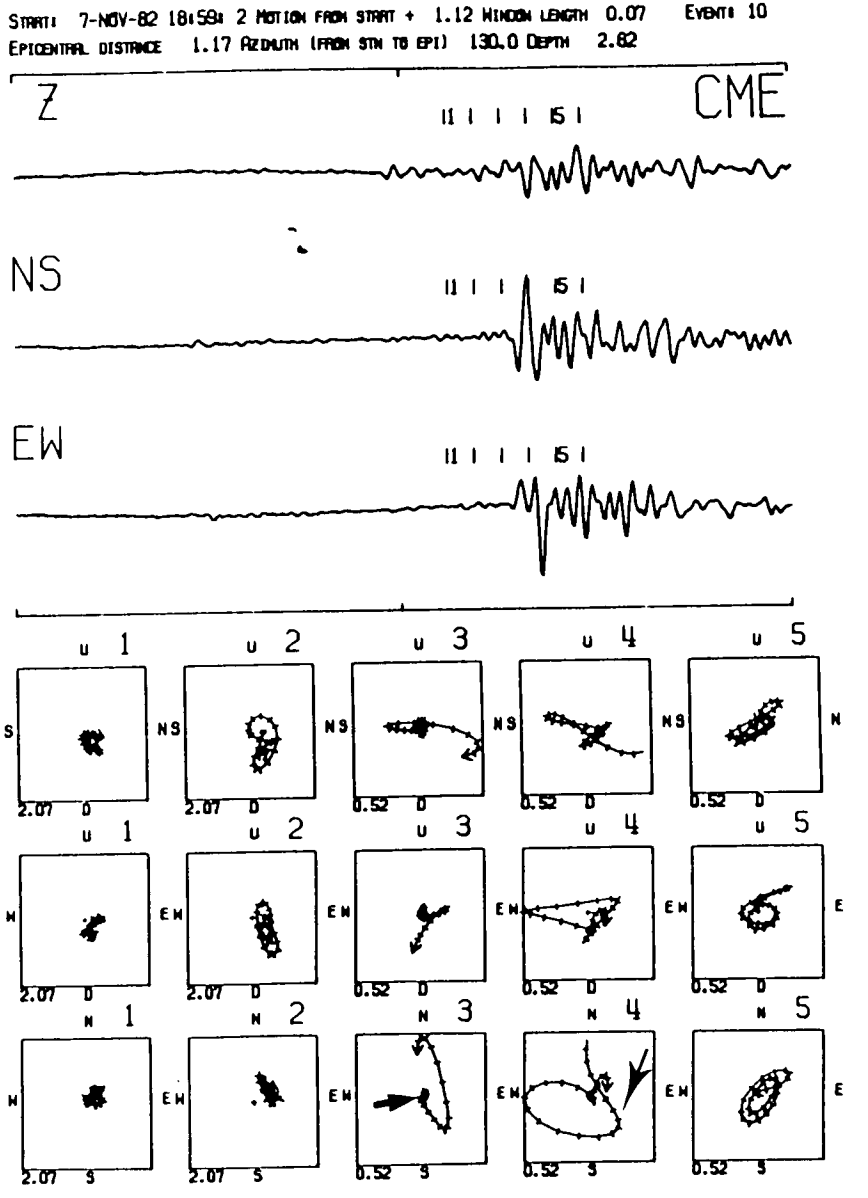

Figure 4.5d

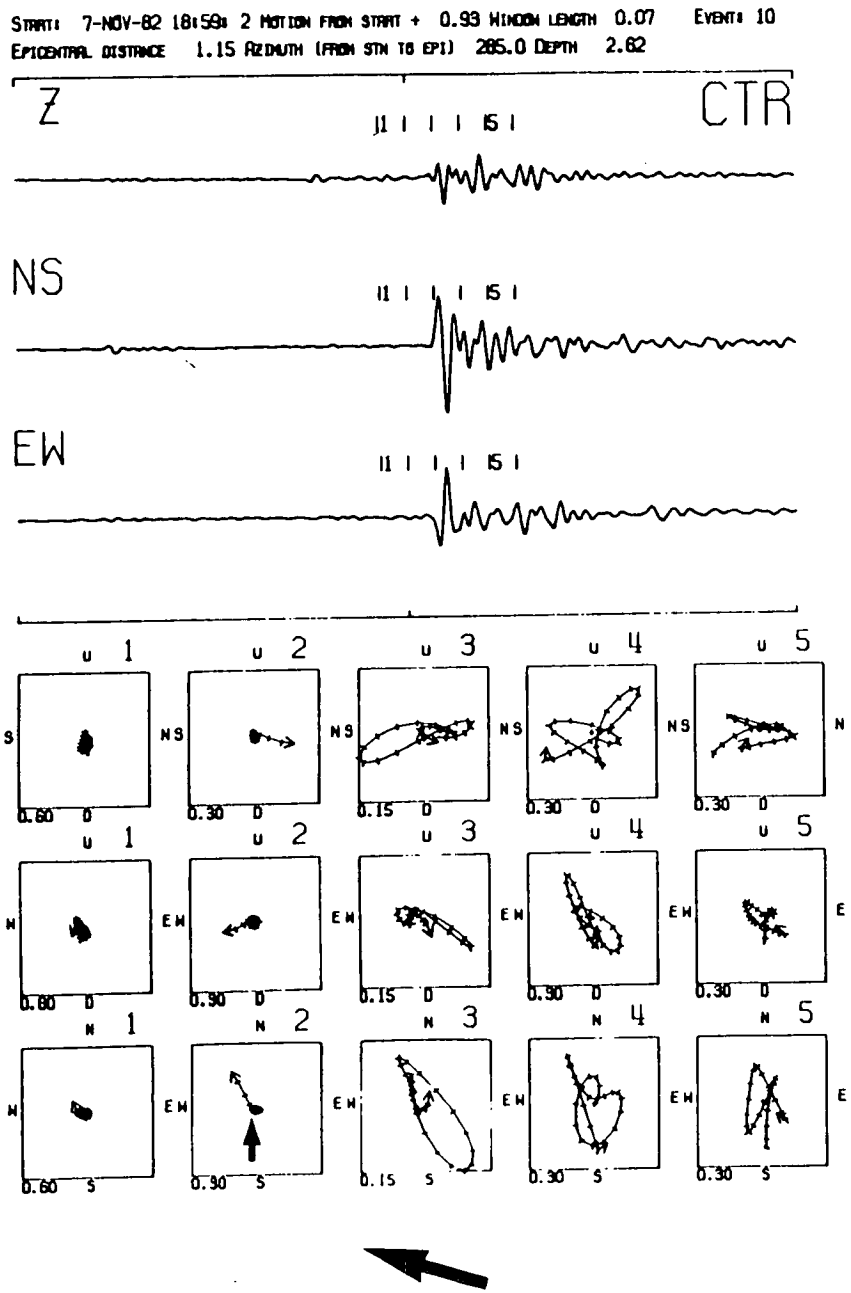

Figure 4.5e

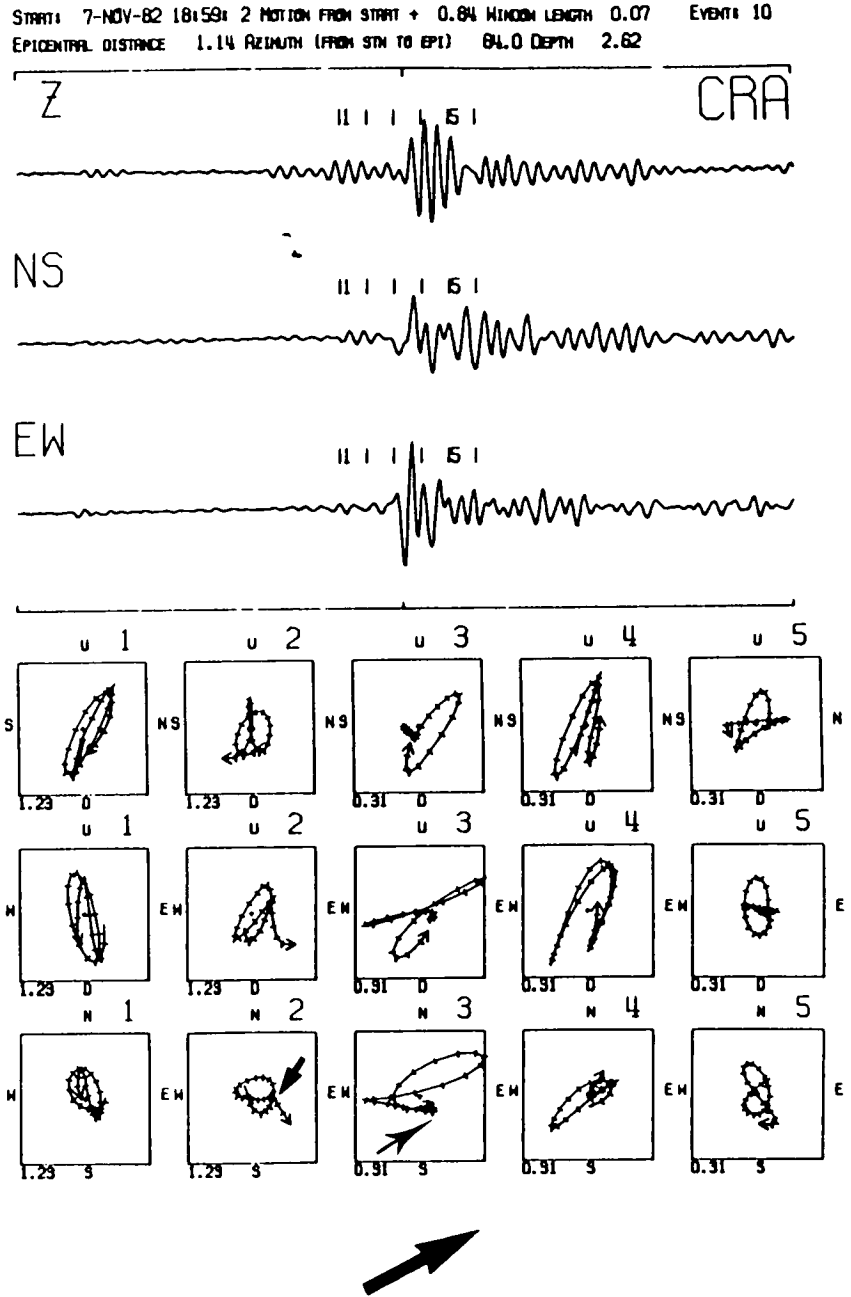

Figure 4.5f

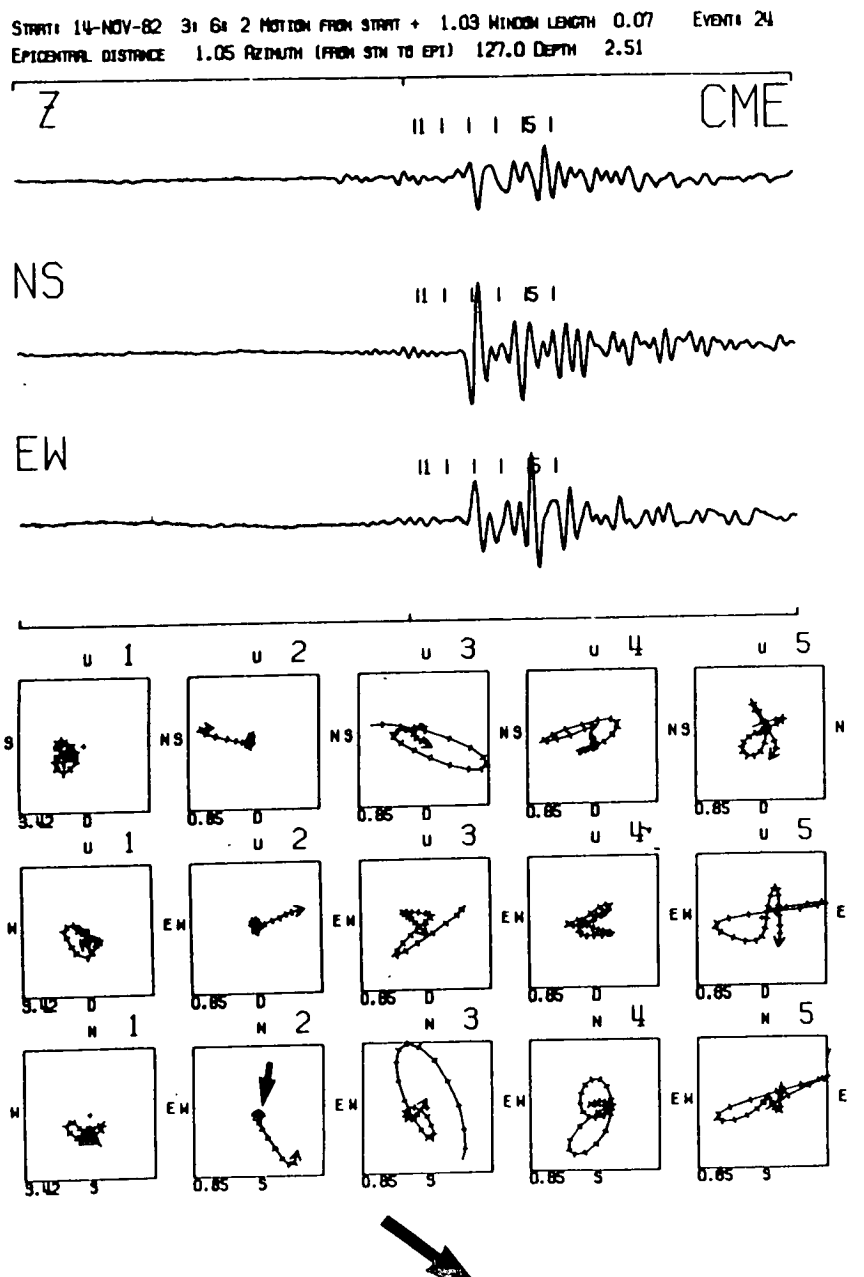

Figure 4.5a

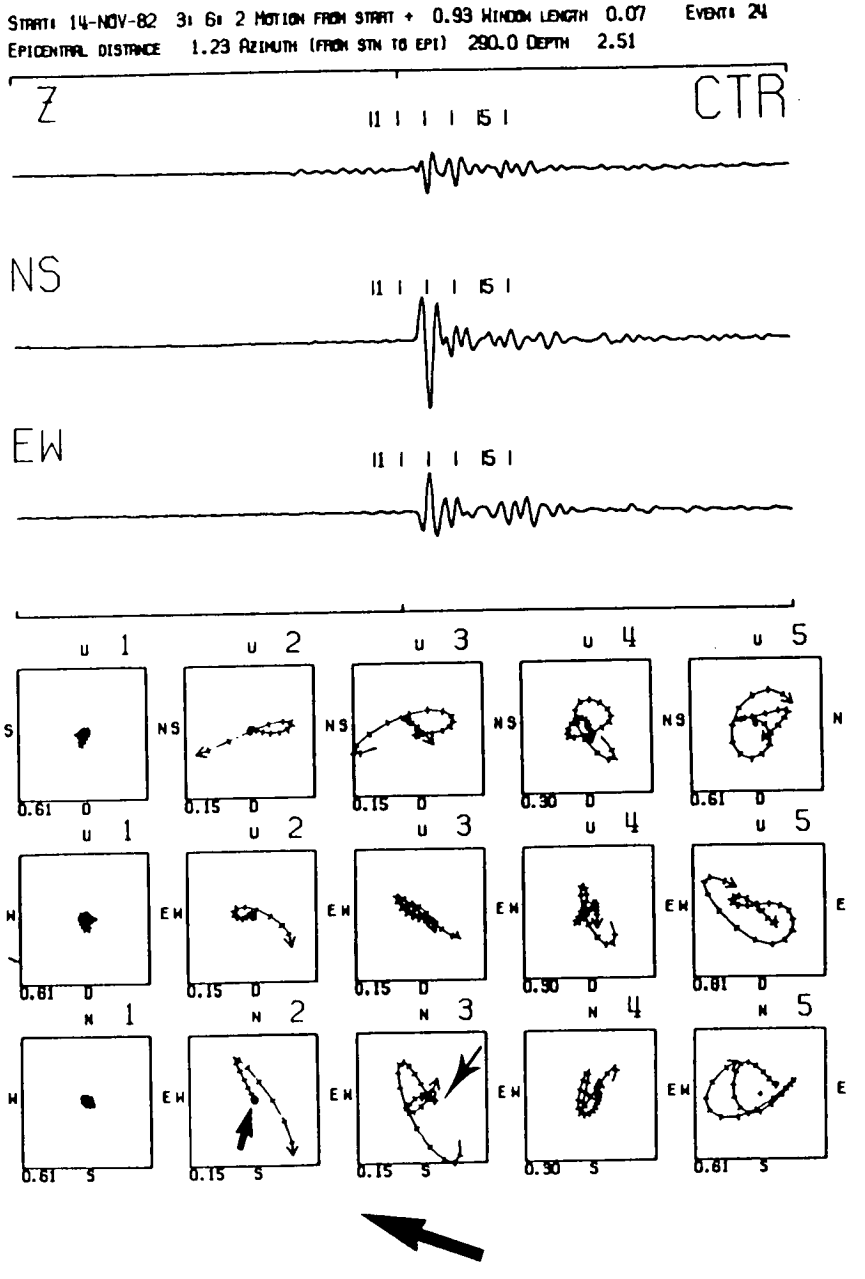

Figure 4.5b

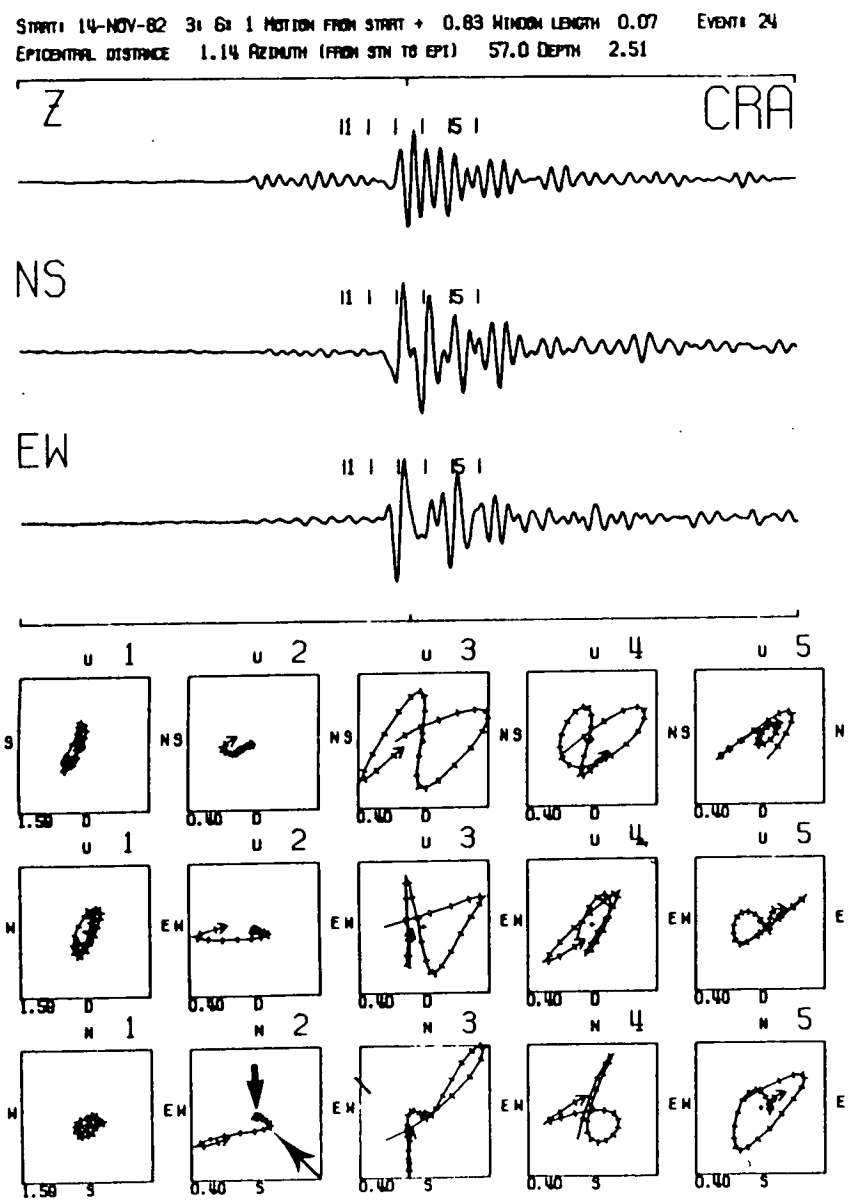

Figure 4.5i

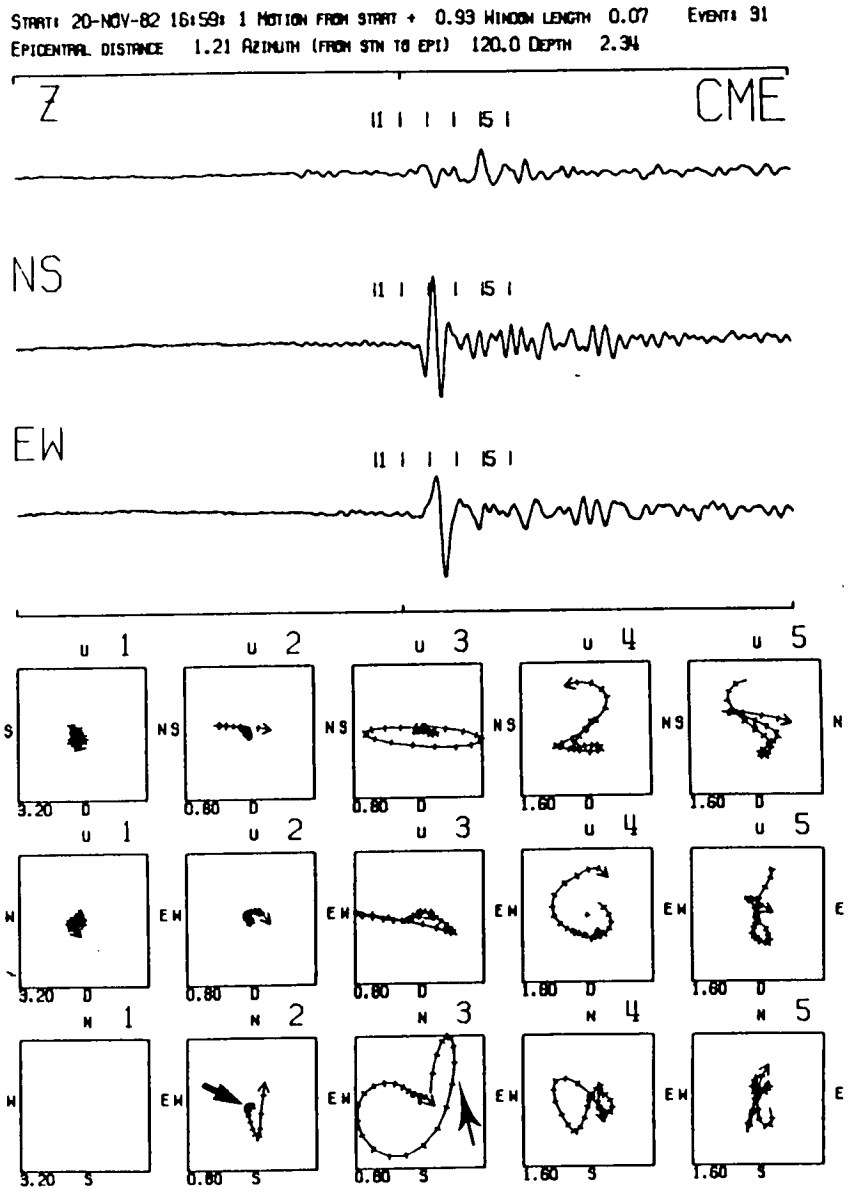

Figure 4.5j

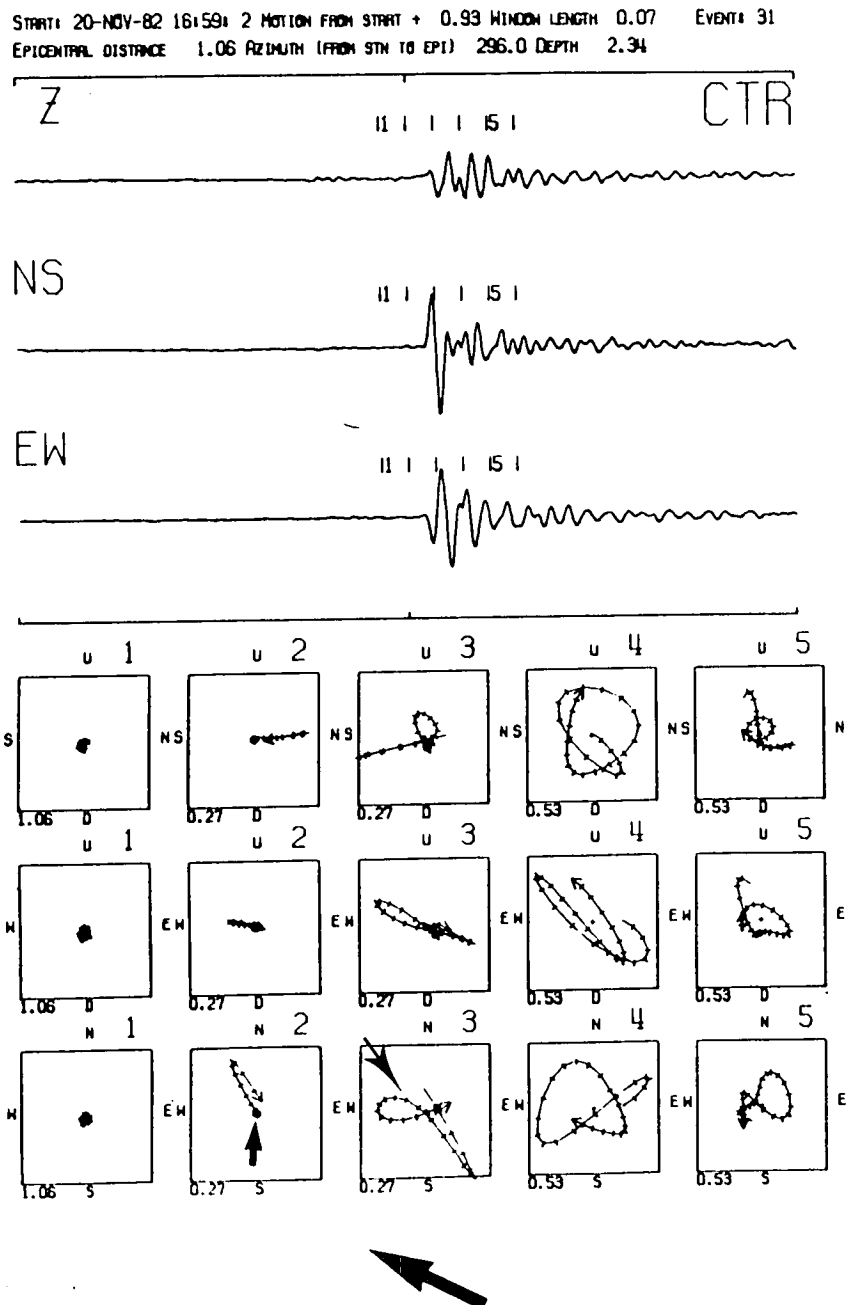

Figure 4.5k

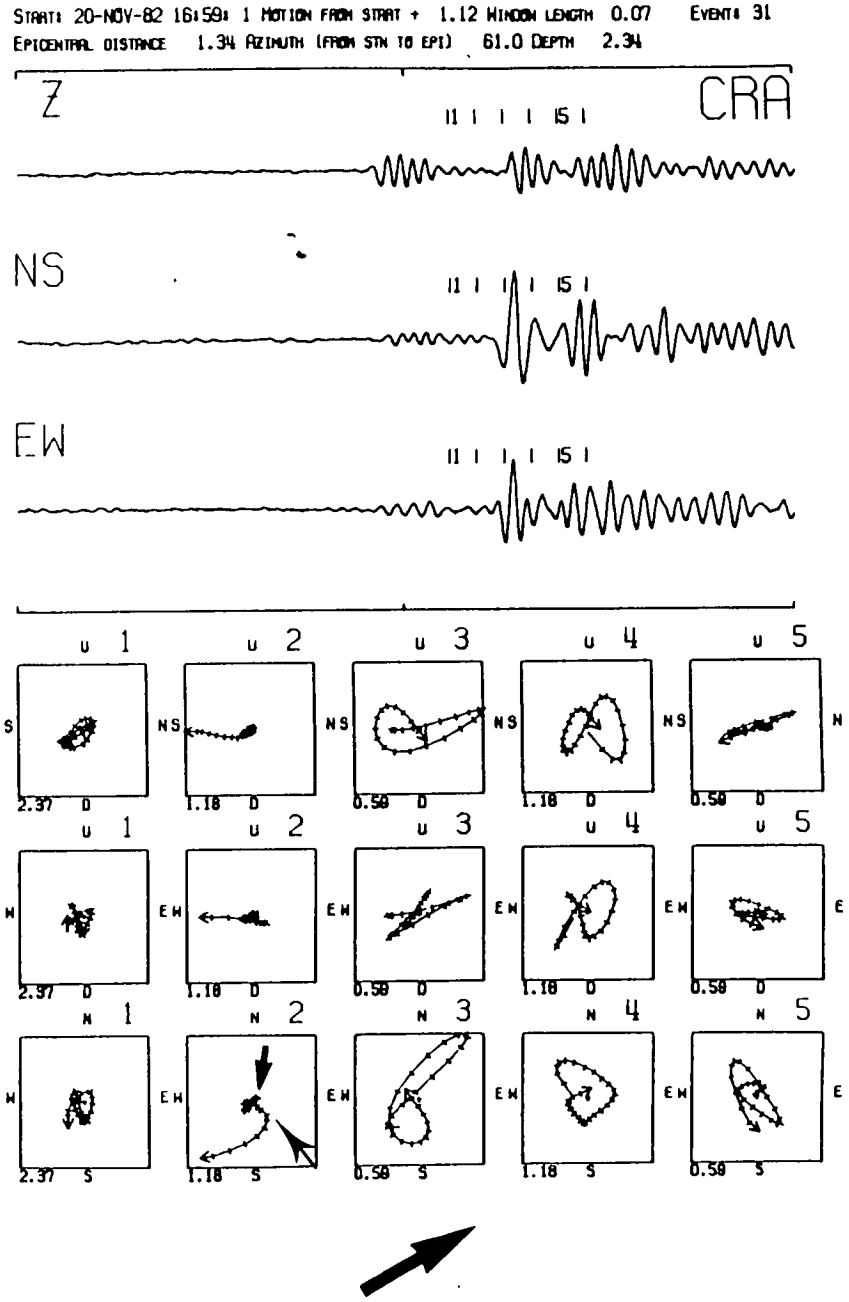

Figure 4.5l

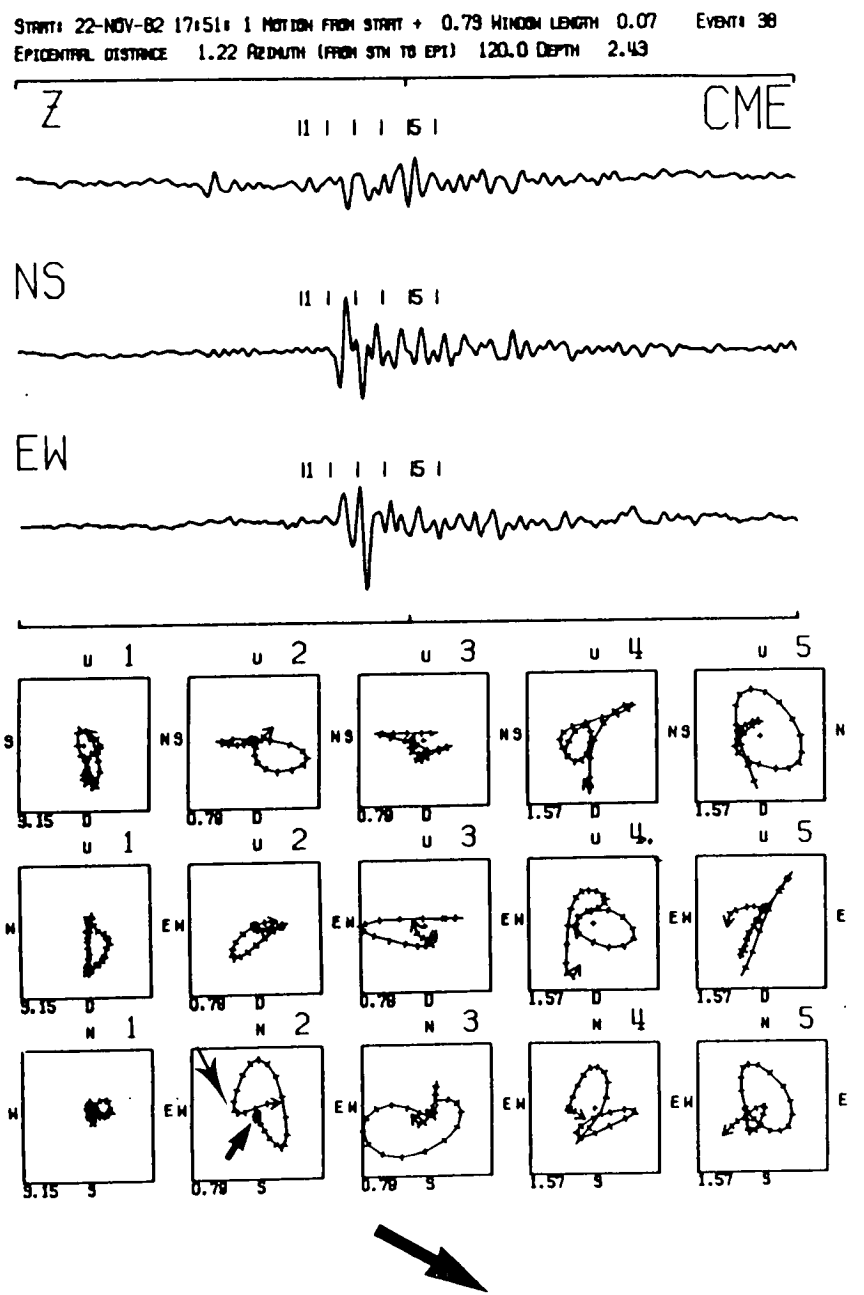

Figure 4.5m

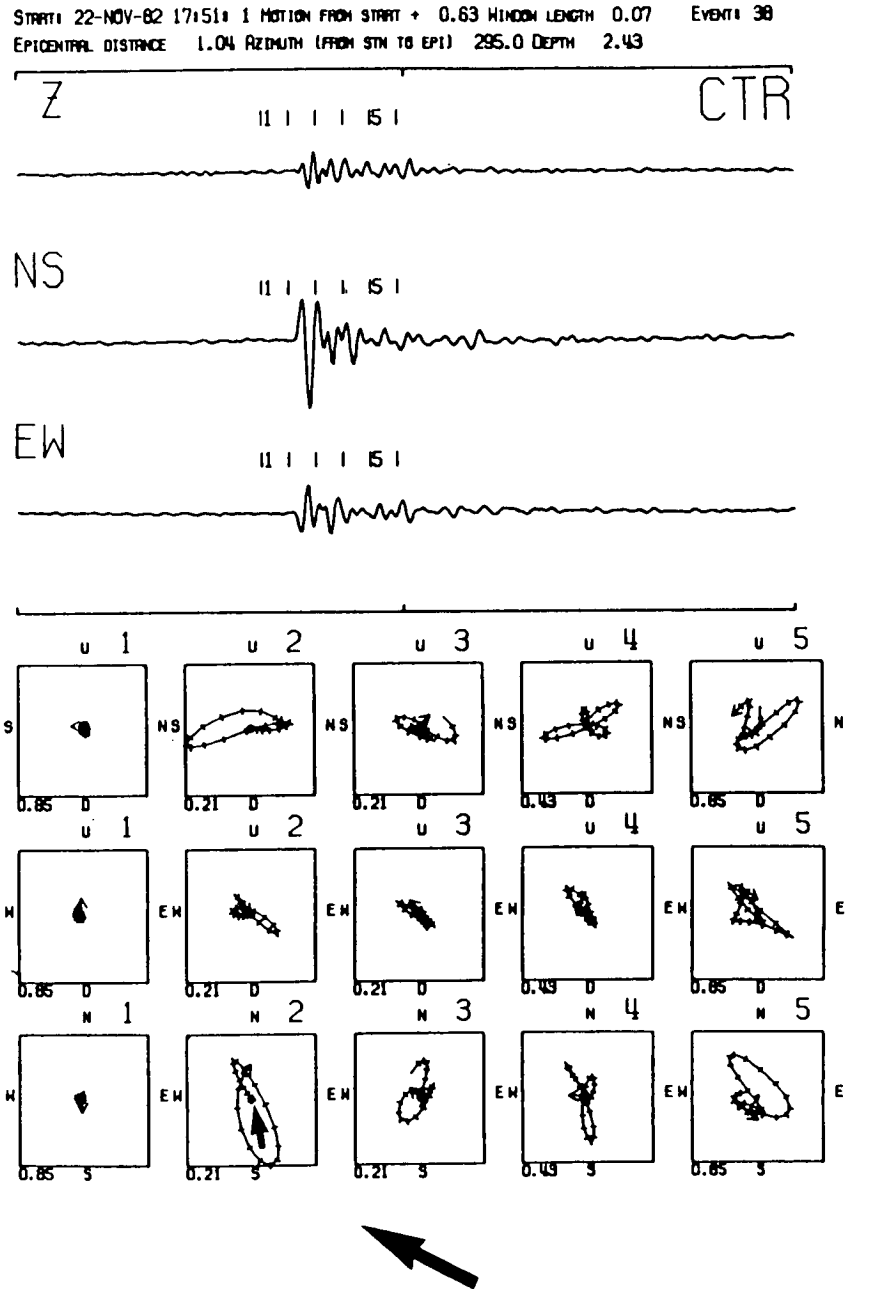

Figure 4.5n

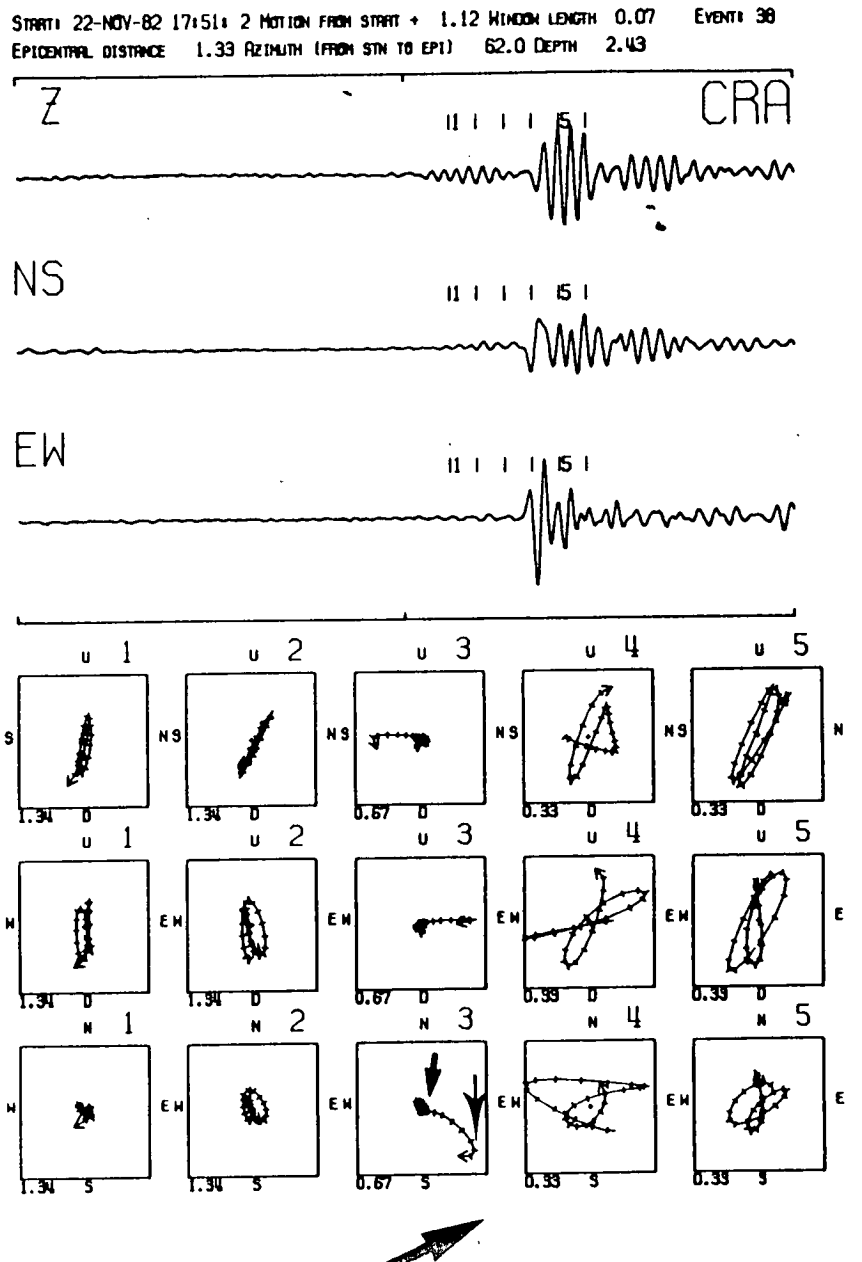
START: 22-NOV-82 17:51: 2 MOTION FROM START + 1.12 WINDOW LENGTH 0.07 EVENT: 38
EPICENTRAL DISTANCE 1.33 AZIMUTH (FROM STN TO EPI) 62.0 DEPTH 2.43
Z
CRA
NS
EW
U 1
U 2
U 3
U 4
U 5
N 1
N 2
N 3
N 4
N 5
S
NS
N
EW
E
1.34
0.67
0.33
0.39
D
S

Figure 4.5o

Figure 4.6

Three-component seismograms and polarization diagrams for a selection of group S acoustic events recorded at stations CME, CTR, and CRA. Notation and format as in Figure 1.2.

	Origin time	Epicentre	Depth
(a-c)	821019 2323 39.08	50-10.12 N 5-10.57 W	1.58
(d-f)	821104 2159 5.71	50-10.12 N 5-10.62 W	1.88

The heavy arrows in the horizontal polarization diagrams mark the shear-wave arrivals, and the heavy arrow below the polarization diagrams mark the 'away' radial direction.

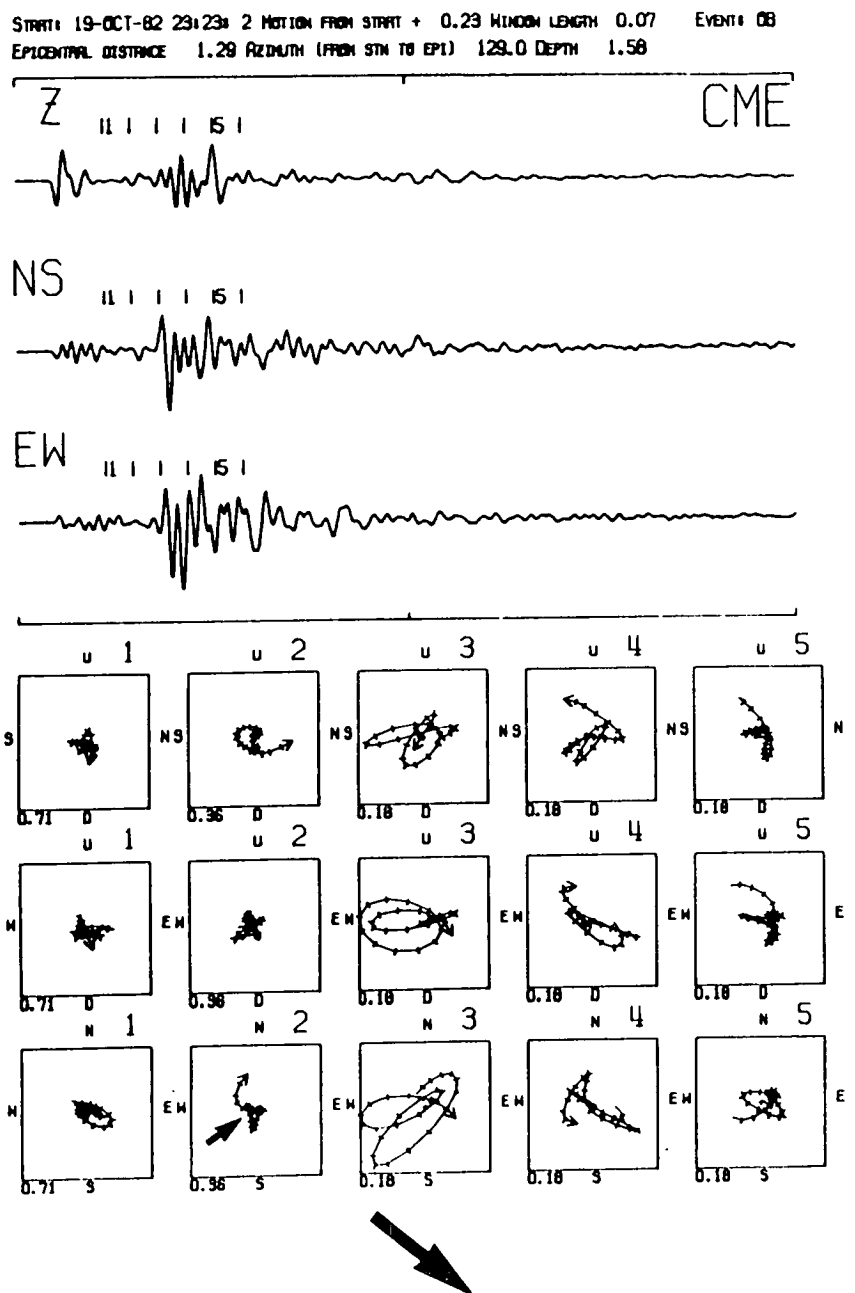

Figure 4.6a

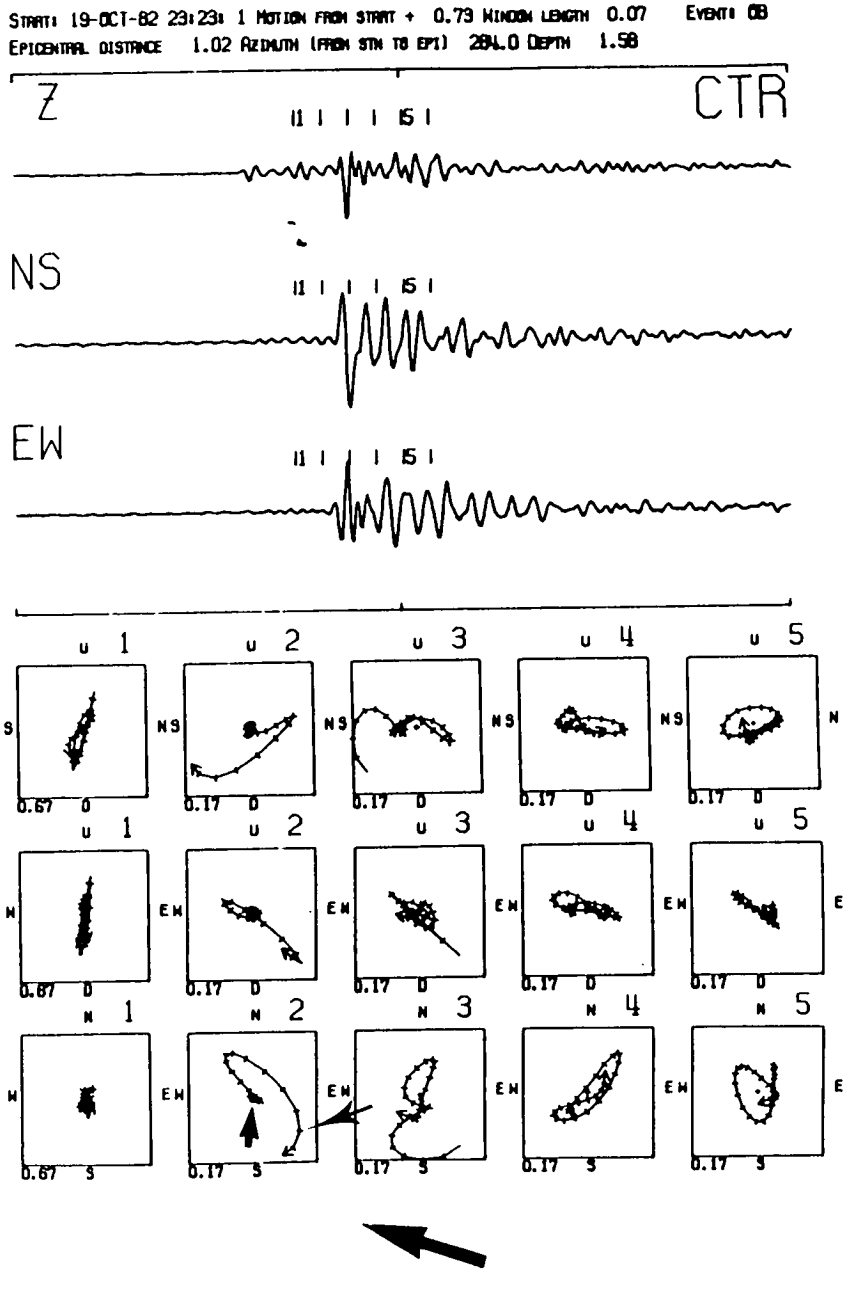

Figure 4.6b

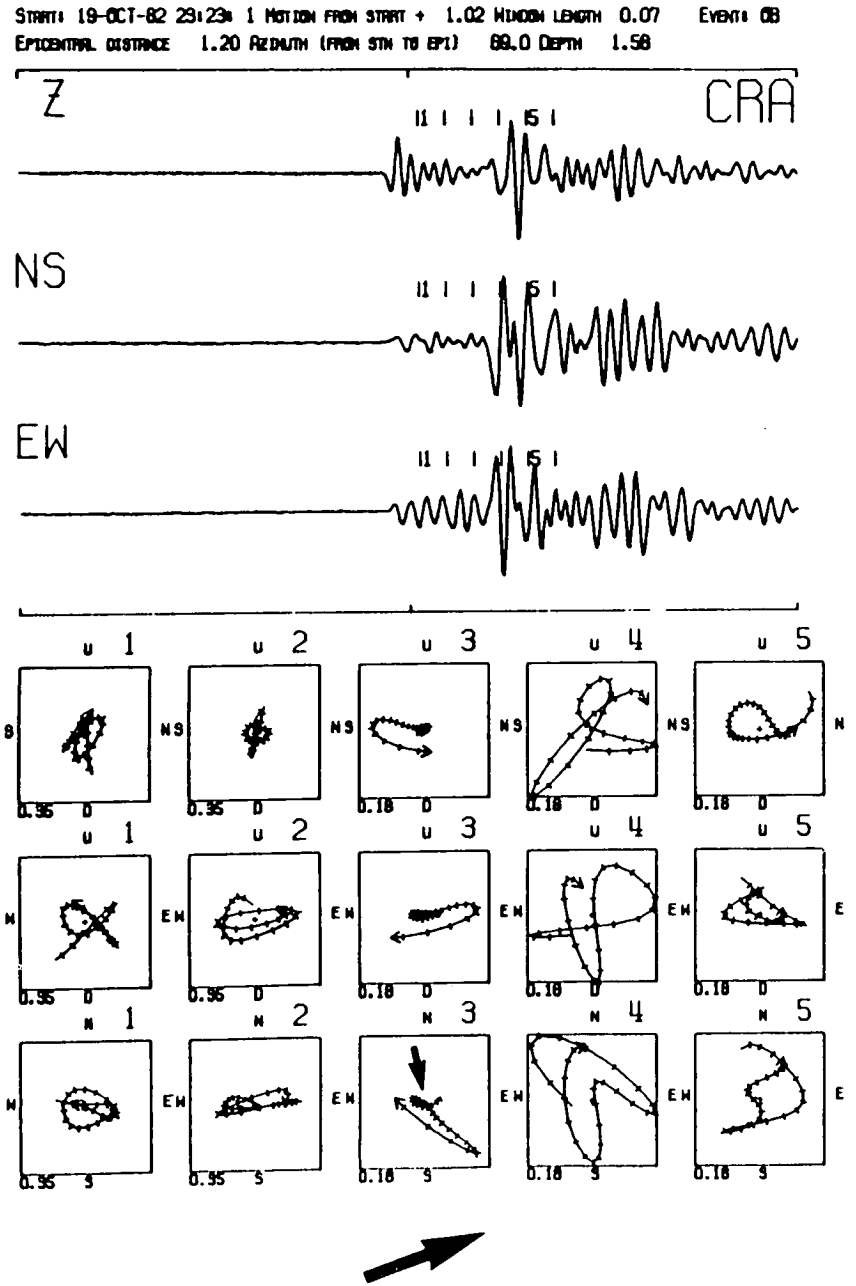

Figure 4.6c

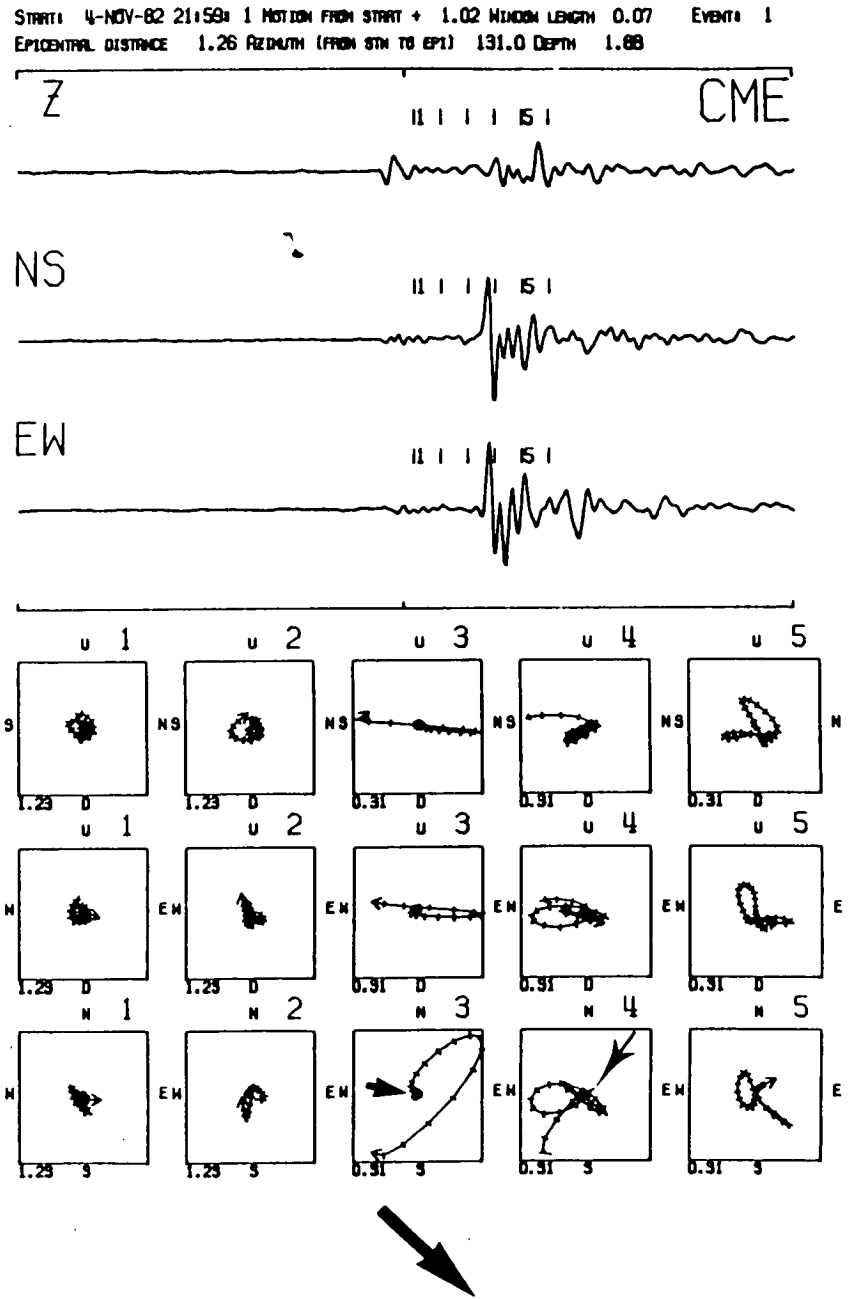

Figure 4.6d

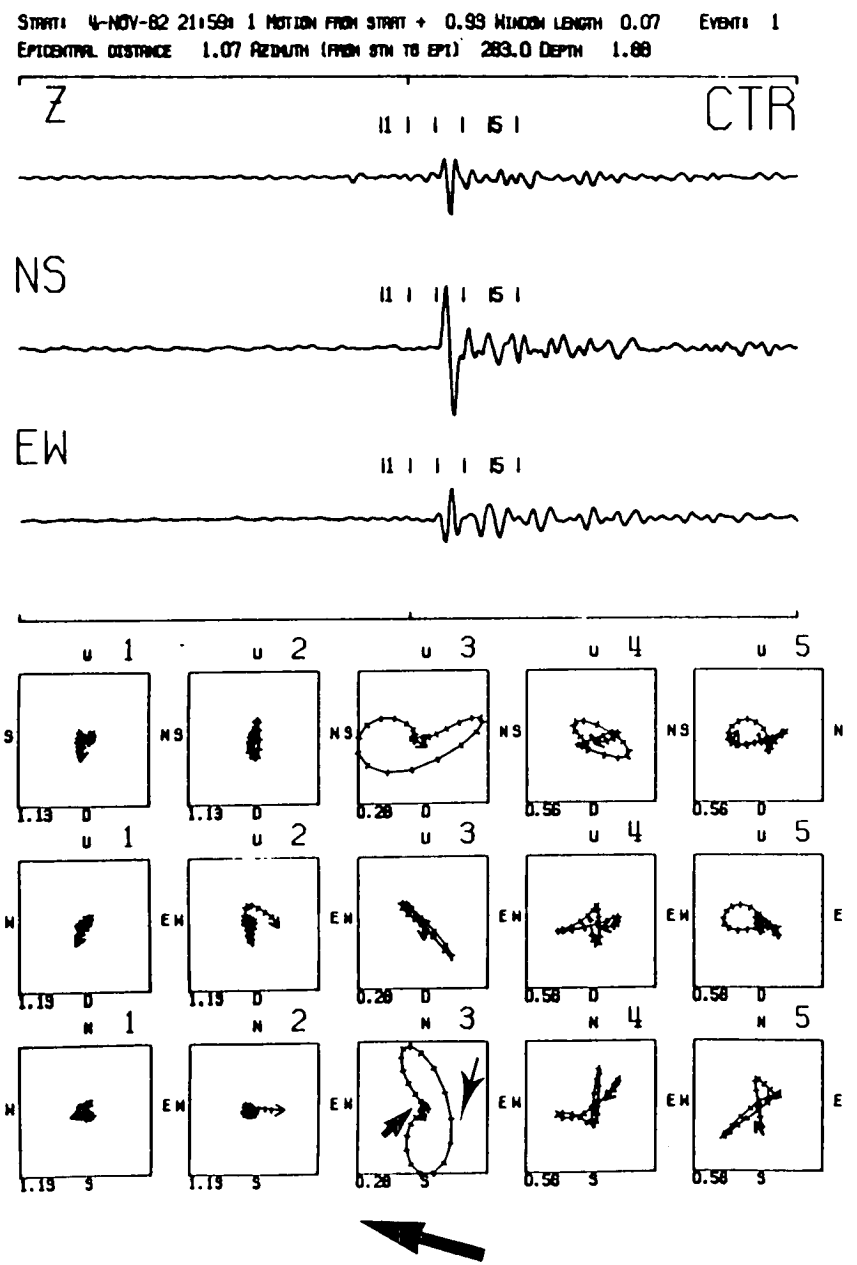

Figure 4.6e

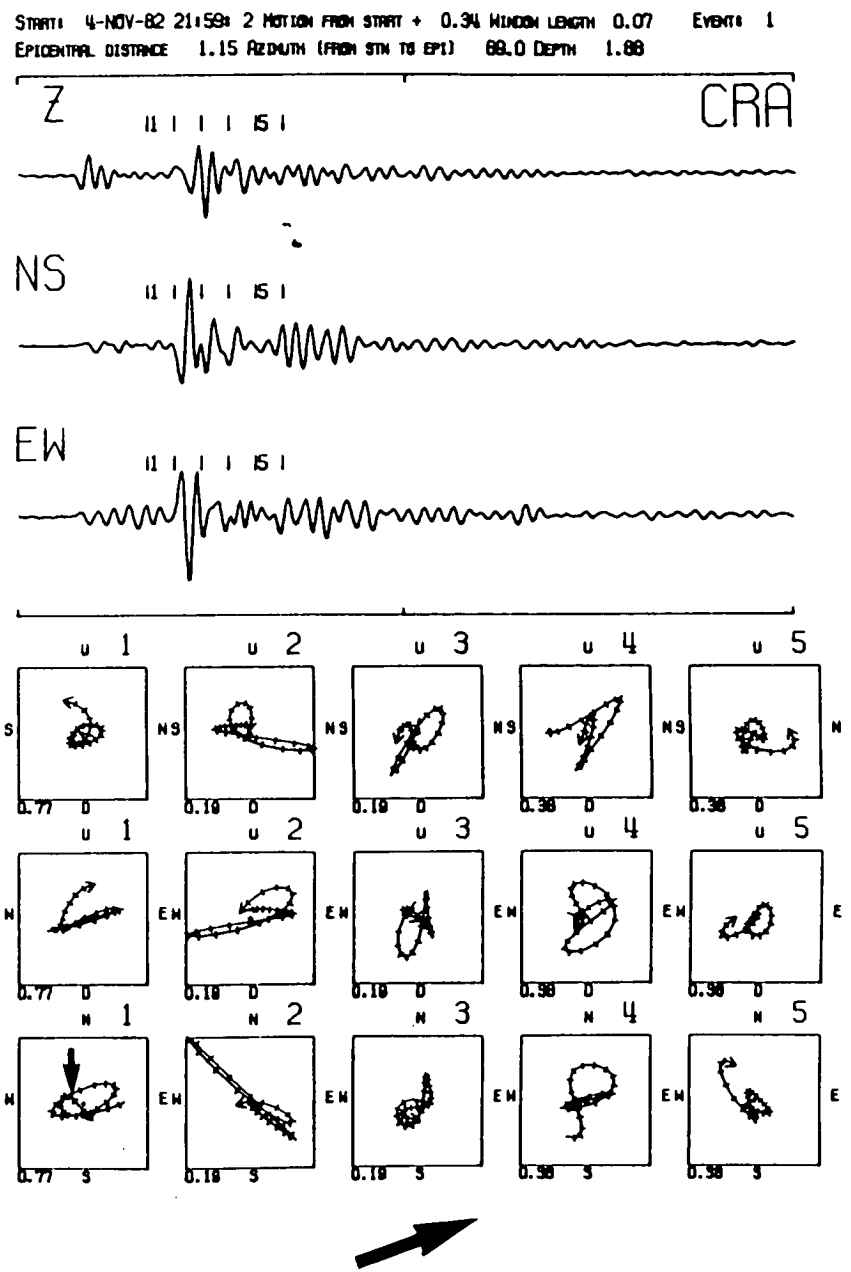

Figure 4.6f

wave onset. This coupled with the high signal to noise ratio, typical of the records, and the impulsiveness of the shear-wave made the determination of the shear-wave arrival straightforward and unambiguous. At CME, CTR, and CRQ the shear-wave excites predominantly horizontal motion which is expected for steeply propagating rays. However at CRA reverberations on the vertical-component are often equal in amplitude to those on the horizontal-components.

An examination of the polarization diagrams shows that the shear-wave particle motion is repeatable for many of the acoustic events. Therefore it appears that the source location and source mechanism are unchanged for many events, so that the initial shear-wave polarization from the source and the ray path to the station are unchanged for these events. This prompted the division of the events into groups based on similarity of shear-wave particle motion. Two distinct groups emerge: 37 events in one group, and 6 events in the other group.

Epicentral maps, cross-sections, and time against depth plots of each group are illustrated in Figures 4.7 and 4.8. The hypocentral depths of the larger group of events are about 0.5 km deeper than the smaller group of events. For this reason the larger group consisting of 37 events is referred to as group D(eep) and the smaller group of 6 events is labelled group S(hallow). Group D events cluster directly below the wellhead at depths of about 2.5 km, whereas group S event hypocentres are located just above the hydrofractured zone with depths less than 2 km. This difference in depth may be the main reason for the different shear-wave particle motion of each group since only rays from the group D event cluster pass through the main hydrofractured region. Note, also, that the event of 19 October 1982, which occurred prior to the main phase of hydrofracturing, belongs to group S.

The distinguishing features of the horizontal shear-wave particle motion at

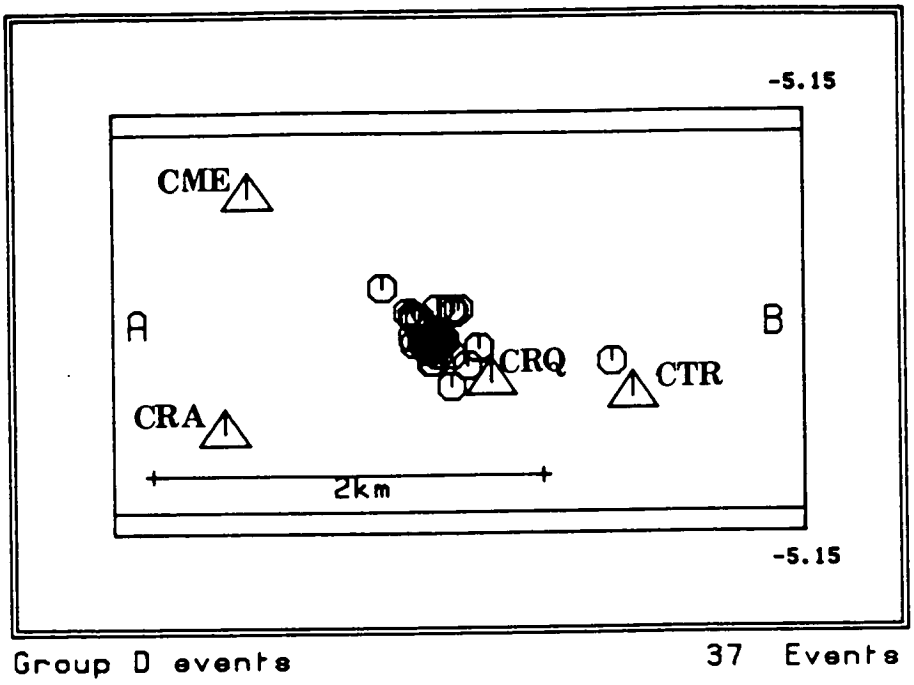

Figure 4.7a

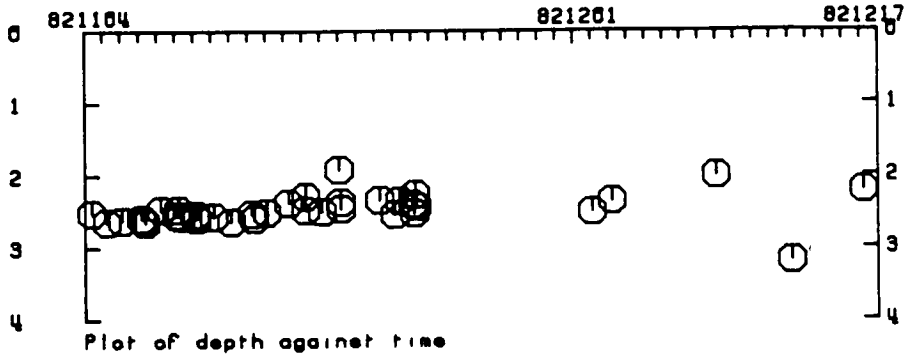

Figure 4.7b

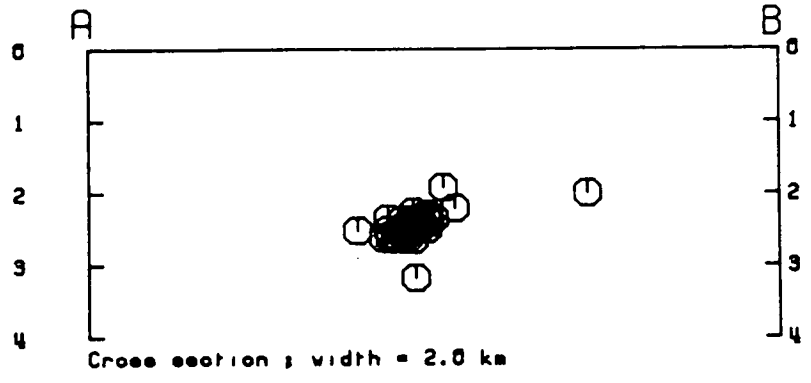

Figure 4.7c

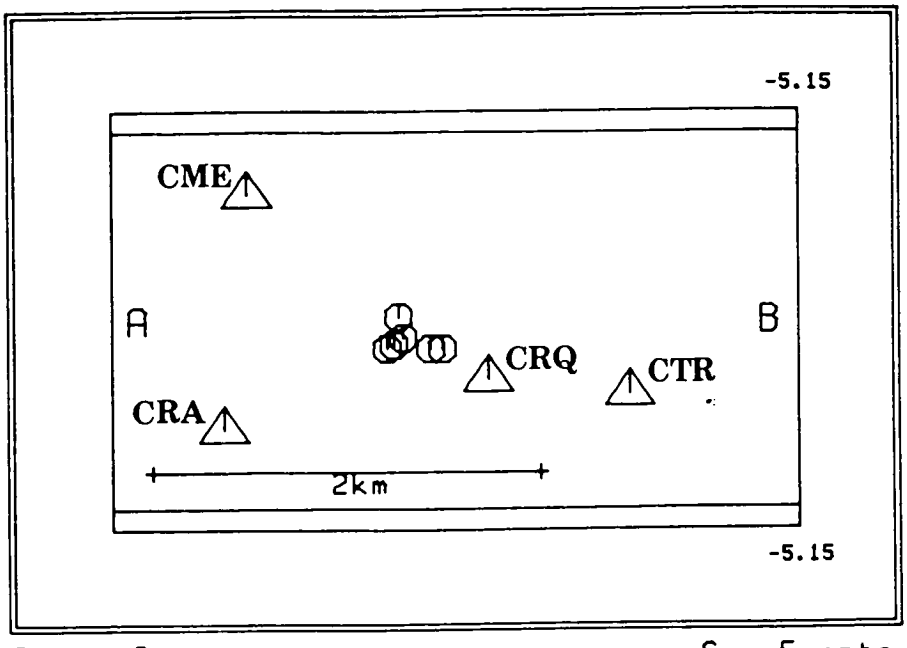

Group S events 6 Events

Figure 4.8a

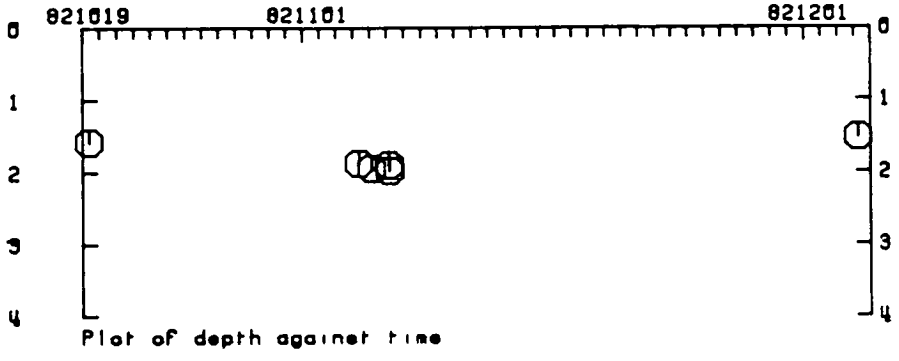

Figure 4.8b

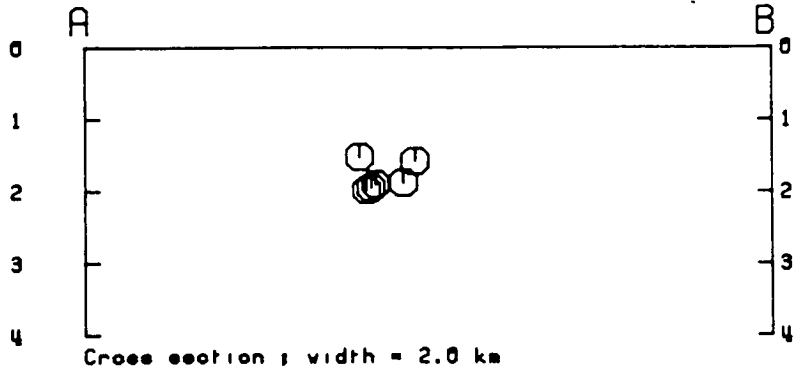

Figure 4.8c

each station characteristic of group D events are described below.

CME - Southeast to south first motion. Linear onset followed by elliptical motion with an east-west axis.

CTR - Northwest first motion. Linear onset followed by elliptical motion about the same axis.

CRA - Southeast to south first motion quickly followed by westerly motion (0.01 second after onset) then northeast motion.

The events of group D are divided into five subgroups based on minor differences in the shear-wave particle motion. Figures 4.5a to 4.5o illustrate seismograms from each of the five subgroups and show the characteristic shear-wave particle motion of group D events and the subgroups. Over half of the events in group D generate the shear-wave particle motion shown in Figures 4.6d to 4.6e. This is the most frequent type of shear-wave particle motion observed at the HDR site.

The horizontal shear-wave particle motion at each station CME, CTR, and CRA characteristic of group S events is described below and examples are shown in Figure 4.6.

CME - Northeast first motion. Northeast-southwest trending ellipse, sometimes followed by east-west trending ellipse after 0.04 seconds.

CTR - Northwest first motion. Northwest-southeast trending ellipse. About 0.03 seconds after the onset particle motion becomes more elliptical.

CRA - Southeast first motion. Linear particle motion trending northwest-southeast.

From the 61 events used for shear-wave particle motion analysis only 18 have shear-wave particle motion which cannot be classified into either group D or S. However the direction of the shear-wave first motion for most of these events at each station is the same as the shear-wave first motions of group D or S events, even although the subsequent particle motion differs. For

example, of the selected 61 events recorded at CTR the orientation of the shear-wave first motion on only two records is not in a northwest direction. Similarly, at CME only 4 records from 61 show shear-wave first motions which differ from the first motions characteristic of either group D or S events.

The sharp change in direction of shear-wave particle motion characteristic of shear-wave splitting is observed frequently at CME (see Figures 4.5a,d,j,m) and CRA (see Figures 4.5c,i,l), and occasionally at CTR, for example see Figure 4.5k. The type of shear-wave particle motion expected for two shear-wave arrivals is observed at all the three-component stations. This suggests that such particle motion is not generated by local effects at the station site but derives from an effectively anisotropic crack distribution within the granite rock mass.

4.5.1 Orientation of the shear-wave polarizations

The vector shear-wave polarizations, measured at each station within the shear-wave window, are plotted on an equal-area projection of the lower focal sphere centred on the receiver. The azimuthal distribution of both vector and non-vector shear-wave polarization angles are plotted as histograms. Figure 4.9 shows equal-area projections out to 40^{o} incidence angles and histogram plots for all the shear-wave polarizations recorded at each station. Since the polarity of the first motion of the shear-wave (the vector polarization) is primarily dependant on the source mechanism and not the medium, only non-vector polarizations are discussed here. Vector polarizations are considered in the next chapter dealing with sources.

The shear-wave polarizations generally align approximately NW-SE at each station, with the direction of the alignment indicated by the peaks in the corresponding histograms (see Figure 4.9). The mean values (between N 0^{o}E and N 180^{o}E) of the non-vector shear-wave polarization angles at CME, CTR,

CRA, and CRQ are N 125°E, N 151°E, N 131°E, and N 164°E respectively, with corresponding modal values of N 165°E, N 155°E, N 135°E, and N 175°E. The mean and modal values are similar at CTR, CRA, and CRQ but a 40° difference in these values occurs at CME. This is because a small number of the polarization angles measured at CME lie in the range N 0°E to N 10°E which bias the mean to a lower value.

Equal-area projections and histograms for the deep and shallow event groups are shown in Figures 4.10 and 4.11 respectively. Group S shear-wave polarizations plot further towards the 40° circumference which is expected because of their shallower depths. Most of the shear-wave polarizations at CTR and CRA align within ±20° of N 150°E for group D and S events. At CME most shear-wave polarizations of group D events align about N 150°E also, but group S event polarizations at CME align N 45°E - approximately right angles to the dominant trend.

Since the seismicity is tightly clustered at the base of the wells the ray paths from source to receiver only plot in a single quadrant of the focal sphere for each station. However if we make the assumption that the granite is laterally homogeneous, which is implied from mineralogical studies, then plotting all the polarizations from all the stations on an upper focal sphere centred on the source gives good azimuthal coverage for rays propagating within the granite. This assumes that two parallel rays separated within the granite would produce identical particle motion upon incidence at the surface. The shear-wave polarizations from all the stations and events are plotted on an equal-area projection of the upper focal sphere centred on the source with the corresponding histogram in Figure 4.12. The histogram of the non-vector shear-wave polarization angles peaks in the range N 150°E - N 160°E, clearly illustrating a distinct shear-wave polarization alignment.

Figure 4.9

Orientations of the shear-wave polarizations from all the selected HDR acoustic events measured at the three-component stations - CME, CTR, CRA, and CRQ. The upper diagrams are lower equal-area projections, out to incidence angles of 40^{o}, of the horizontal shear-wave polarizations at the free surface. The middle and lower diagrams are histograms showing the azimuthal distribution of the vector and non-vector shear-wave polarization angles at each station respectively.

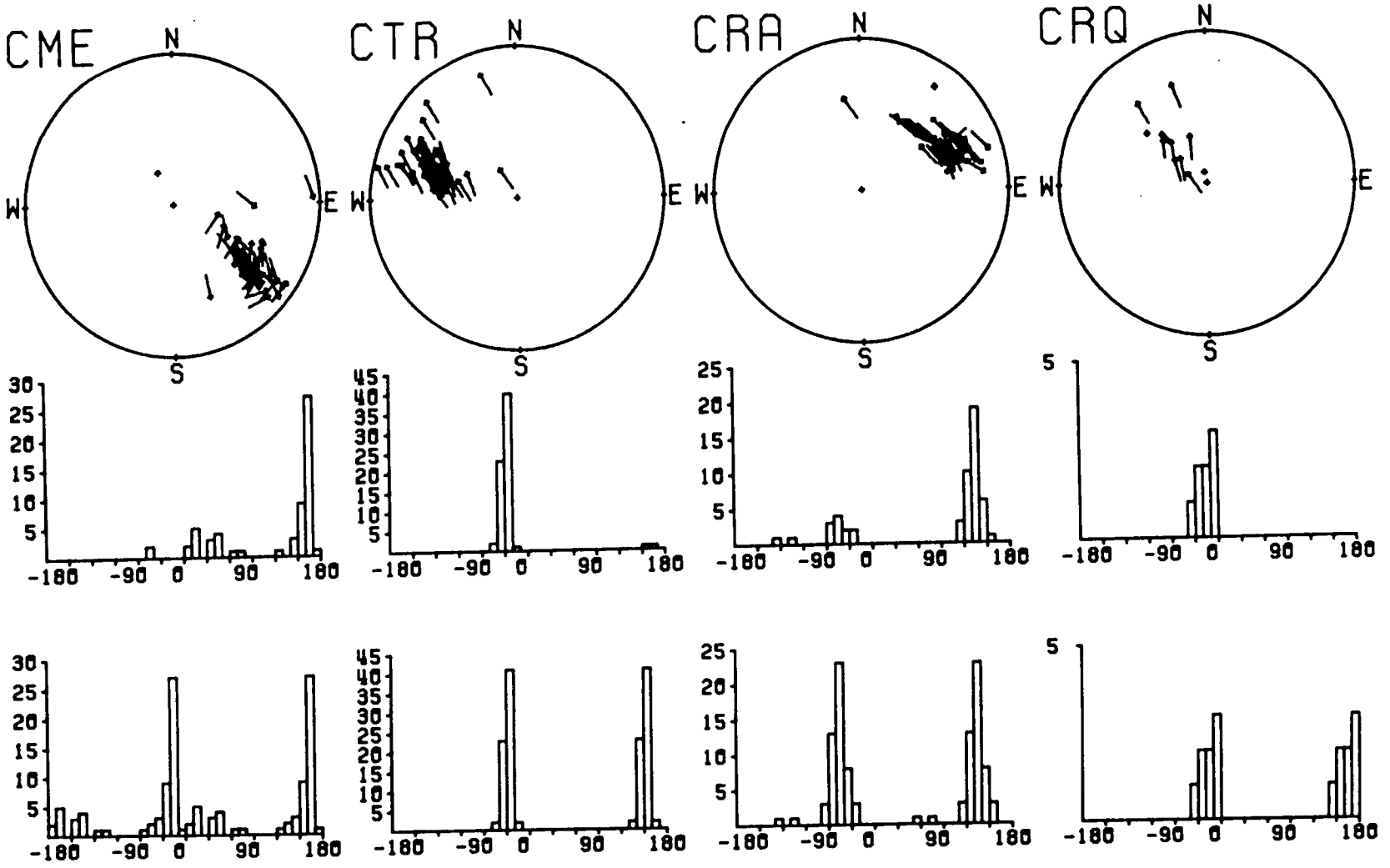
HDR events Shear-wave polarizations
CME
CTR
CRA
CRQ
N
S
E
W
-180
-90
0
90
180

Figure 4.9

Figure 4.10
Orientations of the shear-wave polarizations from group D events observed at three-component stations - CME, CTR, CRA, and CRQ. Notation and format as in Figure 4.9.

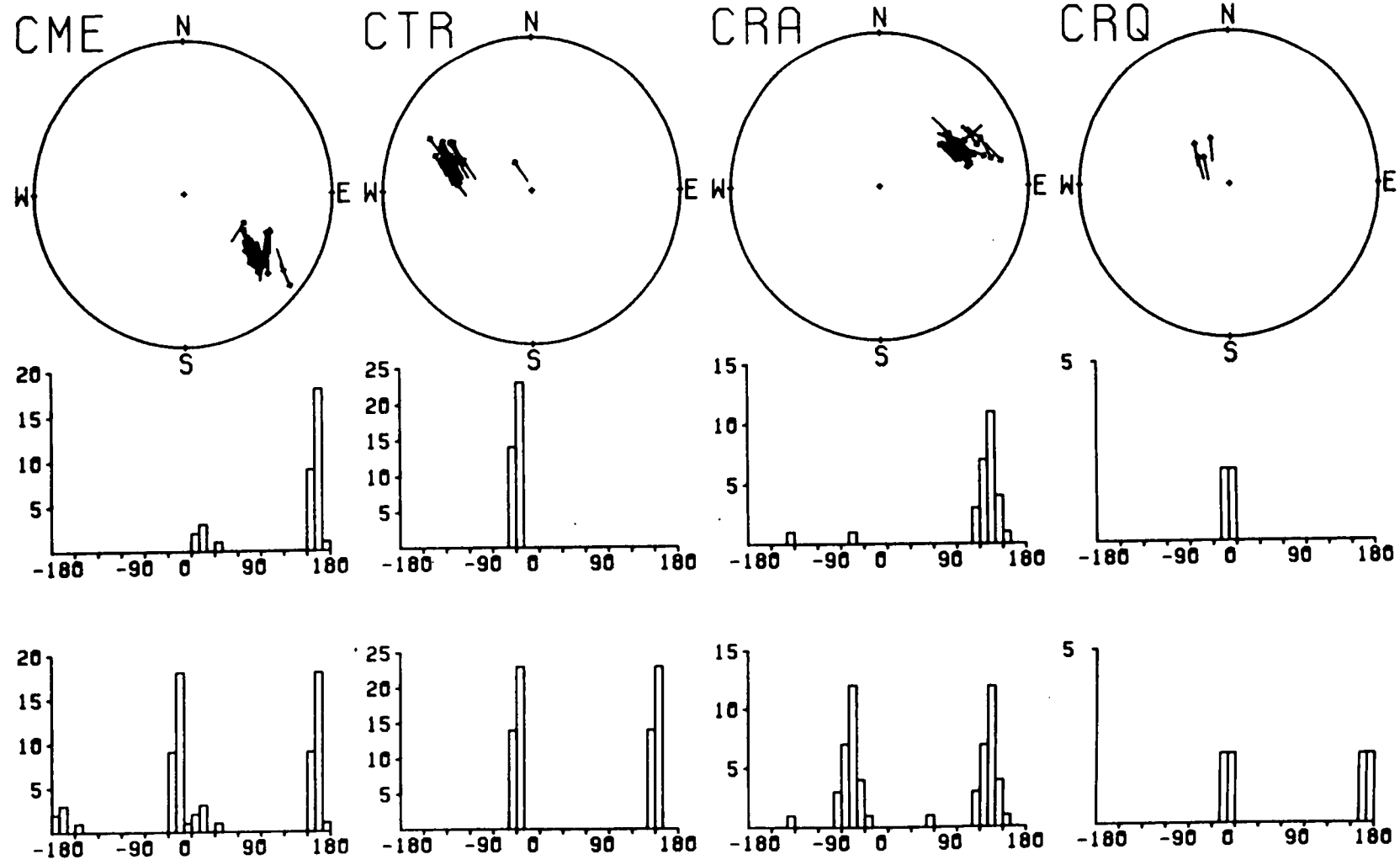
Group D events
Shear-wave polarizations
CME
CTR
CRA
CRQ
N
S
E
W
-180
-90
0
90
180

Figure 4.10

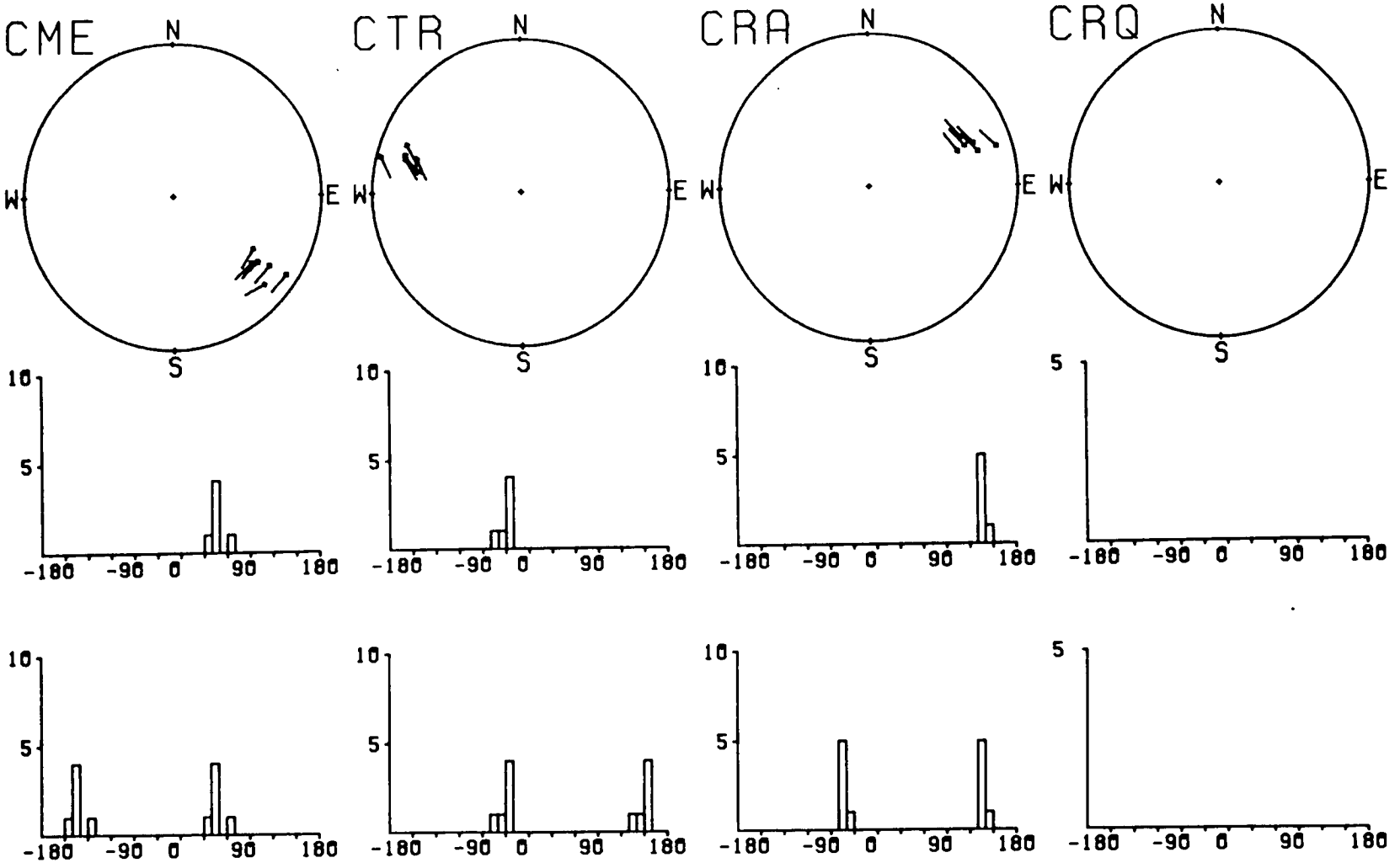
Group S events Shear-wave polarizations
CME
CTR
CRA
CRQ
N
S
E
W
10
5
-180
-90
0
90
180

Figure 4.11

Figure 4.12
Composite plots of the shear-wave polarizations from the HDR acoustic events. Upper equal-area projection centred on the source and out to incidence angles of 40° of all the horizontal shear-wave polarizations measured at CME, CTR, CRA, and CRQ. Composite histograms of the vector (upper) and non-vector (lower) shear-wave polarization angles are shown below.

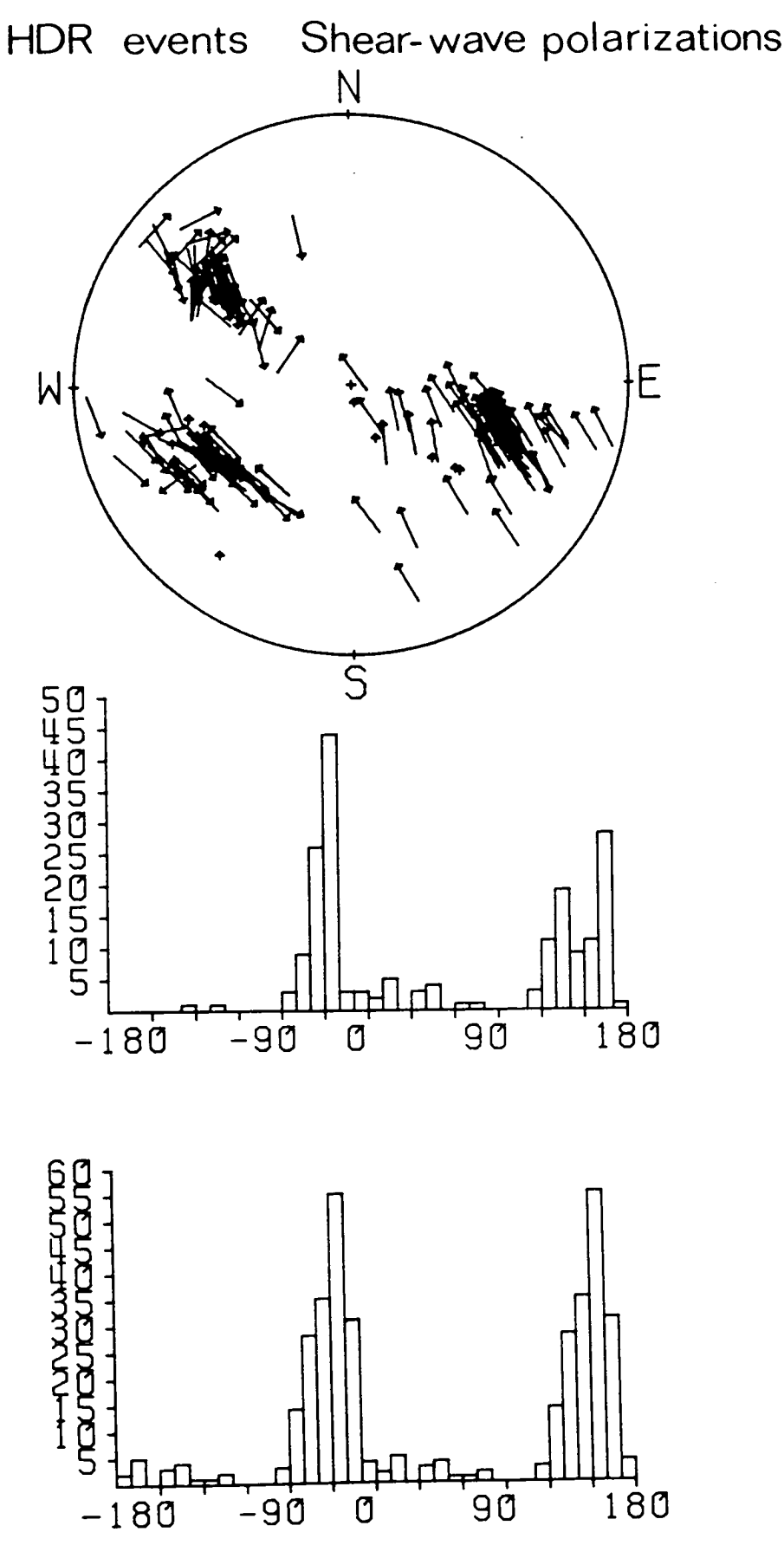
HDR events Shear-wave polarizations
N
W
E
S
-180
-90
0
90
180
-180
-90
0
90
180

Figure 4.12

4.5.2 Time delays

Where possible the time delay between two split shear-waves is measured. As already discussed, the determination of the time delay is subjective even when the onset of the first shear-wave is easily identified since it is often difficult to estimate the onset of the second shear-wave. Its onset is likely to coincide with either a change from linear to elliptical particle motion or with a sharp change in direction of particle motion. In Figure 4.5k the direction of shear-wave particle motion changes sharply 0.05 seconds after the shear-wave arrival and this gives the value of the time delay at CTR. More often, however, the time delay is more difficult to estimate objectively as can be seen from polarization diagrams in Figures 4.5a,c,d,f,i.

Since shear-wave time delays are dependant on path length, they are corrected to equivalent time delays for rays travelling a fixed distance of 2.5 km - a typical ray path length of an HDR event. For group D events the time delay at CME is, in general, about 0.05 seconds (for example see Figure 4.5d); the time delay at CRA is estimated as about 0.01 second (for example see Figure 4.5c), and the time delay at CTR is similar to that at CME, when shear-wave splitting is observed (for example see Figure 4.5k). Shear-wave splitting is not so easily identifiable on records of group S events and so time delay estimation is more subjective. However time delays of 0.03 seconds can be interpreted from records at CTR (for example see Figure 4.6b) and large time delays of 0.075 seconds are initially interpreted from seismic records at CRA (for example see Figure 4.6c).

The distribution of time delays for group D and S events is displayed on equal-area projections in Figure 4.13. The time delays are normalised before plotting on each projection so different scales apply for each time delay distribution. Figure 4.13 shows that distinct patterns of time delays emerge for each group. The time delay distribution of group D events indicates that

wave propagation to the northwest and southeast results in time delays of the order of 0.04 seconds, but time delays for southwest rays is considerably less at 0.01 second. Although not clearly illustrated in Figure 4.13 because of normalisation, similar delays to those of group D events occur to the northwest and southeast for group S events. However, large time delays of 0.07 seconds occur to the southwest, in contrast to the time delays of 0.01 second for group D events. The equal-area projection of all time delays in Figure 4.14 clearly shows this contrast.

A coherent pattern of time delays is formed upon the omission of the 0.07 second time delays. It is time delays of 0.03 to 0.05 seconds in the northwest and southeast, and time delays of about 0.01 seconds in the southwest. This interpretation suggests that the large time delay values measured at CRA do not record the time difference between anisotropic split shear-waves. Hence the later phase may be a reflected or converted phase. This illustrates the difficulties involved in estimating time delays from the shear-wave particle motion, and shows that time delay estimation essentially involves interpretation of the shear-wave particle motion.

4.6 **A preliminary anisotropic interpretation**

A preliminary examination of the observations reveal two features which suggest that the shear-waves propagate through an effectively anisotropic medium. The abrupt changes in direction of shear-wave particle motion characteristic of shear-wave splitting are often observed suggesting that two shear-waves, with different polarizations and velocities, travel along a single ray path. Secondly the shear-wave polarizations at stations CME, CTR, and CRA are aligned within $\pm 20^{o}$ of N 150^{o}E. Shear-wave polarization alignments have been recorded by the TDP networks operating in northern Turkey (Booth et al. 1984), where the mechanism causing the alignment has been attributed

Figure 4.13
Shear-wave time delays for group D and S acoustic events on an upper equal-area projection centred on the source and out to incidence angles of 40°. Time delays are corrected for propagation over a path length of 2.5 km. The time delays in each projection are normalised.

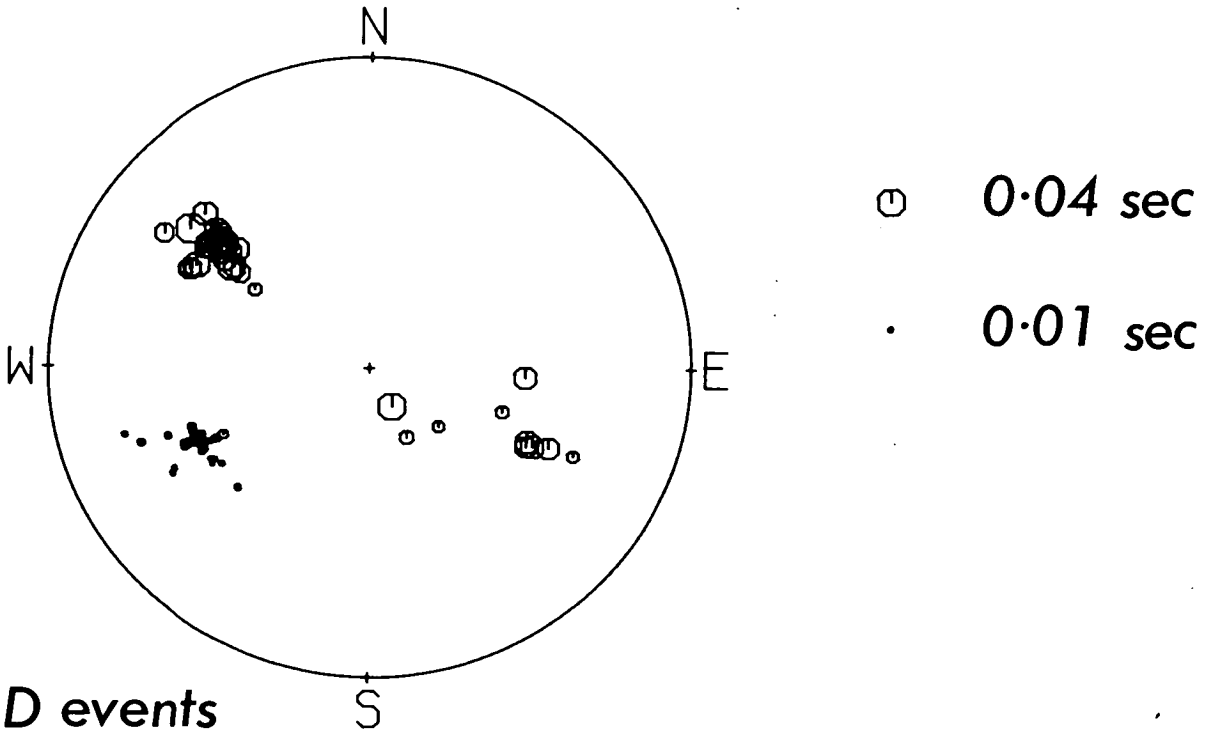

Figure 4.13a

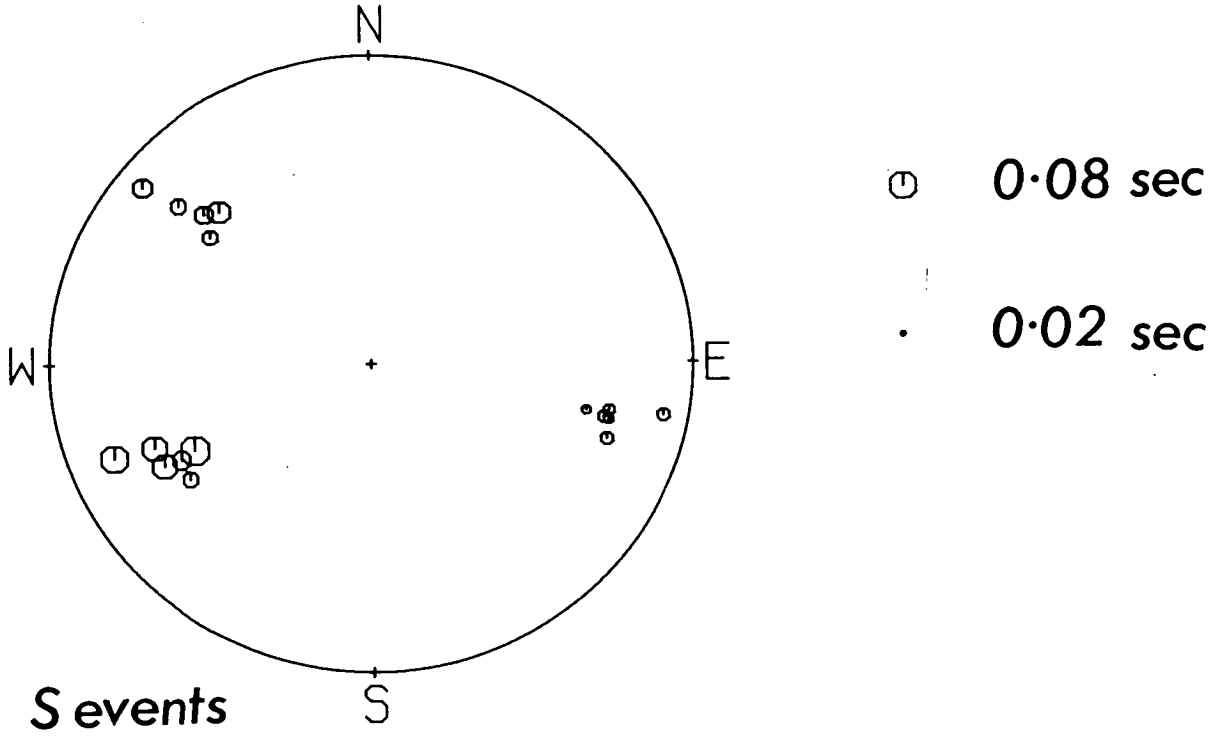

Figure 4.13b

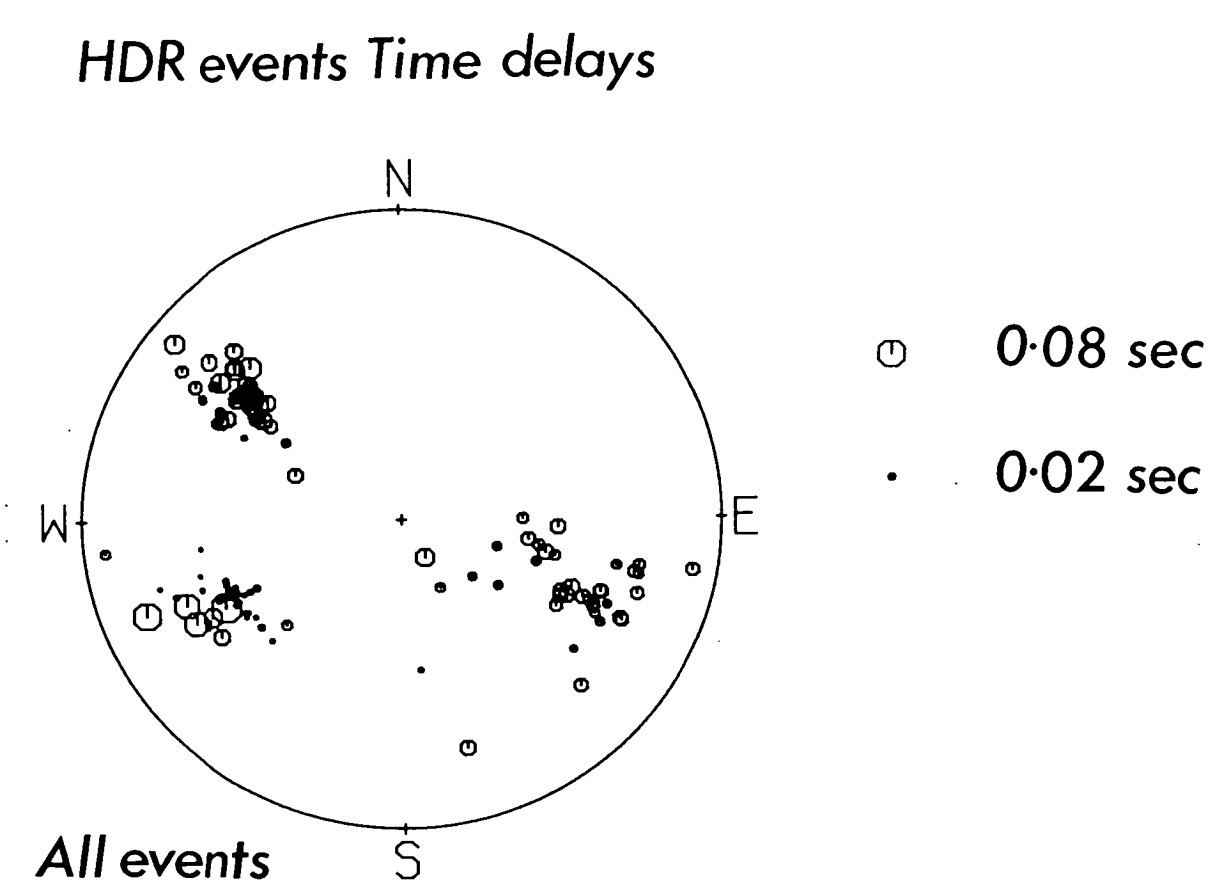

Figure 4.14

to wave propagation through a vertical parallel crack structure (Crampin & Booth 1984).

4.6.1 An anisotropic model

If these phenomena are a consequence of wave propagation through crack structures which are effectively anisotropic then the shear-wave particle motion and polarization will display patterns controlled by the in situ anisotropy. Without resorting to detailed modelling we will see if the observations are consistent with the simplest crack structure most likely to pervade the granite -a system of liquid filled parallel penny-shaped cracks.

Stresses have been applied to rock samples to examine the relationship between stress field, crack geometry, and acoustic wave velocity. The results showed that when the applied stress was varied the crack geometry varied causing a change in seismic velocity (Nur & Simmons 1969a; Hadley 1975). Therefore the geometry of crack structures is largely controlled by the prevailing stress field. Crampin & McGonigle (1981) interpretation of Gupta (1973c) demonstrated that a system of parallel penny shaped cracks will develop under a triaxial system of stress when $\sigma_1 > \sigma_2 >> \sigma_3$, where σ_1, σ_2, and σ_3 are the maximum, intermediate, and minimum compressive stress axes respectively. The circular crack surfaces are parallel to the intermediate and maximum stress axes, and are perpendicular to the axis of minimum compressive stress. A schematic diagram of the crack structure is illustrated in Figure 4.15.

Two in situ stress measurement programmes have been undertaken within the Carnmenellis granite. One used the overcoring technique at a depth of 0.79 km in South Crofty Mine located about 10 km northwest of the HDR site (Pine et al. 1983a), and the other used the hydrofracture technique to a depth of 2 km in the boreholes at the HDR site (Pine et al. 1983b). The results of

Figure 4.15
A schematic diagram of circular penny-shaped cracks in a vertical parallel crack structure. This structure has effective hexagonal symmetry and the axes of the hexagonal symmetry system are superimposed. The c-axis is the axis of hexagonal symmetry.

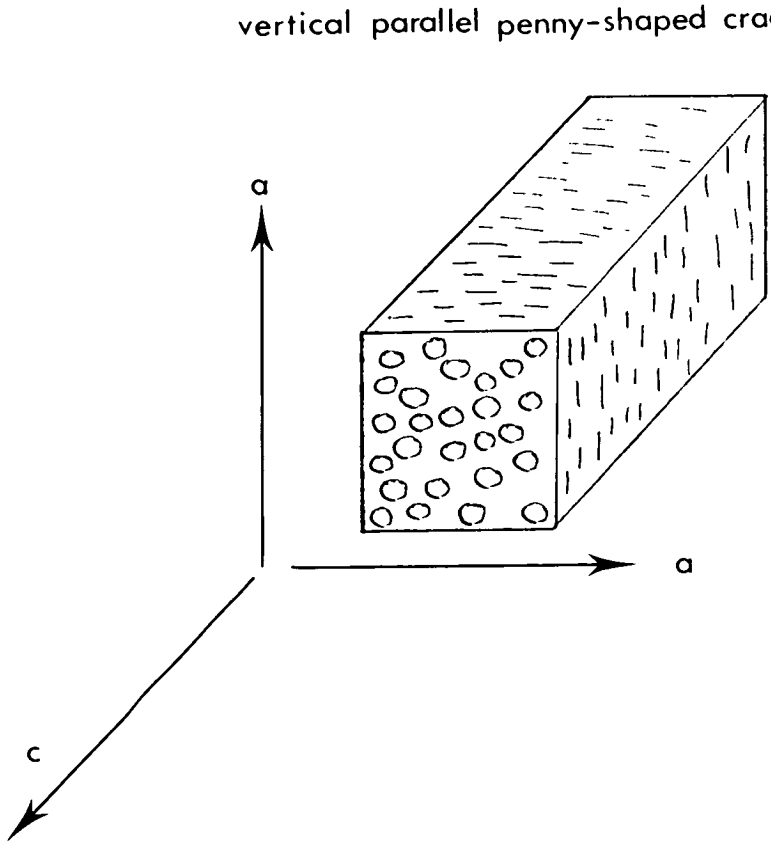

Figure 4.15

these measurements are summarised in Pine & Batchelor (1982). Tables of the average principal stress directions and magnitudes at 0.79 km depth and of estimated in situ stresses at 2 km depth have been extracted from their report, and are shown in Table 4.3. The in situ stress measurements show that the maximum and minimum compressive stress axes are horizontal and trend at N 130°E and N 40°E respectively. Table 4.3 shows that the magnitudes of the stresses σ_1, σ_2, and σ_3 measured at 0.79 km depth do not satisfy the above stress criteria for parallel cracks, but their values at a depth of 2 km satisfy $\sigma_1 > \sigma_2 >> \sigma_3$. Note that the orientation of the principal stress axes at 2 km depth are assumed to be the same as their orientations at 0.79 km depth.

Hence under the prevailing stress field at the HDR site we suggest the presence of parallel penny shaped cracks within the whole granite rock mass. The crack surfaces are perpendicular to the σ_3 stress axis and parallel to the σ_1 and σ_2 axes. Such vertical alignments of cracks are expected below the immediate surface layers in regions with a non-lithostatic stress field, and it has been shown that vertical cracks are produced by most hydraulic fracturing operations (Hubbert & Willis 1957; Zoback & Zoback 1980). This implies that the vertical parallel crack structure can be taken as a reasonable first approximation to the real crack distribution.

The crack structure is effectively anisotropic provided the crack dimensions are significantly smaller than the seismic wavelength and the crack density is of sufficient magnitude to affect the bulk physical properties of the granite. Therefore an anisotropic symmetry system and its orientation must be determined to model wave propagation through the crack structure. Crampin (1978) has shown that the body-wave velocity variations in a vertical parallel crack structure may be successfully modelled by an homogeneous anisotropic elastic medium with hexagonal symmetry, when the axis of hexagonal symmetry is orientated perpendicular to the circular crack surfaces.

Table 4.3 (a) Average principal stress directions and magnitudes at 0.79 km and 2 km depth. (b) Relative magnitude of the principal stress with respect to the minimum compressive stress at 0.79 km and 2 km depth. (From Pine & Batchelor 1982).

STRESS	MAGNITUDE (MPa)	AZIMUTH	DIP
0.79 km depth			
σ_1	45.6	128.8°	0.7°
σ_2	19.8	11.7°	89.0°
σ_3	12.9	40.1°	-0.7°
2 km depth			
σ_1	60-80	130.0°	0.0°
σ_2	52	--	90.0°
σ_3	30	40.0°	0.0°

(a)

$\sigma_1-\sigma_3$		$\sigma_2-\sigma_3$		$\sigma_3-\sigma_3$
0.79 km depth				
32.7		6.9		0.0
2 km depth				
30-50	>	22	>>	0.0

(b)

The crack structure HCS01, from Crampin (1984), is chosen as the anisotropic model because it is a liquid filled crack structure of hexagonal symmetry with P-wave and shear-wave velocites similar to those measured in the granite. The in situ stress at the HDR site suggest that the symmetry axes of the hexagonal symmetry system are orientated as

c - axis (parallel to σ_3)	N 40°E	horizontal
a - axis (parallel to σ_1)	N 130°E	horizontal
a - axis (parallel to σ_2)	-	vertical

The body-wave velocity variations for rays propagating in the c-a plane and a-a plane are shown in Figure 4.16a and the anisotropic symmetry axes are superimposed on an equal-area projection of the shear-wave polarizations in Figure 4.16b.

4.6.2 Comparison of observed and predicted shear-wave particle motion

We can now see if the observations satisfy theoretical predictions arising from seismic waves travelling through a vertical parallel crack structure trending N 130°E. In Figure 4.16b the equal-area projection of polarizations with symmetry axes superimposed shows that for each of the three-component stations many ray paths lie close to the symmetry planes imposed by the crack geometry. Therefore, to simplify, we assume that source to receiver ray paths propagate in anisotropic symmetry planes. Also, since the degree of velocity anisotropy observed in the crust is small we regard the deviation of phase and group velocity vectors as negligible. These assumptions enable the estimation of the approximate orientation of the polarization of the faster shear-wave and relative time delays for each station from the body-wave velocity graphs in Figure 4.16a. Figure 4.16c shows for each station CME, CTR, CRA, and CRQ the sagittal plane with a ray incident at 25° illustrating typical ray paths to the stations. Here the sagittal planes are anisotropic symmetry planes. For

Figure 4.16

Interpretation of the shear-wave polarizations measured at the HDR site, Cornwall. (a) Body-wave velocity variations in a structure with effective hexagonal symmetry. Body-wave velocity in the c-a and a-a symmetry planes of the HCS01 crack structure (Crampin 1984). The QP-, QSR-, and QSP-phases are a quasi P-wave and two quasi shear-waves respectively. Note that the QSR phase is polarized perpendicular to the symmetry plane, and the QSP-phase is polarized parallel to the symmetry plane. The horizontal axis gives the angle between the ray path and the c-axis (see Figure 4.15). The vertical axis gives the body-wave velocity in km/sec.

(b) Upper equal-area projection for incidence angles out to 40° of the shear-wave polarizations measured at Cornwall. The orientation of the hexagonal symmetry planes (c-a, a-a) are indicated by the solid lines. The c-axis is horizontal N 220°E and the a-axes are vertical and horizontal N 130°E. The diagram shows that ray paths to stations CME, CTR, and CRQ are closely confined to the a-a plane, and wave propagation to CRA is closely confined to the c-a plane.

(c) Cross-sectional view of the ray paths to the seismic stations: the sagittal plane.

Left: Ray path to CRA in the c-a plane with incidence angle of 25° giving a direction of wave propagation at 65° from the c-axis. Reference to (a) above indicates that the velocity of the QSR-phase is greater than the velocity of the QSP-phase for this direction of phase propagation. Such splitting is shown schematically on the ray path.

Right: Ray path to CME, CTR, and CRQ in the a-a plane with incidence angle of 25° giving a direction of phase propagation at 65° from the c-axis. Reference to (a) above indicates that the velocity of the QSP-phase is greater than the QSR-phase for this direction of phase propagation. Such splitting is shown schematically on the ray path.

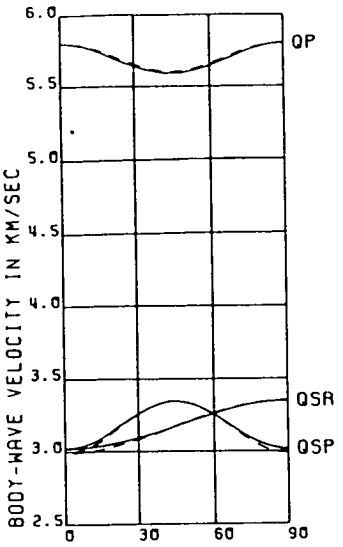

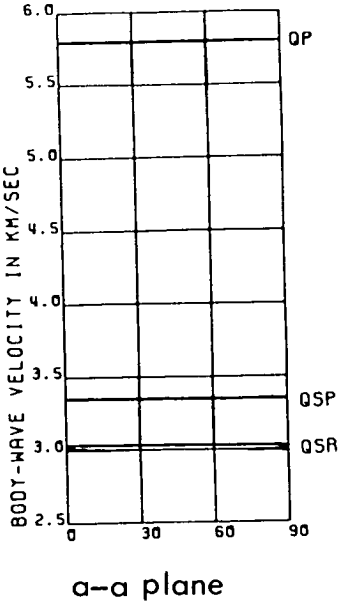

Figure 4.16a

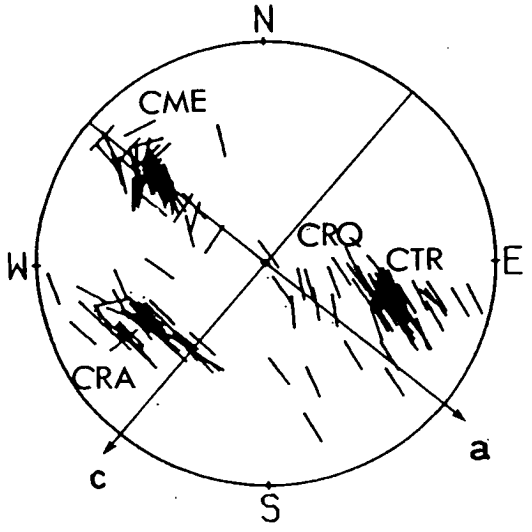

Figure 4.16b

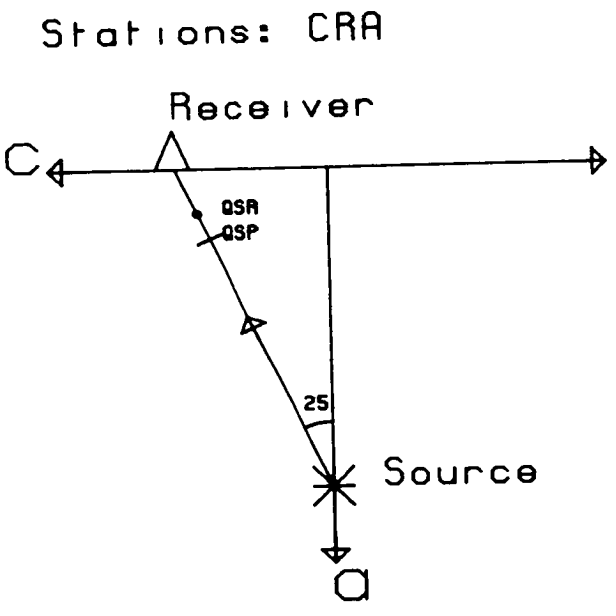

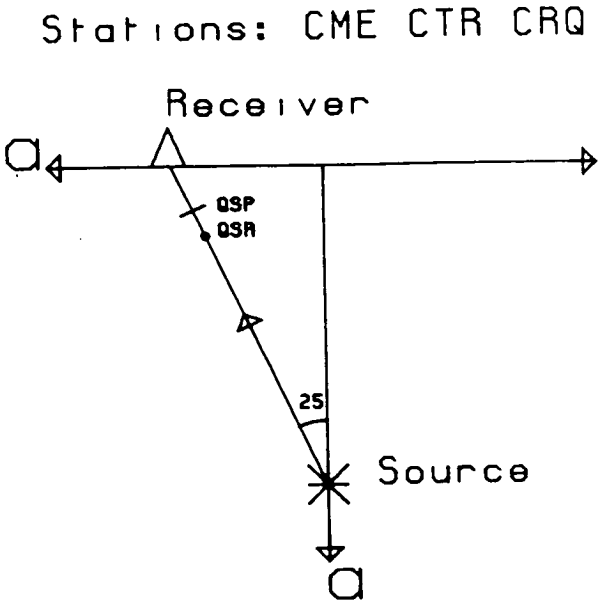

Figure 4.16c

CME, CTR, and CRQ we assume that rays travel in the a-a plane, and for CRA rays propagate in the c-a plane. Note that the QSP-phase is polarized parallel to the sagittal plane and the QSR-phase is polarized at right angles to it.

The body-wave velocity variations in the a-a plane show that the QSP-phase is always the faster phase with a constant time delay between the two shear-waves for any direction of propagation within this plane. In the c-a plane the faster shear-wave varies from the QSP-phase to the QSR-phase as the angle between the phase velocity direction and the c-axis increases from 0^o to 90^o. The QSP-phase is the faster phase for angles less than 60^o, and at greater angles the QSR-phase is the faster phase. At CRA angles of incidence are usually less than 30^o which gives a direction of phase propagation greater than 60^o from the c-axis. In this case the QSR-phase is the faster phase with a much smaller time delay between the two shear-waves than for propagation in the a-a plane. Therefore, at the shear-wave onset, we expect: approximate radial wave motion followed by transverse motion with large time delays at stations CME, CTR, and CRQ, and approximate transverse wave motion followed by radial motion with smaller time delays at CRA.

The horizontal polarization diagrams in Figure 4.5 show that the shear-wave particle motion at CME approximately agrees with the prediction of initial radial motion followed by transverse motion. Note that the heavy arrows below the polarization diagram containing the shear-wave onset point in the 'away' radial direction. Also, the maximum time delay of about 0.05 seconds is observed at stations CME and CTR, in agreement with the crack model. The shear-wave usually onsets within 20^o of the radial direction at CTR and CRQ, but splitting is not commonly observed, contradicting expectation from the model. This can be accounted for within the framework of the model if the source generates a shear-wave polarization parallel to the QSP-preferred vibration direction for rays propagating to CTR and CRQ. Upon entering the

anisotropic zone the incident shear-wave energy will all be resolved into the QSP-vibration direction and no energy will be available for the generation of the QSR-phase. In fact, particle motion characteristic of shear-wave splitting is occasionally observed at CTR in a manner predicted from wave propagation in the model, as shown in Figure 4.5k. Although shear-wave particle motion is often complex at CRA, the shear-wave first motion is usually transverse to the ray path and is followed by shear-wave particle motion in the radial direction. The small time delays of about 0.01 seconds measured at CRA appear to be consistent with the predicted shear-wave propagation.

In Figure 4.17 the equal-area projections of the shear-wave polarizations and time delays for wave propagation through the crack model are compared to the observed shear-wave polarizations and time delays. Good agreement between the theoretical and observed distributions is apparent in both cases. However the histograms in Figure 4.12 show that the direction of alignment of most of the observed shear-wave polarizations is in the range N 150°E - N 160°E, which differs by about 20° from the alignment of the crack model polarizations. A better fit to the observed shear-wave polarization pattern is achieved when the crack structure is rotated 20° clockwise to align the shear-wave polarizations at N 150°E. An improved fit for the time delays occurs also. Hence the observed shear-wave polarization distribution suggests that the vertical parallel crack structure is aligned approximately N 150°E, and not at N 130°E as first suggested. In turn this implies that the axis of maximum compressive stress is aligned at N 150°E at a depth of 2 km - a difference of 20° from its estimated orientation by Pine & Batchelor (1982).

The large time delays of 0.07 seconds measured at CRA for group S events are omitted from the observed pattern of time delays. Coverage of the projection by time delays is far from complete but is sufficient to suggest that it is similar in character to the predicted pattern. Both distributions indicate

Figure 4.17

A comparison of observed shear-wave polarizations and time delays with theoretical distributions determined for the HCS01 liquid-filled crack structure (Crampin 1984). The observations are displayed on an upper equal-area projection centred on the source (out to incidence angles of 40°). The theoretical distributions are displayed on an upper equal-area projection out to incidence angles of 90°, with an inner circle at 40° incidence angle. The unbroken line gives the polarization of the first shear-wave arrival, and the broken line gives the polarization of the second arrival.

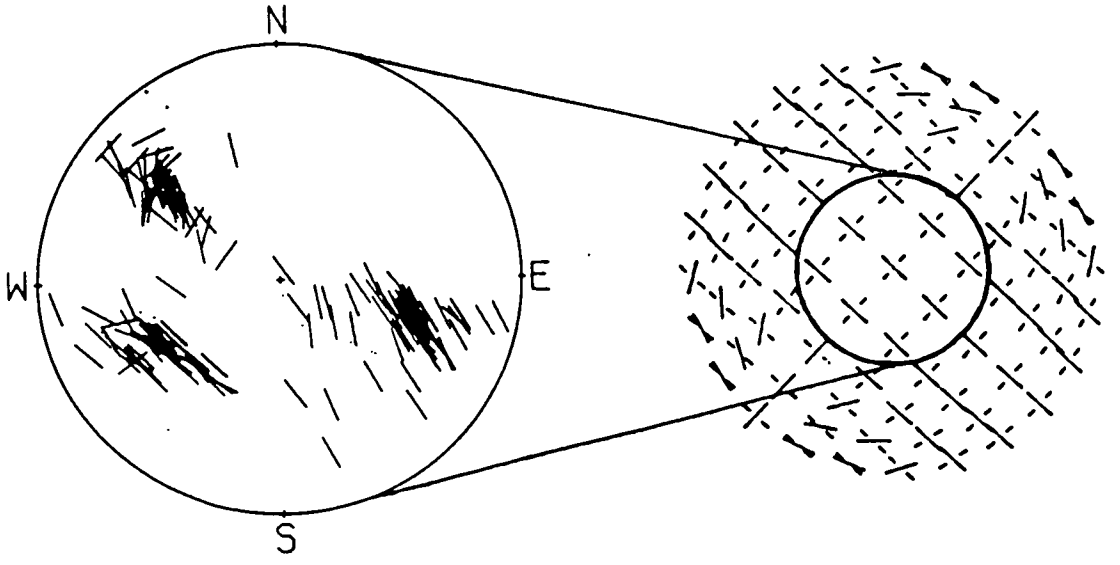

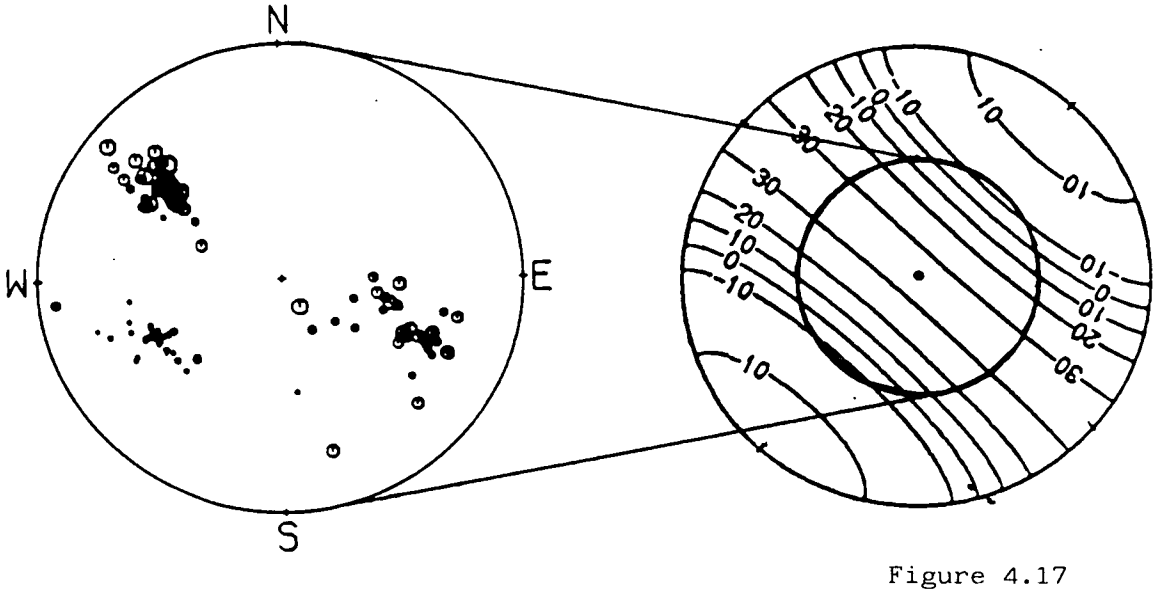

Figure 4.17

large time delays in the northwest and southeast with smaller time delays in the southwest. The good fit of the observations to prediction confirms that the large time delays at CRA arise from misinterpretation of the particle motion as split shear-waves.

The N 45°E alignment of shear-wave polarizations at CME of the group S events (see Figures 4.6a,d and 4.10) apparently contradicts the predicted northwest-southeast alignment of shear-wave polarizations from anisotropy, illustrated in Figure 4.17. However the observed polarizations are approximately parallel to the polarization of the slower QSR-phase, so a source generated shear-wave polarization aligned N 45°E to CME would result in no splitting.

4.6.3 Summary

From this simple qualitative analysis it appears that the presence of an effectively anisotropic structure at depth is highly probable. This is because the observations are characteristic of wave propagation in anisotropic media generally consistent with the *in situ* stress field. The observations which support the interpretation of wave propagation through a northwest-southeast aligned vertical parallel crack structure are given below.

1. The shear-wave particle motion at CME and CRA for most group D events, and at CTR for a few group D events and most group S events, is in broad agreement with the predicted particle motion.

2. The shear-wave first motion polarizations at CME, CTR, and CRA for group D events, and at CTR and CRA for group S events, is in broad agreement with the predicted shear-wave polarizations.

3. The distribution of time delays, measured on records with split shear-waves, is in broad agreement with the predicted time delay distribution.

However some observations appear to be inconsistent with this anisotropic

interpretation. These are outlined below and where possible such observations are explained within the framework of the crack model.

1. Shear-wave splitting is not usually observed at CTR for group D events, nor at CRA for group S events. In both cases the shear-wave first motions are polarized in a northwest-southeast direction. This inconsistency with the model can be explained if the source generated shear-wave propagating to each of these stations is also polarized in a northwest-southeast direction. Upon entry into the anisotropic region no shear-wave splitting would occur as most or all of the incident energy would be resolved into the fast polarization direction.

2. The shear-wave polarization at CME for group S events is polarized at N 45°E, which is at right angles to the orientation of most polarizations. Since the anisotropic vibration directions are orthogonal, this polarization is probably parallel to the slow vibration direction. Hence an explanation similar to the above with a source generated shear-wave polarization orientated N 45°E would suffice. However a later phase suggestive of shear-wave splitting arrives at CME.

For a more complete picture the source mechanism and the free surface must be considered in addition to the medium. As most of the three-component seismograms at the HDR site are recorded within the shear-wave window it is likely that the free surface effects on the shear-waveform are small. Also site elevations in Table 4.1 indicate that there are no dramatic changes in topography surrounding the HDR site which suggests that focusing effects of the SP-phase within the shear-wave window are unlikely. However the source mechanisms of the acoustic events must be considered. The observed shear-wave polarizations could result from source radiated shear-waves which remain unchanged due to propagation through an effectively isotropic and structurally homogeneous medium. Also, knowledge of the

source generated shear-wave polarizations may clarify the interpretation of the observations which appear inconsistent with the anisotropic model. Hence it is useful to have an idea of the source mechanisms generating the seismicity and their shear-wave radiation patterns. This provides the topic for the next chapter.

CHAPTER FIVE

THE CORNWALL DATA 2: SHEAR-WAVE POLARIZATIONS FROM THE SOURCE

The main objective of this chapter is to determine the source mechanisms of the hydrofracture-induced microseismicity at the HDR site, and to synthesise the shear-wave radiation pattern of these sources in order to compare with the observed shear-wave polarizations. Such a comparison will shed light on whether the observed shear-wave polarizations have arisen from wave propagation through anisotropic media, or if they are derived directly from the source.

5.1 Source mechanisms of the hydrofracture-induced seismicity

Two different types of source mechanism are considered for the hydrofracture-induced acoustic events, each dependant on the behaviour of the injected water within the granite rock mass. Fluid injected into vertical cracks at high pressures is likely to force the sides of the crack apart, resulting in tensile crack growth and the generation of seismic events. This mechanism, involving jacking of the fracture plane, may be represented by a compensated linear-vector dipole (CLVD) equivalent body-force system (Julian 1983). Alternatively, fluid may be absorbed by the rock mass, causing an increase in pore pressure. Hence the normal stresses along zones of weakness are reduced, in turn reducing friction on the fracture surface, and so allowing slip along fractures. This shearing mechanism is usually represented by a double couple equivalent body-force system (Aki & Richards 1980).

Knopoff & Randall (1971) showed that the radiation pattern of P-wave first

motion polarities offer a discriminant between the CLVD and double couple equivalent body-force systems, provided coverage of the focal sphere is adequate. Hence the P-wave polarity distribution provides the major basis for determining the source mechanism, but qualitative analysis of shear-wave particle motion, P:S amplitude ratios, geological information, epicentral distribution, and some synthetic seismogram modelling are undertaken for further refinement.

5.1.1 Observations of P-wave polarities

Table 5.1 shows the P-wave polarity read at each station for all 75 acoustic events. These P-wave polarities are plotted on an equal-area projection in Figure 5.1. A projection of the upper focal sphere is used as the first arrivals are upgoing rays because of the proximity of the seismicity to the seismic network. Fourteen events are omitted from the analysis of the seismic source, ten because of poor quality locations, and four because of instrumental overloading.

The three-component station CRQ often failed due to instrumental problems, and only a few readings from this station are available. In total, only 23 acoustic events give clear P-wave polarity readings at seven stations, but there are no acoustic events which give clear readings at all eight stations. Measurements of the P-wave polarities on the outer ring of single-component stations - CCO, CCA, CST, and CBW - are usually clear and unambiguous. The P-wave onset is often impulsive with a large amplitude, and the polarities at each station remain unchanged. However, measurements of P-wave polarities on the inner ring of three-component stations - CTR, CME, and CRA, - are less clear since the P-waves are typically of very small amplitude and are often emergent at CRA and CTR. For example see Figure 4.5j-i.

However, a distinct pattern emerges from the analysis of the observed P-

Table 5.1 P-wave first motion polarities for the selected hydrofracture acoustic events at seismic stations CTR, CME, CRA, CCO, CCA, CST, CBW, CRQ. The date (year-month-day) and the time (hour-minute) of each event is given in column 1. C and D represent clear compressional and dilatational arrivals respectively, with c and d representing less clear compressional and dilatational arrivals respectively.

EVENT	CTR	CME	CRA	CCO	CCA	CST	CBW	CRQ
821019 2323	C	D	D	C	D	C	-	-
821104 1447	-	-	-	-	-	-	-	-
821104 2159	c	D	D	C	D	C	D	-
821104 2353	D	D	C	C	D	C	D	-
821105 349	-	-	-	-	D	C	D	-
821105 5 3	C	D	D	D	C	C	C	-
821105 613	c	D	D	C	D	C	D	-
821105 1412	D	D	C	C	D	C	D	-
821106 426	-	-	-	C	D	C	-	-
821106 810	C	D	D	C	D	C	D	-
821106 1050	C	D	D	C	D	C	D	-
821107 836	D	d	C	C	D	C	D	-
821107 1047	D	d	-	C	D	C	D	-
821107 1859	D	D	C	C	D	C	D	-
821107 2225	D	D	C	C	D	C	D	-
821108 1230	-	D	c	C	D	C	D	-
821109 232	D	D	c	C	D	C	D	-
821109 1019	D	D	c	C	D	C	D	c
821109 1213	-	D	-	C	D	C	D	-
821109 1830	D	D	-	C	D	C	D	-
821109 2256	D	-	d	-	C	C	-	-
821110 612	D	D	C	C	D	C	D	-
821110 1018	D	D	C	C	D	C	D	-
821111 821	D	D	C	C	D	C	D	-
821112 542	D	D	C	C	D	C	D	-
821113 1323	-	D	-	C	D	C	D	-
821113 2211	-	D	d	C	D	C	D	-
821114 3 1	D	D	C	c	D	C	d	-
821114 3 6	D	D	C	C	D	C	D	-
821115 1652	d	-	-	C	D	C	D	-
821116 1048	-	D	-	C	D	C	D	-
821116 1211	-	D	-	C	D	C	D	-
821117 514	D	c	C	C	D	C	D	-
821118 132	-	D	c	C	D	-	D	-
821118 7 7	-	D	-	C	D	C	-	-
821118 748	D	D	c	C	D	C	D	-
821119 027	C	-	c	C	-	-	-	-
821120 1659	d	D	C	C	D	C	D	D
821121 444	D	-	-	c	d	c	-	-
821121 522	D	c	D	D	D	C	D	-
821121 2257	-	D	-	C	D	C	D	-
821122 356	d	D	C	C	D	C	D	-
821122 812	D	D	c	C	D	C	D	-
821122 1416	d	-	C	C	D	C	D	-

Table 5.1 continued.

EVENT	CTR	CME	CRA	CCO	CCA	CST	CBW	CRQ
821122 1751	-	D	d	-	-	-	-	-
821123 857	-	-	c	C	D	C	D	-
821123 1821	-	-	c	-	-	C	-	-
821127 634	D	C	C	-	C	C	-	D
821128 213	D	-	D	-	-	C	d	D
821201 1226	-	-	-	-	-	-	-	-
821202 419	d	D	C	c	D	c	-	-
821203 1058	-	-	-	C	D	C	D	-
821203 2218	c	D	D	C	D	C	D	-
821204 1611	D	-	-	-	-	C	-	-
821204 1714	C	D	D	C	D	C	d	-
821208 2024	D	D	C	C	D	C	D	-
821209 035	D	D	c	C	D	C	-	-
821213 1317	D	C	D	C	D	C	D	-
821217 14 9	D	D	C	C	D	C	D	-
821219 032	-	-	-	C	D	C	D	-
821228 443	C	D	C	-	-	D	d	-
821228 518	D	D	C	C	D	C	D	-
830102 2 1	-	-	-	-	-	-	-	-
830104 1232	D	C	d	C	D	C	D	-
830112 227	C	-	C	C	D	C	D	-
830113 1342	C	-	C	-	D	D	-	-
830117 757	C	-	D	D	-	C	-	-
830119 929	D	-	D	C	D	C	-	-
830120 1950	D	-	C	C	D	D	c	-
830121 9 7	-	-	D	C	D	C	-	-
830121 916	-	-	C	C	D	C	D	-
830124 1958	D	C	C	C	d	C	D	-
830124 2311	-	-	-	-	-	-	-	-
830125 1242	d	D	D	C	D	C	-	-
830126 12 5	-	D	-	D	-	C	-	-

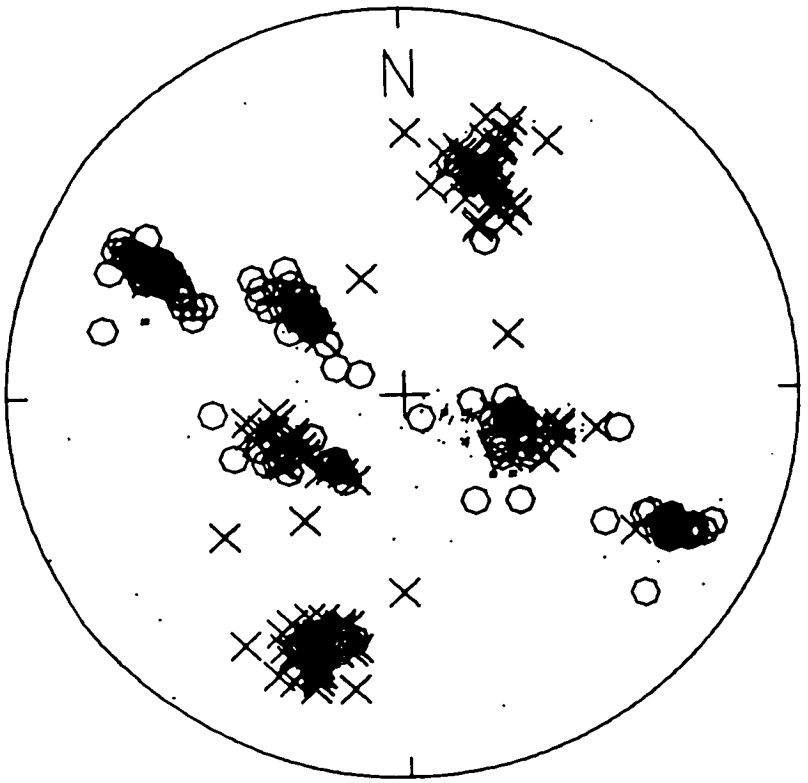

P-wave first motion polarities

Figure 5.1

wave polarities, which is consistent for many of the events under study. P-wave polarities are clearly identified at all of the stations CME, CCO, CCA, CST, and CBW for 35 of the acoustic events with the polarity observed at each station unchanged for all of these events. The polarity of the P-wave onsets are: dilatations at CME, CCA, and CBW; compressions at CCO and CST. For many other acoustic events the polarities, when measurable, are consistent with the above observations.

P-wave polarities are the same as those given above for the 23 acoustic events with polarities readable at every station (excluding CRQ). The polarities observed at the other two stations, CTR and CRA, are shown below.

	GROUP 1	GROUP 2
CTR	dilatational	compressional
CRA	compressional	dilatational
no. of events	18 (37)	5 (6)

Two P-wave polarity groups are distinguished. Group 1 represents the most frequently occurring polarity distribution consisting of 18 events, and group 2 consists of 5 events. Also, the particle motion of the shear-wave recorded at the three-component stations CME, CTR, and CRA is similar for events within a single group. Similarity of shear-wave particle motion is used to expand the polarity groups. In this way acoustic events which do not generate clear P-wave onsets at every station are included in the polarity groups above provided the shear-wave particle motion is similar to the shear-wave particle motion of other events within the group. This significantly increases the number of events associated with each group, and suggests that the two polarity patterns represent the most frequently occurring mechanisms of the larger magnitude acoustic events. The number of events in groups 1 and 2 increases from 18 to 37, and 5 to 6 respectively, with the increased values shown in brackets above.

These two polarity/shear-wave particle motion groups constitute over 70% of the acoustic events under study.

Based on the assumption that each polarity group derives from a different source mechanism, the events have effectively been divided into groups of similar source mechanism. The use of shear-wave particle motion gives an additional control in the separation of events into source mechanism groups. Since the number of P-wave polarity readings per event is small this division of events into groups of similar mechanism allows the combination of P-wave first motion polarity maps of the focal sphere. As different earthquake foci give rise to different source-station geometries the coverage of the focal sphere is usually extended (Evans 1983).

Equal-area projections of the observed P-wave polarities from the two groups are shown in Figure 5.2. In this case, coverage of the focal sphere is not greatly increased by using composite plots (polarities clearly mark out station positions on the projection) because the seismicity occupies a small spatial volume at the base of the HDR wells. Therefore ray path orientation to each station is relatively unchanged for different events. However the station distribution is sufficient to enable a study of source mechanism.

Note that polarity groups 1 and 2 correspond to the shear-wave particle motion groups D and S respectively, of the previous chapter. This suggests that the deeper events have a different source mechanism than the shallower events. The deeper and group 1 events are now referred to as group D, and the shallow and group 2 events constitute group S, as in chapter four.

5.1.2 Jacking source mechanism

A jacking source mechanism describes the process whereby the two opposing surfaces of a fracture are pushed apart (instead of slipping past each other) with the release of seismic energy. Pine & Batchelor (1984) pointed out that a

Figure 5.2
Composite plot of P-wave first motion polarities for (a) group D and (b) group S events. Equal-area projection of the upper focal sphere. Circles: dilatations. Crosses: compressions

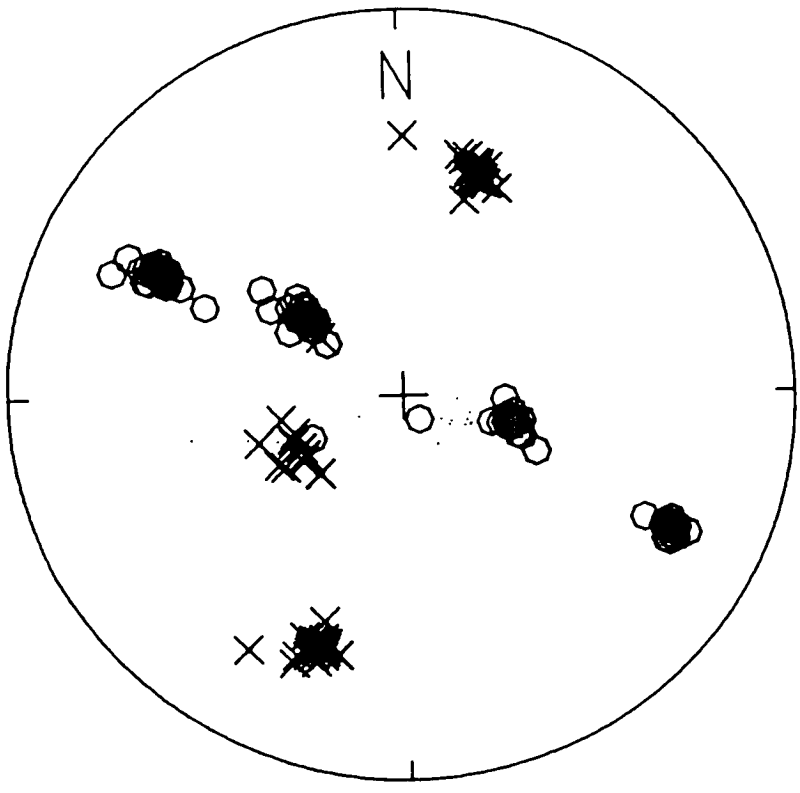

D events

Figure 5.2a

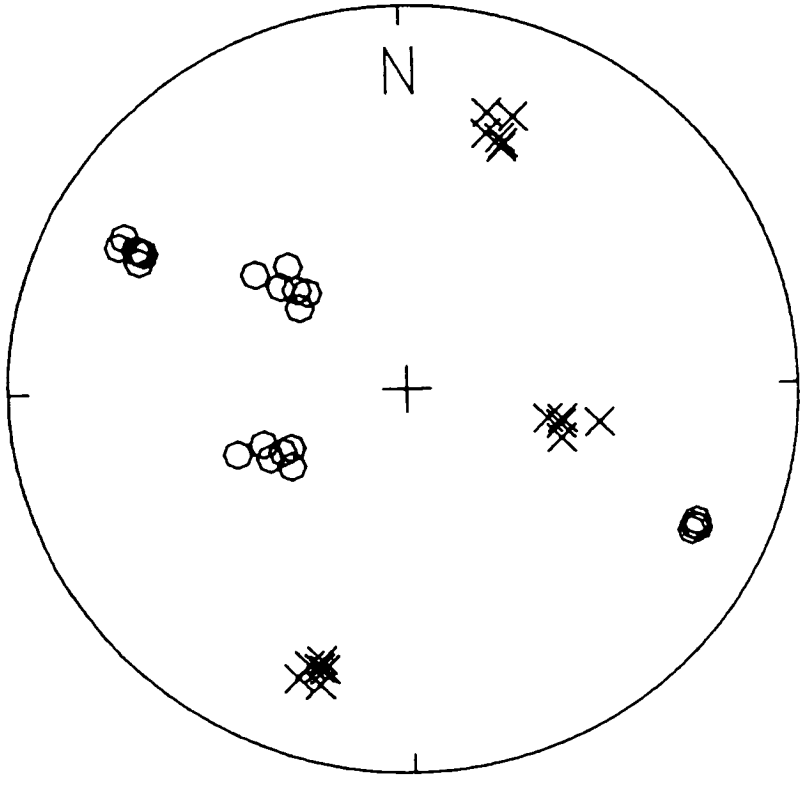

S events

Figure 5.2b

jacking source mechanism usually only predominates over shearing when the maximum and minimum compressive stresses are equal, or when the plane of fracture is perpendicular to the axis of minimum compressive stress. Although these conditions do not prevail at the HDR site, Pine & Batchelor (1984) suggested that jacking may be possible under the high pressures caused by high flow-rate hydraulic injections.

As discussed in chapter four, two major subvertical joint sets dominate the structure of the granite. One joint set strikes approximately N 155°E - N 335°E (hereafter referred to as the NW-SE joint set), and the other strikes N 75°E - N 255°E (hereafter referred to as the the NE-SW joint set). The in situ stress configuration at the HDR site (see Table 4.3) suggests that only the NW-SE trending joint planes are susceptible to jacking since the minimum compressive stresses are almost perpendicular to these joints. The other joint set, the NE-SW trending joints, are more likely to be compressed as opposed to pushed apart since the maximum compressive stresses, perpendicular to this joint set, will offer resistance to jacking (see Table 4.3). Using the CLVD body-force representation of a jacking source we will see if there is any evidence for jacking from the seismic data. The CLVD body-force system consists of three dipoles in the ratio 2: -1: -1. The tensional dipole is orientated at right angles to the fracture surface, with the magnitude of the implosive dipoles sufficient to produce no change in source volume (Julian 1983). Therefore, the tensional component of the CLVD source is constrained to trend NE-SW, approximately parallel to the axis of minimum compression and perpendicular to the NW-SE joint set.

The P-wave and shear-wave radiation patterns generated by a pure CLVD source representing jacking on a vertical plane striking N 150°E, are shown in Figure 5.3. Each radiation pattern is plotted on an equal-area projection of the upper focal sphere centred on the source. The arrows indicate the

direction of first motion, and their lengths indicate relative amplitudes in the horizontal plane. The P-wave nodal surfaces separate the dilatational first motions (inward directed arrows) located in the central region of the equal-area projection from the compressional first motions (outward directed arrows) towards the northeast and southwest edges. Hence similar observed P-wave polarity patterns are expected if jacking is the predominant mechanism of the hydrofracture-induced events. Now considering the shear-wave radiation in the lower diagram of Figure 5.3, we see that the horizontal shear-wave polarizations exhibit a dominant trend of orientation aligned N 60°E - at right angles to the fracture plane. Minimum shear-wave amplitudes are orientated parallel to the fracture plane. Note that the directional trend of shear-wave polarizations from the CLVD source is approximately perpendicular to the orientation of the observed shear-wave polarizations, at about N 150°E.

The P-wave radiation in Figure 5.3 shows that for a jacking source dilatational P-wave first motions are expected at all of the three-component stations CME, CRA, CTR, and CRQ, with dilatations also onsetting at CCA and CBW, and compressional first motions at CST and CCO. Neither of the two observed polarity distributions is compatible with the expected P-wave polarity pattern from a jacking source, since in both patterns compressional onsets occur in the central area of the plot (see Figure 5.2). This suggests that jacking, if present, is not a dominant feature of the source mechanisms. However, some of the 75 acoustic events generate P-wave polarity patterns which could satisfy the CLVD radiation pattern. Also a study of source mechanisms associated with the induced seismicity at the HDR site (Walker 1984) illustrates some P-wave polarity distributions which are consistent with a jacking source. Therefore some synthetic seismogram modelling is undertaken to determine if a jacking mechanism could be responsible for any

Figure 5.3
The P-wave and shear-wave radiation patterns from a jacking (CLVD) source mechanism on a N 150°E trending vertical joint plane. (a) Equal-area projection of the upper focal sphere showing the horizontal P-wave polarizations. An inward directed polarization is a dilatation, and an outward directed polarization is a compression. (b) Equal-area projection of the upper focal sphere showing the horizontal shear-wave polarizations. The solid circle in each diagram is the shear-wave window defined by an incidence angle of 40°.

CLVD source

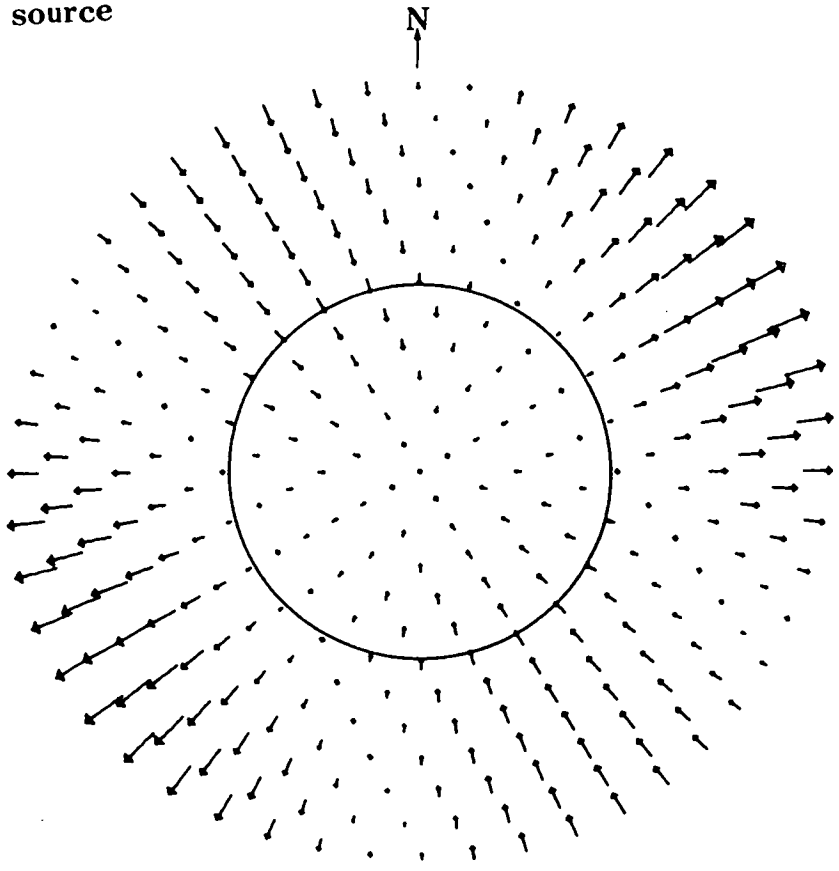

P-wave radiation

Figure 5.3a

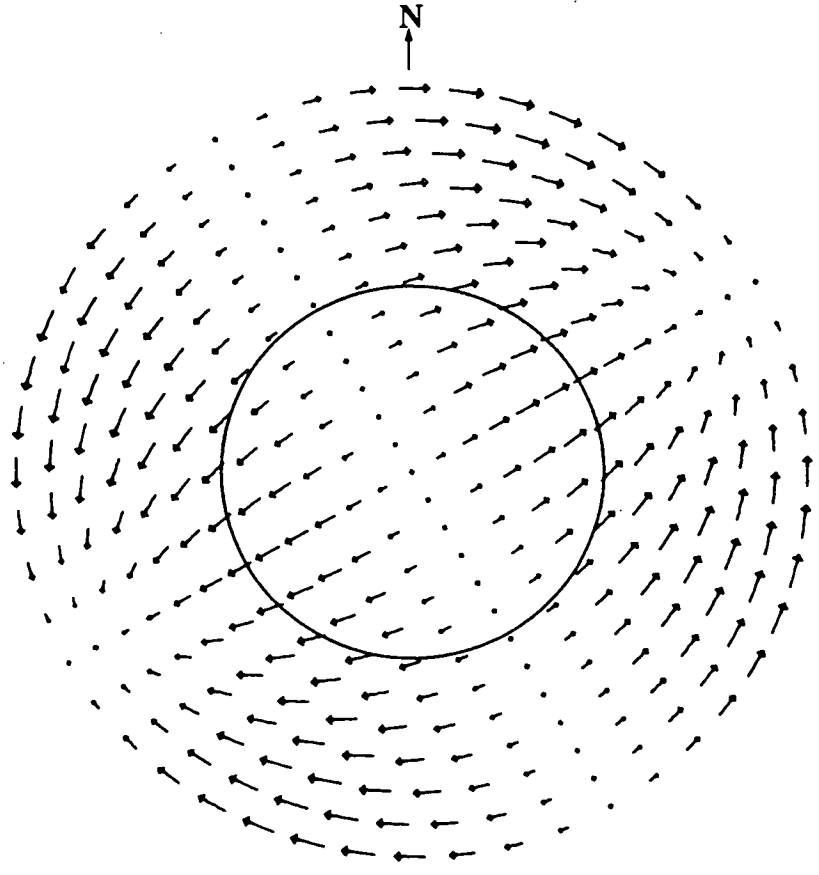

Figure 5.3b

Shear-wave radiation

of the larger magnitude acoustic events.

Kennett's synthetic seismogram package (1980) is used, and input parameters are chosen to model, as close as possible, the source, the structure, and source-station geometry at the HDR site. The source-station geometry and orientation of the CLVD body-forces with respect to a Cartesian axes system, with the x, y, and z axes orientated N 60°E, N 150°E, and vertical respectively, are illustrated in Figure 5.4a. In addition, the orientation of the axes, the NW-SE trending joint set, the principal stress axes, and the positions of the three-component stations are shown in an equal-area projection in Figure 5.4b. The source is pure CLVD with off diagonal elements of the moment tensor equal to zero, and the diagonal elements in the ratio 2: -1: -1. The tensional dipole is parallel to the x-axis, and the implosive dipoles are parallel to the y and z axes. The source depth is 2 km and station epicentral distances are 1.2 km - the approximate epicentral distances to stations CME, CTR, and CRA from the base of the wellhead. The source-time function is a single frequency pulse of 25 Hz, which is propagated through an isotropic half-space with velocities of V_p=5.7 km/sec, V_s=3.22 km/sec, attenuations Q_p^{-1}=0.002, Q_s^{-1}=0.004 and density p=2.9 gm/cm^3. Three-component velocity seismograms (vertical-, radial-, transverse-components) are generated at 10° intervals from the x-axis clockwise through 90° to the y-axis. Such an azimuthal range is sufficient for complete description of the amplitude characteristics of the seismograms in the range 0° to 360°, because of symmetry inherent in the CLVD source.

The suite of synthetic seismograms is presented in Figure 5.5, and it shows that considerable shear-wave energy can be generated by a CLVD source mechanism. The ratio of P:S amplitude ratios can be used to ascertain whether jacking is a probable source mechanism of some of the acoustic events.

Figure 5.4
(a) Source-receiver geometry for synthetic seismograms. It indicates the orientation of the CLVD body force system, and rays propagating from the source to receivers on the X- and Y-axes. Source depth is 2 km. Epicentral distance is 1.2 km. The CLVD extensional dipole is orientated parallel to the X-axis, and the implosive components are vertical and parallel to the Y-axis. (b) Equal-area projection of the upper focal sphere centred on the CLVD source and out to incidence angles of 40°. The solid lines mark the range of the strikes of the NW-SE joint set. Triangles mark the three-component stations. Dashed lines are the X- and Y-axes of (a) above superimposed on the projection. The orientation of the principal stresses are also shown.

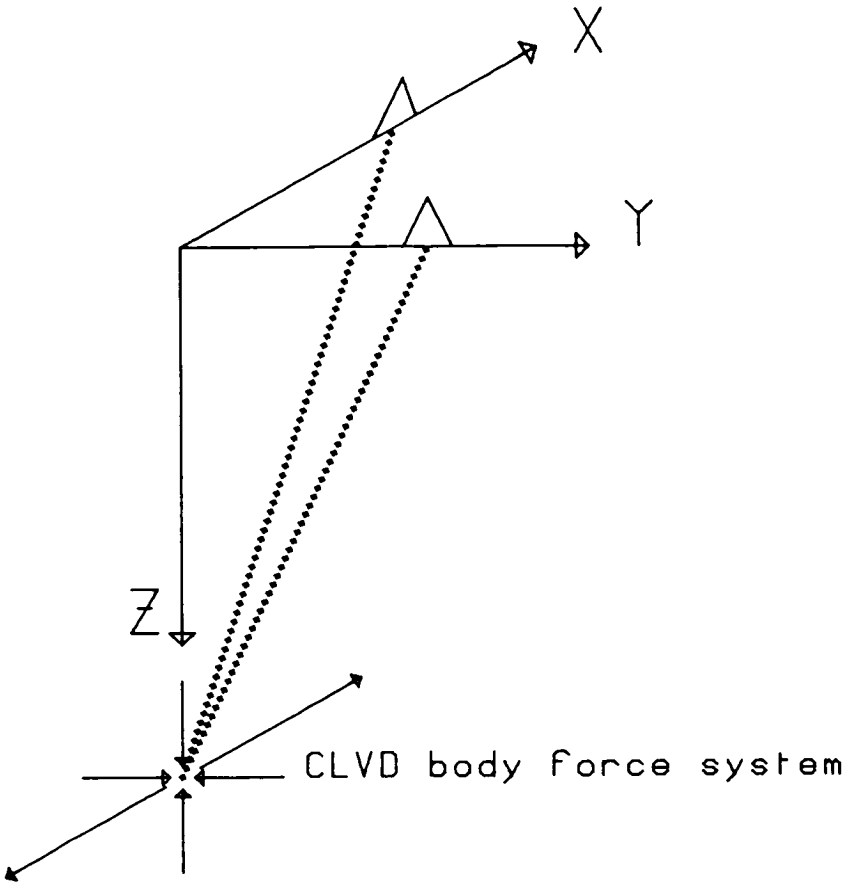

Figure 5.4a

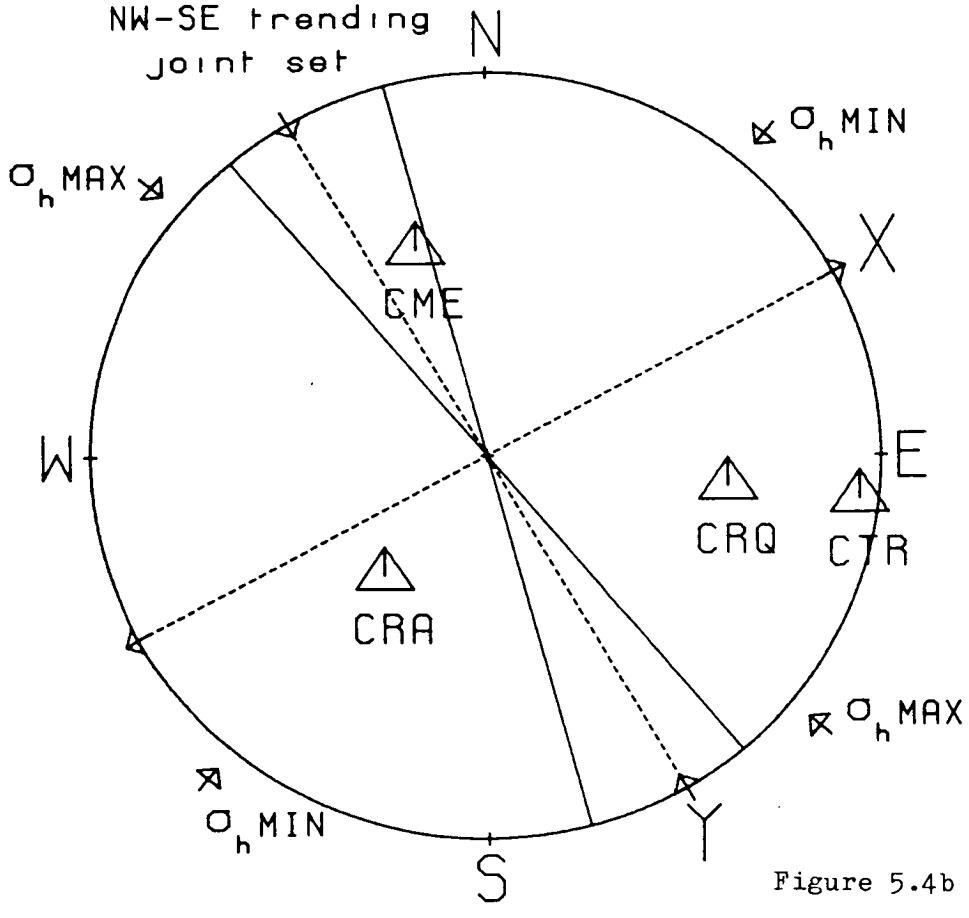

Figure 5.4b

Figure 5.5
Synthetic seismograms from a CLVD point source in an isotropic half space. Source-receiver geometry is shown in Figure 5.4. Three-component seismograms at azimuths 0° to 90° clockwise from the X-axis. Numbers below each three-component set indicate azimuth from X-axis. V-vertical; R-radial; T-transverse. Details given in the text.

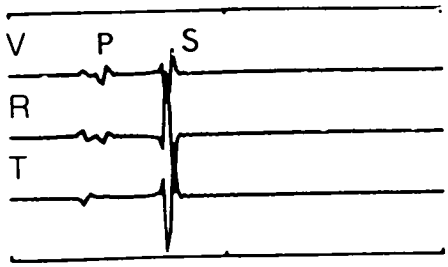

40

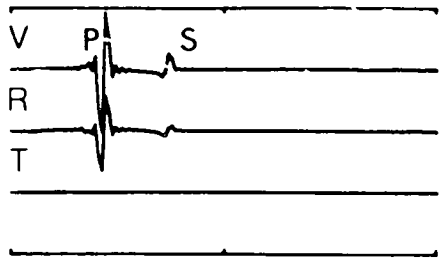

90

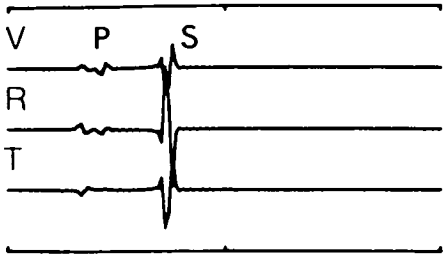

30

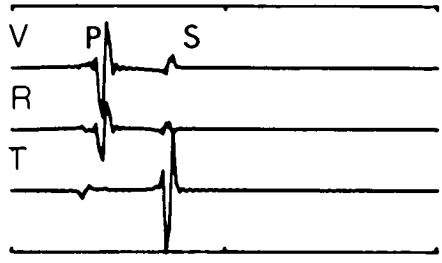

80

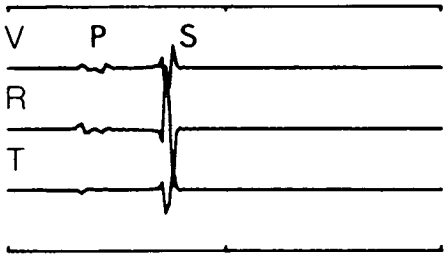

20

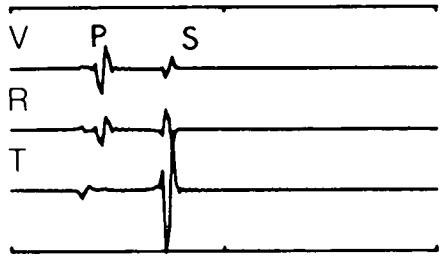

70

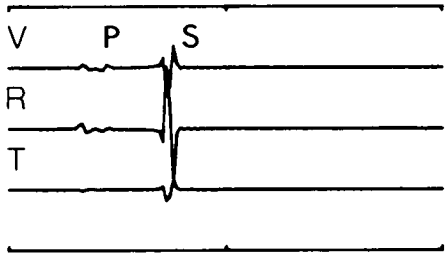

10

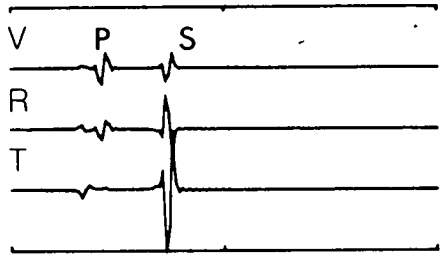

60

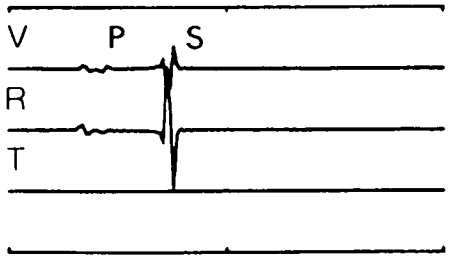

0

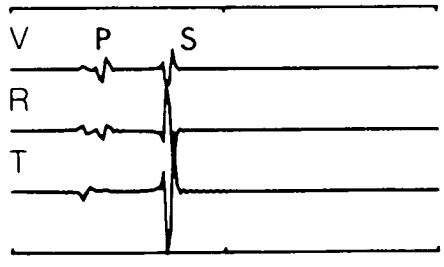

50

Figure 5.5

From Figure 5.4b we see that the ray path propagating to CME from the CLVD source is orientated at angles of greater than 70° from the x-axis. At stations CTR, CRQ, and CRA ray paths are orientated at angles less than 40° from the x-axis. The synthetic seismograms indicate that from 0° to 40° the P:S amplitude ratios are small, but from 70° to 90° the P:S amplitude ratios are large. Therefore if the acoustic events with appropriate P-wave polarity patterns are generated by a CLVD source then large P:S amplitude ratios should be observed at CME, with small P:S amplitude ratios at CTR, CRA, and CRQ. The P:S amplitude ratios at stations CTR, CRQ, and CRA are small (<0.3) in agreement with the predicted amplitude ratios from a CLVD source, but small P:S amplitude ratios are also observed at station CME. For example see Figure 4.5b, where the P-wave polarities may be compatible with the radiation pattern from a jacking source.

In conclusion, the observations of the P-wave polarity distribution, the P:S amplitude ratios, and the N 150°E alignment of shear-wave polarizations suggest that jacking sources do not generate the larger magnitude acoustic events induced by the hydrofracturing. From an investigation of stress parameters measured at the HDR site Pine & Batchelor (1984) concluded that jacking did not prevail at the HDR site, in agreement with the conclusion presented here.

5.1.3 Shear dislocation source mechanism

Since jacking did not generate the acoustic events the seismic source mechanism is probably shear. Shear dislocation consists of slip along a fracture, and is now regarded as the most common earthquake source mechanism. The orientation of the fault plane, and the direction of slip can be determined from fault plane solutions. Here the fault plane solutions are determined for each P-wave polarity distribution to assess the range of fault

parameters - strike, dip, and rake - which satisfy the observations. The procedure adopted for the evaluation of fault plane solutions is outlined in Appendix A (after Aki & Richards 1980), along with definitions of the strike, dip, and rake. The range of strike, dip, and rake values which can generate the observed P-wave polarity distributions of the group D and S events are given in Table 5.2, and fault plane solutions are shown in Figure 5.6.

Figure 5.6 shows that only one set of nodal planes satisfies both P-wave polarity patterns. The strike of one of the nodal planes ranges from N 130°E to N 190°E with the other nodal plane orientated from N 45°E to N 100°E. In general the nodal planes dip steeply (70°), with the exception of the east-west trending nodal planes for the P-wave polarity pattern of group S events. These planes can dip as shallow as 40°. The range of fault plane solutions in Figure 5.6 indicates that faulting is predominantly strike-slip with either left-lateral motion on north to northwest trending nodal planes, or right-lateral movement on east to northeast trending nodal planes. Up to 40° dip-slip faulting is possible in the generation of group S events P-wave polarity pattern but the mechanism generating the P-wave polarity pattern of group D events is limited to almost pure strike-slip. The P- and T-axes derived from the fault plane solutions strike from east-west to northwest-southeast and north-south to northeast-southwest respectively. They are almost horizontal in the case of group D mechanisms, but are inclined at about 30° from horizontal for group S mechanisms. These axes represent the principal moments of the source, and when faulting occurs in homogeneous rock the P- and T-axes are parallel to the orientation of the maximum and minimum principal stress axes respectively.

The fault plane solutions in Figure 5.6 show that a wide range of shear sources can generate the observed P-wave polarity patterns of the group D and S events. It is desirable, however, to obtain more refined fault plane solutions

for the generation of reasonably well constrained shear-wave radiation patterns.

Constraints on the orientation of the fault plane can be imposed since it is probable that faulting occurred along the pre-existing fractures within the granite. Therefore the strike and dip of the fault plane is likely to be limited to the orientation of the joint planes within the granite, and the slip vector will then be constrained by the range of orientations of the auxiliary planes. Fault plane solutions are carried out with the strike and dip of the fault plane restricted to the orientation of the two major joint sets for each polarity group. The dip is fixed at 90° since the joint planes are subvertical. Although horizontal joints are also pervasive in the granite, neither of the observed P-wave polarity patterns could be generated from slip on a horizontal plane.

The fault plane solutions constrained to the in situ joint orientations are shown in Figures 5.7 and 5.8, with the range of strike, dip, and rake values given in Table 5.2. Figures 5.8a and 5.9a indicate that no distinction can be made between faulting on the NW-SE or NE-SW joint sets solely from P-wave polarity data for group D events. However the fault plane solutions in Figures 5.8b and 5.9b indicate that only left-lateral strike-slip faulting, with a significant dip-slip component of up to 60°, on the NW-SE trending joint planes is compatible with the P-wave polarity distribution of group S events.

Some synthetic seismograms are generated to illustrate that the P:S amplitude ratios from the shear sources (double couple force system) are consistent with the low P:S amplitude ratios at stations CME, CTR, and CRA. Once again, Kennett's synthetic seismogram package (1980) is used, with structure and source-time functions the same as before. Figures 5.9 and 5.10 each show three synthetic seismograms for typical shear sources at azimuths and incidence angles corresponding to the positions of stations CME, CTR, and CRA. Low P:S amplitude ratios are clearly seen on each seismogram.

Table 5.2 Range of fault parameters - strike, dip, and rake - which satisfy the P-wave polarity distributions of group D and group S events. The first two sections give the range of fault parameters for the northwest to north trending nodal planes and northeast to east trending nodal planes shown in Figure 5.6. The bottom two sections give the range of fault parameters constrained to in-situ joint plane orientations.

FAULT PLANE	DEEP EVENTS (GROUP D)	SHALLOW EVENTS (GROUP S)
fps NW to N planes		
strike	N 128°E to N 192°E	N 136°E to N 192°E
dip	70° to 90°	60° to 90°
rake	15° to 25°	-25° to -65°
fps NE to E planes		
strike	N 45°E to N 100°E	N 230°E to N 275°E
dip	70° to 90°	30° to 65°
rake	160° to 180°	-140° to -180°
NW-SE joint set		
strike	N 140°E to N 165°E	N 140°E to N 165°E
dip	90°	90°
rake	0° to 20°	-30° to -60°
NE-SW joint set		
strike	N 60°E to N 90°E	
dip	90°	
rake	-170° to -160°	

Figure 5.6
A range of fault plane solutions for group D and S acoustic events. (a) group D events. (b) group S events. Equal-area projections of the upper focal sphere. Open circles are dilatations. Closed circles are compressions. Stars on great circles indicate possible slip vectors.

Extreme fault planes

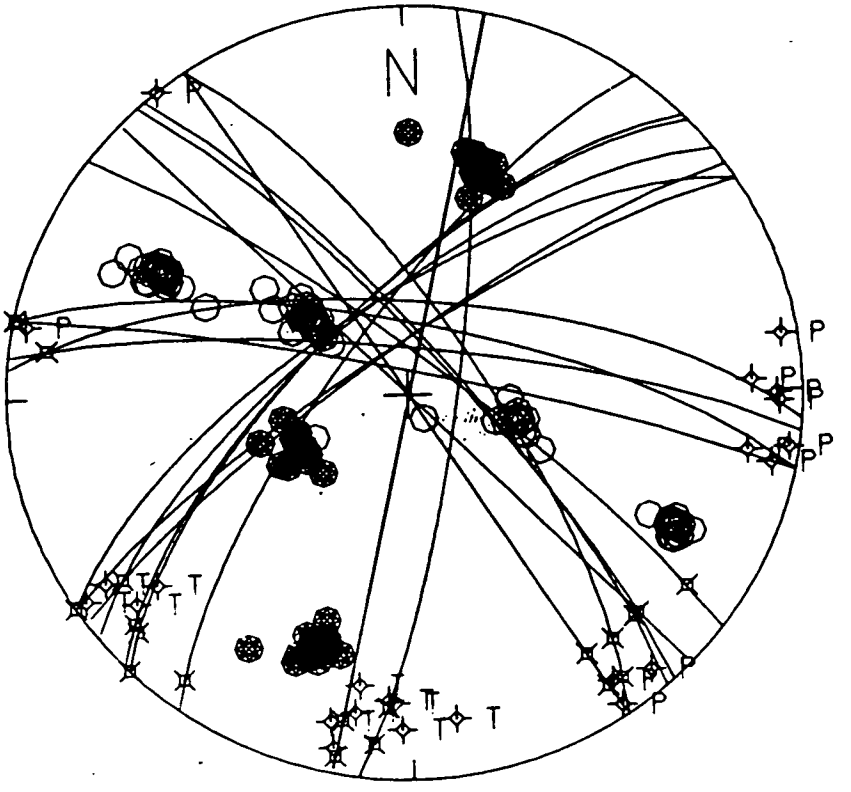

D events

Figure 5.6a

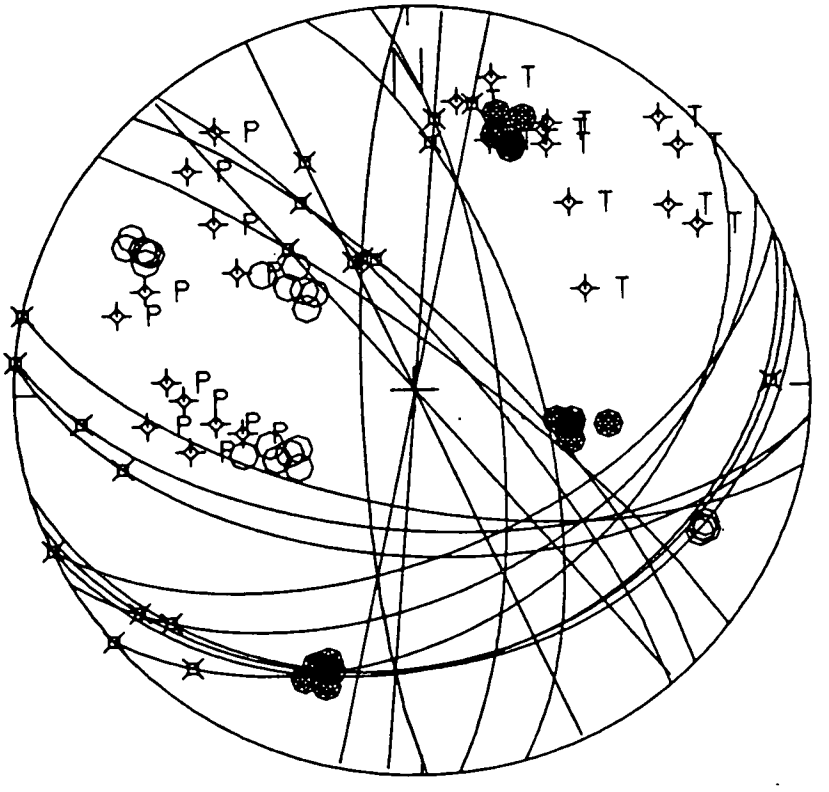

S events

Figure 5.6b

Figure 5.7
Fault plane solutions for group D and S acoustic events with the fault plane constrained to NW-SE joint set. (a) group D events. (b) group S events. Notation and format as in Figure 5.6.

NW-SE joint set

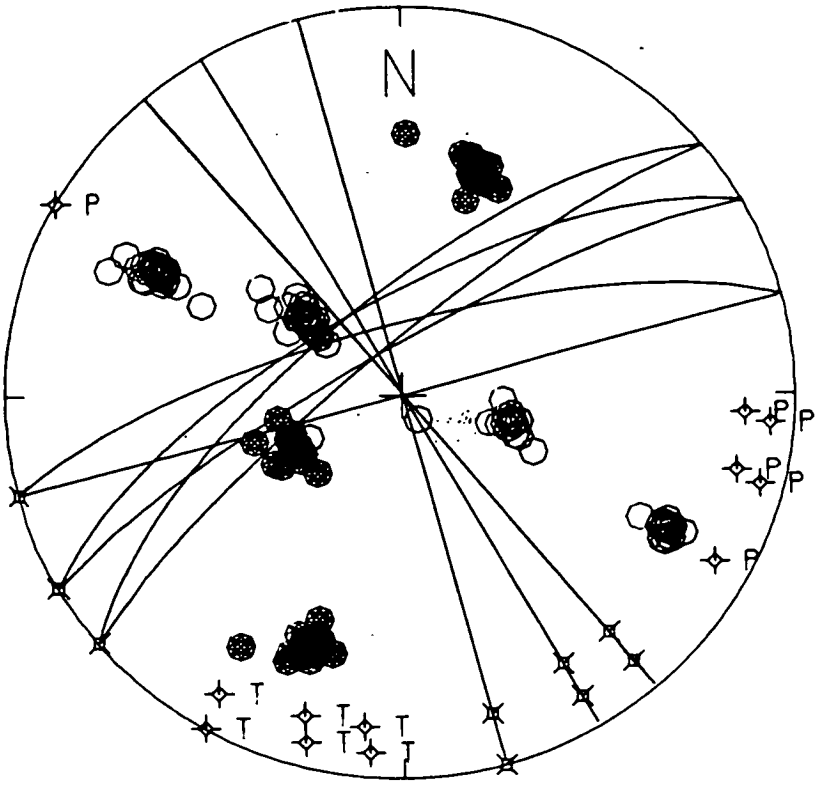

D events

Figure 5.7a

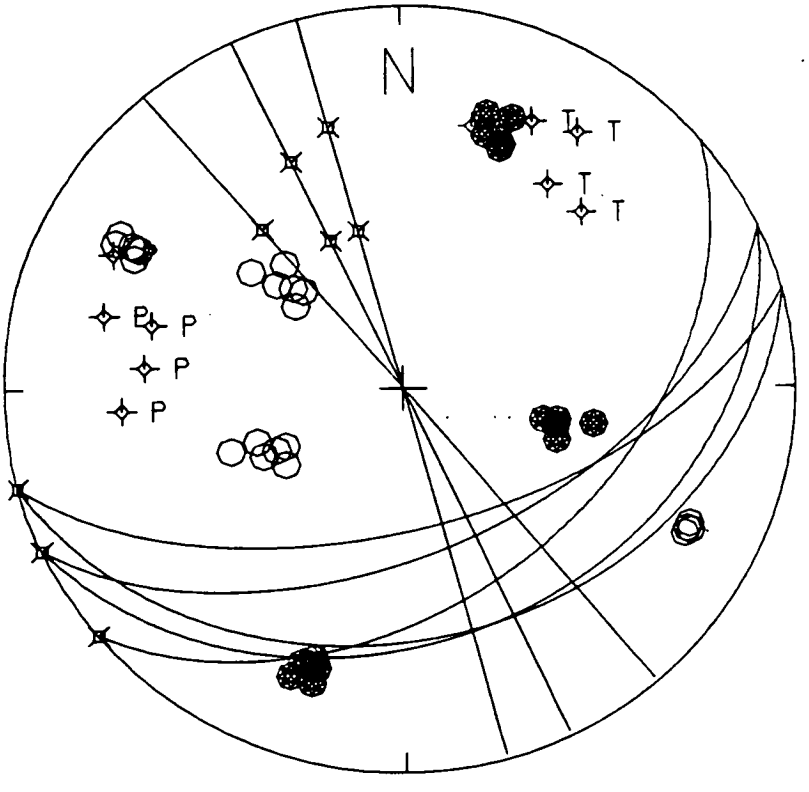

S events

Figure 5.7b

Figure 5.8
Fault plane solutions for group D and S acoustic events with the fault plane constrained to NE-SW trending joint set. (a) group D events. (b) group S events. Notation and format as in Figure 5.6. Note that faulting on this joint set does not satisfy the P-wave polarity distribution of group S events.

NE-SW joint set

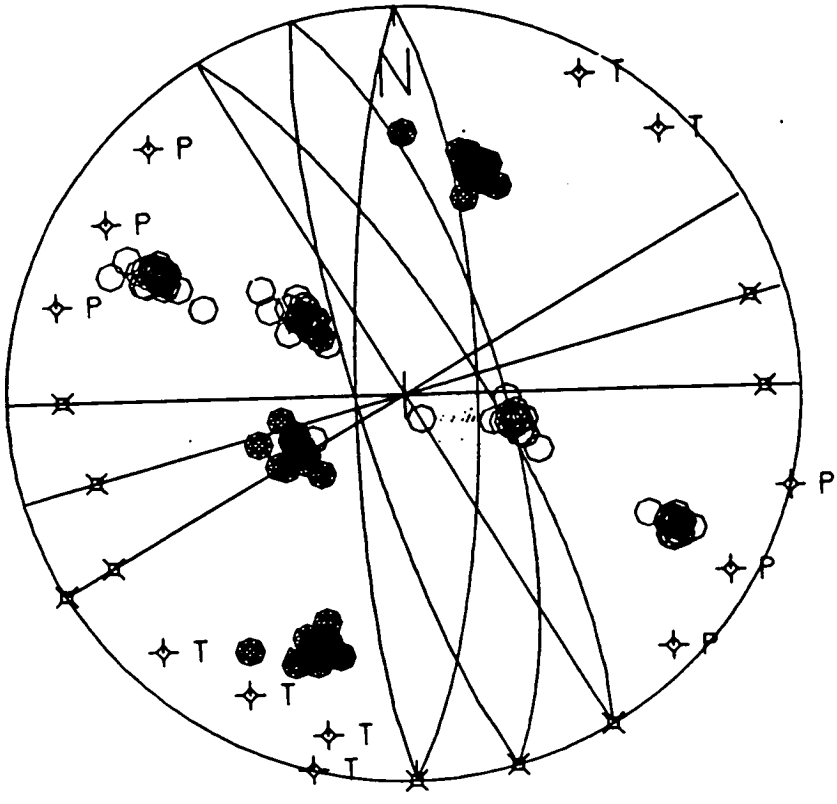

D events

Figure 5.8a

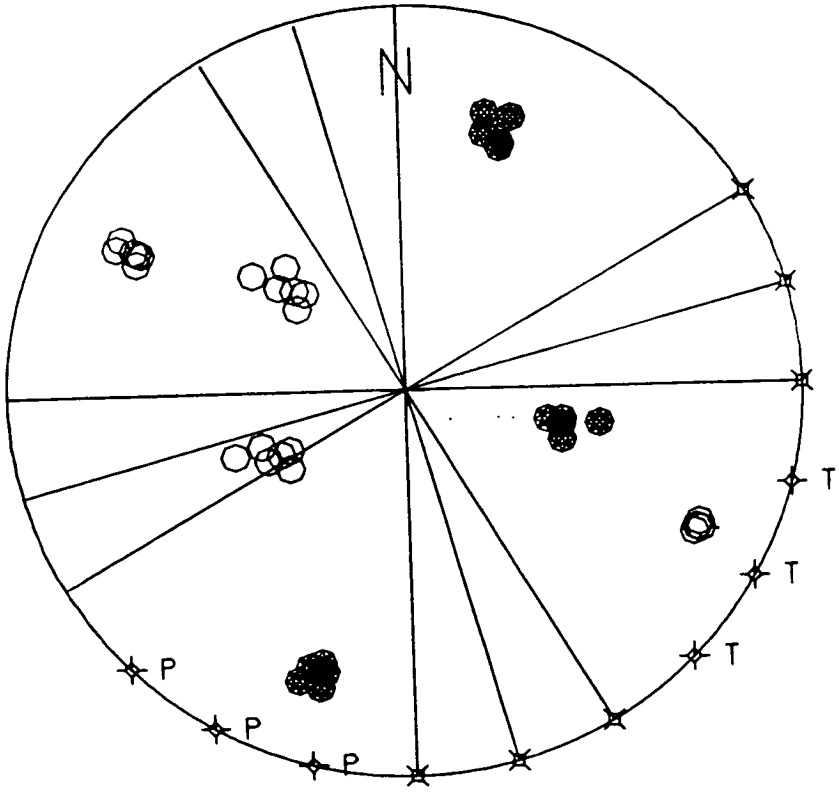

S events

Figure 5.8b

Figure 5.9

Synthetic seismogram from a double couple point source in an isotropic half space. Strike 165°; Dip 90°; Rake 15°. A possible mechanism for group D events. Seismograms are generated at azimuths and incident angles typical of stations CME, CTR, and CRA. V-vertical; R-radial; T-transverse. Source depth is 2 km.

station	epicentral distance	azimuth (source to station)
CME	1.1 km	310°
CTR	1.1 km	110°
CRA	1.1 km	240°

D

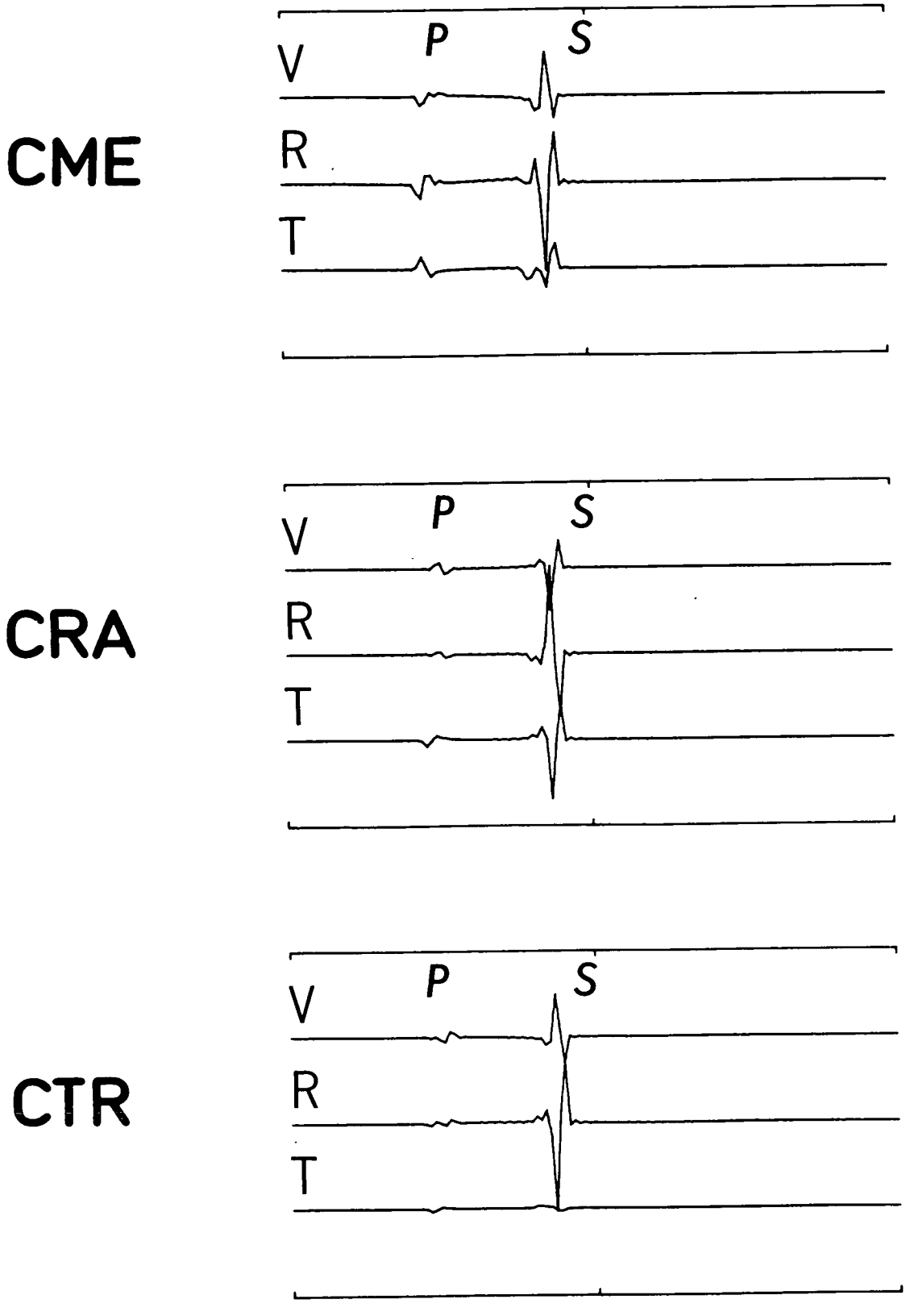

Figure 5.9

Figure 5.10
Synthetic seismograms for a double couple point source in an isotropic half space. Strike 165°; Dip 90°; Rake -45°. A possible mechanism for group S events. Notation and format as in Figure 5.9.

S

CME

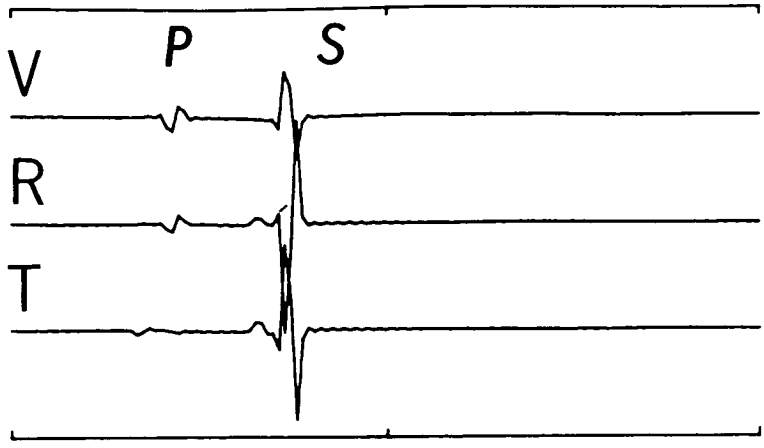

CRA

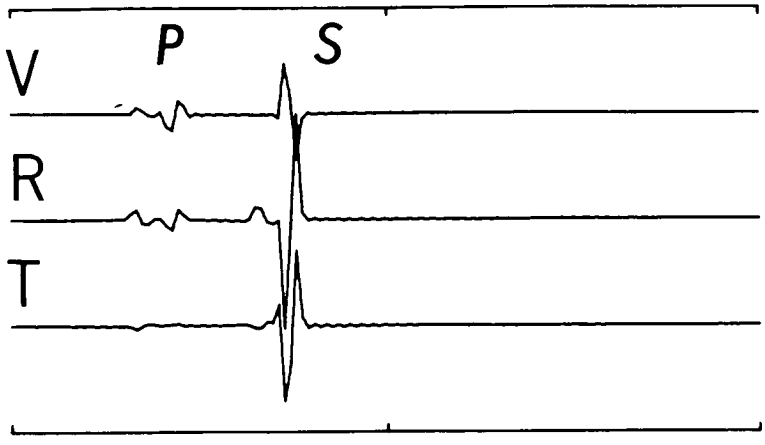

CTR

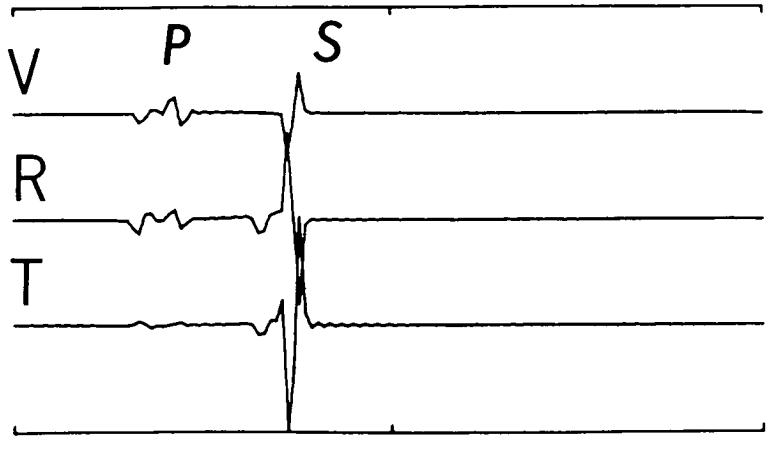

Figure 5.10

5.1.4 Interpretation of source mechanism data

The pattern of observed P-wave polarities and the observed P:S amplitude ratios indicate that the acoustic events are not generated by a jacking source. Therefore jacking is not induced by the hydraulic injections, or, alternatively, the energy release from a jacking source is not sufficient for detection at the surface. Since the P-wave polarity distribution of both group D and S events is similar, the source mechanisms of each are likely to be similar. Therefore, I suggest that both P-wave polarity distributions are generated by essentially the same source mechanism: left-lateral strike-slip faulting on the set of NW-SE trending subvertical joint planes. The reasons for preferring this source mechanism are discussed below.

Firstly, faulting on the other major joint set in the granite - NE-SW trending subvertical joint planes - only satisfies the polarity pattern of the deeper events. The polarity pattern of the shallower events, and in particular, the event of 19 October recorded prior to hydrofracturing, can only be generated by faulting on the NW-SE joint set. This implies that the in situ stresses, prior to hydrofracturing, had created conditions closer to incipient failure on the NW-SE trending joints than on the NE-SW joint set. Hence fluid injection would more readily initiate slip on the NW-SE fractures.

Secondly, further support for faulting on the NW-SE subvertical joints is given by the NW-SE directional alignment of epicentres (see Figure 4.3). The epicentres align at about N 140°E suggesting that faulting occurs on the more westerly (as opposed to northerly) trending planes of the NW-SE joint set. In contrast, non-nodal P-wave amplitudes at CME and the dilatational first motion at the centre of the projection in Figure 5.5a suggest that faulting, at least for group D events, is likely to occur on the more northerly trending joints - striking N 165°E - of the NW-SE joint set. Also faulting on such joints means that the P-and T-axes align almost parallel to the in situ measurements

of the maximum and minimum compressive stress axes respectively. However, since faulting most probably occurs on pre-existing fractures the P- and T-axes do not represent the principal stress axes, and the angle between the principal stress axes and the corresponding P- and T-axes could be as great as 90° (McKenzie 1969). Hence from the information available it is not possible to determine a more exact fault plane orientation other than generally NW-SE.

Note that the generation of the polarity pattern of the shallower events of group S require more dip-slip faulting (up to 35°) than the deeper events polarity pattern. This indicates that faulting may become more strike-slip with increasing depth.

5.2 **Theoretical shear-wave radiation from the hydrofracture source mechanisms**

Now that the source mechanisms of the hydrofracture-induced acoustic events have been estimated from the P-wave polarity distribution, the shear-wave radiation pattern from such sources is generated for comparison to the observed shear-wave polarizations. The equations used to synthesise the far-field shear-wave radiation patterns are given in Appendix B.

5.2.1 Comparison of predicted and observed shear-wave polarizations

A range of synthetic shear-wave radiation patterns are generated for faulting on the NW-SE joint set, the most likely source mechanism responsible for the P-wave polarity distributions of group D and S events. The horizontal shear-wave polarization vectors from shear sources are plotted on equal-area projections of the upper focal sphere centred on the source. The equal-area projections of shear-wave radiation patterns from the source and the observed shear-wave polarizations for group D and S events are shown in Figure 5.11. The upper plots are shear-wave radiation patterns from group D mechanisms

Figure 5.11

A comparison of source generated and observed shear-wave polarizations for group D and S events. Horizontal shear-wave polarizations from three focal mechanisms on upper equal-area projections (out to 90°) centred on the source. Solid circle on each projection marks 40° incidence angle. Strike, dip, and rake are indicated below each projection. To the far right the observed shear-wave polarizations are plotted on an upper equal-area projection (out to 40° incidence angle).

Top row: group D events.

Bottom row: group S events.

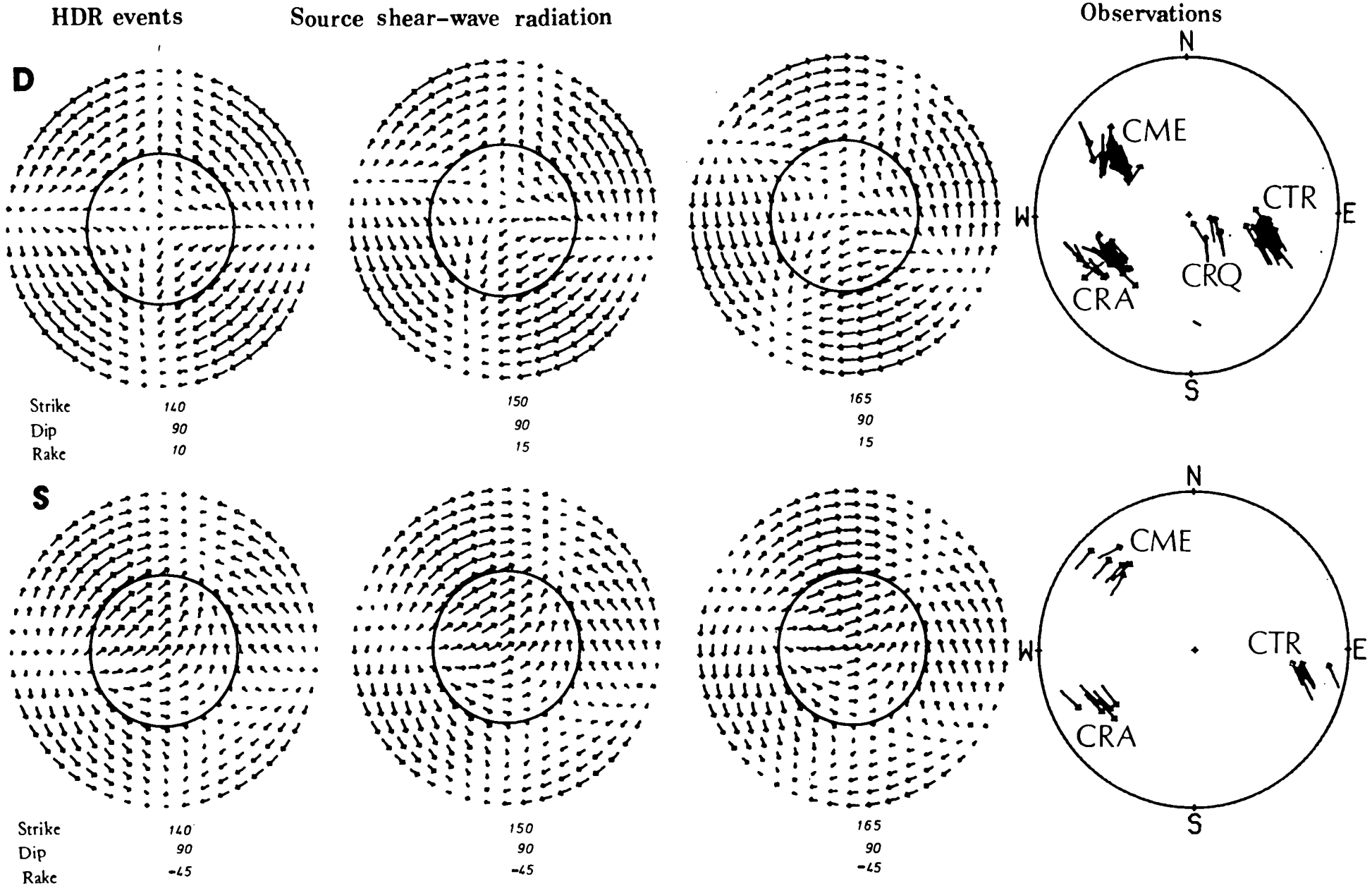
HDR events
Source shear-wave radiation
Observations
D
Strike 140
Dip 90
Rake 10
150
90
15
165
90
15
N
W
E
S
CME
CTR
CRQ
CRA
S
Strike 140
Dip 90
Rake -45
150
90
-45
165
90
-45
N
W
E
S
CME
CTR
CRA

Figure 5.11

(see Figure 5.7a and Table 5.2) - faulting on vertical planes with strikes of N 140°E, N 150°E, and N 165°E, and rakes of 10°, 15°, and 15° respectively. The lower plots are the shear-wave radiation patterns generated by group S mechanisms (see Figure 5.7b and Table 5.2) - faulting on vertical planes with strikes of N 140°E, N 150°E, and N 165°E with rake values of -45° in each case. These shear-wave polarizations are plotted for incidence angles out to 90° so the main features of the shear-wave radiation from the shear sources are readily observed. A circle at 40° incidence angle defines the shear-wave window on the equal-area projections. To allow comparison, the observed shear-wave polarizations are plotted out to incidence angles of 40° on an upper equal-area projection of the focal sphere centred on the source for group D and group S events.

Within the shear-wave window the shear-wave polarization directions from group D mechanisms are highly dependant on the azimuth of the ray path, whereas the shear-wave polarizations from group S mechanisms are more stable and exhibit a northeasterly directional trend. The variability of the orientation of the shear-wave polarization characteristic of group D events arises because the null axis of the fault plane solution lies within the shear-wave window.

We can now see if the shear-wave radiation patterns of group D and S mechanisms are consistent with the interpretation of wave propagation through the vertical parallel crack structure discussed in chapter four. To do so, the predicted shear-wave polarization is compared to the observed at appropriate incidence angles and azimuths on the equal-area projections in Figure 5.11. Shear-wave polarizations for rays travelling to CME, CTR, and CRA are located in the northwest, southeast, and southwest quadrants respectively of the 40° circles in Figure 5.11. If the anisotropic interpretation proves correct, the source generated shear-wave polarizations should be

modified on travelling through the crack structure to produce the particle motion observed at the three-component stations.

To recap, in the vertical parallel crack structure the fast vibration direction is orientated within ± 20° of N 150°E, and the slow vibration direction is orientated at right angles to this. No shear-wave splitting is observed at CME and CRA for group S events, nor at CTR for group D events. To explain this in terms of the anisotropic model, it was suggested that the source generated shear-wave polarizations for rays propagating to CRA, CTR, and CME are orientated parallel to the anisotropic vibration directions. The lower diagrams in Figure 5.11 indicate that group S mechanisms do generate shear-wave polarizations orientated about N 150°E, parallel to the fast vibration direction, at the azimuths and incident angles for rays travelling to CRA, and about N 50°E, parallel to the slow direction, for rays to CME. In both cases there is excellent agreement between the observed and predicted shear-wave polarization orientation. A similar comparison with CTR and group D radiations is perhaps less convincing but there is a fair degree of correlation between the orientation of the observed and source generated shear-wave polarization for faulting on the vertical plane striking N 165°E.

Also, Figure 5.11 indicates that the source generated shear-wave polarizations are not parallel to the anisotropic vibration directions for rays propagating to stations where shear-wave splitting is observed eg. CME, CRA - group D mechanisms; CTR - group S mechanisms. The predominant orientation of the first cycle of the shear-wave at CRA for group D events is often NE-SW, with only the first motion orientated to the southeast (see Figure 4.5c). The shear-wave polarizations from the source at incident angles and azimuths for waves travelling to CRA are, in general, orientated close to NE-SW for group D events. Therefore most of the seismic energy would be resolved into the NE-SW slow vibration direction, which appears compatible

with the observations. Also, note that the shear-wave polarity (the sense of the vector) from the source is always in agreement with the observed shear-wave polarity. Hence the shear-wave radiation patterns from the probable seismic sources of the acoustic events supports the interpretation of the shear-wave particle motion in terms of an effectively anisotropic crack structure within the granite.

5.2.2 Histograms

Figures 5.12 and 5.13 show histograms of the azimuthal variation of non-vector and vector shear-wave polarization angles from the above sources for ray paths uniformly distributed over the shear-wave window. The histogram of polarization angles from the group S mechanisms peaks sharply from N 50°E to N 80°E (vector polarizations) as the strike of the fault increases from N 140°E to N 165°E. The histograms from group D mechanisms show a more uniform distribution of polarization angles, with a peak at about N 120°W (vector polarizations). These histograms, however, cannot be compared with histograms of the observed shear-wave polarization angle since the latter are strongly dependant on source-receiver geometry. Hence to allow comparison, Figures 5.14 and 5.15 show histograms of observed shear-wave polarization angles superimposed on histograms of polarization angles calculated at azimuths and incident angles imposed by source-receiver geometry.

The distribution of the theoretical shear-wave polarization angles is dramatically altered from that in Figures 5.12 and 5.13. The histograms show that when source location and mechanism are relatively unchanged for many events the shear-wave polarizations are aligned at a given station because the orientation of the shear-wave polarization from the source is unchanged. Hence in this situation shear-wave polarization alignments are expected, and should not be confused with anisotropic-induced alignments. However the shear-wave polarizations from the source should, in general, be aligned at

different orientations at different stations whereas for wave propagation through vertical parallel cracks shear-wave polarization orientations at different stations should be similar.

Both predicted and observed histograms have three peaks. Each peak is indicative of the characteristic polarization angle either at a single station or several stations from the almost fixed source-receiver geometry. In general the observed and theoretical histograms do not correlate particularly well, but fairly good correlation is apparent for the vector distribution in histogram SL2B.

However, it is clear that the better means of comparison is via the equal-area projection display of the shear-wave polarizations. On such plots the general trend in orientation exhibited by shear-wave polarizations over the shear-wave window can be easily identified. This is useful, since location errors, particularly in depth, or minor variations in source mechanism give some degree of flexibility with respect to the position of the shear-wave polarization upon comparison of observed and calculated polarizations. On using histograms this flexibility is lost since there is no information on ray path orientation.

Note that it is difficult to quantitatively estimate the degree of fit of the observed to the predicted shear-wave polarizations, since the simplest statistical tests assume that the underlying orientation distribution is Von Mises (the orientation equivalent of a Gaussian distribution). Here, the underlying distribution is mathematically defined by the equations describing shear-wave radiation from a double couple source, making the application of such tests invalid.

5.2.3 Discussion

A preliminary study of the shear-wave particle motion revealed that shear-

Figure 5.12
Histograms showing the theoretical azimuthal distribution of shear-wave polarization angles. Polarizations are calculated uniformly over the shear-wave window for the focal mechanisms of Figure 5.11. Polarity is neglected. Top row: group D mechanisms positioned in same order as in Figure 5.11. Bottom row: group S mechanisms positioned in same order as in Figure 5.11.

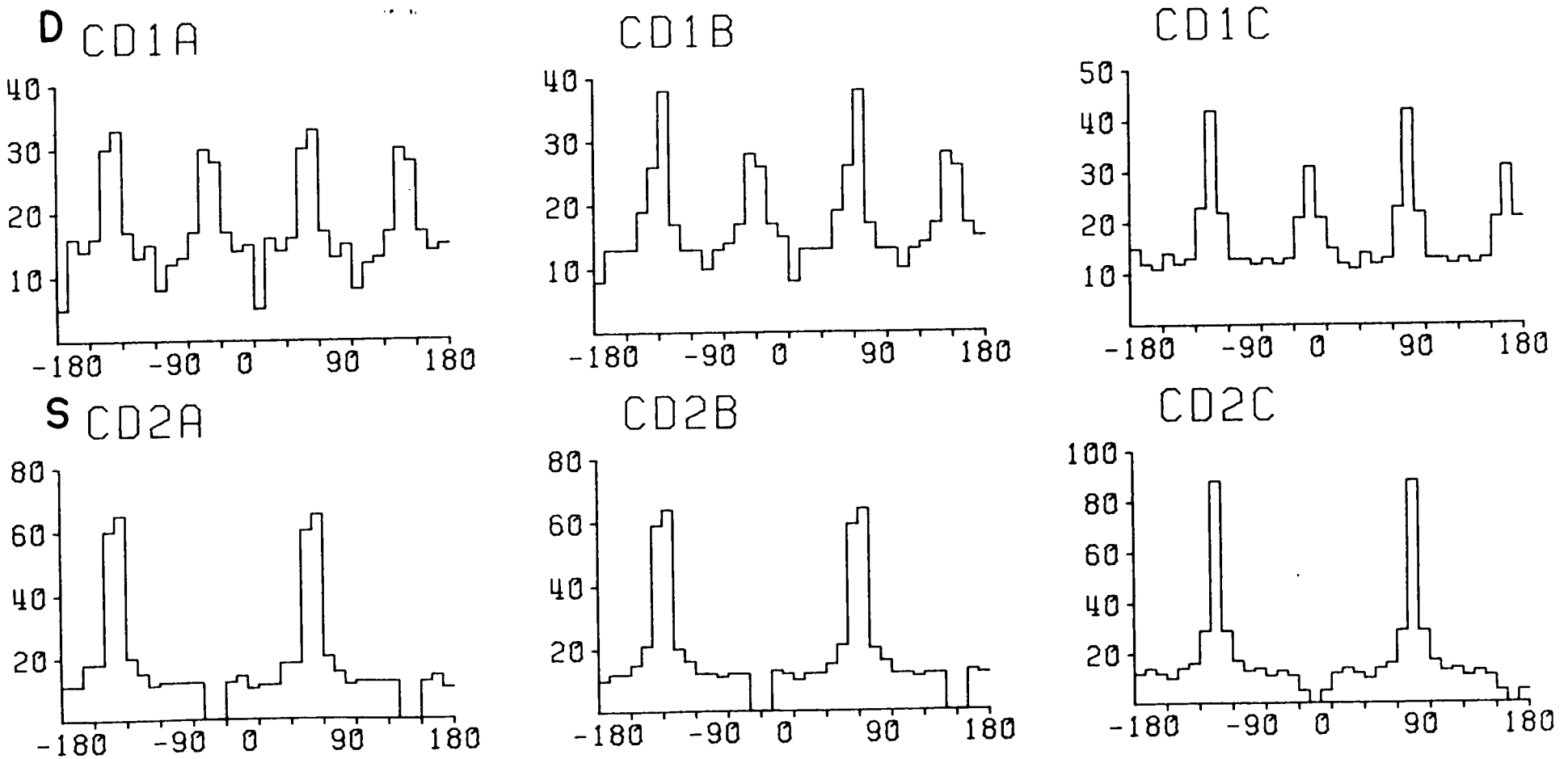
D CD1A
40
30
20
10
-180
-90
0
90
180
CD1B
40
30
20
10
-180
-90
0
90
180
CD1C
50
40
30
20
10
-180
-90
0
90
180
S CD2A
80
60
40
20
-180
-90
0
90
180
CD2B
80
60
40
20
-180
-90
0
90
180
CD2C
100
80
60
40
20
-180
-90
0
90
180

Figure 5.12

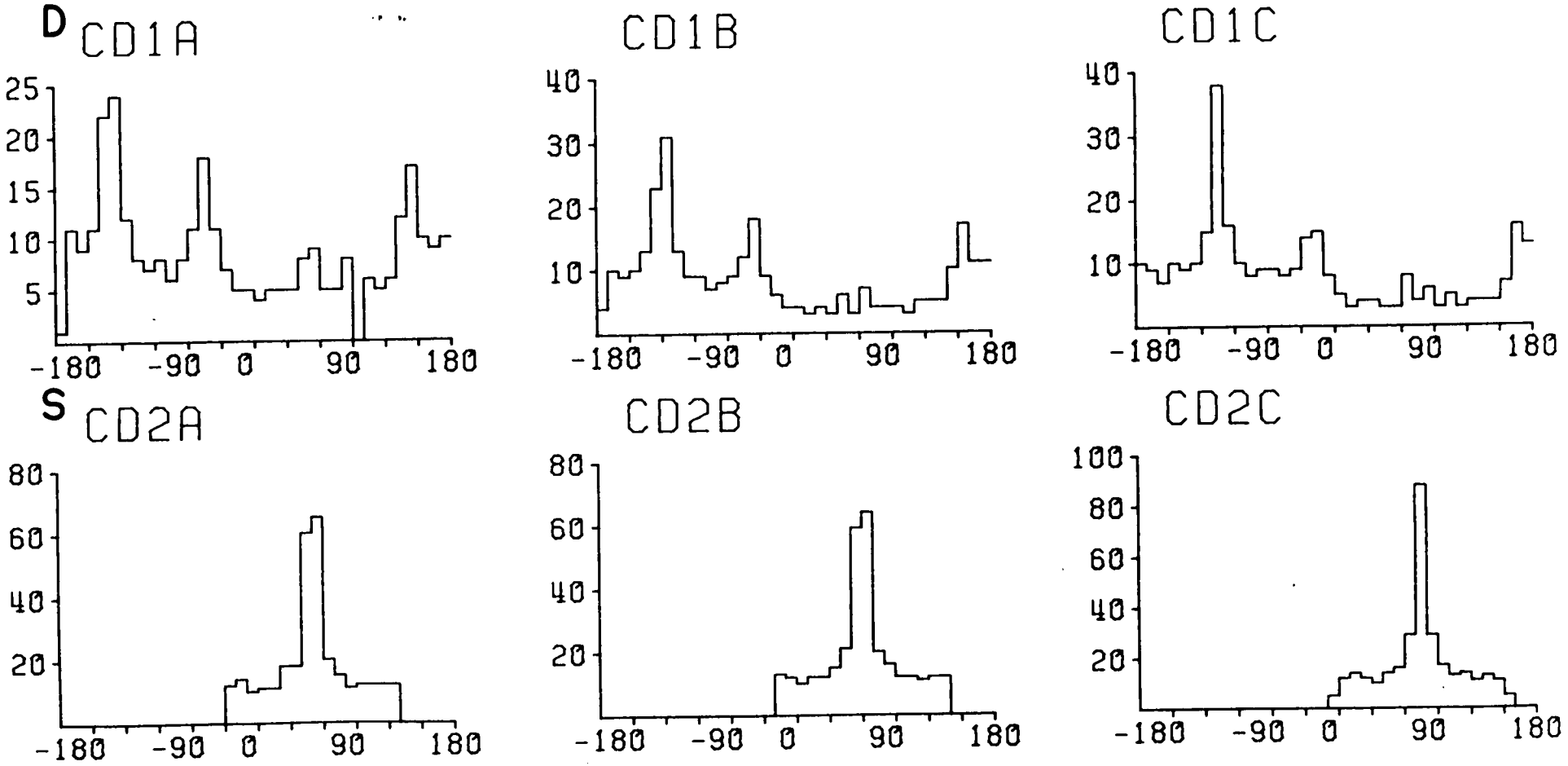
D CD1A
25
20
15
10
5
-180
-90
0
90
180
CD1B
40
30
20
10
-180
-90
0
90
180
CD1C
40
30
20
10
-180
-90
0
90
180
S CD2A
80
60
40
20
-180
-90
0
90
180
CD2B
80
60
40
20
-180
-90
0
90
180
CD2C
100
80
60
40
20
-180
-90
0
90
180

Figure 5.13

Figure 5.14
The distribution of observed shear-wave polarization angles at stations CME, CTR, and CRA (dashed lines) compared with the corresponding predicted distributions (solid lines) calculated at appropriate source-station geometries. Polarity is neglected. Peaks of observed polarizations are marked by the station at which they were recorded.
Top row: group D mechanisms positioned in same order as in Figure 5.11.
Bottom row: group S mechanisms positioned in same order as in Figure 5.11.

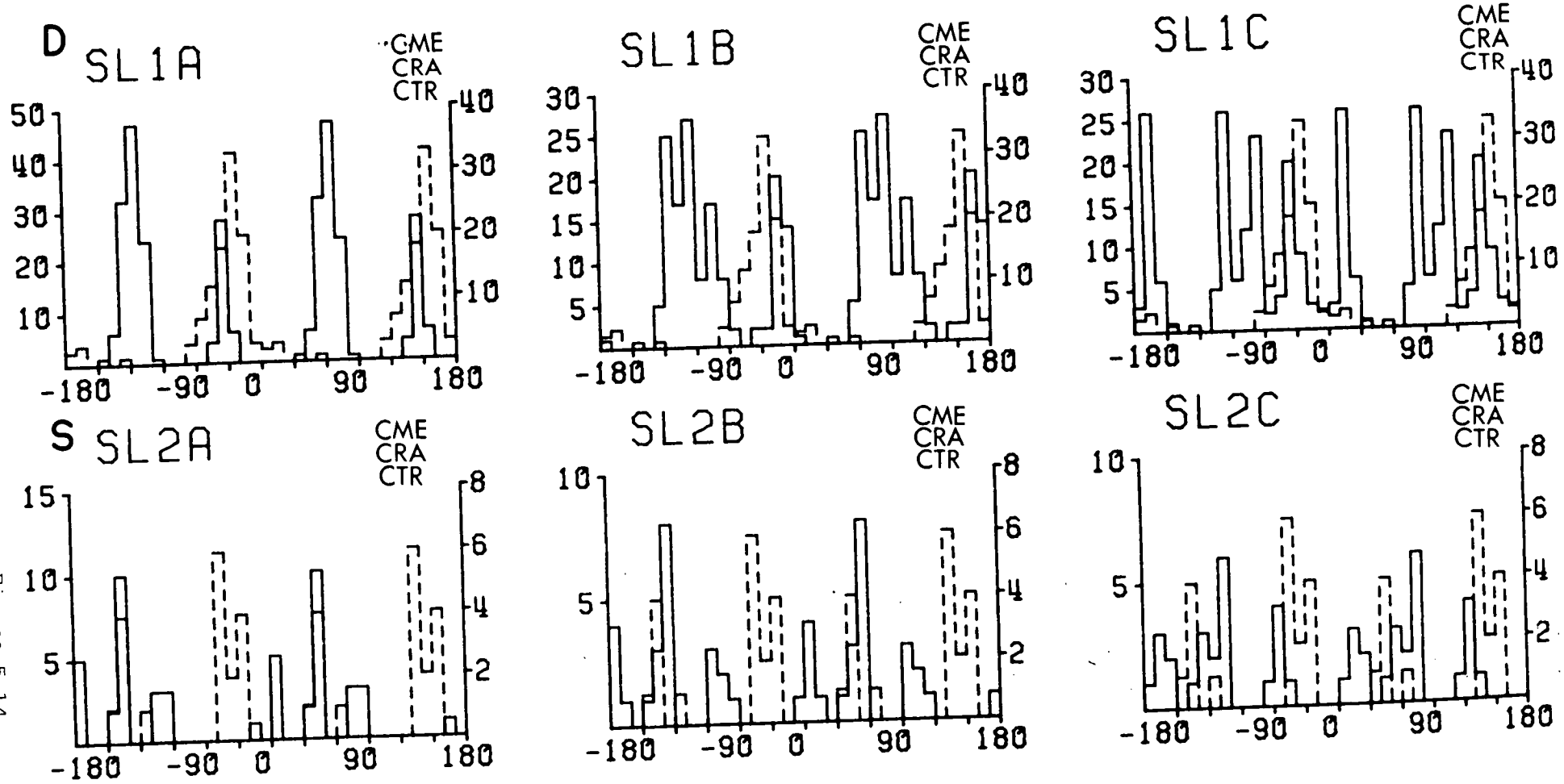
D SL1A
CME
CRA
CTR
50
40
30
20
10
40
30
20
10
-180
-90
0
90
180
SL1B
CME
CRA
CTR
30
25
20
15
10
5
40
30
20
10
-180
-90
0
90
180
SL1C
CME
CRA
CTR
30
25
20
15
10
5
40
30
20
10
-180
-90
0
90
180
S SL2A
CME
CRA
CTR
15
10
5
8
6
4
2
-180
-90
0
90
180
SL2B
CME
CRA
CTR
10
5
8
6
4
2
-180
-90
0
90
180
SL2C
CME
CRA
CTR
10
5
8
6
4
2
-180
-90
0
90
180

Figure 5.14

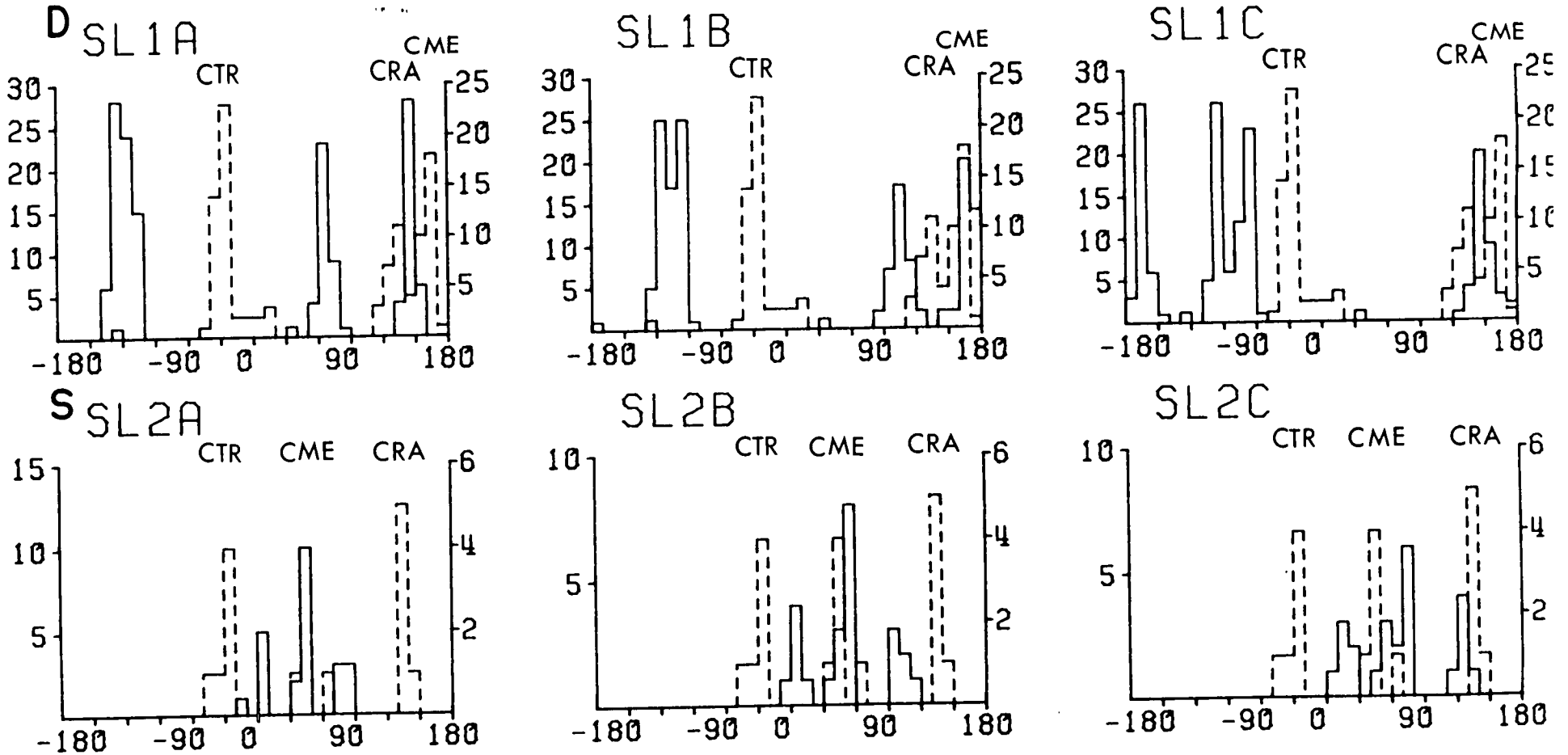
D SL1A
CTR
CME
CRA
SL1B
CTR
CME
CRA
SL1C
CTR
CME
CRA
S SL2A
CTR CME CRA
SL2B
CTR CME CRA
SL2C
CTR CME CRA
-180 -90 0 90 180

Figure 5.15

wave splitting is observed on many seismograms and the shear-wave polarizations, in general, align approximately N 150°E. Both these features were interpreted with some success as wave propagation through a vertical parallel crack structure orientated approximately N 150°E. The alignment of the shear-wave polarizations at N 150°E suggested that the horizontal axis of compression at 2 km depth is also in this direction. This direction is about 20° away from the axis of compression estimated from in situ stress measurements, and is approximately parallel to the NW-SE joint set measured at surface outcrops. Subsequently shear-wave radiation patterns from the seismic sources were synthesised and compared to the observed shear-wave polarizations. In general, the shear-wave radiation patterns from shear sources were consistent with the anisotropic model suggested in chapter four. Consequently the evidence presented here suggests the presence of effective seismic anisotropy within the granite rock mass.

In a study of the seismicity, stresses and hydraulic injection at the HDR site Batchelor (pers. comm.) concluded that no new hydraulic fractures were opened within the hydrofractured zone, but that the seismic activity was caused by shear on pre-existing fractures. This is in agreement with the source mechanism work carried out here, and also suggests that wave interaction solely within the hydrofractured zone is not the cause of the anisotropic effects displayed by the shear-waves. The whole granite rock mass is likely to be effectively anisotropic, due to the alignment of cracks, joints, and microcracks throughout the granite under the prevailing stresses.

There are two observations from the seismic data presented here which also suggest that the anisotropy is not confined to the neighbourhood of the hydraulic fractures but pervades the whole granite rockmass.

The first is that the size of the maximum delay of 0.05 seconds suggests that effective anisotropy exists along most of the ray path. If the anisotropy

only occurred in the immediate vicinity of the hydraulic fractures, the ray path would traverse only a small segment, 0.5 km, say, of effective anisotropy, and assuming a shear-wave velocity of 3.5 km/sec for uncracked granite, the velocity of the slower phase would be about 2.59 km/sec. This gives a shear-wave velocity-anisotropy of 26%, which is probably too large to be realistic. However, if the anisotropy is more widespread, so that the ray paths pass through 2 km, say, of effective anisotropy, the slower split shear-wave would have a velocity of 3.22 km/sec, and the velocity-anisotropy would be a more realistic 8%. Note also that the delays do not appear to increase in any systematic way as the fracturing proceeds, which suggests that either no new fractures are opened or that the anisotropy is not sensitive to the hydraulic fracturing.

The second is that the acoustic event in group S on 19 October before prolonged hydrofracturing had begun was recorded with shear-wave polarizations indistinguishable from those of later group S events after hydrofracturing. Since these polarizations are consistent with the effective anisotropy of aligned cracks, the granite matrix before fracturing also appears to have the anisotropic symmetry of aligned cracks. Thus the effective anisotropy of the granite before fracturing is thought to be the result of isolated water-filled microcracks, which are aligned parallel to the axis of compression of the prevailing stress field by such processes as subcritical crack growth (Crampin et al. 1984).

5.3 Conclusions

The hydrofracture-induced seismic activity is concentrated between the depths of 2 km and 3.5 km, and trends northwestward from the HDR site to a distance of 0.8 km. This region of concentrated seismicity - about 0.8 km in length, 0.4 km in width and 1.5 km in depth - probably defines the extent of

the hydrofracture zone. The seismic source mechanism is shear as opposed to jacking, and the most likely focal mechanism is left-lateral strike-slip on NW-SE trending subvertical joint planes. Two distinct earthquake groups emerged, and their characteristics are summarised below.

(i) Shallow events: depths less than 2 km; hypocentres just above the hydrofracture zone; up to 40° dip-slip faulting on the NW-SE joints.

(ii) Deep events: depths greater than 2 km; hypocentres within the hydrofracture zone; predominantly strike-slip faulting.

The observation of shear-wave splitting, shear-wave polarization alignments, and time delay patterns consistent with the expected crack distribution from the in situ stresses is strongly supportive of wave propagation in effective anisotropic media. These observations indicate that cracks are open within the granite; the cracks are aligned; and that the crack structure is effectively anisotropic to seismic waves. A crack model of liquid-filled circular penny-shaped cracks with effective hexagonal symmetry successfully modelled the observed shear-wave polarizations and time delays.

CHAPTER SIX

THE LIVERMORE DATA

This chapter is concerned with the shear-wave particle motion of microearthquakes from the Livermore Valley area - a region of natural seismic activity situated about 50 km east of San Francisco, California. The shear-wave particle motion is found to be diverse and complicated, with its characteristics largely dependant on the station site. Shear-wave polarizations are estimated, and alignments of their orientations occur at several stations. The presence of an aligned crack structure consistent with stresses derived from fault plane solutions (Cockerham et al. 1980; Follow ill & Mills 1982) could explain these alignments. However the source mechanisms generate shear-wave polarizations with alignments which are also consistent with observations at several stations. In addition, further complexities are introduced by the presence of a laterally heterogeneous geological structure, with sharp seismic velocity contrasts between different rock units. It is probable that the observed pattern of shear-wave polarizations is derived from a combination of three factors - seismic source, subsurface geological structure, and cracks.

In this chapter I will present: an outline of the geological structure and seismicity of the Livermore Valley area; the criteria used for selecting events for this study; discuss the shear-wave particle motion and polarizations, and finally undertake a comparison of shear-wave polarizations generated directly from appropriate sources with the observed shear-wave polarizations.

6.1 The Livermore Valley: location and geology

The Livermore Valley is an east-west trending valley in central California in the zone of active faulting and seismicity which comprises the San Andreas fault system in the San Francisco Bay region. The valley extends approximately 25 km east-west and 11 km north-south, and is bounded by the Calaveras fault in the west, the Greenville fault in the east, the Las Positas fault and Diablo Mountain Range to the south, and Mount Diablo to the north. The valley boundaries are shown in a generalized geological map of the area in Figure 6.1a.

A detailed geological description of the Livermore Valley is given by Carpenter et al. (1980). The basement rocks consist of highly deformed marine clastic rocks, cherts, greenstones, and some ultramafics belonging to the Franciscan assemblage - a lithologically heterogeneous and structurally complicated unit. The basement outcrops in the north at Mount Diablo and to the south in the Diablo Range. The Great Valley sequence, consisting of moderately deformed marine sedimentary rocks stucturally overlies the Franciscan basement, and is exposed on the surrounding hills to the north, east, and west of the valley. The Great Valley sequence was thrust over the Franciscan rocks along the Coast Range Thrust, which marked the existence of a subduction zone during late Jurassic and early Tertiary times. Within the Livermore Valley, the Franciscan and Great Valley sequences are overlain by Eocene to upper Miocene marine sediments which, in turn, are overlain by poorly consolidated, coarse grained lacustrine and fluvial deposits dating from the Pliocene to the Holocene. These poorly consolidated sediments may exceed 1.2 km thickness in the valley.

6.2 Seismicity in the Livermore Valley

The dominant mechanism along the numerous northwest trending faults in

Figure 6.1
(a) A generalized geological map of the Livermore region (after Taylor & Scheimer 1982). (b) Schematic structural cross-section through the Livermore Valley taken along line AA'. Values are the P-wave velocities. CRT: Coast Range Thrust. (After Taylor & Scheimer 1982).

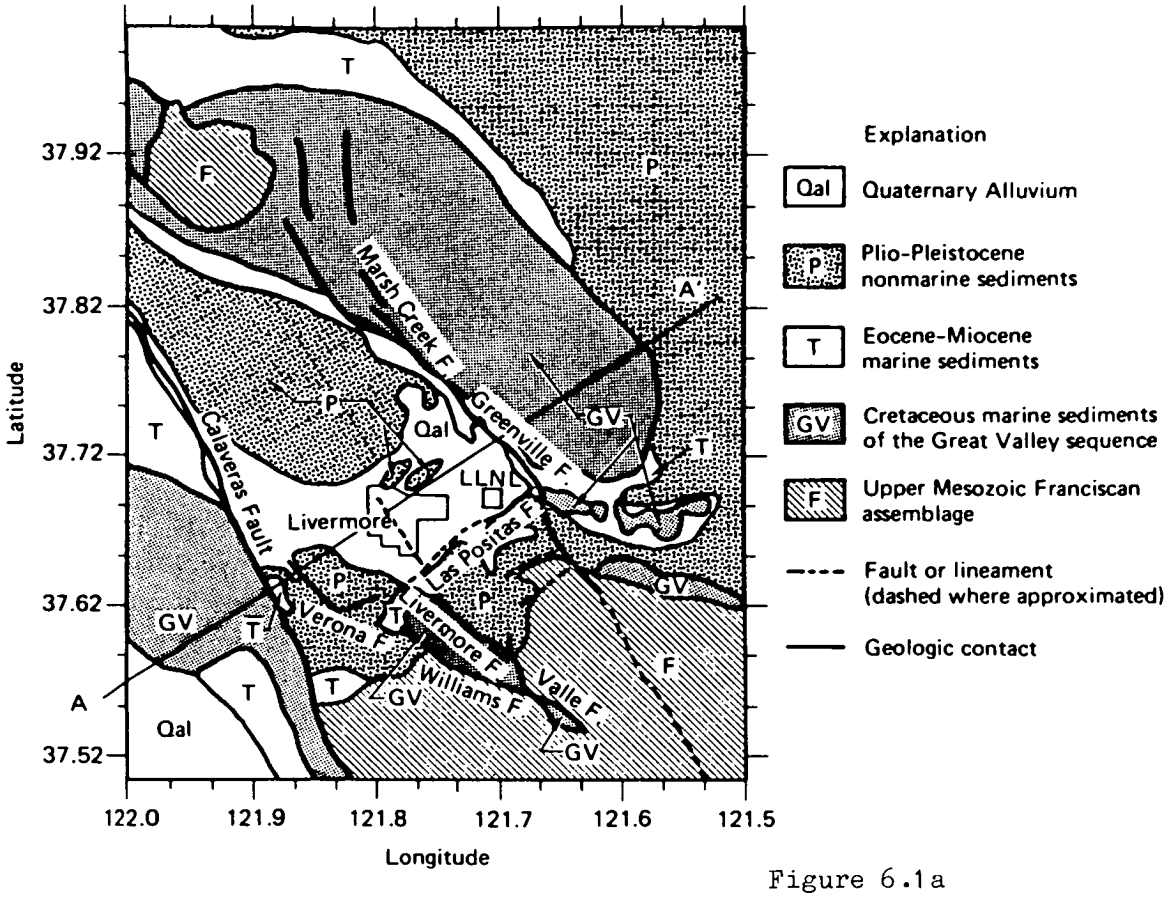

Figure 6.1a

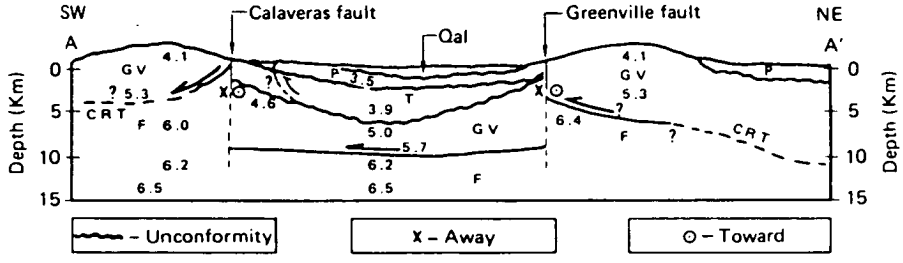

Figure 6.1b

the area - San Andreas, Hayward, Calaveras, Greenville, and Marsh Creek - is right-lateral strike-slip. Strike-slip activity probably began about 6 million years ago when the Mendocino triple junction was at the latitude of Livermore. As the triple junction migrated northward thrusting associated with the Coast Range subduction zone gave way to a strike-slip mechanism along transform faults.

Up to 1980 studies of the seismicity in the Livermore Valley indicated a highly complex and spatially diffuse pattern of strain release (Lee et al. 1971; Bolt & Miller 1975). Seismic activity was poorly correlated with known faults east of the Hayward fault. Ellsworth & Marks (1980) suggested that the absence of clear correlation is partly related to the inadequacy of seismic station coverage and to incomplete knowledge of the crustal structure. Subsequently the Lawrence Livermore National Laboratory (LLNL) contracted the United States Geological Survey (USGS) to install seven three-component short period stations within the Livermore Valley area as part of a program to assess geological hazards at the laboratory site. Refraction studies followed, and detailed crustal models of the Livermore Valley have been developed (Follow Hill & Mills 1982; Taylor & Scheimer 1982; Scheimer et al. 1982). A schematic structural cross-section across the Livermore Valley is shown in Figure 6.1b. The P-wave velocity of each geological rock unit discussed in section 6.1 is given. The cross-section indicates that sharp velocity contrasts occur laterally and vertically, particularly between the low velocity sediments in the valley and rocks of the Great Valley or Franciscan units.

Over the last ten years a few strong earthquakes have been recorded along the eastern edge of the valley near the Greenville fault. A magnitude 4.6 (M_L) earthquake occurred 10 km east of Livermore in 1977 with a focal depth of 10 km. Strong motion records from this event are discussed by Maley (1978). More recently, on 24 January 1980 a M_L=5.9 earthquake occurred on the

northern extension of the Greenville fault. A series of aftershocks followed, which included a M_L=5.3 earthquake about 10 km southeast of the principal shock. This earthquake series has been well documented (Cockerham et al. 1980; Bolt et al. 1980; Follow ill & Mills 1982), and surface fault breaks were observed by Bonilla et al. (1980). The aftershock sequence was concentrated along a 20 km segment of the Marsh Creek and Greenville faults, with a diffuse zone of epicentres extending to the southeast for approximately 25 km (Cockerham et al. 1980). Focal mechanisms of the principal earthquakes and many of the aftershocks were consistent with right-lateral strike-slip on the Greenville fault system. The P- and T- axes from fault plane solutions by Cockerham et al. (1980) suggested north-northeast to south-southwest compression in the area.

Follow ill & Mills (1982) studied the seismicity of the valley area up to eight months after the January 1980 mainshock. They discovered differences in focal depths, patterns of epicentral locations and focal mechanisms in the northern and southern region of the Livermore Valley. Focal depths in the northern regions (north of the LLNL site) were usually between 5 km and 11 km which were slightly greater than focal depths (2 km to 8 km) in the southern regions (south of the LLNL site). The seismicity was distributed diffusely in the south, and focal mechanisms were a mixture of strike-slip and thrust. This contrasted with the linear epicentral distribution and right-lateral strike-slip faulting along the surface trace of the Greenville fault in the north. They speculated that the more diffuse pattern of locations and focal mechanisms in the south results from general north-south compression tectonics in a localized zone of deformation between the Livermore Valley and the Diablo Range to the south.

6.3 The LLNL seismic network

Seismicity in the Livermore Valley and adjacent areas has been located accurately on a routine basis since the installation of the LLNL seismic network during January 1980. The station distribution with respect to the faults in the area is illustrated in Figure 6.2, and their latitude, longitude, elevation, and site geology is given in Table 6.1. The data analysed here was recorded at the three-component stations - CDV, CMN, CPN, CVL, CSA, CPS, and CDA, all of which are labelled in Figures 6.2 and 6.3. All the stations are standard USGS short period systems with a pass band from 1 to 10 Hz.

The data recorded by the seismic network was telemetred to the LLNL where it was routinely digitized at 64 samples per second (sps) up until Spring 1981. Since then the data has been digitized at 128 sps, after passing through an antialias filter with a 3 db point of 25 Hz (Taylor & Scheimer 1982). The vertical-components of the three-component stations were set at higher gains and lower saturation levels than the corresponding horizontals (Follow ill & Mills 1982).

6.4 Selection of earthquakes for shear-wave particle motion analysis

More than 3000 earthquakes were located by the LLNL seismic network between January 1980 and December 1982. The computer program HYPO71 (Lee & Lahr 1972) was used with the average velocity model of the Livermore Valley (Scheimer et al. 1980) for hypocentral location. About 2000 events were recorded in 1980 - over 500 in January alone - with seismic activity remaining stable at about 30 events/month through 1981 and 1982. The seismicity was distributed fairly uniformly over the Livermore Valley with clusters of activity developed to the north (along the Greenville fault) and to the south (in the area bounded by the Las Positas, Williams, and Greenville faults).

Table 6.1 Latitude, longitude, elevation and site rock of the three-component stations of the LLNL seismic network in the Livermore Valley, California USA. Gravel is the Livermore gravel which consists of debris from Franciscan rocks: pebbly sand, silt and sand. The Great Valley rocks are discussed in the text.

STATION	LATITUDE N	LONGITUDE W	ELEVATION (KM)	SITE ROCK
CDA	37.7300	121.7283	0.1900	sandstone
CDV	37.5663	121.6800	0.2500	Great Valley
CMN	37.6275	121.7083	0.2450	gravel
CPN	37.6502	121.8617	0.2000	gravel
CPS	37.6900	121.7000	0.1550	alluvium
CSA	37.6738	121.7027	0.2150	gravel
CVL	37.6263	121.8357	0.2450	gravel
CAL	37.4512	121.7992	0.2650	------
CAO	37.3493	121.5327	0.6280	------
CVA	37.6187	121.7587	0.1980	gravel

Events were selected for shear-wave particle motion analysis during my visit to the LLNL. Primarily due to the limited time period of my stay (one month) complete quality control of the seismograms selected from over 20 000 available was not possible. However earthquake magnitudes, which were easily accessible, provided a guide of signal:noise ratio and hence quality. Inspection of seismograms at LLNL indicated that signal:noise ratio was generally best for earthquakes with magnitudes in the range $1.0 < M_L < 2.0$. Higher magnitudes tended to result in saturated records at stations near the epicentre.

Earthquakes were selected from two spatial zones: one zone is to the north of the laboratory site - hereafter called the Greenville zone - with the other to the south in the area bounded by the Las Positas, Williams, and Greenville faults -the LWG zone. The separation into north and south geographic zones was carried out to ensure that the selected events are representative of the seismicity in the valley region as discussed by Follow ill & Mills (1982). The hypocentral parameters of the selected events are given in Table 6.2.

An inspection of some polarization diagrams from the January 1980 aftershock sequence by Crampin & Scheimer revealed shear-wave particle motion with a first motion polarization parallel to the north-south trending axis of maximum compression followed by later splitting. As already discussed, similar observations have been made in northern Turkey during the Turkish Dilatancy Project (Booth et al. 1984) and at the HDR site in Cornwall discussed in this dissertation. Following this, Scheimer suggested analysis of seismograms from the January 1980 aftershocks which occurred along the northern end of the Greenville fault. Sixty-four events were selected, with $M_L > 1.0$ and hypocentral locations mostly of A and B quality, from a rectangular area with vertices (37° 40.25'N, 121° 43.59'W), (37° 42.9'N, 121° 38.11'W), (37° 49.02'N, 121° 43.59'W), and (37° 45.74'N, 121° 48.44'W). Twenty

events which occurred after February 1980 were included to increase time coverage. An epicentral map of these events is shown in Figure 6.2, along with a NW-SE cross-section. The epicentres cluster along the surface trace of the Greenville fault with earthquake depths generally below 10 km. The earthquakes to the south of CDA, however, tend to occur at shallower depths (between 5 km and 10 km). Note that station CPS is located at the LLNL site.

The second spatial zone is the area bounded by the Las Positas, Williams, and Greenville faults (the LWG zone) in the centre of the seismic network. A circle with a 10 km radius centred at the three-component station CMN defined the selection area. Selected events were constrained to occur between August 1980 and December 1982, with location quality restricted to A and B, and $M_L > 1.0$. One hundred and sixteen events satisfied this criteria from which sixty-six were selected based on signal:noise ratio in the vertical-components. An epicentral map and an east-west cross-section of these events is shown in Figure 6.3. The more diffuse seismicity to the south of the LLNL discussed by Follow[illegible]ill & Mills (1982) is evident in the more scattered epicentral distribution. Some epicentres are clustered, notably at the intersection of the Williams and Valle faults, and in the east along the Greenville fault. Generally depths range between 5 and 7 km, although some earthquakes to the north have depths greater than 10 km.

6.5 Shear-wave particle motion analysis

Over seven hundred seismogram traces with corresponding polarization diagrams are generated from the one hundred and thirty events selected. One hundred and thirty-eight seismograms are disregarded because of instrumental problems eg. dead components or instrumental noise. Also on many seismic records, notably at CPS, waveform amplitudes on the east-west component are often less than those on the north-south component. This raises doubts over

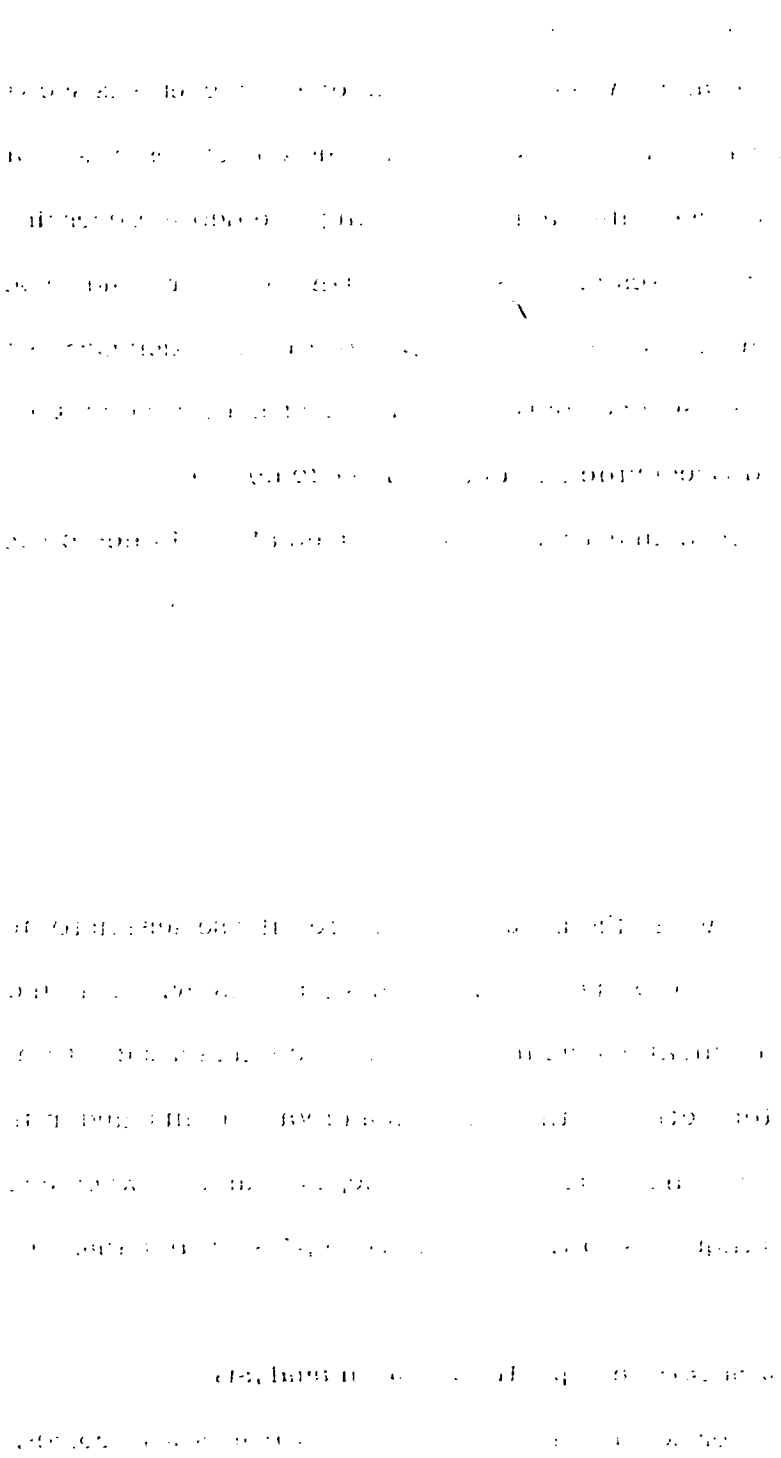

Figure 6.2
The hypocentral distribution of selected events in the Greenville zone. Locations provided by the LLNL. (a) Map showing epicentres (circles), three-component stations (triangles), and fault traces (solid lines). The major faults are named. (b) Northwest-southeast cross-section, A-B. The vertical axis is depth marked in kilometres.

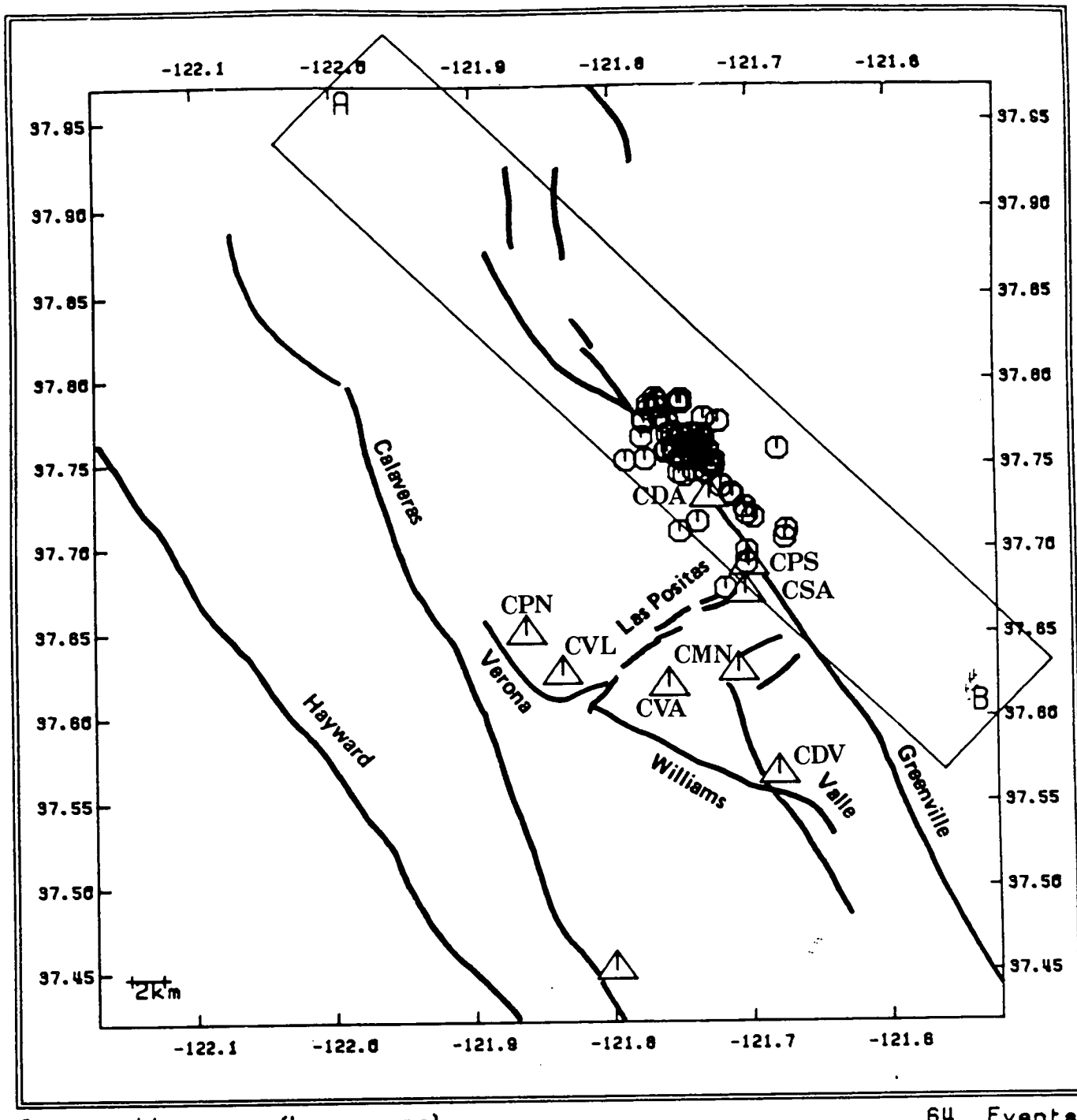

Figure 6.2a

Figure 6.2b

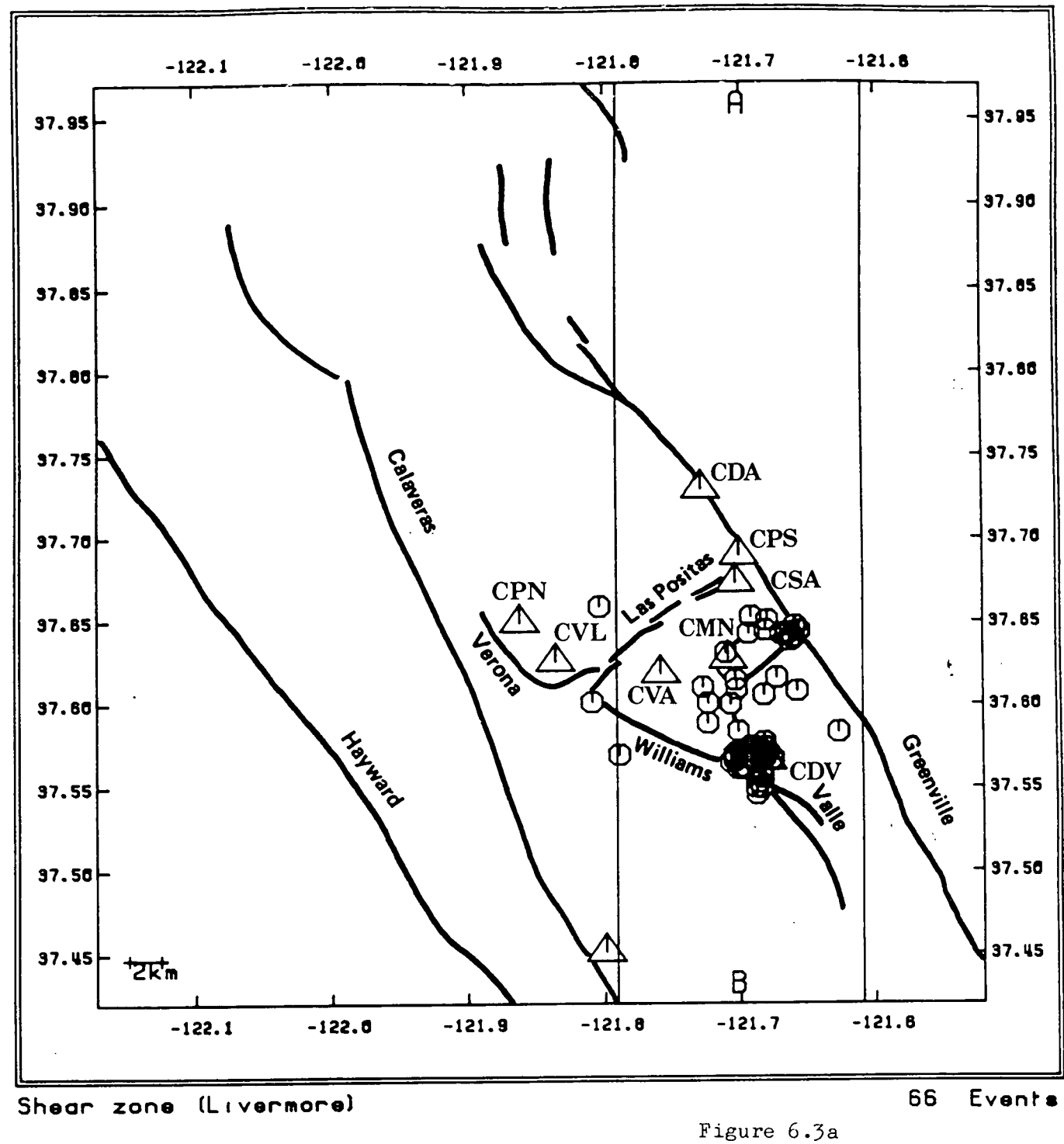

Figure 6.3a

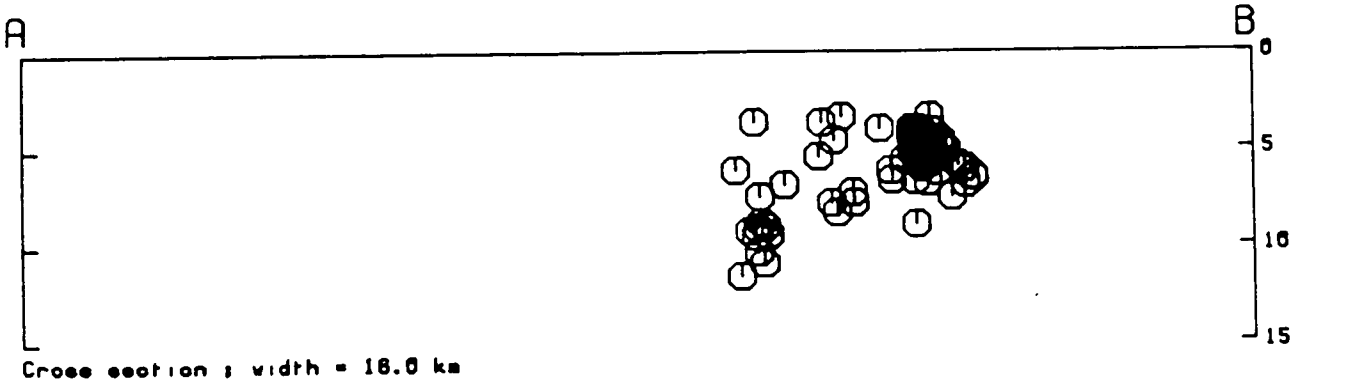

Figure 6.3b

Table 6.2 Date, origin time, epicentre, and depth of the selected events from the Livermore Valley seismicity, California.

DATE	ORIGIN TIME	LATITUDE N	LONGITUDE W	DEPTH (KM)
800124	22 9 8.80	37-45.43	121-44.11	10.82
800124	2253 26.22	37-47.18	121-44.89	10.35
800124	23 5 23.74	37-42.60	121-45.01	4.84
800125	056 6.47	37-45.16	121-46.48	2.96
800125	4 0 50.62	37-43.09	121-41.80	8.50
800125	720 18.40	37-45.16	121-44.78	10.64
800125	739 29.56	37-47.19	121-45.93	12.50
800125	2020 41.56	37-44.58	121-44.77	9.48
800125	2335 23.80	37-42.95	121-44.21	8.71
800125	2352 13.54	37-46.02	121-45.27	11.39
800126	156 31.25	37-44.67	121-45.00	10.36
800126	4 3 26.08	37-47.01	121-46.01	11.16
800126	433 56.57	37-45.19	121-44.96	10.59
800126	815 36.86	37-45.49	121-45.51	10.44
800126	824 26.27	37-45.26	121-44.41	11.08
800126	1020 19.65	37-47.00	121-45.87	12.73
800126	1342 53.73	37-43.23	121-42.08	5.35
800126	16 1 7.06	37-46.92	121-46.28	11.21
800127	248 8.70	37-44.97	121-43.69	11.70
800127	353 29.60	37-42.38	121-40.43	5.16
800127	411 39.87	37-45.72	121-44.77	12.45
800127	417 25.25	37-45.63	121-44.55	13.19
800127	429 44.22	37-44.93	121-43.64	12.29
800127	7 9 26.81	37-45.60	121-45.27	10.88
800127	936 28.70	37-46.13	121-45.25	12.48
800127	1031 46.51	37-46.64	121-45.80	13.32
800127	1043 28.31	37-44.93	121-43.52	13.34
800127	1239 14.72	37-46.04	121-45.47	11.58
800127	1338 8.61	37-43.87	121-42.69	5.72
800127	14 0 53.39	37-45.03	121-43.70	13.95
800127	1711 9.90	37-45.11	121-47.34	10.33
800128	1145 42.63	37-46.46	121-46.50	7.18
800129	2 5 35.34	37-47.32	121-46.01	9.32
800129	1226 51.78	37-44.21	121-43.17	5.70
800201	222 11.94	37-45.41	121-45.59	10.75
800201	456 54.73	37-45.35	121-45.20	11.45
800203	19 7 39.98	37-43.95	121-42.76	5.38
800205	1347 36.23	37-45.62	121-44.32	10.27
800206	1 9 7.68	37-45.95	121-46.63	2.58
800208	320 13.59	37-45.09	121-43.50	11.92
800210	445 43.20	37-45.97	121-44.95	10.88
800213	127 37.84	37-45.60	121-44.43	12.22
800312	1242 3.12	37-42.65	121-40.36	10.69
800328	2037 9.38	37-46.49	121-43.29	12.99
800407	2319 2.77	37-41.50	121-42.10	5.58
800412	2218 57.69	37-47.07	121-46.33	10.43
800513	1736 38.66	37-46.03	121-44.86	9.86
800531	958 26.25	37-44.75	121-44.37	10.44
800602	748 1.05	37-43.47	121-42.17	3.91
800607	1516 21.14	37-41.90	121-42.08	7.65
800708	1432 54.56	37-47.29	121-44.91	8.41
800712	820 20.69	37-45.85	121-43.94	11.64
800826	957 33.83	37-34.31	121-41.51	4.00
800827	11 3 24.22	37-34.27	121-41.88	5.02

Table 6.2 continued.

DATE	ORIGIN TIME	LATITUDE N	LONGITUDE W	DEPTH (KM)
800829	420 27.47	37-33.99	121-41.27	5.81
800829	812 45.91	37-33.72	121-41.88	5.53
800830	232 7.43	37-34.08	121-40.90	5.78
800901	114 45.13	37-34.39	121-41.36	4.94
800903	927 31.85	37-34.21	121-42.22	4.54
800904	2 5 39.39	37-34.38	121-41.48	4.64
800904	444 16.97	37-34.33	121-41.34	4.51
800904	2034 4.77	37-34.45	121-41.35	5.18
800910	18 9 4.38	37-34.45	121-41.22	4.39
800918	051 35.90	37-34.64	121-40.90	5.60
800918	1443 35.82	37-39.56	121-48.21	6.29
800930	2121 57.87	37-45.80	121-44.21	9.76
801003	056 58.17	37-34.37	121-41.62	6.72
801004	18 8 12.78	37-34.48	121-41.52	4.30
801017	4 1 0.75	37-36.35	121-40.90	3.39
801017	10 0 22.60	37-36.02	121-42.39	7.84
801018	1214 44.73	37-34.45	121-40.90	4.00
801030	1024 34.54	37-36.97	121-40.34	5.46
801128	246 30.61	37-34.99	121-37.62	6.66
801128	1149 1.59	37-37.89	121-42.60	6.93
801129	15 1 43.54	37-46.46	121-45.49	11.11
801201	11 1 35.22	37-38.69	121-40.84	3.68
801214	11 2 43.03	37-34.35	121-41.40	5.04
801227	823 11.97	37-44.73	121-43.80	9.50
801230	646 27.85	37-35.32	121-43.43	4.01
810102	0 2 10.78	37-46.04	121-44.09	11.53
810105	1215 40.61	37-34.17	121-40.99	4.17
810113	1821 26.57	37-34.25	121-40.77	4.50
810123	619 1.97	37-46.06	121-44.40	10.75
810125	019 29.42	37-34.12	121-41.89	5.33
810206	229 35.44	37-45.45	121-43.74	11.86
810217	911 20.84	37-38.55	121-40.17	7.55
810228	1933 23.46	37-34.17	121-42.26	4.87
810228	2217 58.62	37-33.92	121-42.41	4.16
810301	056 31.64	37-33.97	121-42.23	3.37
810301	849 13.32	37-34.08	121-42.21	4.77
810303	2033 54.85	37-45.50	121-44.07	11.96
810326	16 3 16.17	37-34.05	121-42.25	4.62
810508	314 23.74	37-33.37	121-40.98	7.53
810519	134 2.20	37-34.02	121-40.54	6.79
810520	2 2 52.76	37-33.66	121-41.89	5.00
810525	1356 44.89	37-34.14	121-40.99	6.00
810617	755 20.64	37-46.56	121-46.55	9.55
810706	147 9.99	37-47.17	121-45.03	11.28
810729	626 37.88	37-38.40	121-39.62	9.09
810812	047 54.93	37-40.60	121-43.02	5.91
810819	3 6 57.94	37-38.59	121-41.58	10.43
810919	2139 17.73	37-33.68	121-42.09	4.62
810922	2049 21.64	37-32.99	121-41.00	6.88
811006	145 9.11	37-39.20	121-41.48	6.18
811006	1144 36.55	37-36.05	121-43.41	7.30
811006	1343 14.78	37-36.63	121-43.64	7.85
811025	1556 29.55	37-35.03	121-42.05	6.17
811124	332 42.62	37-36.89	121-42.17	3.70

Table 6.2 continued.

DATE	ORIGIN TIME	LATITUDE N	LONGITUDE W	DEPTH (KM)
811221	138 18.96	37-34.30	121-41.43	4.68
820115	1133 22.36	37-34.43	121-41.47	5.26
820201	616 31.87	37-32.77	121-41.21	6.52
820213	1550 14.59	37-38.32	121-39.77	9.51
820214	1738 49.02	37-38.51	121-39.94	8.87
820306	1418 48.26	37-39.05	121-40.76	11.67
820321	11 2 2.44	37-45.51	121-40.72	14.75
820325	216 34.98	37-33.74	121-41.73	6.25
820403	1137 24.84	37-38.61	121-39.89	9.17
820405	313 33.12	37-46.62	121-43.91	12.03
820411	2138 34.22	37-38.84	121-39.55	9.33
820518	1538 19.58	37-33.01	121-41.25	6.07
820617	355 54.19	37-38.66	121-39.37	9.60
820710	529 29.02	37-36.09	121-48.54	3.78
820802	1452 12.68	37-33.94	121-41.36	5.51
820803	2129 52.72	37-33.52	121-41.02	5.13
820814	2140 28.54	37-34.18	121-47.36	6.08
820820	318 43.93	37-38.43	121-39.64	10.99
820822	855 35.00	37-36.48	121-39.45	8.33
820829	2126 0.46	37-33.19	121-41.12	5.91
820914	859 46.42	37-34.35	121-41.99	8.95
821101	1147 15.49	37-36.56	121-42.12	4.62

the accuracy of the calibration of the horizontal components at CPS, and such records are not used in the analysis.

It is not possible to group events based on similarity of shear-wave particle motion, as carried out previously with seismic records from the hydrofracture seismicity at the HDR site, Cornwall. However, the general characteristics of the seismogram appear to be largely dependant on the station at which it is recorded. For example, seismograms recorded at stations CMN and CSA, both located on Livermore gravel, usually have impulsive shear-wave arrivals with most of the energy in the first cycle of the shear-wave coda. In contrast, seismograms from CPN and CVL often show emergent shear-wave arrivals with signal noise interfering with their onsets. These stations are also situated on Livermore gravel, but in a region of elevated topography in the East Bay Hills to the west of Livermore Valley. At stations sited on the alluvium such as CPS low frequency phases of about 2 Hz often onset prior to the shear-wave.

A representative event from each zone is chosen to illustrate the characteristic shear-wave particle motion at each station. Seismograms and polarization diagrams are illustrated in Figures 6.4 and 6.5. Figure 6.4 shows three-component seismograms and polarization diagrams, rotated into a vertical, radial, and transverse coordinate system, for an event at a depth of 11.92 km from the Greenville zone. Station CDA is nearest to the source at an epicentral distance of 2.40 km, and the most distant station is CDV at an epicentral distance of 20.93 km. The exact point of the shear-wave onset at CDA is not clear, but it arrives during the second window (see Figure 6.4a). The shear-wave particle motion is initially linear, becomes elliptical after about 0.2 seconds and is suggestive of the arrival of split shear-waves. The signal noise between the P-wave and shear-wave arrival and the lengthy shear-wave coda (over 4 seconds) suggests that much of the seismic energy radiated

by the source is scattered by the medium. In contrast, the shear-wave arrival at more distant stations, CSA and CMN in Figures 6.4b and 6.4c, is impulsive with little interference from signal noise. The duration of the shear-wave codas at both stations is less than one second. At CMN the shear-wave onsets with linear particle motion which becomes elliptical after about 0.25 seconds - once again suggesting the arrival of split shear-waves. The seismograms and polarization diagrams at stations CPN, CVL, and CDV illustrated in Figures 6.4def are more reverberative and have higher frequency content than at stations CSA and CMN. The exact time of the shear-wave onset is difficult to distinguish at stations CPN and CVL, but linear particle motion in the second window probably marks the shear-wave arrival at CDV in Figure 6.4f. Note that some of the seismograms are suggestive of double events: apparent double P-wave onset at CMN and CPN in Figures 6.4cd; separation of phases in shear-wave coda at CMN in Figure 6.4c, and the reverberative nature of the seismograms. However a double high amplitude P-wave pulse would be expected at CSA for a double event and this is not observed.

Three-component seismograms and polarization diagrams, rotated as in Figure 6.4, are shown in Figure 6.5 for an event at a depth of 5.81 km from the LWG zone. The seismograms in Figure 6.5 illustrate that the magnitude of this event must be large enough to overload the closer stations CDV and CMN (see Figure 6.5ab) to be detected with high signal noise at the more peripheral stations. At CSA in Figure 6.5c an early radial onset is clearly observed in the third window, possibly an SP-phase arriving before the direct shear-wave. Also a 5 Hz pulse onsets, possibly an S to P converted phase, about two seconds after the P-wave at CSA. The shear-wave arrival at stations CVL and CPN can be clearly identified in windows 2 and 3 respectively in Figures 6.5e and 6.5f, but in both cases the shear-wave particle motion is elliptical. At the furthest station, CDA, where the epicentral distance is 18.55 km, the shear-

Figure 6.4

Three-component seismograms and polarization diagrams for an event from the Greenville zone recorded on 8 February 1980, with epicentre 37° 45.09'N, 121° 43.50'W, and a depth of 11.92 km. The north-south and east-west seismogram traces are shown above the vertical (V), radial (R), and transverse (T) traces. The horizontal and vertical gains are normalised upon rotation. Directions: A-away from source; T-towards source; R-right looking from source; L-left looking from source; U-up; D-down. Time between cross bars is 0.015625 seconds (64sps) and the window length is 0.3 seconds. The heavy arrows in the horizontal polarization diagrams indicate probable shear-wave arrivals.

	station	epicentral distance	azimuth (source to station)
(a)	CDA	2.40 km	N 187°E
(b)	CSA	8.84 km	N 167°E
(c)	CMN	13.84 km	N 174°E
(d)	CPN	16.94 km	N 227°E
(e)	CVL	16.98 km	N 215°E
(f)	CDV	20.93 km	N 169°E

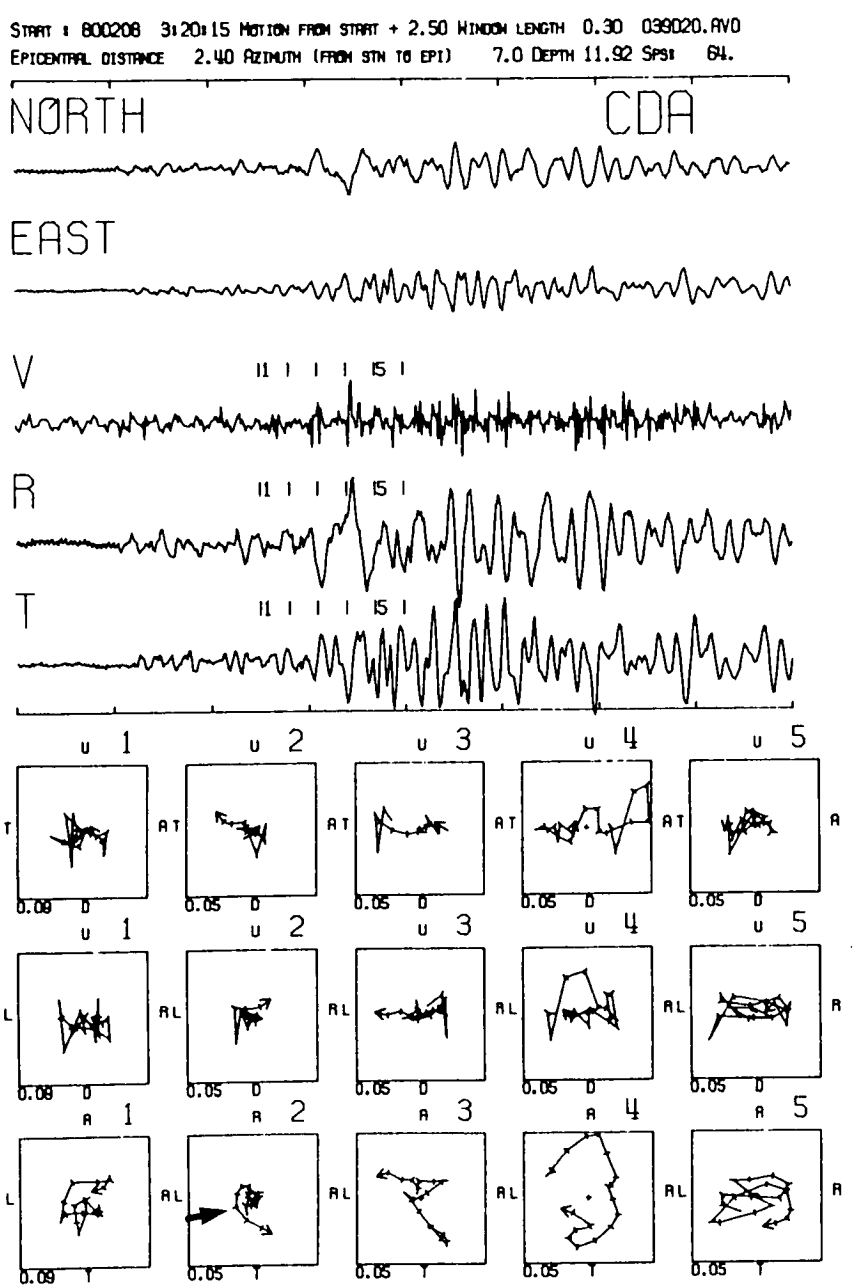

Figure 6.4a

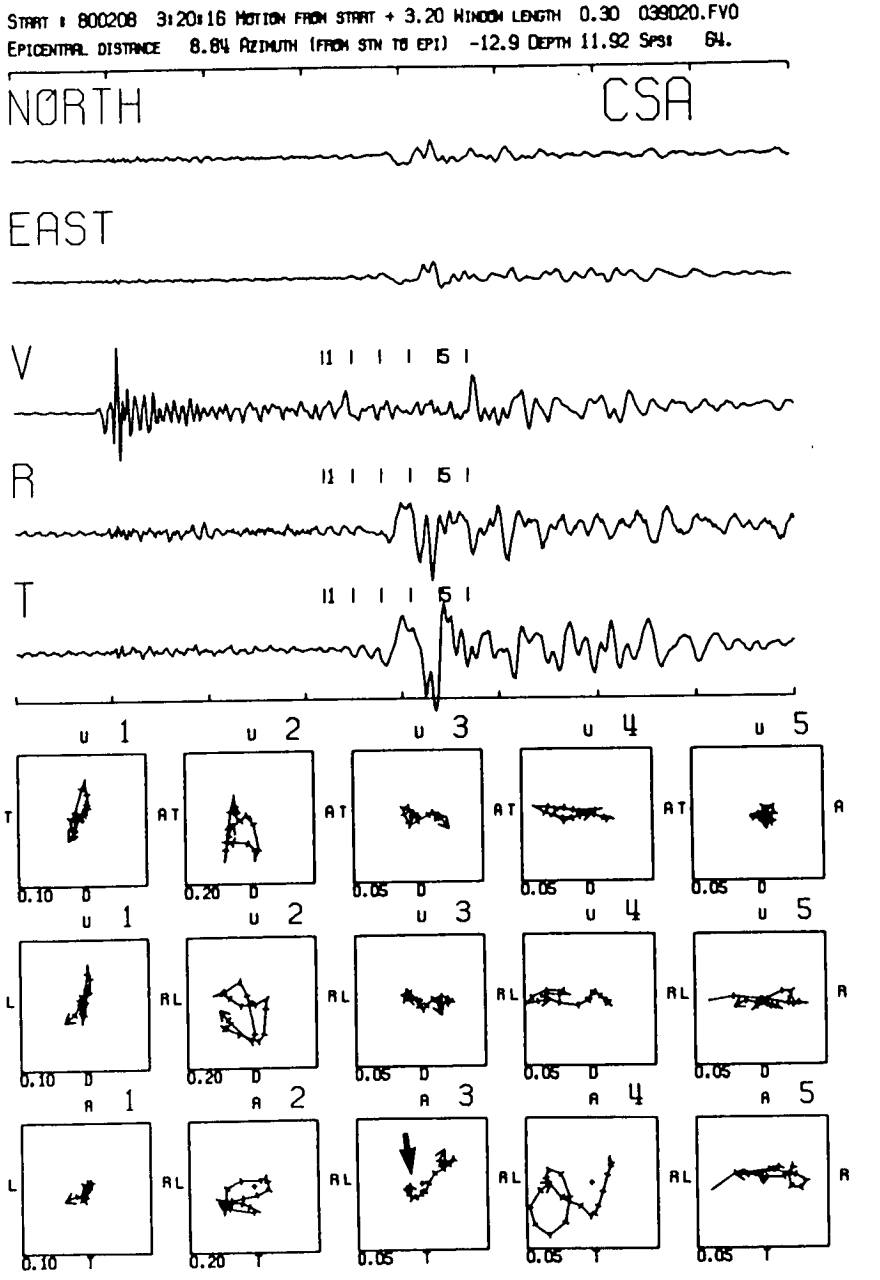

Figure 6.4b

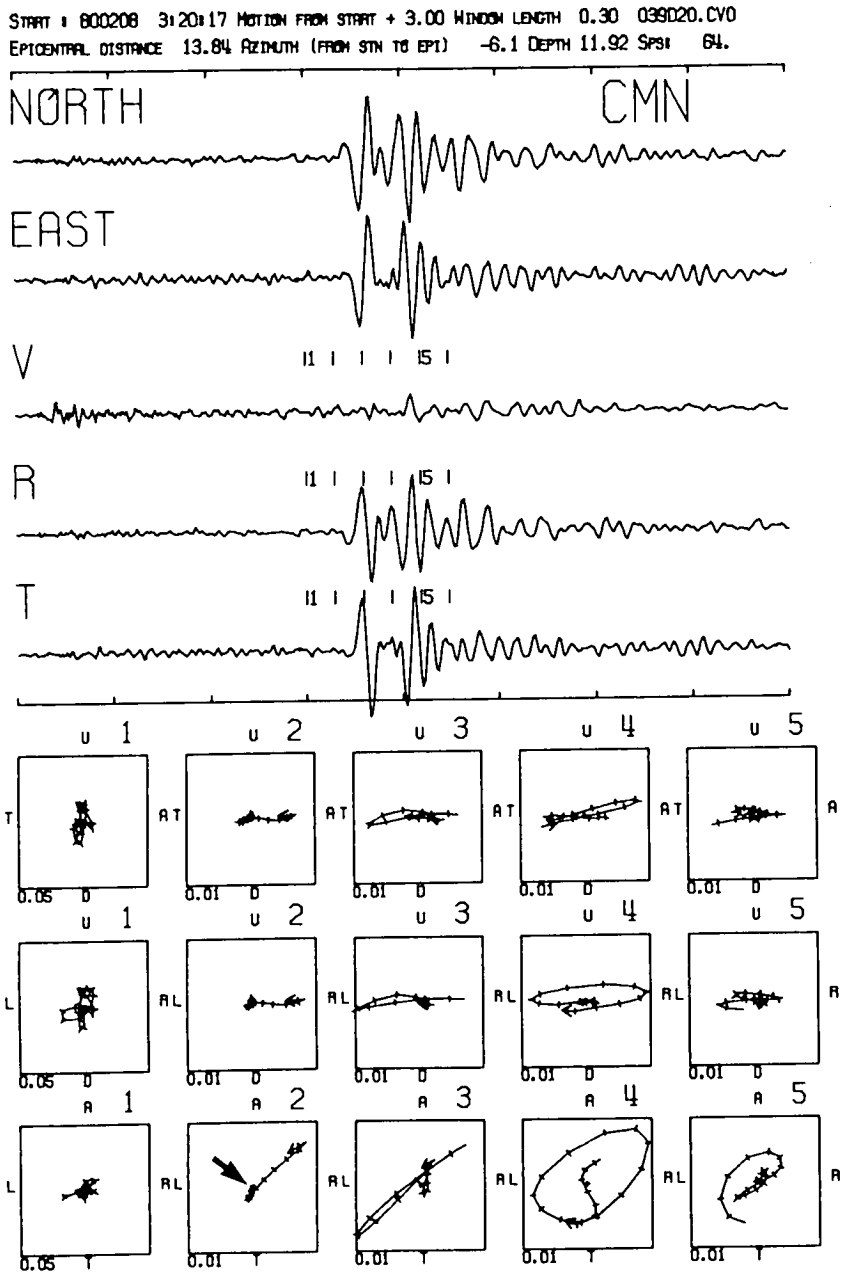

Figure 6.4c

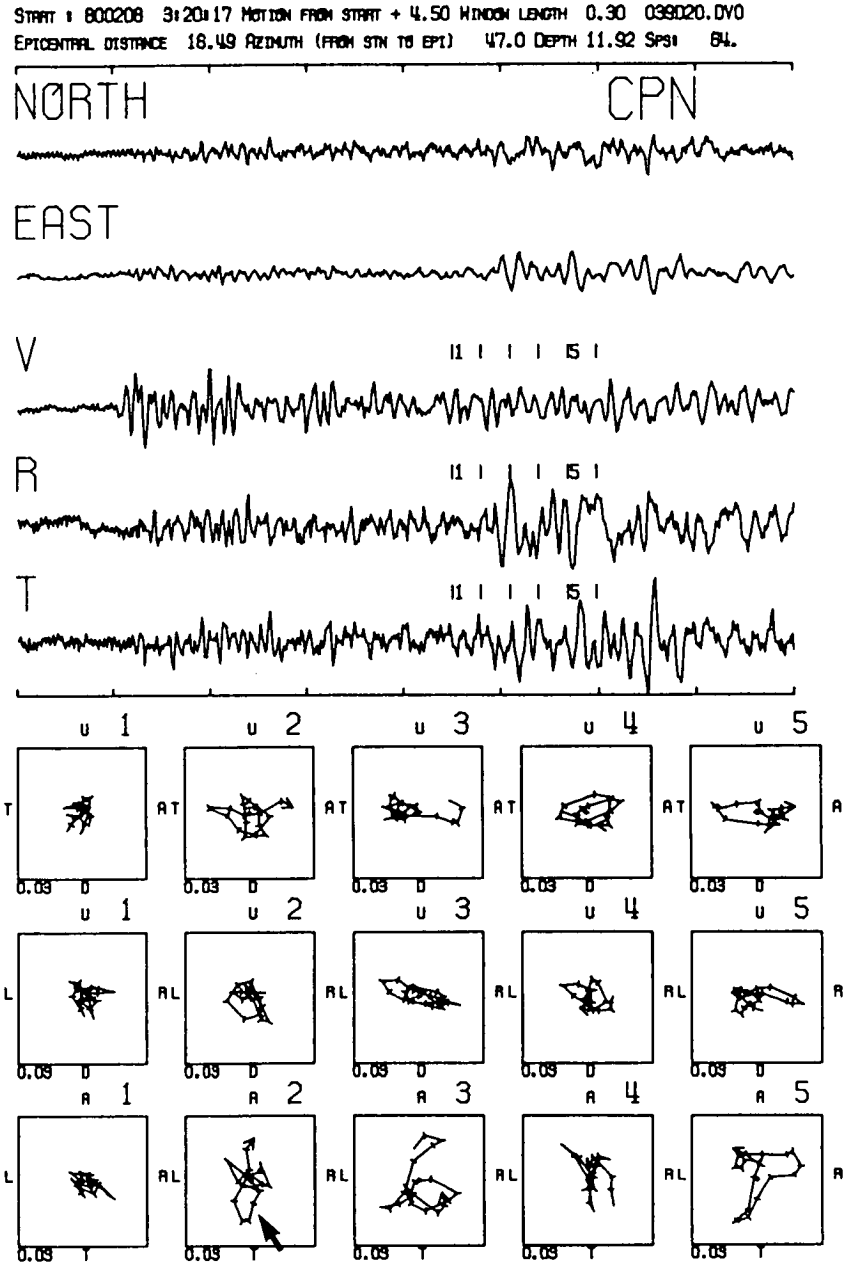

Figure 6.4d

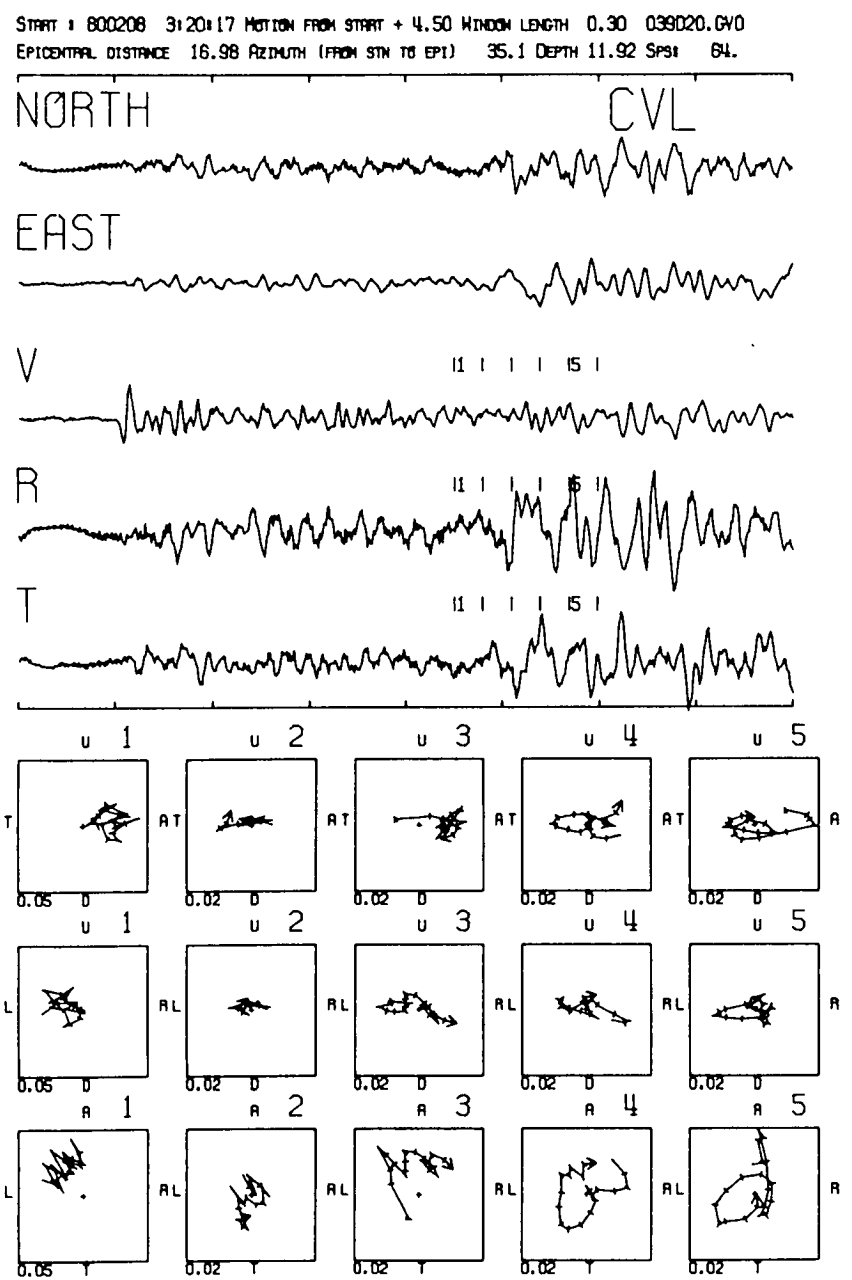

Figure 6.4e

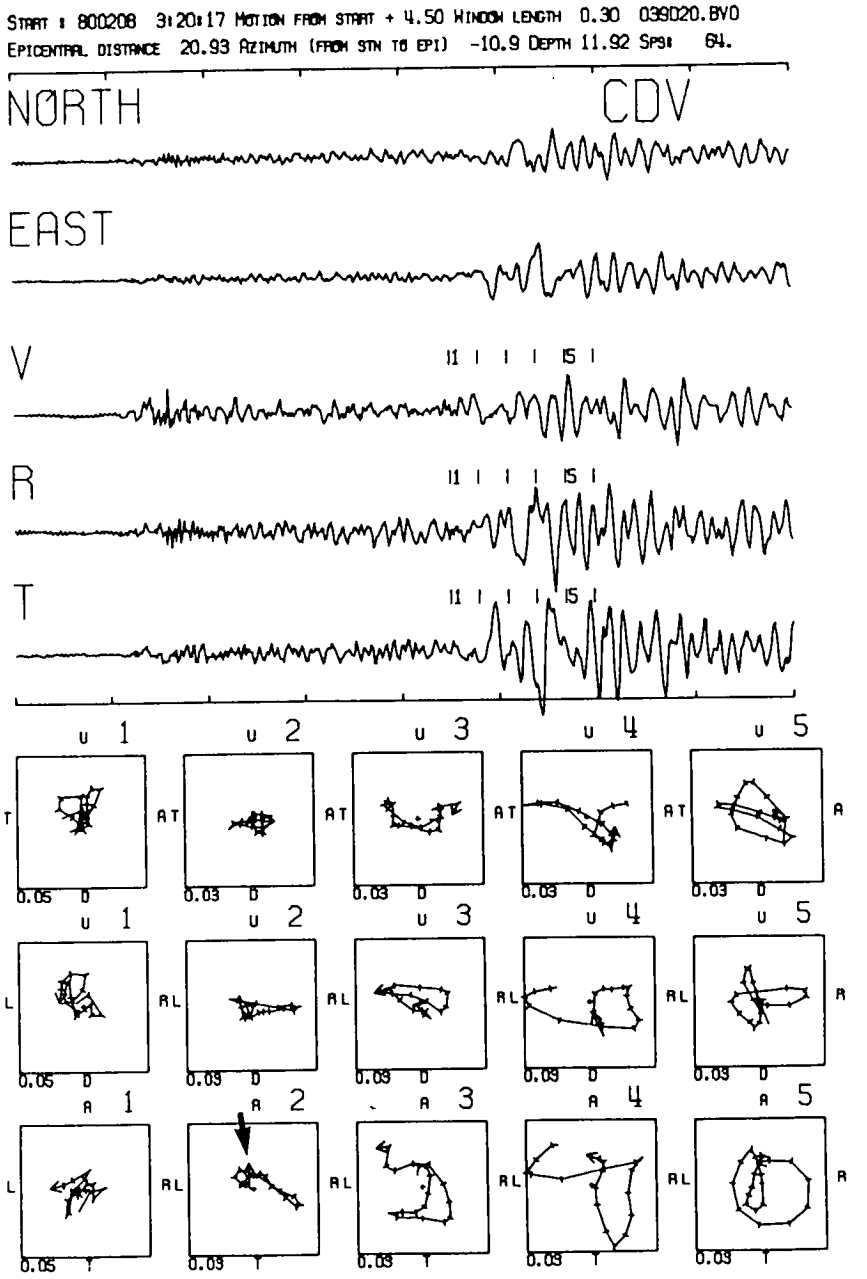

Figure 6.4f

Figure 6.5

Three-component seismograms and polarization diagrams for an event from the LWG zone recorded on 29 August 1980, with epicentre 37° 33.99'N, 121° 41.27'W and a depth of 5.81 km. Notation and format as in Figure 6.4.

	station	epicentral distance	azimuth (source to station)
(a)	CDV	0.89 km	N 92°E
(b)	CMN	7.01 km	N 345°E
(c)	CSA	11.98 km	N 354°E
(d)	CPS	13.75 km	N 355°E
(e)	CVL	14.85 km	N 297°E
(f)	CPN	17.94 km	N 301°E
(g)	CDA	18.50 km	N 349°E

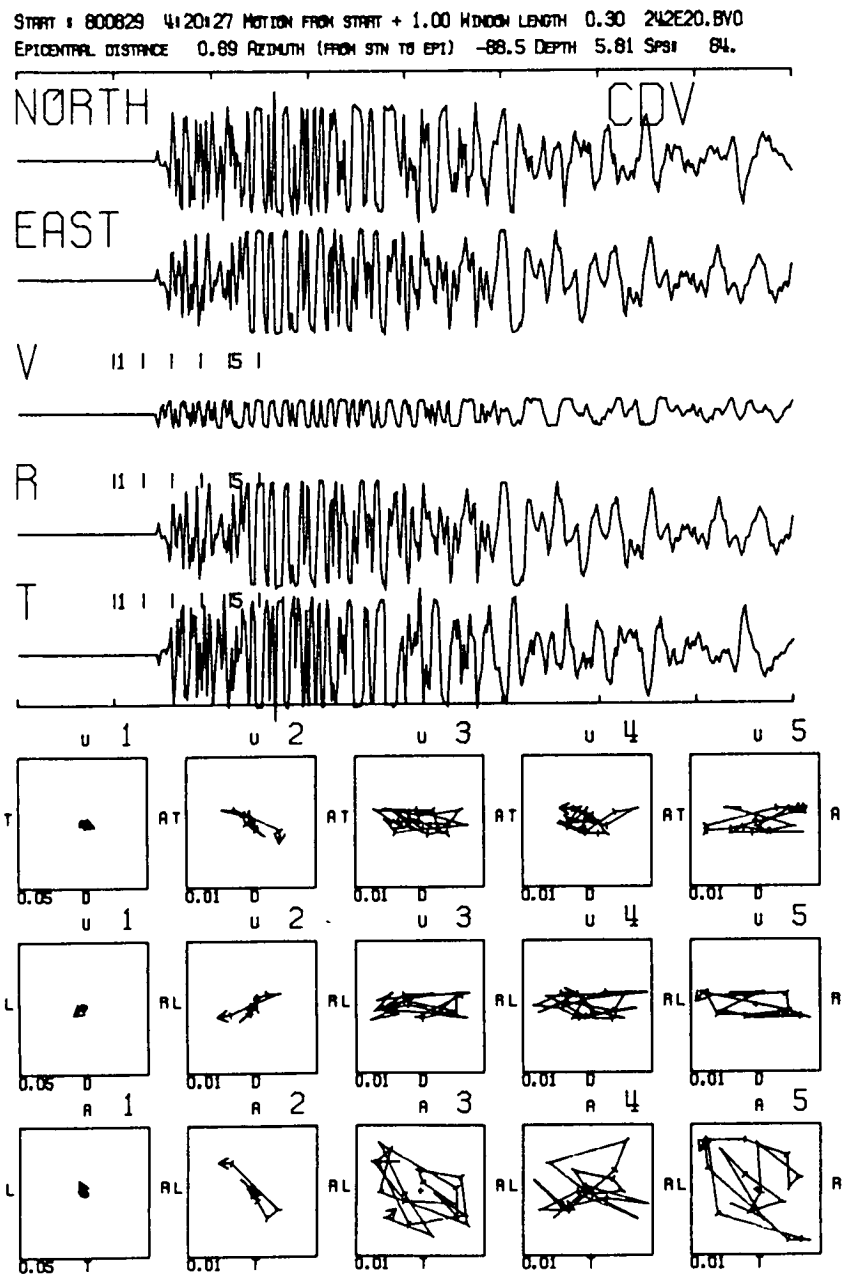

Figure 6.5a

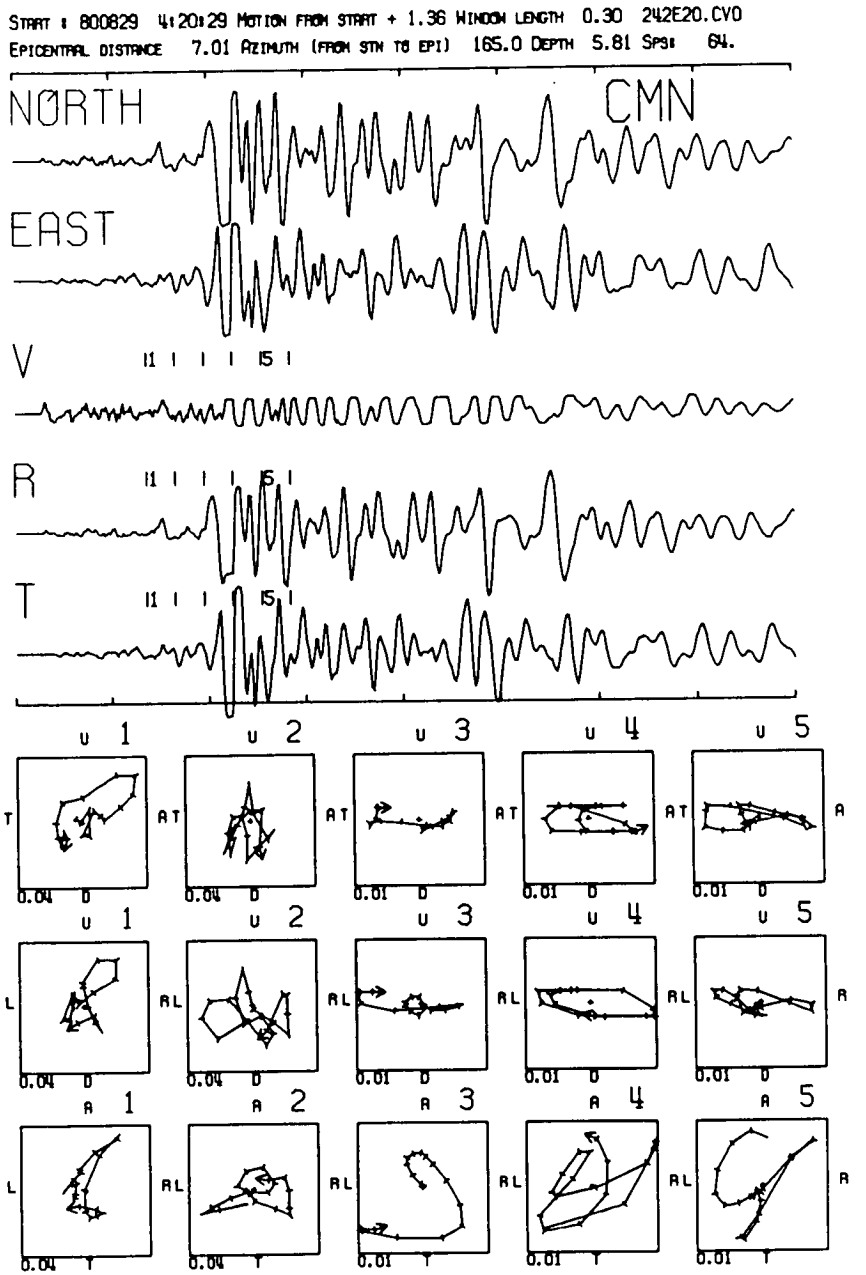

Figure 6.5b

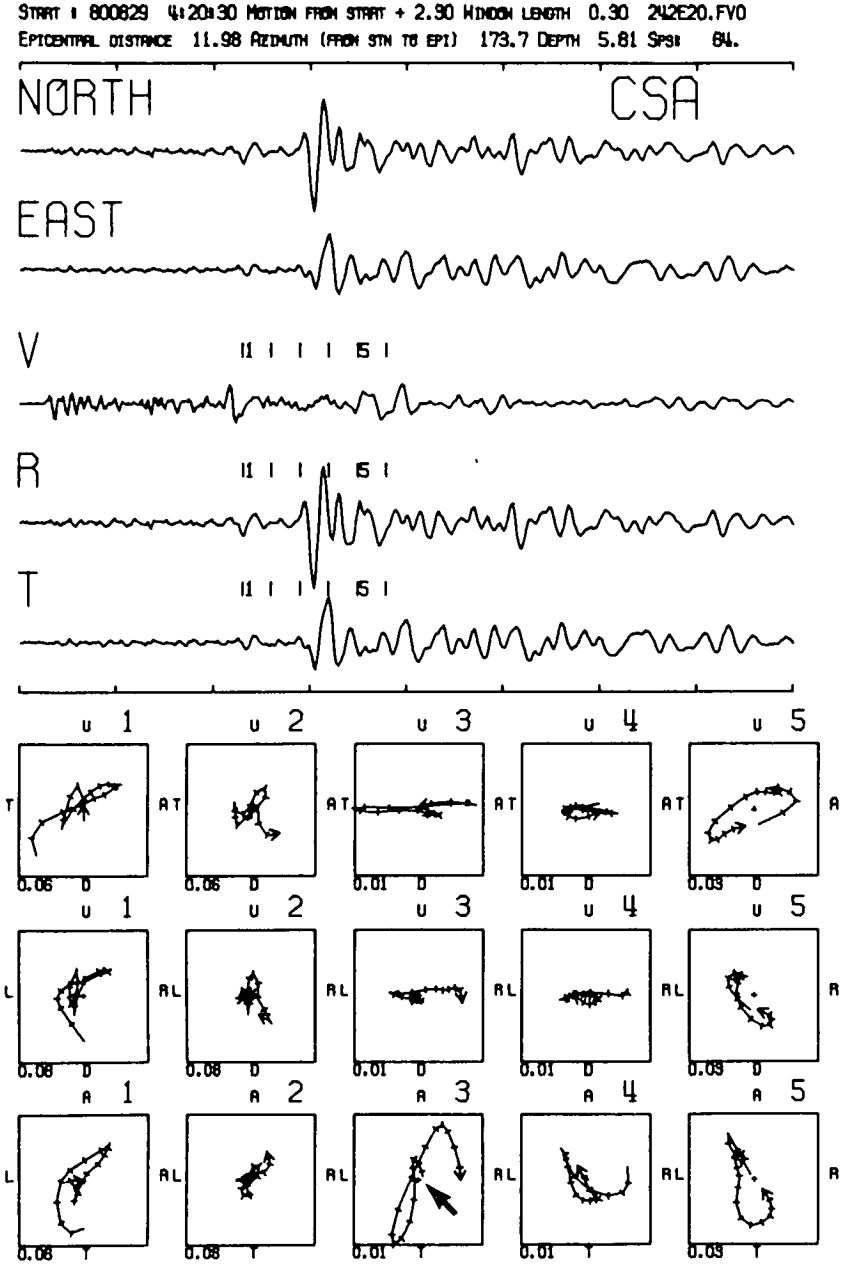

Figure 6.5c

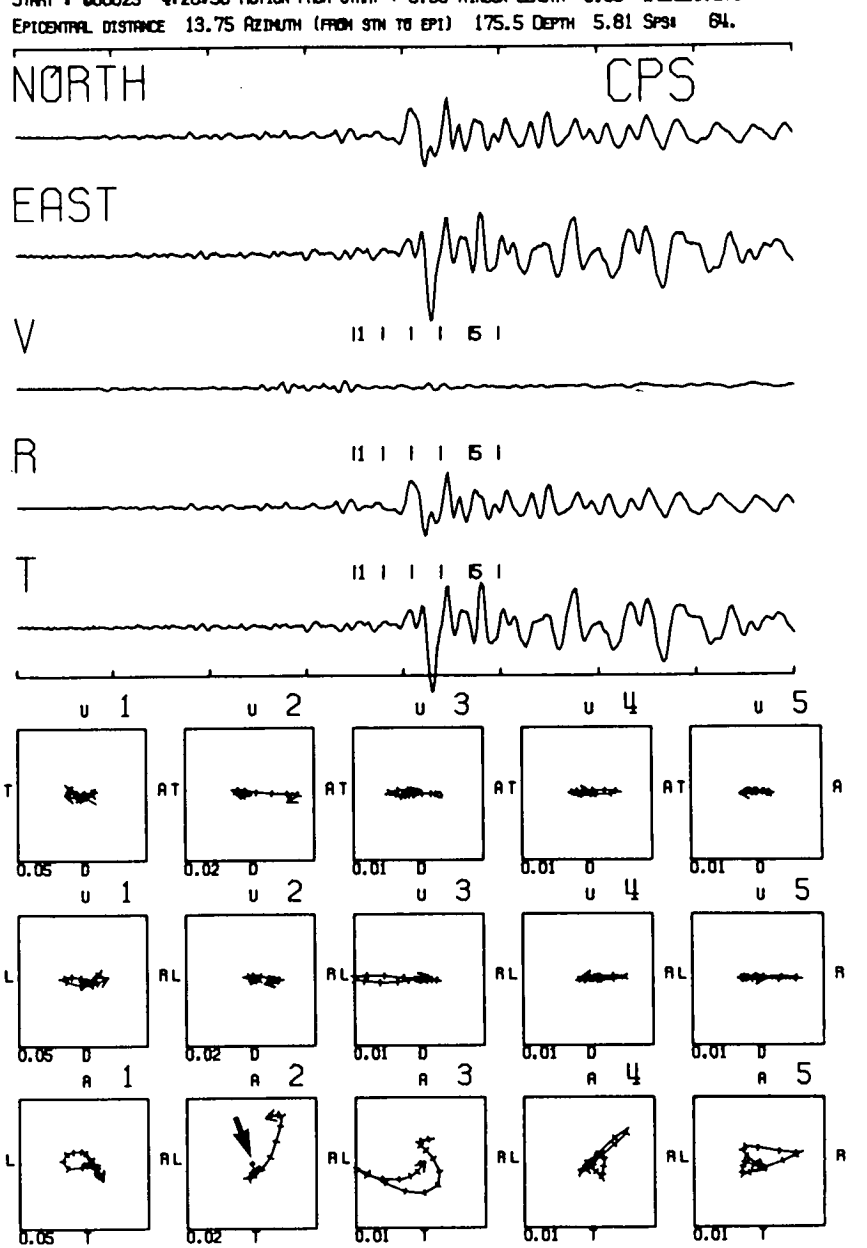

Figure 6.5d

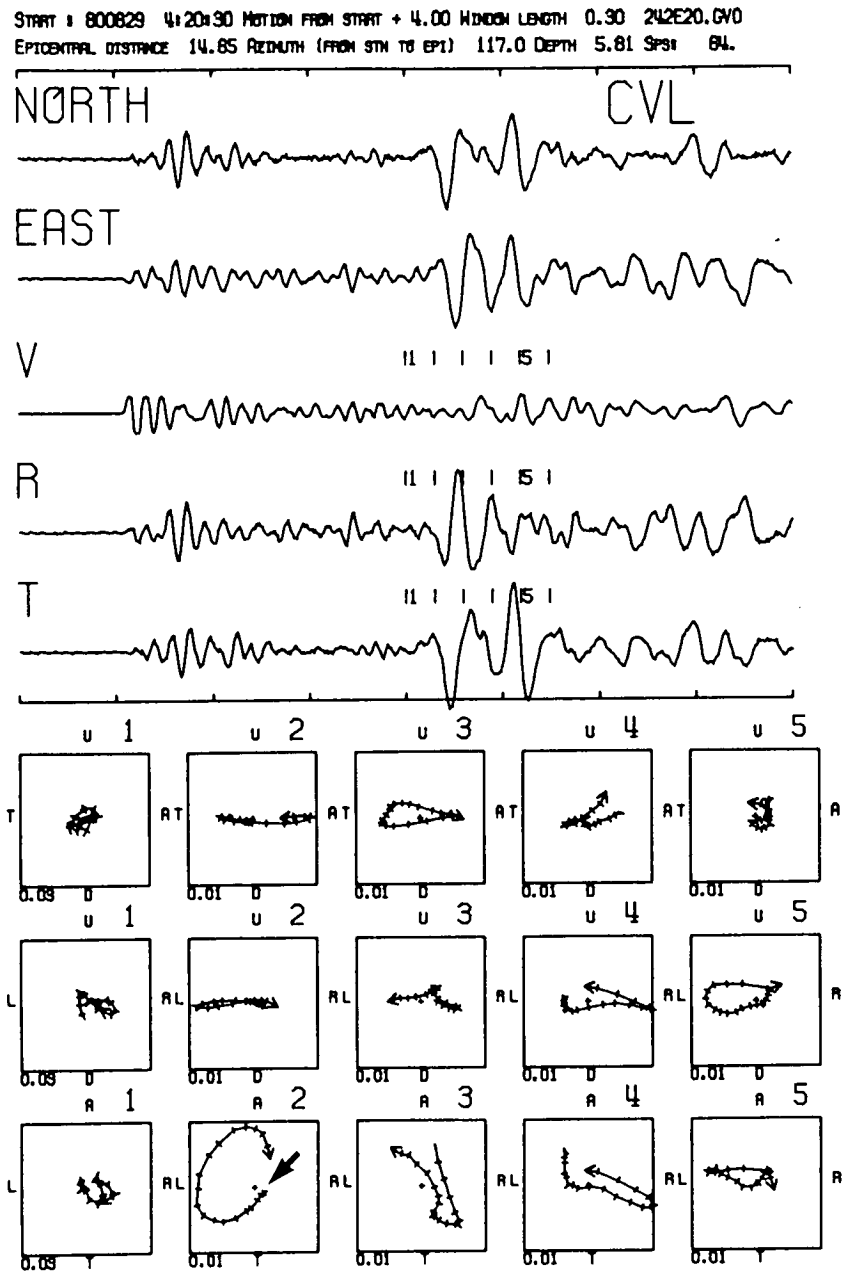

Figure 6.5e

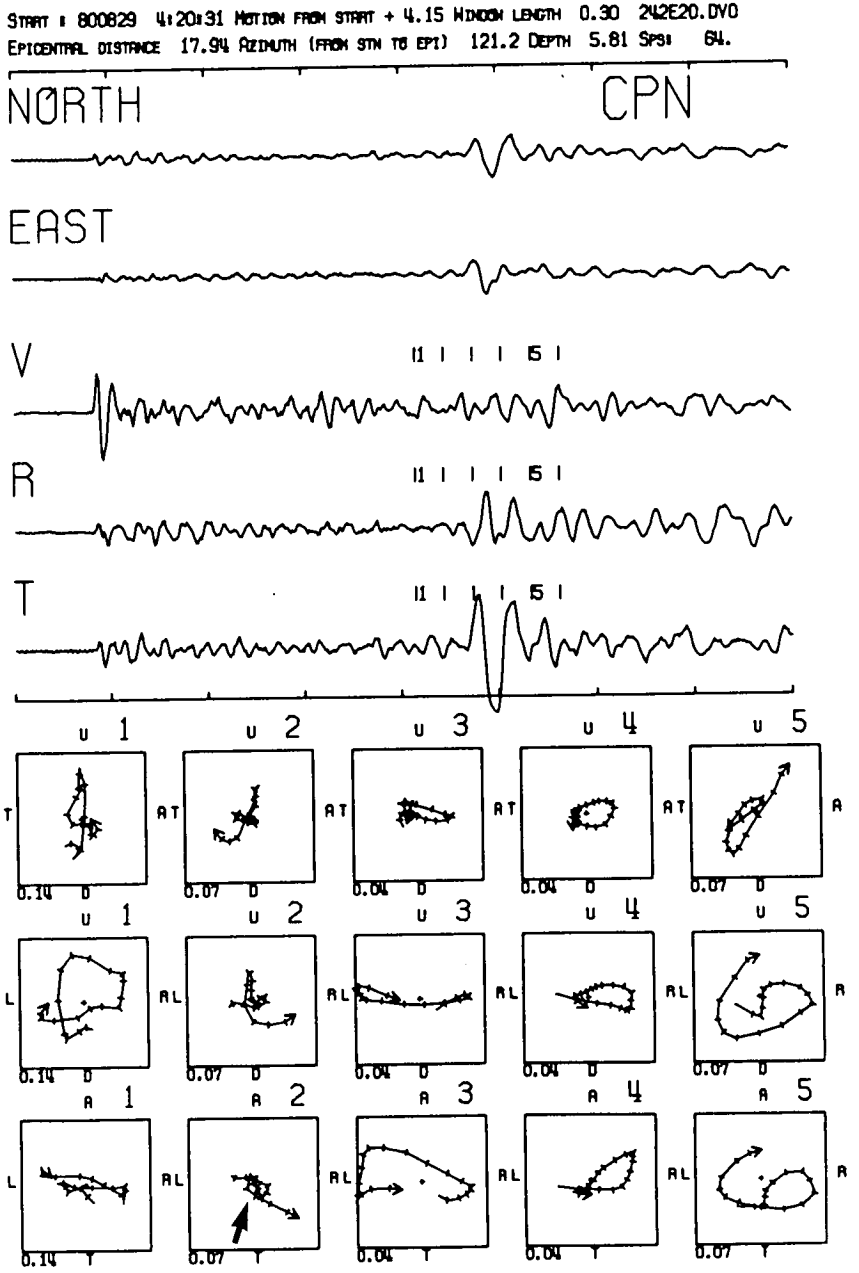

Figure 6.5f

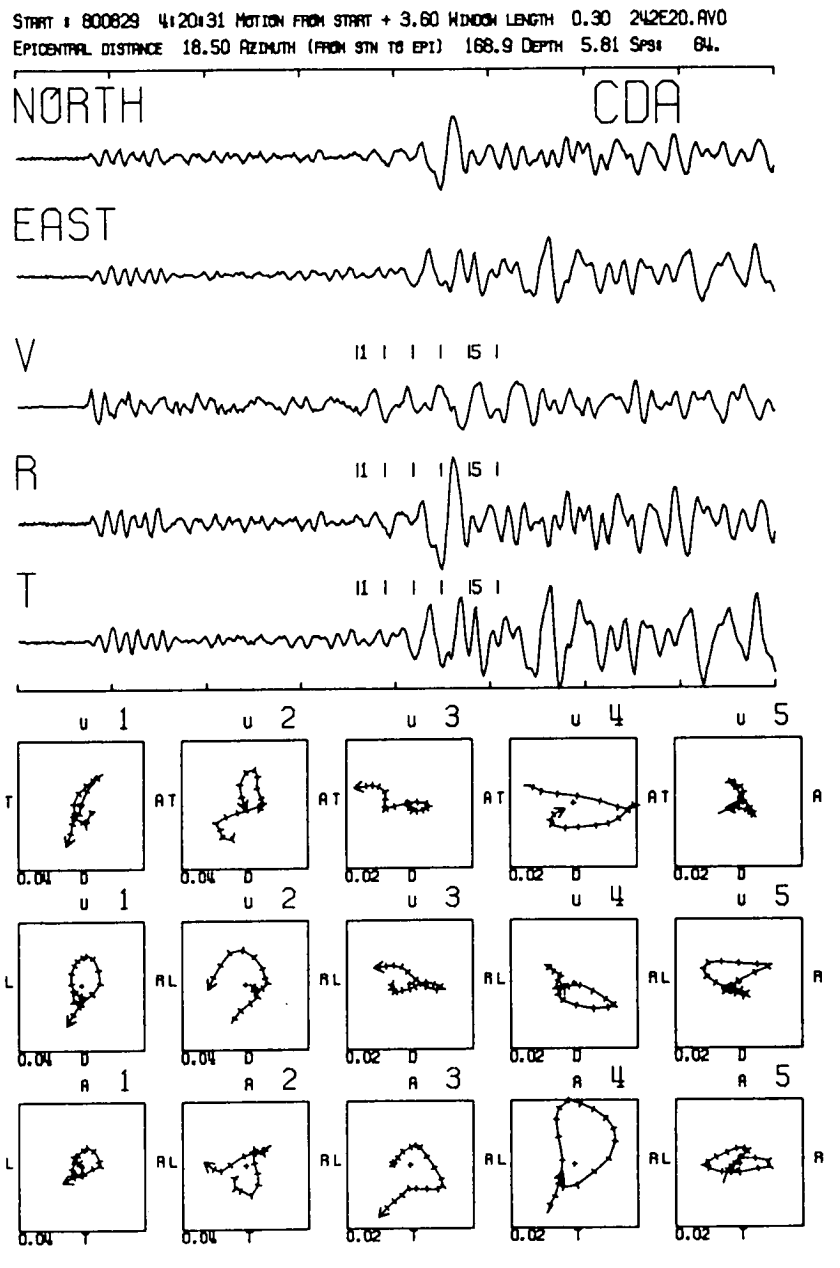
START = 800829 4:20:31 MOTION FROM START + 3.60 WINDOW LENGTH 0.30 242E20.AVO
EPICENTRAL DISTANCE 18.50 AZIMUTH (FROM STN TO EPI) 168.9 DEPTH 5.81 SPS= 64.
NORTH
CDA
EAST
V
R
T
U 1
U 2
U 3
U 4
U 5
A 1
A 2
A 3
A 4
A 5
0.04
0.02

Figure 6.5g

Figure 6.6

A three-component seismogram and polarization diagrams for an event from the Livermore Valley recorded on 28 November 1980, with epicentre 37° 37.89'N, 121° 42.60'W, and a depth of 6.93 km. The seismogram was recorded at station CPN at an epicentral distance of 13.55 km, and at an azimuth of N 279°E from the epicentre. Notation and format as in Figure 6.4. The heavy arrow in the horizontal polarization diagram indicates a possible SP-phase arrival.

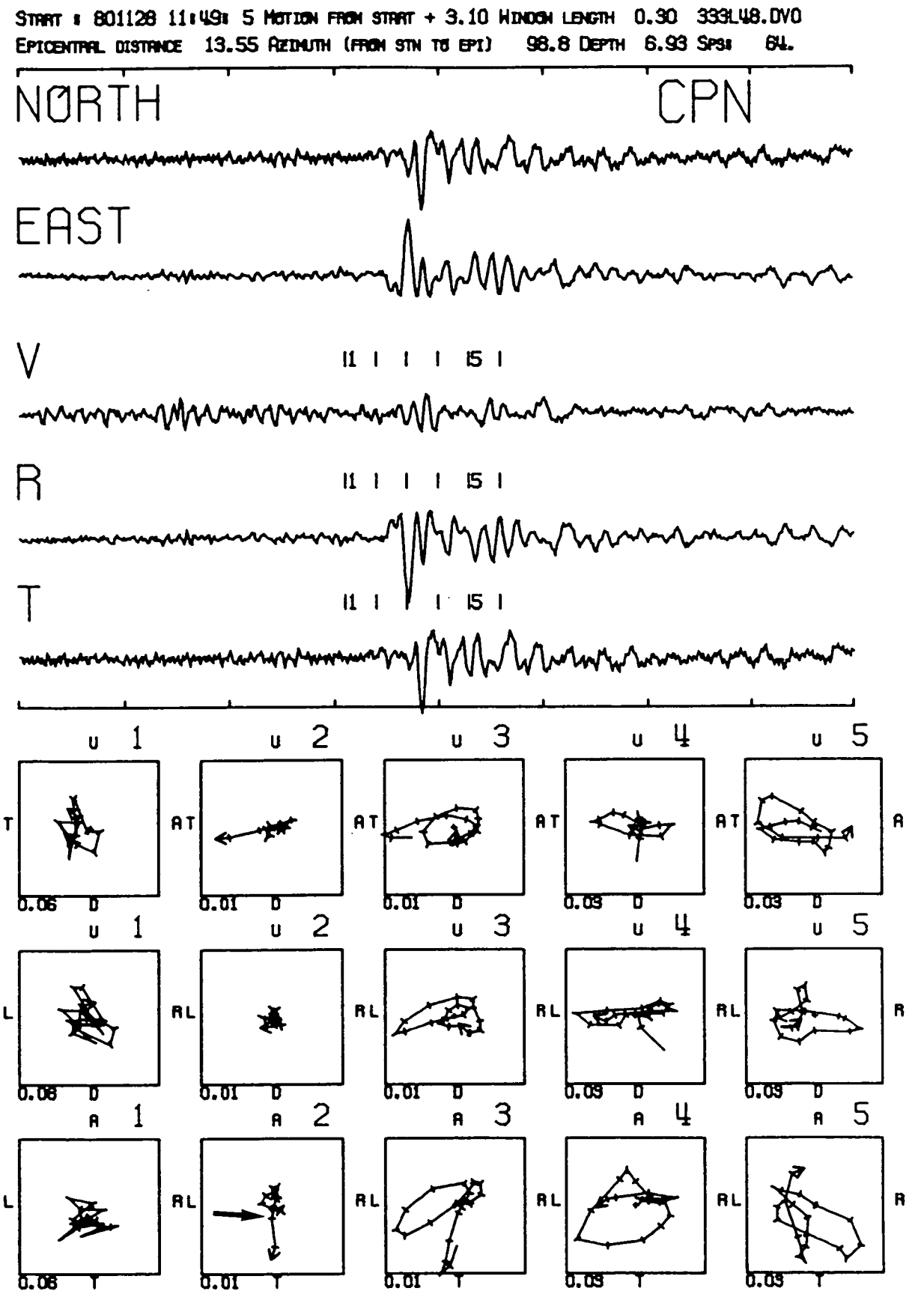
START : 801128 11:49: 5 MOTION FROM START + 3.10 WINDOW LENGTH 0.30 333L48.DVO
EPICENTRAL DISTANCE 13.55 AZIMUTH (FROM STN TO EPI) 98.8 DEPTH 6.93 SPS: 64.
NORTH
CPN
EAST
V
R
T
U 1
U 2
U 3
U 4
U 5
A 1
A 2
A 3
A 4
A 5
0.06
0.01
0.03

Figure 6.6

wave arrival is emergent and the shear-wave coda is more than 4 seconds long - similar to the seismogram at CDA for the Greenville group event. In addition a seismogram of another LWG event at an epicentral distance of 13.55 km and depth of 6.93 km is included in Figure 6.6 as it shows a possible SP-phase arrival - a radially polarized precursor to the direct shear-wave.

In general shear-wave frequencies are often about 5 Hz which gives a seismic wavelength in the order of 0.5 km for a shear-wave velocity of 2.25 km/sec. The reverberative nature of most seismograms is indicative of the generation of a suite of phases. This is not unexpected since the surface geological expression shows many faults, and a range of rock types, with varying seismic velocities, in a relatively small area. Symmetric pulses, probably converted phases, are observed on the vertical-component of several records, most notably at station CSA. Also the observation of early radial arrivals to the shear-wave on many seismograms outside the shear-wave window at stations CMN, CSA, CPS, CVL, and CPN suggest that the SP-phase may be predominant in this region.

A notable difference between the seismograms of the Greenville and LWG event is that seismograms of the Greenville event retain high frequencies at distant stations whereas those of the LWG event do not. A comparison of seismograms at CPN and CVL for both events in Figures 6.4de and 6.5ef clearly illustrates this point. It can be explained since, in general, attenuation of seismic energy decreases with depth. Consequently the ray path of the shallower LWG event travels in the more attenuative upper layers, and so lower frequency seismograms tend to be produced.

6.5.1 Extension of the shear-wave window

One feature characteristic of the seismograms in Figures 6.4, 6.5, and 6.6 is the lack of vertical excitation upon the arrival of the shear-wave. This

suggests that the ray path of the direct shear-wave is either steeply refracted until it is almost vertical, or, that the shear-wave first arrival is a head wave from interfaces below the source. In either case it is important to note that the particle motion of the shear-wave, regardless of epicentral distance, is not likely to be modified by free surface interaction because the local angle of incidence is less than the critical angle. Therefore the incident angle is not particularly sensitive to epicentral distance and depth, so seismograms recorded outside the shear-wave window (as defined in chapter two) can be included in the shear-wave particle motion analysis. Steeply refracted ray paths may be expected in a region which comprises of low velocity sediments overlying a higher velocity basement.

The epicentral maps and cross-sections in Figures 6.2 and 6.3 indicate that for each event only one or two seismograms are recorded within the shear-wave window. Therefore inclusion of seismograms outside the shear-wave window results in a fourfold increase in the amount of data available for shear-wave polarization analysis. In addition the shear-wave arrival and particle motion is often clearer on seismograms outside the shear-wave window than those within. For example Figure 6.7 shows seismograms and polarization diagrams from two events recorded at station CDV. The epicentral distances are 0.39 km and 1.7 km for depths of 6.79 km and 5.00 km respectively, so the events are well within the shear-wave window. The shear-wave onset is difficult to determine amid the signal noise and the shear-wave particle motion is complex. The same applies for the seismogram at CDA in Figure 6.4a which is recorded within the shear-wave window. In contrast, the shear-wave arrivals at CMN and CSA, from events outside the shear-wave window, in Figures 6.4bc and 6.5bc are often impulsive with linear particle motion.

Consequently shear-wave polarizations must be plotted on equal-area

Figure 6.7

Three-component seismograms for two events from the Livermore Valley recorded at station CDV at epicentral distances of 0.39 km and 1.71 km. Notation and format as in Figure 6.4 except time between cross bars is 0.0078125 seconds (128 sps). These seismograms indicate difficulties in determining the direction of the shear-wave onset at CDV.

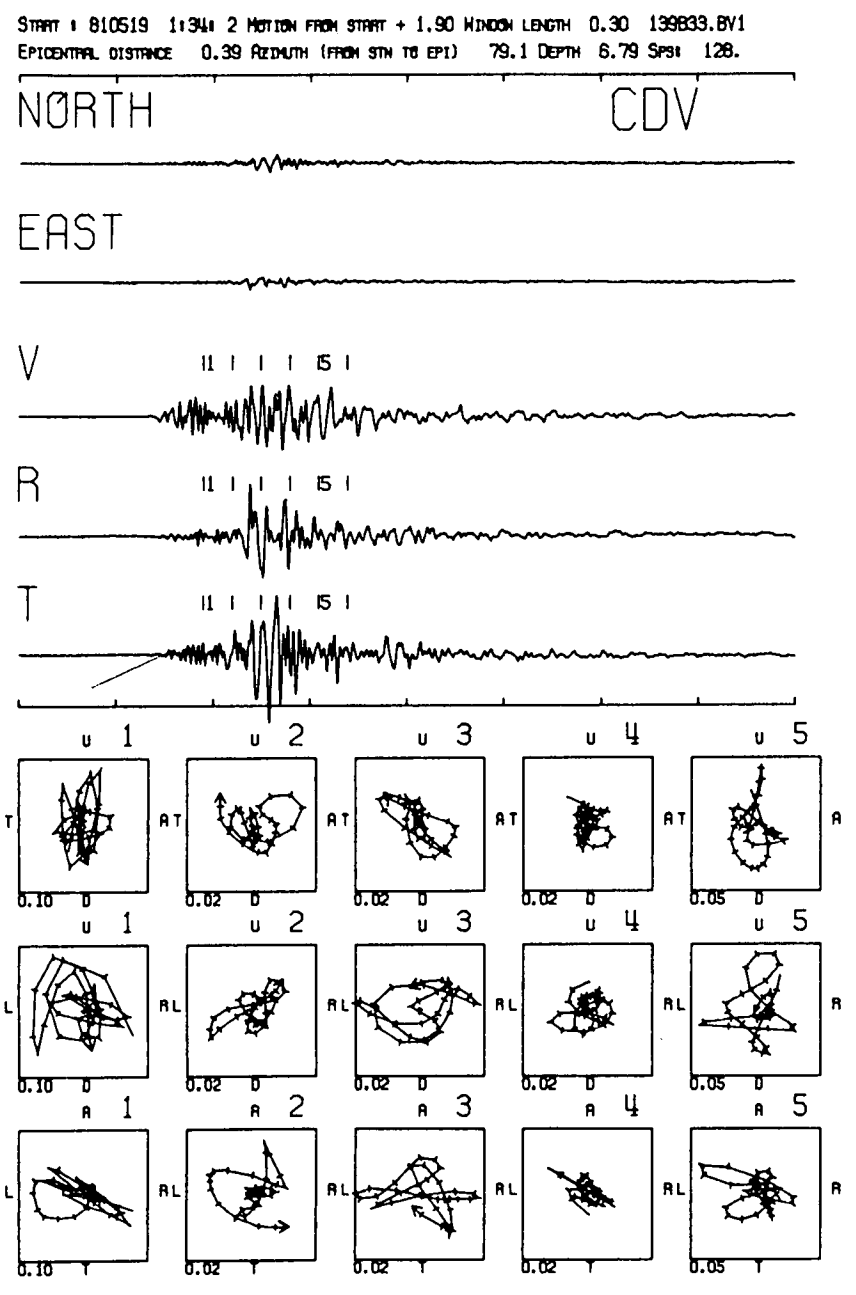

Figure 6.7a

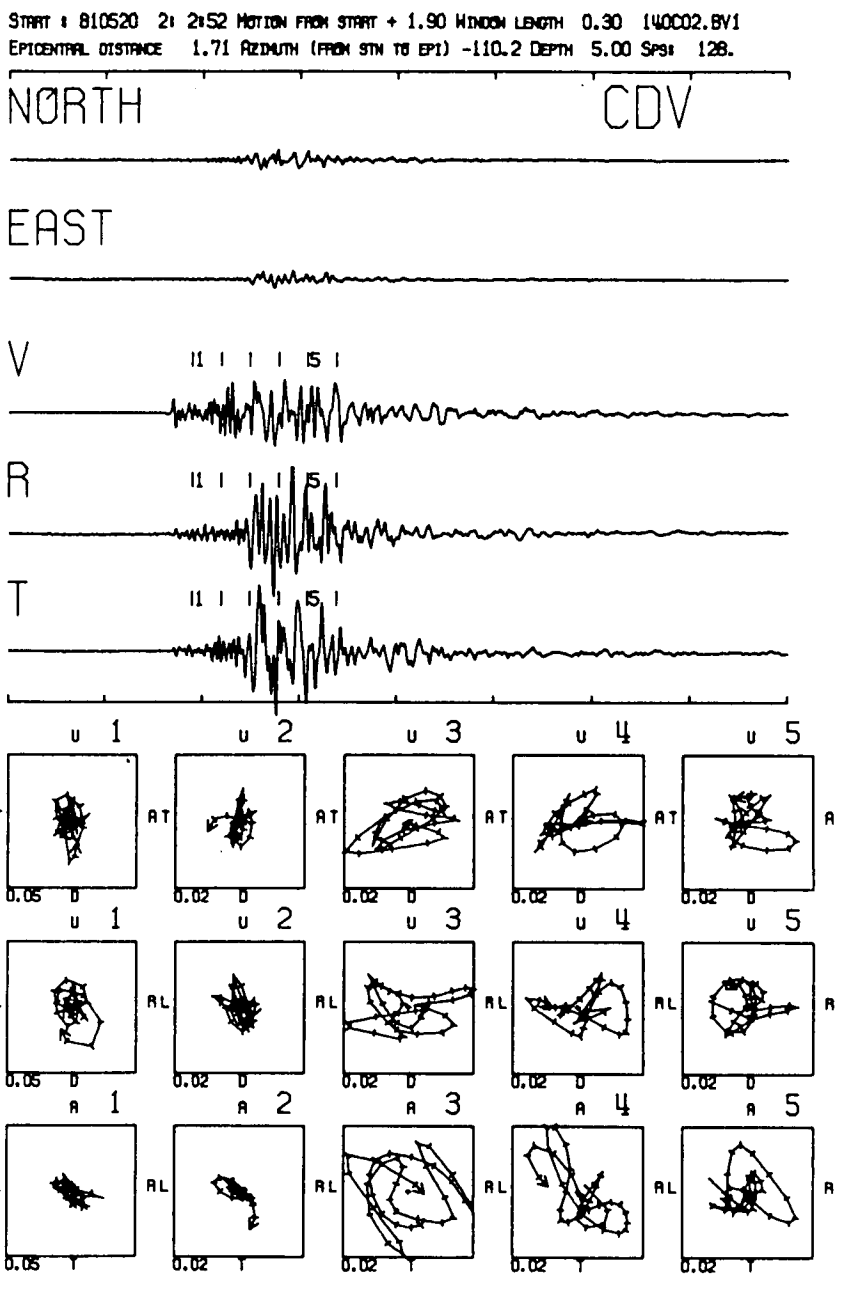

Figure 6.7b

projections based on the incidence angles of curved ray paths propagating through a subsurface velocity structure to each station instead of the simple formula previously used ($i=\tan^{-1}e/d$, where i is the incidence angle, e is the epicentral distance, and d is the depth). This is possible for the Livermore data set as much effort has been put into the development of the velocity model of the Livermore Valley (Taylor & Scheimer 1982). A ray tracing computer program is written to determine take-off and incidence angles of direct and head shear-waves propagating through the shear-wave velocity model of the Livermore Valley area for a given epicentral distance and depth. It also determined whether the shear-wave first arrival is a head or direct wave. The shear-wave velocity model is determined from the average P-wave velocity model of Taylor & Scheimer (1982) with Vp/Vs=1.78 (see Table 6.3). The results show that most shear-wave arrivals from events in both zones are steeply refracted direct rays. Head waves are only observed as first arrivals at large epicentral distances. For example head waves are the first arriving shear-wave beyond epicentral distances of 21.4 km and 51.8 km for source depths of 5 km and 10 km respectively, and are not detected until epicentral distances of 15.8 km and 30.8 km for these depths. However when head waves are generated they will interfere with the direct shear-wave arrival and, if their amplitude is large, modify the shear-wave particle motion of the direct ray. Therefore shear-wave polarization measurements at large epicentral distances must be treated with caution.

6.5.2 Orientation of the shear-wave polarizations

Where possible estimates of the shear-wave polarization directions are made for all earthquakes. The shear-wave polarization angle is measured with respect to the 'away' radial direction in polarization diagrams which are rotated into a radial/transverse coordinate system. The value is then added to

Table 6.3 Livermore average velocity model (Scheimer pers. comm. (1983). Vp/Vs is 1.78.

P-wave velocity (km/sec)	Depth to upper interface (km)
3.4	0.0
4.0	1.0
4.6	2.0
4.8	3.0
5.0	4.0
5.1	5.0
5.3	6.0
5.6	7.0
5.9	12.0
6.2	17.0
8.0	25.0

the azimuth of the station with respect to the earthquake to give the shear-wave polarization angle with respect to geographic north. In this way subjective bias is reduced (Booth et al. 1984). The direction of the first motion is often uncertain because of signal noise interference with the shear-wave arrival. Therefore the polarity of the shear-wave first motion is not discussed in this study.

Figures 6.8 and 6.9 show equal-area projections out to incidence angles of 90° of shear-wave polarizations, along with histograms illustrating the azimuthal distribution of the shear-wave polarization angles, at eight stations for events from the Greenville and LWG zones respectively. Here the velocity structure is not taken into account and polarizations are plotted on the projections as in chapters three, four, and five, with the direct ray path assumed to be linear. This demonstrates that a large number of shear-wave polarizations plot outside the shear-wave window, defined by an inner circle of 40° incidence angle, in both Figures 6.8 and 6.9 when the subsurface velocity structure is not considered. Station CDA for the Greenville group events and CDV for the LWG group events are the only exceptions, with most shear-wave polarizations at these stations falling within the 40° incidence angle circle.

However, upon consideration of the velocity structure at depth the ray paths become curved, and most shear-wave polarizations plot within the 40° incidence angle inner circle as shown in Figures 6.10 and 6.11. This illustrates the importance of a well defined velocity structure for determining the size of the shear-wave window in terms of the epicentral distance to a given station in areas where the subsurface velocity is known to vary considerably. Upon taking the velocity structure into account events which appear outside the shear-wave window may be shifted within.

Figures 6.10 and 6.11 indicate that distinct parallel alignments of the shear-wave polarizations are observed at stations CMN, CSA, and CDA, with weaker

Figure 6.8
Shear-wave polarizations from Greenville zone events measured at the three-component stations - CMN, CPS, CDA, CDV, CVA, CVL, and CPN. The polarizations at each station are displayed on lower equal-area projections (out to 90° incidence angle) and histograms. The inner circle on each projection defines the shear-wave window at an incidence angle of 40°.

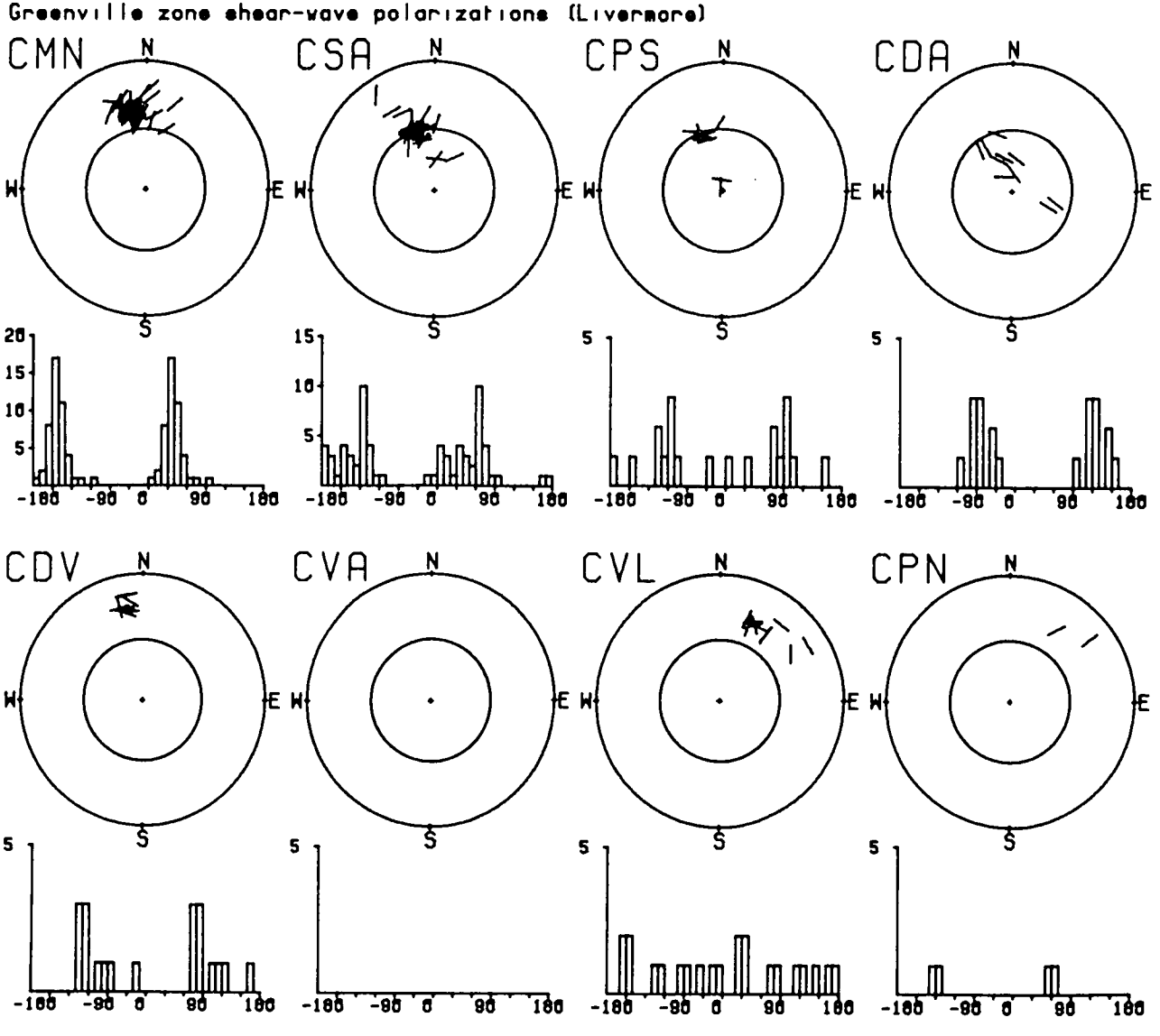
Greenville zone shear-wave polarizations (Livermore)
CMN
CSA
CPS
CDA
CDV
CVA
CVL
CPN
N
S
E
W
-180
-90
0
90
180

Figure 6.8

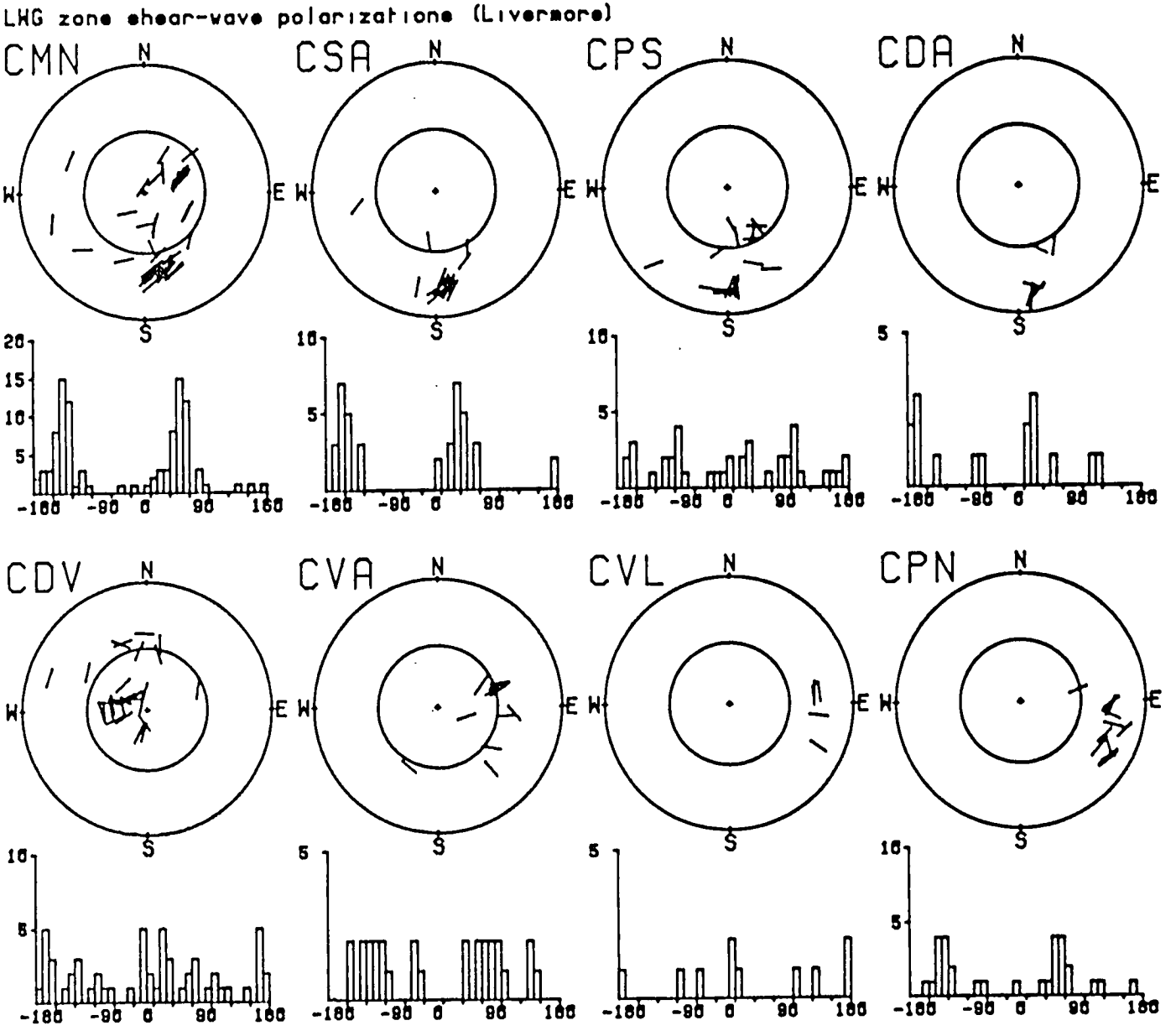
LHG zone shear-wave polarizations (Livermore)
CMN
CSA
CPS
CDA
CDV
CVA
CVL
CPN
N
S
E
W
-180
-90
0
90
180

Figure 6.9

Figure 6.10
Shear-wave polarizations from Greenville zone events displayed on lower equal-area projections as in Figure 5.8. Position of each polarization is a function of azimuth and incident angle when the ray path is curved by the subsurface velocity structure.

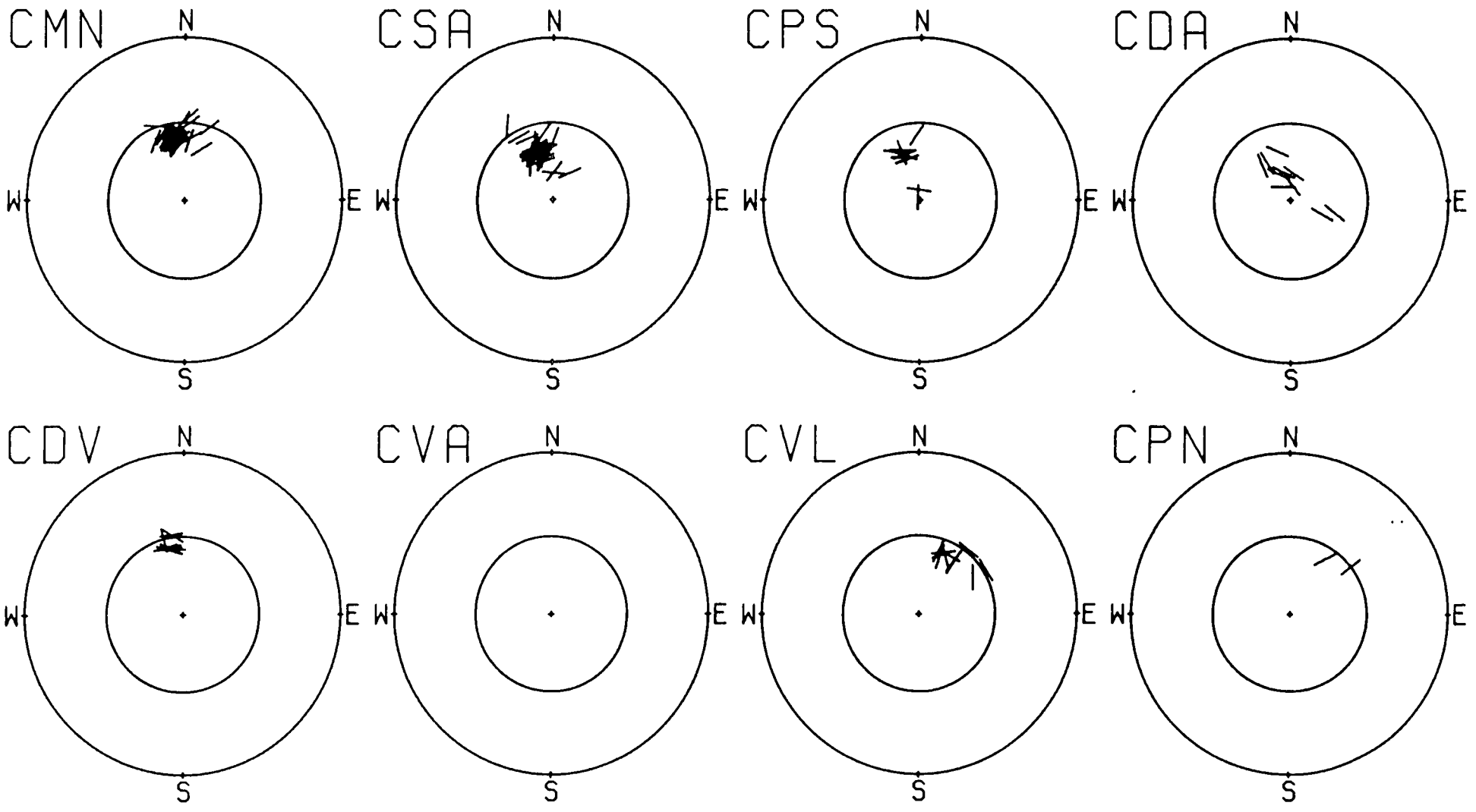
Greenville zone shear-wave polarizations (Livermore)
CMN
CSA
CPS
CDA
CDV
CVA
CVL
CPN
N
S
E
W

Figure 6.10

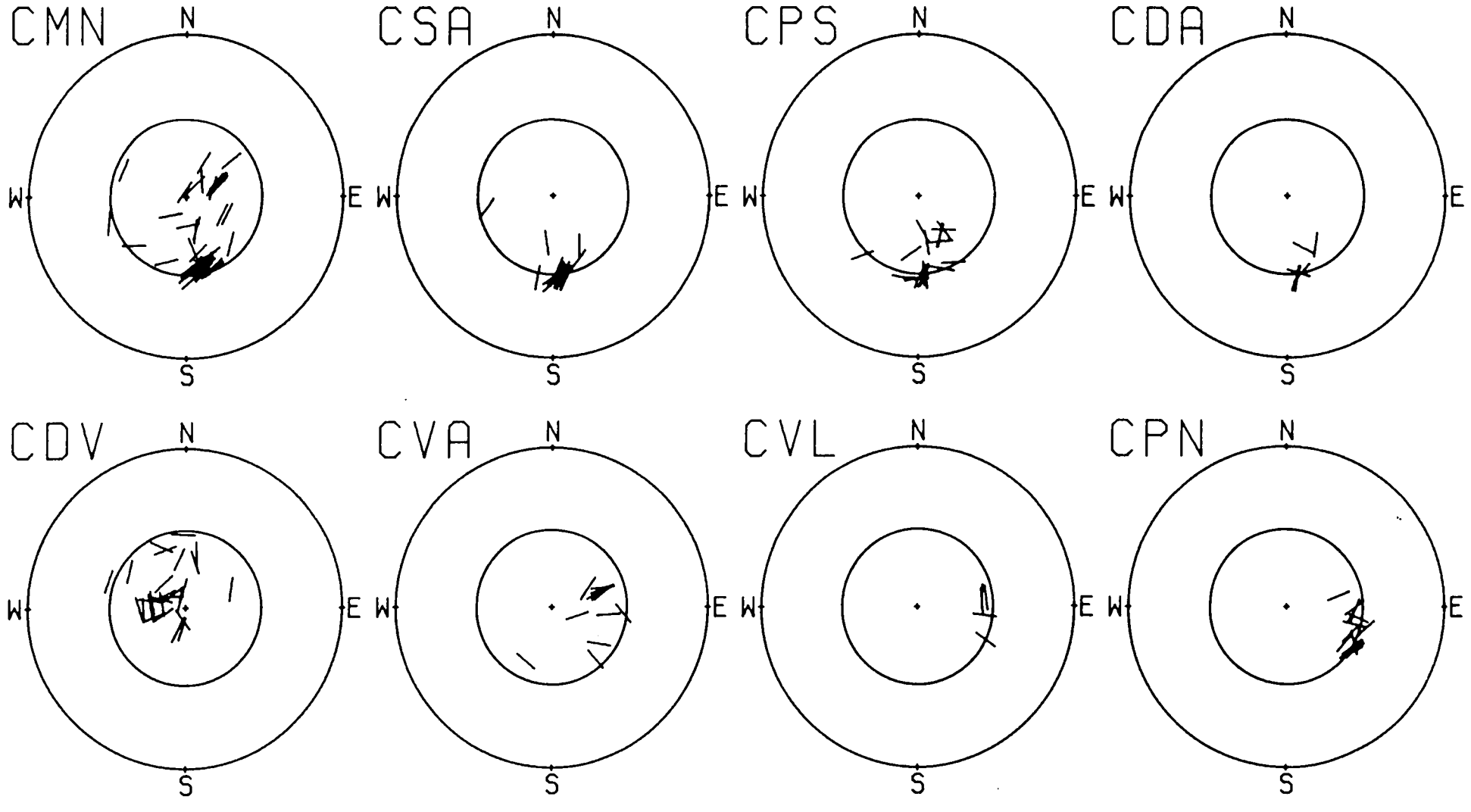
LWG zone shear-wave polarizations (Livermore)
CMN
CSA
CPS
CDA
CDV
CVA
CVL
CPN
N
S
E
W

Figure 6.11

alignments occurring at CVA and CPN. Firstly consider the shear-wave polarizations of events from the Greenville zone shown in Figure 6.10. With the exception of station CDA the shear-wave polarizations cluster in the northern section of each equal-area projection. This is because the Greenville group event hypocentres occupy a small zone to the north of the network. The alignment of shear-wave polarizations at CMN is clearly illustrated in the equal-area projection and in the histogram of shear-wave polarization angles which peaks sharply in the range N 40°E to N 50°E (see Figure 6.8). The shear-wave polarizations at CSA appear slightly more dispersed in the equal-area projection, but an alignment at about N 65°E is clearly indicated in the corresponding histogram (see Figure 6.8). However at CDA the shear-wave polarizations align at approximately right angles to those at CMN and CSA, with the histogram of shear-wave polarization angles in Figure 6.8 peaking at N 120°E. Reliable measurements of the shear-wave polarization angle at the other stations are sparse. No measurements are recorded at CVA and only two are made at CPN, primarily because of the reverberative nature of the seismograms at both these stations.

The distribution of shear-wave polarizations from events in the LWG zone is shown in Figure 6.11. The epicentral maps in Figures 6.2 and 6.3 indicate that the LWG epicentral locations are more dispersed than the Greenville epicentres. Therefore there is better azimuthal coverage of the equal-area projections by the shear-wave polarization pattern of the LWG events than the Greenville events. Distinct alignments of shear-wave polarizations are observed at stations CMN - histogram peak at N 45°E - and CSA - histogram peak at N 25°E - with weaker alignments in a similar direction at CPN and CVA. The shear-wave polarizations at CDV and CPS are scattered with no overall alignment, and there are only a few measurements at the other stations CVL and CDA. Difficulty in recognising the first motion of the shear-

wave because of signal noise between P-wave and shear-wave arrivals may, to some extent, explain the almost random patterns of shear-wave polarizations at stations CDV and CPS. This problem is illustrated by the seismograms at CDV in Figure 6.7.

To summarise, at stations CMN and CSA the shear-wave polarizations align in an approximate northeast-southwest direction for events from both the Greenville and LWG zones. Weaker alignments, also in a northeast-southwest direction, are observed at CPN and CVA. However a northwest-southeast alignment of shear-wave polarizations is observed at CDA for events from the Greenville zone. The shear-wave polarizations at CDV, CPS, and CVL appear to be orientated randomly. A combined composite equal-area projection and histogram of polarizations from both zones is shown in Figure 6.12. Almost all the shear-wave polarizations plot within the shear-wave window, and the histogram peaks in the range N 30°E to N 40°E, suggesting a shear-wave polarization alignment in this direction.

6.5.3 Time delays

Signal noise, which often obscured the exact arrival time of the shear-wave, and the complexity of the subsequent shear-wave particle motion usually made the measurement of time delays difficult. Therefore measurements of the time delay between split shear-waves are sparse and no coherent spatial or temporal pattern develops.

6.6 Comparison of observed and predicted shear-wave polarizations

This section presents a comparison between observed shear-wave polarizations and those predicted from fault plane solutions. As in chapter five, far-field radiation patterns of the horizontal shear-wave polarization are generated. However, in this case, we do not determine fault plane solutions for

Figure 6.12
All the shear-wave polarizations measured from the Livermore events displayed on a single lower equal-area projection and histogram. Ray path is dependant on velocity structure.

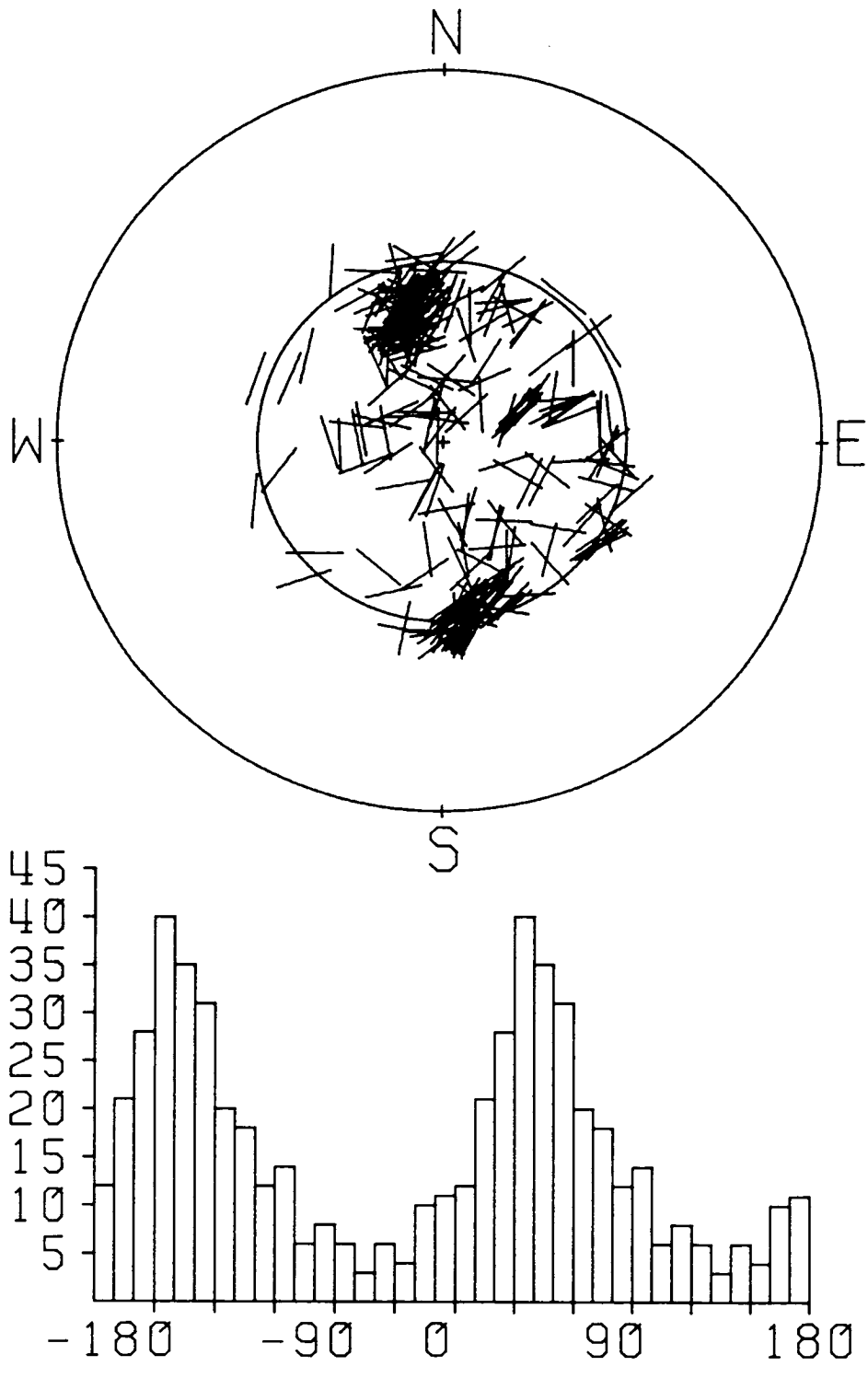

Figure 6.12

the selected events. Instead, the results from focal mechanism studies in the Livermore Valley area (Bolt et al. 1981; Follow ill & Mills 1982) are used . Hence it is assumed that source mechanisms in the valley area have remained relatively stable throughout the last few years. The work of Cockerham et al. (1980) and others indicates this to be likely. Follow ill & Mills (1982) have shown that right-lateral strike-slip predominates in the Greenville zone, with a mixture of strike-slip and thrust mechanisms in the LWG zone.

Two shear-wave radiation patterns are shown in Figure 6.13. The upper is right-lateral strike-slip faulting on a vertical plane striking N 165°E. Such faulting corresponds to the source mechanism of the January 1980 main shock (Bolt et al. 1981) along the northern extension of the Greenville fault. The lower diagram shows horizontal shear-wave polarizations from thrusting on a plane dipping at 70° and striking N 105°E. This mechanism has been extracted from Follow ill & Mills (1982) study on focal mechanisms. Both radiation patterns illustrate the shear-wave polarizations observed at a receiver from a uniform distribution of the appropriate source mechanism, and are compared to the observed patterns of polarizations. The strike-slip mechanism is characteristic of focal mechanisms in both the Greenville and LWG zones, whereas thrusting only occurs within the LWG zone. The observed shear-wave polarizations for the Greenville and LWG zones are shown in Figures 6.14 and 6.15 respectively. Note that they are plotted on the equal-area projection as a function of azimuth and take-off angle (assuming the velocity structure in Table 6.3). Therefore the effect of the curved ray path is removed, and observed (Figures 6.14 and 6.15) and predicted (Figure 6.13) can be compared at appropriate azimuths and incident angles for each station.

The alignment of shear-wave polarizations at stations CMN, CSA, CPS, CDA, and CDV of the Greenville events in Figure 6.14 and at station CPN of the LWG events in Figure 6.15 correlate reasonably well with the predicted

polarizations from a strike-slip source. The radiation pattern from the thrust mechanism is only compared to the LWG zone polarizations in Figure 6.15, and little correlation emerges. Hence the comparison between observed and predicted reveals some correlation for strike-slip faulting, but little correlation is apparent for thrusting.

6.7 Discussion

The orientation of the shear-wave polarizations from Livermore are much more diverse and scattered than those recorded at the HDR site, Cornwall, and in northern Turkey (Booth et al. 1984) - both areas where the shear-wave polarization distribution can be explained by the presence of crack structures aligned by the prevailing stresses. However there is some evidence of a northeast-southwest alignment of shear-wave polarizations, particularly at stations CMN and CSA (see Figures 6.10, 6.11, and 6.12). The orientation of the alignment is approximately parallel to the strike of many faults in the area and to the directions of the axis of maximum compressive stress derived from fault plane solutions of microearthquakes, recorded in the Livermore Valley over an eight month period in 1980 (Follow ill & Mills 1982). This observation is similar to observations made in Cornwall where the shear-wave polarizations align approximately parallel to the strikes of joints and the compressive stress axis. Therefore the aligned crack structures which have been suggested as an explanation of the Cornish observations may be present in the crust at Livermore.

There are some observations to suggest the presence of open cracks within the crust in the Livermore Valley area. Stierman et al. (1979) report on the presence of macrocracks within the upper few kilometres of the crust in the Gabilan Range, part of the Central Coast Ranges about 200 km south of Livermore. Here the P-wave velocity increases with depth more slowly than

Figure 6.13
Horizontal shear-wave polarizations from a strike-slip focal mechanism (after Bolt et al. 1981), and a thrust focal mechanism (after Followhill & Mills 1982). These mechanisms are representative of source mechanisms in the Livermore Valley area. Polarizations are plotted on a lower equal-area projection centred at the receiver for a uniform distribution of the source mechanism.

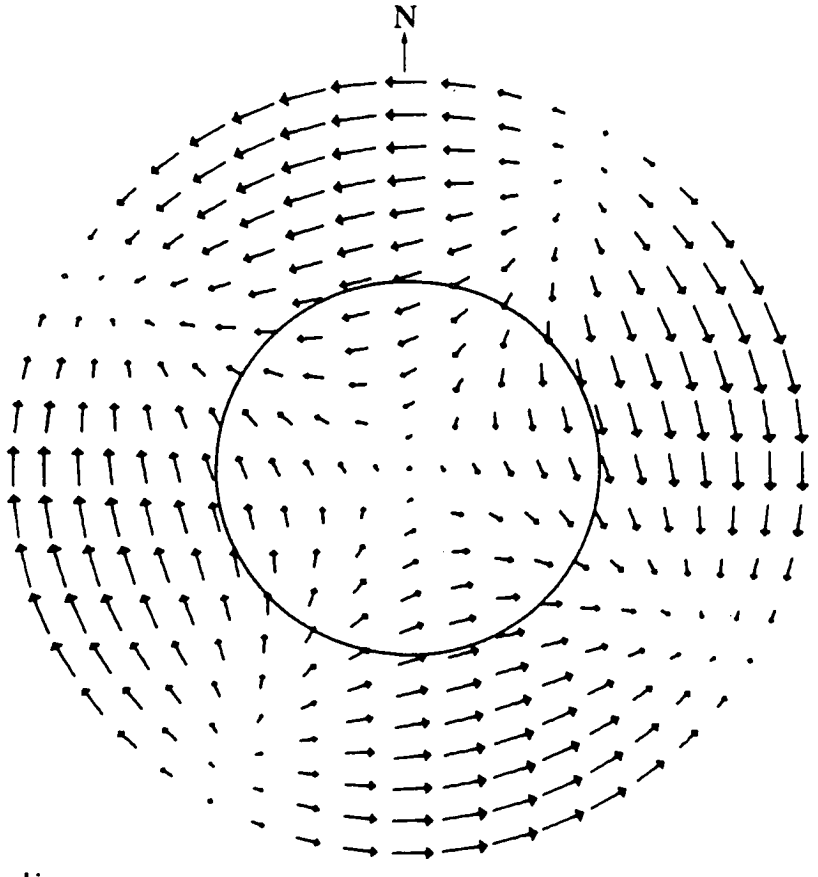

Strike-slip

Figure 6.13a

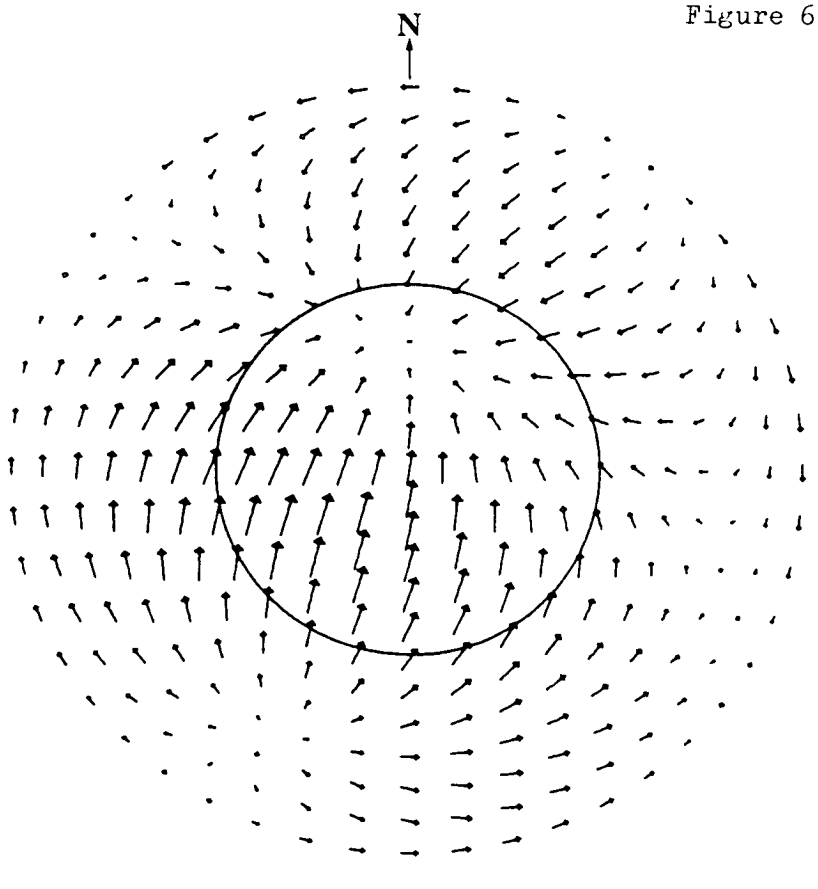

Thrust

Figure 6.13b

Figure 6.14
Greenville zone shear-wave polarizations displayed on lower equal-area projections centred on the receiver. Position of each polarization is a function of azimuth and take-off angle to allow direct comparison of observations with Figure 6.13.

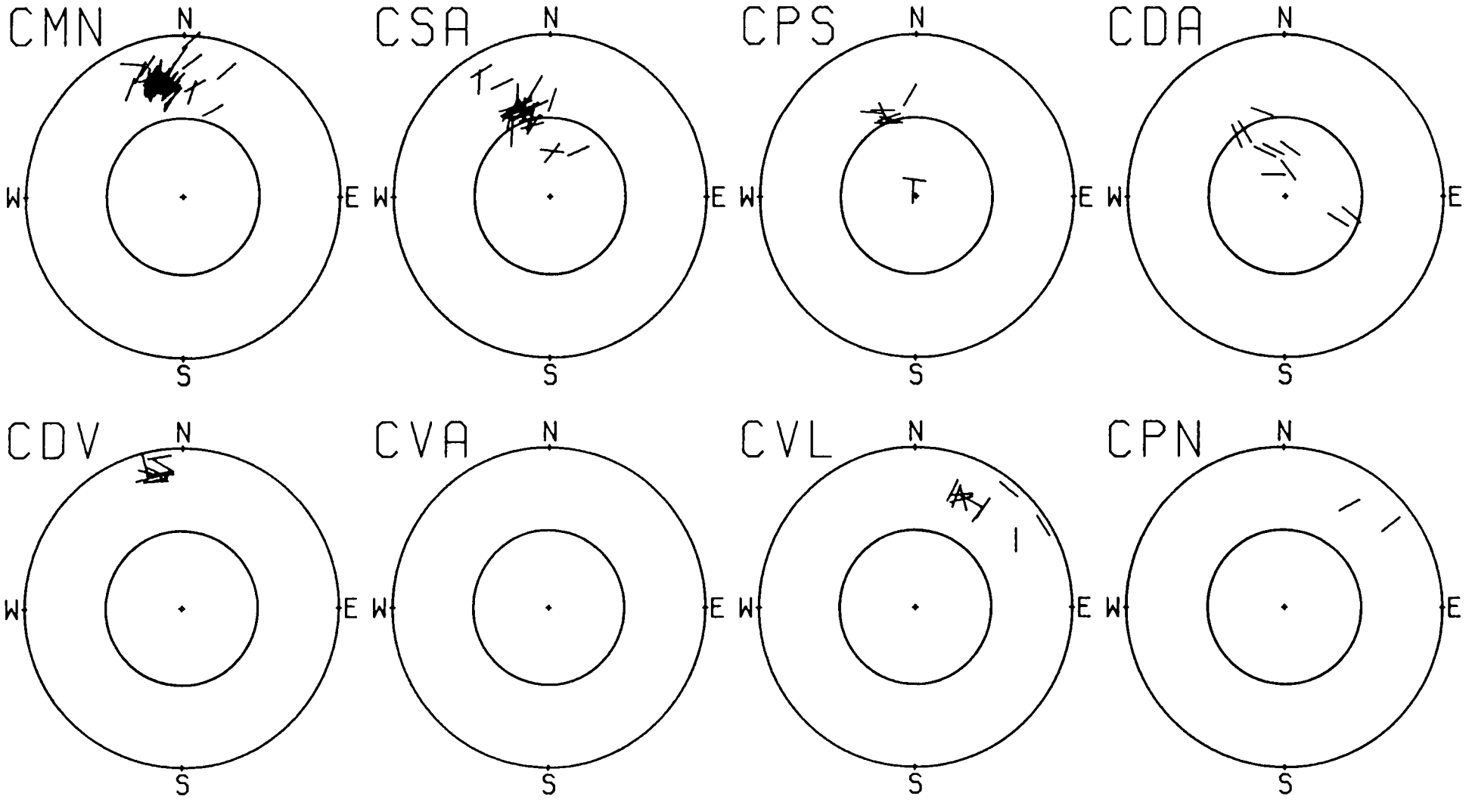
Greenville zone shear-wave polarizations (Livermore)
CMN
CSA
CPS
CDA
CDV
CVA
CVL
CPN
N
S
E
W

Figure 6.14

Figure 6.15
LWG zone shear-wave polarizations displayed on lower equal-area projections centred on the receiver. Notation and format as in Figure 6.14 to allow direct comparison of observed and predicted polarizations in Figure 6.13.

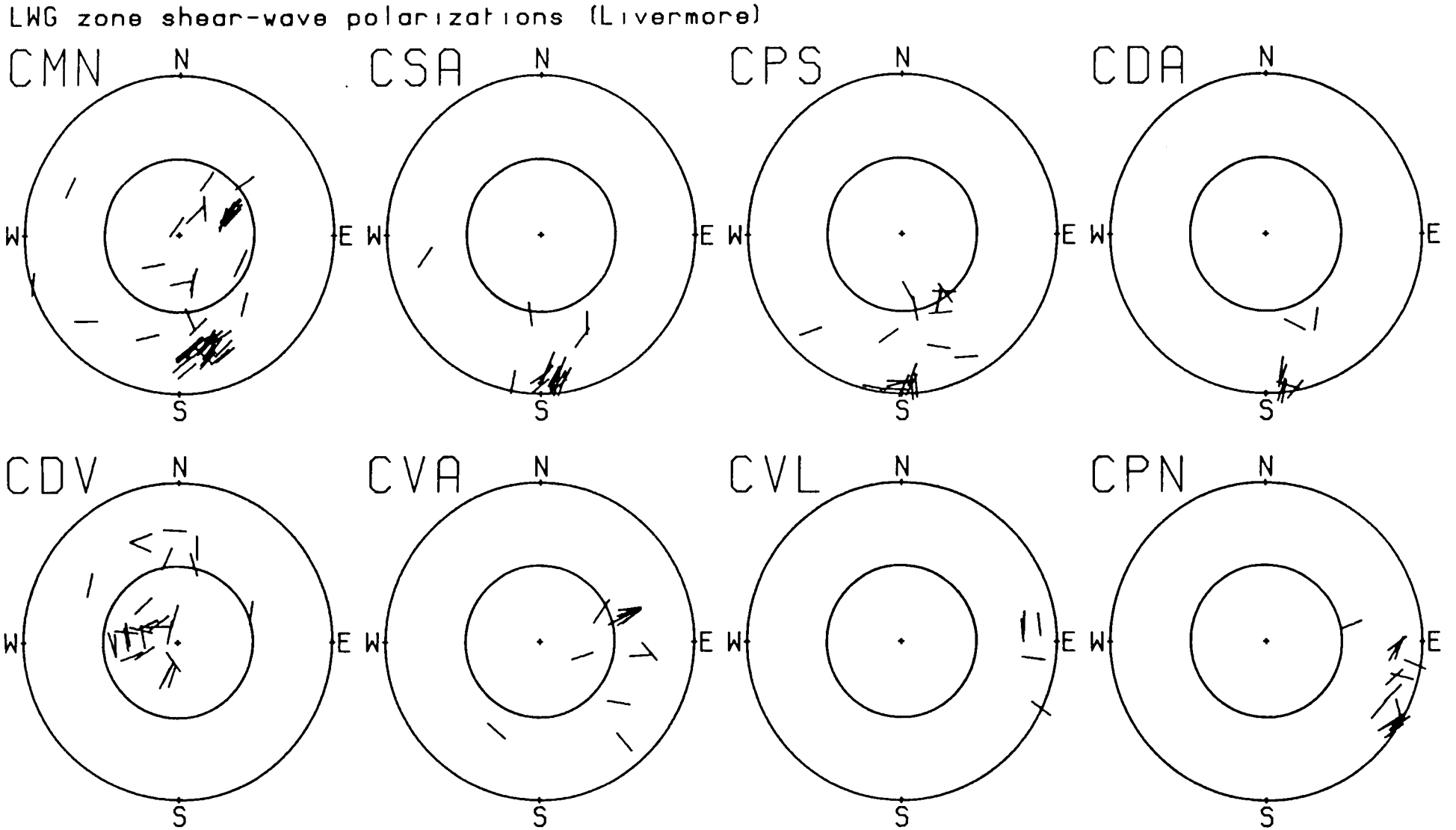
LWG zone shear-wave polarizations (Livermore)
CMN
CSA
CPS
CDA
CDV
CVA
CVL
CPN
N
S
E
W

Figure 6.15

predicted by laboratory experiments at crustal temperatures and pressures (Nur & Simmons 1969; Stierman 1976). This led Stierman et al. (1979) to conclude that macrocracks are not so easily closed as extrapolation of laboratory data suggests, and so remain open at depths of about 5 km. The P-wave velocity structure of the Livermore Valley is similar to that in the Central Coast Ranges (Taylor & Scheimer 1982), therefore it is likely that macrocracks and microcracks remain open in the upper crust at Livermore also. According to the hypothesis of Extended Dilatancy Anisotropy (Crampin et al. 1984b) the action of a deviatoric stress field will align the cracks, and provided the magnitudes of the maximum, intermediate, and minimum principal stresses satisfy $\sigma_1 > \sigma_2 >> \sigma_3$ a vertical parallel crack structure of circular penny shaped cracks would develop.

I suggest that the orientations of the shear-wave polarizations at the Livermore Valley can be explained qualitatively in terms of two co-existing models: a crack model controlled by in situ stress, and a geological model encompassing the subsurface geological structure. The crack model is responsible for the alignment of shear-wave polarizations at about N 35°E - most clearly observed at CMN and CSA. The random alignments of shear-wave polarizations and highly reverberative seismograms at stations CDV, CPS, and CVL are probably a result of wave propagation through a heterogeneous and complex geological structure. There is much evidence for a laterally heterogeneous geological structure in the Livermore Valley area: basement structural relief; varied topography; significant differences in the seismic section in and around the valley, and the wide variation in the station corrections used in hypocentral location (Follow i l & Mills 1982). At stations CDV, CPS, and CVL the interference of converted phases or multiple reflections with the direct shear-wave arrival would mask the effects due to the crack model. Therefore it is only when the shear-wave is recorded free

from interference of other phases that shear-wave polarization alignments emerge.

Further work is required to clarify the above interpretation since the one hundred and thirty events studied here is only a small subset of the total number of events located in the Livermore Valley area (over 3000). An opportunity is available at Livermore to initiate a extensive study of shear-wave polarizations. It is one of the few places operating a permanent three-component seismic network enabling a selection of good quality seismic records over a large time span for shear-wave studies.

6.8 Conclusions

One hundred and thirty events were selected from over 3000 events located in the Livermore Valley area, California. Analysis of the shear-waves revealed some signs of effective anisotropy at depth. When the shear-wave was recorded free from interference of spurious phases, as at stations CMN and CSA, particle motion characteristic of shear-wave splitting was observed and shear-wave polarization alignments emerged. The alignments trended at about N 35^{o}E, approximately parallel to the direction of maximum compressive stress. However random shear-wave polarization alingments were observed at stations CDV, CVL, and CPN. The reverberative nature of seismograms at these stations suggested that other phases interfered with the direct shear-wave arrival. The orientations of shear-wave polarizations from typical sources in the valley region was similar to the observed polarizations at stations CMN, CSA, CPS, CDA, CDV, and CPN. The conclusion drawn from the study is that the pattern of shear-wave polarizations, and the shear-wave particle motion is probably derived from a combination of source effects, subsurface geological structure, and cracks - with no individual factor having overall influence. However more work is required to confirm this.

During analysis of this data set the shear-wave window was extended based on the subsurface seismic velocity structure. This enabled the inclusion of many events in shear-wave particle motion analysis, even although many were outwith the shear-wave window as it was defined in chapter two.

CHAPTER SEVEN

CONCLUSIONS AND FURTHER WORK

7.1 Conclusions

The objective of the dissertation was to identify and assess effective seismic anisotropy in the upper crust from the analysis of shear-wave particle motion. Shear-wave splitting is diagnostic of wave propagation in anisotropic media, and recent work (Crampin & McGonigle 1981; Crampin & Booth 1984) has suggested that effectively anisotropic crack structures may be mapped from the analysis of recorded shear-wavetrains. The shear-wave particle motion was quantified by measuring the horizontal shear-wave polarization, and by displaying the polarizations in equal-area projections of the focal sphere and histograms. The data consisted of three-component short period seismic records collected from three areas of local seismic activity - from Monticello in South Carolina, USA; from a Hot Dry Rock site, Cornwall in the UK, and from the Livermore Valley in California, USA. The conclusions of the study are presented here.

The first data set analysed was recorded at Monticello reservoir in South Carolina. The seismic activity was induced by the creation of the reservoir, and occurred at shallow depths of less than 3 km. The sharp changes in direction of particle motion characteristic of shear-wave splitting were observed on a few seismic records. However, the observation of transversely-polarized shear-waves from most events recorded outside the shear-wave window suggested that shear-wave interaction at the free surface masked any effects of anisotropy on the shear-waves. Also hypocentral location errors and an insufficient amount of data would have inhibited interpretation in terms of

an underlying crack structure.

The next data set analysed was recorded at the site of a Hot Dry Rock experiment in Cornwall, UK. The injection of water at high pressures into homogeneous granite induced low magnitude seismicity of less than M_L=0.1 between depths of 2 km and 3.5 km. The hydrofracture-induced acoustic events were generated by shearing along pre-existing fractures as opposed to jacking of the fracture plane. The most likely focal mechanism was left-lateral strike-slip on northwest-southeast trending subvertical fractures. A comparison of the observed and predicted shear-wave radiation from the focal mechanisms suggested that the medium influenced wave propagation sufficiently to modify the orientation of the shear-wave polarization from the source. The observation of shear-wave splitting, alignments of the orientation of the shear-wave polarizations, and patterns of time delays between the split shear-waves all consistent with wave propagation through a simple crack distribution estimated from in situ stresses was strongly supportive of an effectively anisotropic crack structure within the granite. A crack model of circular penny-shaped cracks with effective hexagonal symmetry modelled, with some success, the observed shear-wave polarization and time delay patterns.

The HDR study indicated that the shear-wave polarizations from acoustic events recorded outside the cracked HDR reservoir can be interpreted in terms of the crack geometry, the stress alignments, and the orientation of hydraulic fractures. Hence, of practical importance to future HDR projects it is important to note that the orientation of hydraulic fractures can be predicted from shear-wave polarizations through the rock prior to the commencement of hydraulic injections. Also, shear-wave particle motion from an event before the main phase of hydrofracturing and time delay values suggested that the effective anisotropy extends beyond the zone of

hydrofracturing. This supports the hypothesis of Extensive Dilatancy Anisotropy (Crampin et al. 1984b) which suggests that liquid-filled cracks are ubiquitous in the upper crust and are aligned by stress-induced processes to create effectively anisotropic zones within the upper crust. Consequently the monitoring of shear-waves to evaluate crack geometries and changes in crack geometries may be useful in earthquake prediction studies.

The final data set analysed was recorded in the Livermore Valley area in California. The seismic activity occurred at depths ranging between 5 km and 15 km, and is associated with plate movements along the San Andreas fault system. When the shear-wave was recorded free from interference particle motion characteristic of shear-wave splitting was observed, and shear-wave polarization alignments were observed also. The orientation of the shear-wave polarizations trended approximately parallel to the fault traces and to some focal mechanism estimates of the axis of maximum compressive stress in the area. This suggested that an aligned crack structure with similar symmetry and orientation to that at the HDR site may be present in the upper crust of the Livermore Valley area. However more observations are required for confirmation.

The study of the Livermore data set showed that the evaluation of crack structures in areas of natural seismic activity from the shear-waves can be difficult because of non-anisotropic effects affecting the shear-wave. In particular much seismic energy radiated by the microearthquakes was scattered by the medium which caused problems in identification of the shear-wave on many seismograms. To some extent this can be overcome if a large quantity of data is available. In which case there is usually enough good quality records for analysis.

7.2 Further Work

From quantification and interpretation of the shear-wave particle motion an estimation of the symmetry and orientation of an effectively anisotropic crack structure can be made. Since, until recently, little attention has been given to the observations of shear-wave polarizations and particle motion there is scope for further work.

Many numerical techniques for modelling crack structures have been developed. The recognition that crack distributions are effectively anisotropic to seismic waves means that numerical techniques for modelling anisotropic structures can be used for modelling crack structures. More computer programming for numerical modelling is always required, but the most productive avenue for further work lies in the recording and interpretation of observed shear-wavetrains, and in the development of field experiments designed to evaluate the symmetry and orientation of crack structures.

More use of three-component seismic stations, and the widespread deployment of three-component seismic networks is suggested as this would provide a large amount of data for shear-wave analysis. Also the analysis of seismic records from existing three-component networks is recommended. In particular the LLNL three-component seismic network in the Livermore Valley offers a significant quantity of data for shear-wave particle motion analysis, of which only a little has been analysed.

The use of artificial shear-wave sources, such as Vibroseis, is recommended when possible. In which case the form of the shear-wave input to the medium is defined and controllable. This avoids one of the main problems encountered in the study - the reliable determination of the shear-wave polarization orientation from the source.

The use of subsurface three-component geophones would overcome the problems associated with the shear-waves at the free surface. Field

experiments incorporating Vibroseis sources and downwell three-component geophones defines the characteristics of both the source and receiver. Therefore the effects of source and receiver can be identified and removed, and the seismogram can be interpretated in terms of wave propagation through the medium.

REFERENCES

Aki, K. & Richards, P.G., 1980. **Quantitative Seismology**, volumes I & II, W.H. Freeman and Company.

Aki, K., Fehler, M., Aamodt, R.L., Albright, J.N., Potter, R.M., Pearson, C.M. & Tester, J.W., 1982. Interpretation of seismic data from hydraulic fracturing experiments at Fenton Hill, New Mexico, Hot Dry Rock Geothermal Site, **J.geophys.Res.**, 87, 936-944.

Ando, M. & Ishikawa, Y., 1982. Observations of shear-wave velocity polarization anisotropy beneath Honshu, Japan: two masses with different polarizations in the upper mantle, **J.Phys.Earth**, 30, 191-199.

Atkinson, B.K., 1979. A fracture mechanics study of subcritical tensile cracking of quartz in wet enviroments, **Pure.appl.Geophys.**, 117, 1011-1024.

Backus, G.E., 1962. Long-wave elastic anisotropy produced by horizontal layering, **J.geophys.Res.**, 67, 4427-4440.

Bamford, D. & Nunn, K.R., 1976. In situ seismic measurements of crack anisotropy in the Carboniferous Limestone of north-west England, **Geophys.Pros.**, 27, 322-338.

Bezgodkov, V.A. & Yegorkina, G.V., 1984. Experimental study of the anisotropy of longitudinal and transverse wave velocities from local earthquake records, **Geophys.J.R.astr.Soc.**, 76, 179-189.

Bolt, B.A., McEvilly, T.V. & Uhrhammer, R.A., 1981. The Livermore Valley, California, sequence of January 1980, **Bull.seism.Soc.Am.**, 71, 451-463.

Bonilla, M.G., Lienkaemper, J.J. & Tinsley, J.C., 1980. Surface faulting near Livermore, California, associated with the January 1980 earthquakes, **USGS Open File Report** 80-523.

Booth, D.C. & Crampin, S., 1983. The anisotropic reflectivity technique: anomalous reflected arrivals from an anisotropic upper mantle, **Geophys.J.R.astr.Soc.**, 72, 767-782.

Booth, D.C., Crampin, S., Evans, J.R. & Roberts, G., 1984. Shear-wave polarizations near the North Anatolian Fault: I, evidence for anisotropy-induced shear-wave splitting, **Geophys.J.R.astr.Soc.**, submitted.

Bouchon, M., 1978. The importance of the surface or interface P-wave in near earthquake studies, **Bull.seism.Soc.Am.**, 68, 1293-1311.

Brace, W.F., 1980. Permeability of crystalline and argillaceous rocks, **Abstr.Int. J.Rock.Mech.Min.Sci.Geomech.**, 17, 241-251.

Brooks, M., Doody, J.J. & Al-Rawi, F.R.J., 1984. Major crustal reflectors beneath SW England, **J.geol.Soc.London**, 141, 97-103.

Carpenter, D.W., Sweeney, J.J., Kasameyer, P.W., Knauss, K.G. & Shlemon, R.J., 1982. Geology of the Lawrence Livermore National Laboratory Site and adjacent areas, **Lawrence Livermore National Laboratory UCRL Report** 53316.

Christensen, N.I., 1984. The magnitude, symmetry and origin of upper mantle anisotropy based on fabric analyses of ultramafic tectonites, **Geophys.J.R.astr. Soc.**, 76, 89-111.

Cockerham, R.S., Lester, F.W. & Ellsworth, W.L., 1980. A preliminary report on the Livermore Valley earthquake sequence 24 January - 26 February, 1980, **USGS Open File Report** 80-714.

Crampin, S., 1978. Seismic-wave propagation through a cracked solid: polarization as a possible dilatancy diagnostic, **Geophys.J.R.astr.Soc**, 53, 467-496.

Crampin, S., 1981. A review of wave motion in anisotropic and cracked elastic media, **Wave Motion**, 3, 343-391.

Crampin, S., 1983. Shear-wave polarizations: A plea for three-component recording to evaluate anisotropy, **Brit.Geol.Surv.Glob.Seism.intern.report**, No. 193.

Crampin, S., 1984. Effective anisotropic elastic constants for wave propagation through cracked solids, **Geophys.J.R.astr.Soc.**, 76, 135-145.

Crampin, S. & Booth, D.C., 1984. Shear-wave polarizations near the North Anatolian Fault: II, interpretation in terms of crack-induced anisotropy, **Geophys.J.R.astr.Soc.**, submitted.

Crampin, S., Chesnokov, E.M. & Hipkin, R.G., 1984a. Seismic anisotropy - the state of the art: II, **Geophys.J.R.astr.Soc.**, 76, 1-16.

Crampin, S., Evans, J.R & Atkinson, B.K., 1984b. Earthquake prediction: a new physical basis, **Geophys.J.R.astr.Soc.**, 76, 146-156.

Crampin, S., Evans J.R., Doyle, M. & Davis J.P., 1981. Comments on papers about shear-wave splitting in dilatancy-induced anisotropy by I.N. Gupta and by A. Ryall and W.U. Savage, **Bull.seism.Soc.Am.**, 71, 375-377.

Crampin, S., Evans, J.R., Üçer, S.B., Doyle, M., Davis, J.P., Yegorkina, G.V. & Miller, A., 1980. Observations of dilatancy-induced polarization-anomalies and earthquake prediction, **Nature**, 286, 874-877.

Crampin, S., Evans, J. & Üçer, S.B., 1984c. Analysis of records of local earthquakes: the Turkish Dilatancy Projects (TDP1 and TDP2), **Geophys.J.R.astr.Soc.**, in press.

Crampin, S. & McGonigle, R., 1981. The variation of delays in stress-induced anisotropic polarization anomalies, **Geophys.J.R.astr.Soc.**, 64, 115-131.

Crampin, S., Stephen,R.A. & McGonigle, R., 1982. The polarization of P-waves in anisotropic media, **Geophys.J.R.astr.Soc.**, 68, 477-485.

Dorman , L.M., 1972. Seismic crustal anisotropy in northern Georgia, **Bull.seism.Soc.Am.**, 62, 39-45.

Doornbos, D.J., 1981. Seismic moment tensors, **Identification of Seismic Sources - Earthquake or Underground Explosion**, Edited by Husebye, E.S. & Mykkeltveit, S., 207-232.

Ellsworth, W.L. & Marks, S.M., 1980. Seismicity of the Livermore Valley, California, region 1969-1979, **USGS Open File Report** 80-515.

Evans, A.C., 1981. 'Propagation and Dissipation of VHF Rayleigh Waves in Scotland', **Ph.D. Thesis, Univ. of Edinburgh.**

Evans, D.M., 1966. Man-made earthquakes in Denver, **Geotimes**, 10, 11-18.

Evans, J.R., 1980. ADC: a program for digitising seismic records into a format suitable for automatic processing, **Inst.Geol.Sci.Glob.Seism.intern.report**, No. 136.

Evans, J.R., 1984. Effects of the free surface on shear-wavetrains, **Geophys.J.R.astr.Soc.**, 76, 165-172.

Fehler, M., 1981. Changes in P-wave velocity during operation of a Hot Dry Rock Geothermal System, **J.geophys.Res.**, 86, 2925-2928.

Fletcher, J.B., 1982. A comparison between the tectonic stress measured in situ and stress parameters from induced seismicity at Monticello Reservoir, South Carolina, **J.geophys.Res.**, 87, 6931-6944.

Follow*ill*, F.E. & Mills, J.M. Jr., 1982. Locations and focal mechanisms of recent microearthquakes and tectonics of the Livermore Valley, California, **Bull.seism.Soc.Am.**, 72, 821-840.

Fukao, Y., 1984. Evidence from core-reflected shear-waves for anisotropy in

the Earth's mantle, **Nature**, 309, 695-698.

Garbin, H.D. & Knopoff, L., 1973. The compressional modulus of a material permeated by a random distribution of free circular cracks, **Q.Appl.Math.**, 30, 453-464.

Garbin, H.D & Knopoff, L., 1975a. The shear modulus of a material permeated by a random distribution of free circular cracks, **Q.Appl.Math.**, 33, 296-300.

Garbin, H.D. & Knopoff, L., 1975b. Elastic moduli of a medium with liquid-filled cracks, **Q.Appl.Math.**, 33, 301-303.

Geller, R.J., 1976. Body force equivalents for stress drop seismic sources, **Bull.seism.Soc.Am.**, 66, 1801-1804.

Gupta, I.N., 1973a. Seismic velocities in rock subjected to axial loading up to shear fracture, **J.geophys.Res.**, 78, 6936-6942.

Gupta, I.N., 1973b. Dilatancy and premonitory variations of P,S travel times, **Bull.seism.Soc.Am.**, 63, 1157-1161.

Gupta, I.N., 1973c. Premonitory variations in S-wave velocity anisotropy before earthquakes in Nevada, **Science**, 182, 1129-1132.

Hadley, K., 1975. Azimuthal variation of dilatancy, **J.geophys.Res.**, 80, 4845-4850.

Herrmann, R.B., 1976. Some more complexity in S-wave particle motion,

Bull.seism.Soc.Am., 66, 625-632.

Hodgson, J.H., 1959. The mechanics of faulting with special reference to the fault plane work, **Publ. of the Dominion Observatory Ottawa**, vol 20, no. 2.

Houliston, D.J., Laughlin, J. & Waugh, G., 1976. Developments of the seismic data-processing systems of the Institute of Geological Sciences in Edinburgh, **Inst.Geol.Sci.Glob.Seism.intern.report**, No. 74.

Hron, F. & Covey, J.D., 1983. Wavefront divergence, multiples, and converted waves in synthetic seismograms, **Geophys.Pros.**, 31, 436-456.

Hubbert, M.K. & Willis, D.G., 1957. Mechanics of hydraulic fracture, **Trans.A.I.M.E.**, 210, 153-170.

Julian, B.R., 1983. Evidence for dyke intrusion earthquake mechanisms near Long Valley caldera, California, **Nature**, 303, 323-325.

Jeffreys, H., 1965. **Cartesian Tensors**, Cambridge University Press, 92pp.

Keith, C.M. & Crampin, S., 1977a. Seismic body waves in anisotropic media: reflection and refraction at a plane interface, **Geophys.J.R.astr.Soc.**, 49, 181-208.

Keith, C.M. & Crampin, S., 1977b. Seismic body waves in anisotropic media: propagation through a layer, **Geophys.J.R.astr.Soc.**, 49, 209-223.

Keith, C.M. & Crampin, S., 1977c. Seismic body waves in anisotropic media:

synthetic seismograms, **Geophys.J.R.astr.Soc.**, 49, 225-243.

Kempner, W.C. & Gettrust, J.F., 1982a. Ophiolites, synthetic seismograms, and ocean crustal structure: 1. Comparison of ocean bottom seismometer data and synthetic seismograms for the Bay of Islands ophiolite, **J.geophys.Res.**, 87, 8447-8462.

Kempner, W.C. & Gettrust, J.F., 1982b. Ophiolites, synthetic seismograms, and ocean crustal structure: 2. A comparison of synthetic seismograms of the Samail Ophiolite, Oman, and the ROSE refraction data data from the East Pacific Rise, **J.geophys.Res.**, 87, 8463-8476.

Kennett, B.L.N., 1980. Seismic waves in a stratified half space - II. Theoretical seismograms, **Geophys.J.R.astr.Soc.**, 61, 1-10.

Kind, R. & Muller, G., 1975. Computations of SV waves in realistic earth models, **J.Geophys.**, 41, 149-172.

Klein, R.J. & Brown, E.T., 1983. The state of stress in British rocks, **Department of the Enviroment internal report**, DOE/RW/83060.

Kozlovsky, Ye.A., 1984. The World's deepest well, **Sci.Am.**, 251/6, 106-112.

Lamb, H., 1904. On the propagation of tremors over the surface of an elastic solid, **Phil.trans.R.Soc.**, A, 203, 1-42.

Lapwood, E.R., 1949. The disturbance due to a line source in a semi-infinite elastic medium, **Phil.trans.R.Soc.**, A, 242, 63-100.

Lee, W.H.K., Eaton, M.S. & Brabb, E.E., 1971. The earthquake sequence near Danville, California, 1970, **Bull.seism.Soc.Am.**, 61, 1771-1794.

Lee, W.H.K. & Lahr, J.C., 1975. HYPO71 (revised): a computer program for determining hypocentre, magnitude, and first motion pattern of local earthquakes, **USGS Open File Report**, 75-311.

Maley, R.P., 1978. Strong motion records from the Livermore Valley, California earthquake of 22 June 1977, **Bull.seism.Soc.Am.**, 68, 849-853.

Mendiguren, J.A., 1969. Study of focal mechanism of deep earthquakes in Argentina using non linear particle motion of S-waves, **Bull.seism.Soc.Am.**, 59, 1449-1473.

Nakano, H., 1925. On Rayleigh waves, **Japan.J.astr.Geophys.**, 2, 233-326.

Nur, A. & Simmons, G., 1969a. Stress induced velocity anisotropy in rock: an experimental study, **J.geophys.Res.**, 74, 6667-6674.

Nur, A. & Simmons, G., 1969b. The effect of saturation on velocity in low porosity rocks, **Earth and Planetary Science Letters**, 7, 183-193.

Nuttli, O., 1961. The effect of the earth's surface on the S-wave particle motion, **Bull.seism.Soc.Am.**, 51, 237-246.

Nuttli, O., 1964. The determination of the S-wave polarization angles for an earth model with crustal layering, **Bull.seism.Soc.Am.**, 54, 1429-1440.

Nuttli, O. & Whitmore, J.D., 1962. On the determination of the polarization angle of the S-wave, **Bull.seism.Soc.Am.**, 52, 95-107.

Pearson, C.M., 1981. The relationship between microseismicity and high pore pressures during hydraulic stimulation experiments in low permeability granitic rocks, **J.geophys.Res.**, 86, 7855-7864.

Pine, R.J. & Batchelor, A.S., 1982. Geothermal Energy Project: Seismic Hazard Assessment, **Camborne Sch. of Mines**, Geo.Energy Proj., Internal Report No. 2-28.

Pine, R.J. & Batchelor, A.S., 1984. Downward migration of shearing in jointed rock during hydraulic injections, **Int.J.Rock.Mech.Min.Sci. & Geomech.Abstr.**, 21, 249-263.

Pine, R.J., Ledingham, P. & Merrifield, C.M., 1983b. In situ stress measurements in the Carnmenellis Granite - II. Hydrofracture tests at Rosemanowes Quarry to depths of 2000 m, **Int.J.Rock.Mech.Min.Sci. & Geomech.Abstr.**, 20, 63-72.

Pine, R.J., Tunbridge, L.W. & Kwakwa, K., 1983a. In situ stress measurement in the Carnmenellis Granite - I. Overcoring tests at South Crofty Mine at a depth of 790 m, **Int.J.Rock.Mech.Min.Sci. & Geomech.Abstr.**, 20, 51-62.

Ryall, A. & Savage, W.U., 1974. S-wave splitting: Key to earthquake prediction ?, **Bull.seism.Soc.Am.**, 64, 1943-1951.

Scheimer, J.F., Taylor, S.R. & Sharp, M., 1982. Seismicity of the Livermore

Valley region 1969-1981, **Lawrence Livermore National Laboratory UCRL preprint** 86969.

Secor, D.T., Lawrence, S.P., Pitcher, D.M., Prowell, D.C., Simpson, D.H., Smith, W.A. & Snoke, A.W., 1982. Geology of the area of induced seismic activity at Monticello Reservoir, South Carolina, **J.geophys.Res.**, 87, 6945-6957.

Soga, N., Mizutani, H., Spetzler, H. & Martin III, R.J., 1978. The effect of dilatancy on velocity anisotropy in Westerly Granite, **J.geophys.Res.**, 83, 4451-4458.

Stauder, W.S.J., 1960a. S-waves and focal mechanisms: the state of the question, **Bull.seism.Soc.Am.**, 50, 333-346.

Stauder, W.S.J., 1960b. Three Kamchatka earthquakes, **Bull.seism.Soc.Am.**, 50, 347-388.

Stierman, D.J., Healy, J.H. & Kovach, R.L., 1979. Pressure-induced velocity gradient: an alternative to a Pg refractor in the Gabilan Range, Central California, **Bull.seism.Soc.Am.**, 69, 397-415.

Talwani, P., Rastogi, B.K. & Stevenson, D.C., 1980. Induced seismicity and earthquake prediction studies in South Carolina, tenth technical report, contract 14-08-0001-17670, **U.S. Geol. Surv.**, Reston, Va..

Taylor, S.R. & Scheimer, J.F., 1982. P-wave velocity models and earthquake locations in the Livermore Valley region, California, **Bull.seism.Soc.Am.**, 72,

1255-1275.

Tombs, J.M.C., 1977. A study of the space form of the Cornubian granite batholith and its application to detailed gravity surveys in Cornwall, **IGS Mineral Reconnaissance Programme Report** Series No. 11.

Turbitt, T., Walker, A.B., Browitt, C.W.A. & Morgan, S.N., 1984. Monitoring the background and induced seismicity for the Hot Dry Rock Programme in Cornwall, **Brit.Geol.Surv.Glob.Seism.intern.report**, No. 195.

Turchaninov, I.A., Panin, V.I., Markov, G.A., Pavlovskii, V.I., Sharov, N.V. & Ivanov, G.A., 1977. On correlation between seismic velocity anisotropy and stresses in situ, **Pageoph.**, 115, 259-265.

Walker, A.B., 1984. Source mechanisms of the induced events from the Hot Dry Rock Programme in Cornwall, **Brit.Geol.Surv.Glob.Seism.intern.report**, No. 224.

Yegorkina, G.V., Rakitov, V.A., Garetovskaya, I.V. & Yegorova, L.M., 1977. Anisotropy of velocities of seismic waves and the stress state of the earth's crust in the territory of Armenia, **Izvestiya Earth Phys.**, 13, 554-562.

Zoback, M.D. & Hickman, S., 1982. In situ study of the physical mechanisms controlling induced seismicity at Monticello Reservoir, South Carolina, **J.geophys.Res.**, 87, 6959-6974.

Zoback, M.D. & Zoback M.L., 1980. State of stress in conterminous United States, **J.geophys.Res.**, 85, 6113-6156.

APPENDIX A

PROCEDURE FOR DETERMINING THE EARTHQUAKE FOCAL MECHANISM FROM P-WAVE FIRST MOTION POLARITIES

Note: most of this appendix is derived directly from Aki & Richards (1980) but is included as a simple summary of the procedure followed.

A.1 Introduction

In this appendix a procedure for the determination of earthquake focal mechanisms from a distribution of P-wave first motion polarities is outlined. The reason for this is two-fold. It proved difficult to find a reference which gave a simple step by step approach to such solutions, and it illustrates the method used to determine the Cornish acoustic events fault plane solutions.

The radiation pattern of a seismic source is often described on the focal sphere (see Figure A.1a). The focal sphere is a sphere centred on the seismic source with an arbitrary small radius. Information recorded by seismometers on the earth's surface can be transferred to the focal sphere by tracing the ray back from receiver to source to where it intersects the focal sphere. This specifies a point on the focal sphere with angular coordinates $(i_t,\emptyset)$, where i_t is the take-off angle measured from the downward vertical and $\emptyset$ is the event to station azimuth measured clockwise from north. Another mapping is then required to show the focal sphere on a plane surface. The mapping used throughout the dissertation was the Schmidt-Lambert equal-area projection (see Figure A.1b).

The prime objective of focal mechanism studies is to determine the fault parameters. The fault parameters are defined after Aki & Richards (1980), and are shown in Figure A.1c. The fault orientation is specified by the strike

Figure A1

(a) The focal sphere. A sphere of arbitrary small radius is centred on the source. A point is specified on the focal sphere by the azimuth and take-off angle of the ray.

(b) The equal-area projection of the focal sphere. The point P maps onto the point P" on the equatorial plane. (i) sectional view of the focal sphere. (ii) equatorial plane.

(c) The fault parameters illustrated on the footwall.

All diagrams from Aki & Richards (1980).

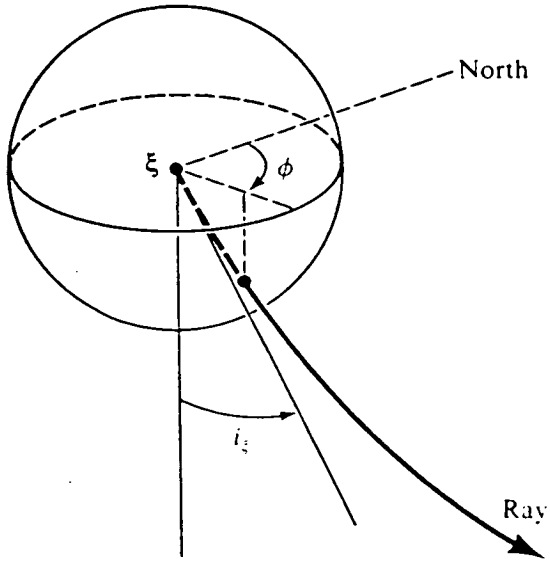

Figure A.1a

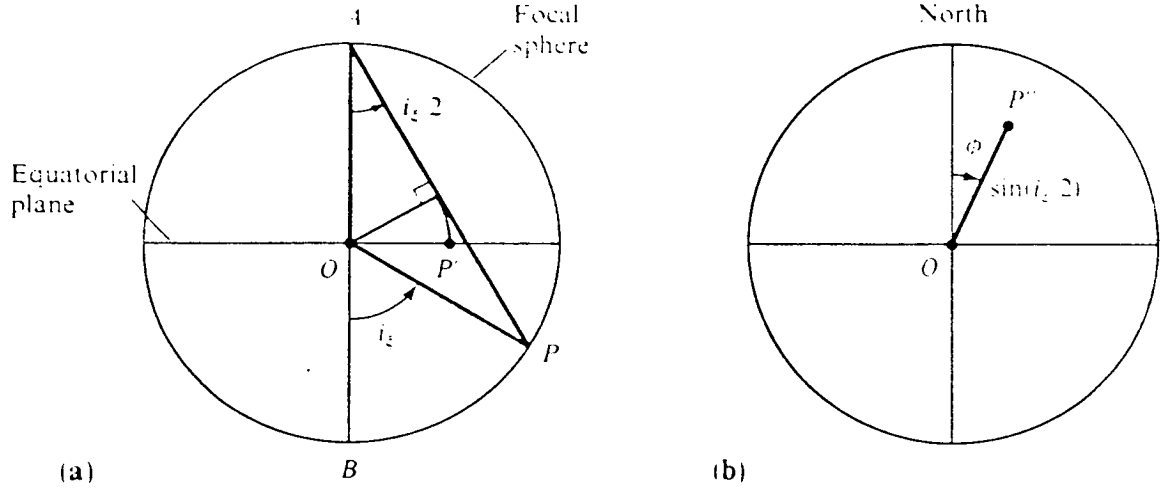

Figure A.1b

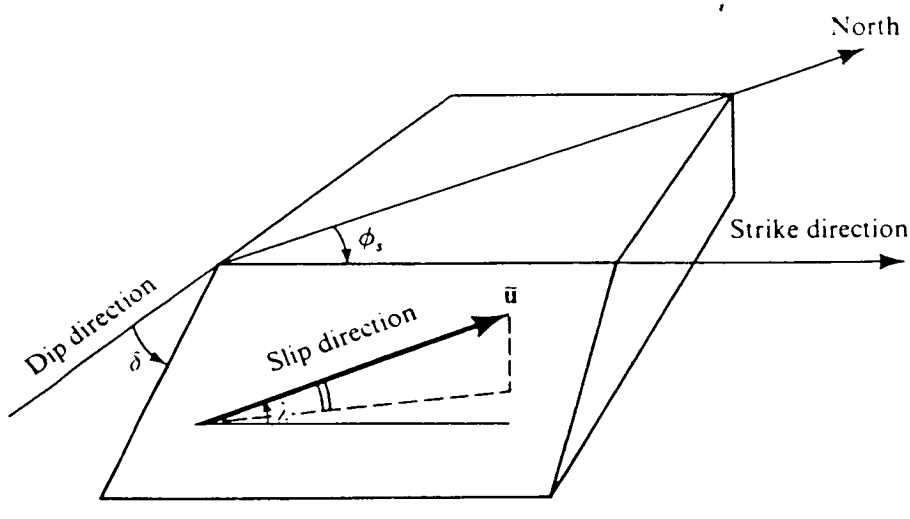

Figure A.1c

ϕ_s and dip δ, and then the rake λ is used to specify the direction of slip. The fault has two surfaces: the foot wall illustrated in Figure A.1c, and the hanging wall. The slip vector defines the direction of motion of the hanging wall relative to the foot wall. The strike is measured clockwise from north with the fault surface dipping down to the right when looking along the strike direction. The dip is measured down from the horizontal. In the case of strike-slip faults when $\delta=90^o$, and $\lambda=0^o, \pm 180^o$, and dip-slip faults when $\delta=90^o$ there is an ambiguity in the strike direction because the choice of the hanging wall and foot wall is arbitrary. A convention is followed for strike definition. For a strike-slip fault either of the two possible strike directions is fixed and the right hand block (as viewed by an observer looking along the strike) is labelled the hanging wall. Hence $\lambda=0^o$ is left-lateral strike-slip and $\lambda=180^o$ is right-lateral. For a dip-slip fault the foot wall is defined to be the down dropped block, and the strike direction is that for which the hanging wall is on the right. The dip-slip fault always has $\lambda=90^o$.

At a given receiver the longitudinal particle motion of the P-wave is either toward the source (downward movement on vertical-component seismogram) or away from the source (upward movement on vertical-component seismogram). The latter is a compressional first motion and the former is a dilatational first motion. Two perpendicular planes called nodal planes divide the dilatations and compressions into quadrants with the P-wave amplitude equal to zero for rays propagating along the nodal planes. One of the nodal planes is the fault plane and the normal of the other nodal plane is the slip vector. The earthquake focal mechanism is estimated from an analysis of the P-wave first motions over the focal sphere.

A.2 **Procedure**

1. For each seismogram determine:

(i) take-off angle at the source, i_t.

(ii) source to station azimuth, $\emptyset$.

(iii) the P-wave polarity - compressional or dilatational.

The P-wave first motions from the seismograms are plotted on an equal-area projection of the focal sphere using different symbols for compressional and dilatational arrivals. The position of a polarity on the projection is given by $(i_t,\emptyset)$. When $i_t < 90^o$ for most or all of the rays we require a lower projection of the focal sphere, when $i_t > 90^o$ for most or all of the rays an upper projection of the focal sphere is used.

2. Once all the P-wave polarities are plotted, two great circles partition the projection into four quadrants with each quadrant having either all compressional or dilatational arrivals. The great circles represent the perpedicular P-wave nodal planes. Note that since these planes are perpendicular the normal to each great circle must lie on the other great circle.

3. One of the nodal planes is the fault plane and the other is called the auxiliary plane. There is an ambiguity in choosing which of the two nodal planes is the fault plane. Evidence other than P (or S) wave first motions is required to infer the fault plane eg. surface features. Upon selecting the fault plane, and assuming that the slip vector of the fault plane is the normal of the auxiliary plane the fault parameters can be determined directly from the equal-area projection.

An illustration is shown in Figure A.2.

(i) Strike direction: The strike direction is plotted as a horizontal vector on the fault plane. Note that the fault dips to the right when looking along the strike. The strike is measured clockwise from north.

(ii) Dip: The dip angle is measured from the circumference to the fault plane.

(iii) Rake: The rake is the angle between the strike direction and the slip

vector. To obtain the rake measure the angle, a^o, between the strike vector and the auxiliary plane normal. The rake is either this angle, a^o, or $(a-180)^o$ depending on the sense of the slip vector. In general this can be resolved from the P-wave polarity of a vertical ray (i.e. whether compressions or dilatations occupy the centre of the equal-area projection).

Dilatations in centre = slip vector points down = normal faulting

then $\lambda = a^o - 180^o$

Compressions in centre = slip vector points up = reverse faulting

then $\lambda = a^o$

The reasoning behind this intuitive approach is shown in Figure A.3. It can be adpated to determine the sense of motion when the fault plane is vertical and vertical ray paths are nodal.

Figure A2

Example of a fault plane solution. Equal-area projection of the upper focal hemisphere. Open circles: dilatations. Closed circles: compressions. The strike, dip, and rake are measured directly from the projection. Strike 242°; Dip 51°; Rake -164°.

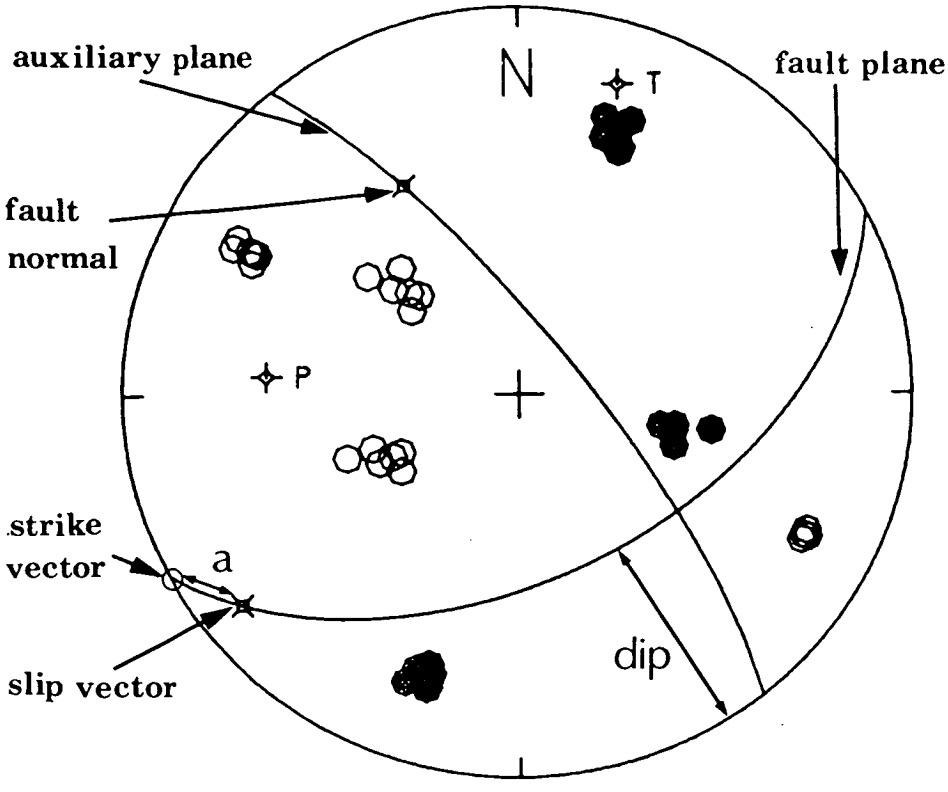

strike	242	
dip	51	
rake	a -180	-164

Figure A.2

Figure A3
Schematic diagram of stress distribution for normal and reverse faulting. The P-wave polarity of a vertical ray is used to distinguish between normal and reverse faulting. Compression: reverse fault. Dilatation: normal fault.

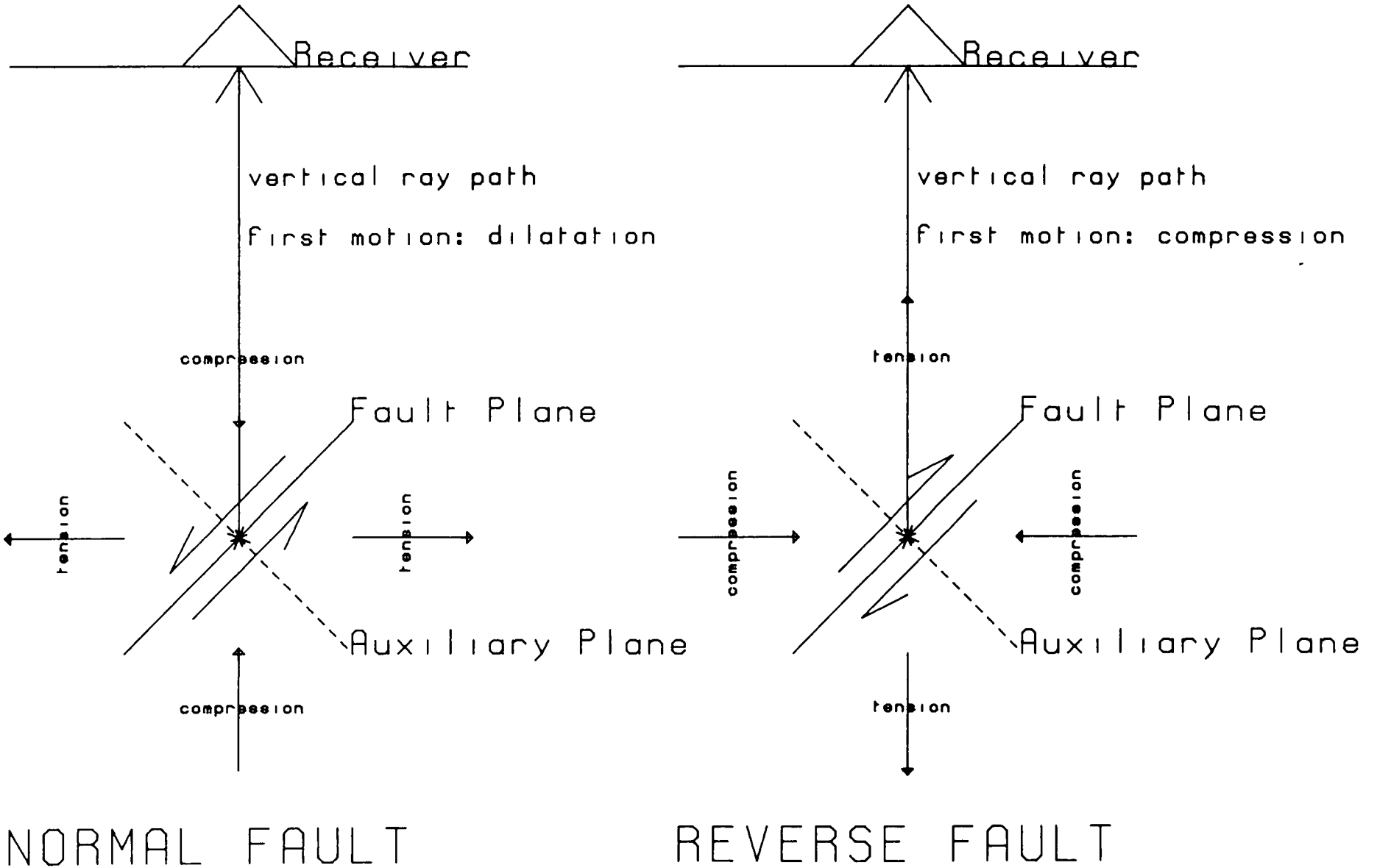
Receiver
vertical ray path
first motion: dilatation
compression
Fault Plane
tension
tension
Auxiliary Plane
compression
NORMAL FAULT
Receiver
vertical ray path
first motion: compression
tension
Fault Plane
compression
compression
Auxiliary Plane
tension
REVERSE FAULT

Figure A.3

APPENDIX B

BODY-WAVE RADIATIONS FROM DOUBLE COUPLE AND CLVD POINT SOURCES

B.1 Double couple point source (shearing)

The equations describing the far-field body-wave radiation due to a double couple point source are presented. The P-wave and shear-wave displacements as a function of azimuth (source to receiver) $\emptyset$, take-off angle (from downward vertical) i_t, and strike $\emptyset_s$, dip δ, and rake λ of the fault are given below (Aki & Richards 1980).

$$\underline{u}_p = F_p \underline{l}$$
$$\underline{u}_{sv} = F_{sv} \underline{m} \qquad \text{(B.1)}$$
$$\underline{u}_{sh} = F_{sh} \underline{n}$$

where

$$\begin{aligned} F_p &= \cos\lambda \sin\delta \sin^2 i_t \sin 2(\emptyset-\emptyset_s) - \cos\lambda \cos\delta \sin 2i_t \cos(\emptyset-\emptyset_s) \\ &\quad + \sin\lambda \sin 2\delta \,(\cos^2 i_t - \sin^2 i_t \sin^2(\emptyset-\emptyset_s)) \\ &\quad + \sin\lambda \cos 2\delta \sin 2i_t \sin(\emptyset-\emptyset_s) \end{aligned}$$

$$\begin{aligned} F_{sv} &= \sin\lambda \cos 2\delta \cos 2i_t \sin(\emptyset-\emptyset_s) - \cos\lambda \cos\delta \cos 2i_t \cos(\emptyset-\emptyset_s) \\ &\quad + 1/2 \cos\lambda \sin\delta \sin 2i_t \sin 2(\emptyset-\emptyset_s) \\ &\quad - 1/2 \sin\lambda \sin 2\delta \sin 2i_t \,(1 + \sin^2(\emptyset-\emptyset_s)) \end{aligned}$$

$$\begin{aligned} F_{sh} &= \cos\lambda \cos\delta \cos i_t \sin(\emptyset-\emptyset_s) + \cos\lambda \sin\delta \sin i_t \cos^2(\emptyset-\emptyset_s) \\ &\quad + \sin\lambda \cos 2\delta \cos i_t \cos(\emptyset-\emptyset_s) \\ &\quad - 1/2 \sin\lambda \sin 2\delta \sin i_t \sin 2(\emptyset-\emptyset_s) \end{aligned}$$

Time dependant terms and terms dependant on the physical properties of the medium are omitted. The vector $\underline{u}_P$ describes the displacement of the P-wave (along the ray path in the direction of the unit vector $\underline{l}$); $\underline{u}_{SV}$ describes the displacement of the SV-wave (perpendicular to the ray path in the sagittal plane in the direction of unit vector $\underline{m}$), and $\underline{u}_{SH}$ describes the displacement of the SH-wave (perpendicular to the sagittal plane in the direction of unit vector $\underline{n}$). To describe the horizontal shear-wave radiation over the focal sphere equation B.1 is computed for a range of take-off angles and azimuths. The displacements are resolved into a Cartesian coordinate system with axes orientated north, east, and vertical. The horizontal shear-wave polarizations are then given by vector addition of the shear-wave displacement vectors in the north and east directions. The computer program FISPOL computes the body-wave radiation patterns following the above procedure, and displays the radiations on an equal-area projection.

B.2 **CLVD point source (jacking)**

A jacking source occurs when the two sides of a fracture plane are pushed apart (as opposed to slipping) with the release of seismic energy. The jacking source mechanism is represented by the compensated linear-vector dipole (CLVD) body-force system (Julian 1983). The CLVD is a body-force system without net force or torque that has no explosive, implosive, or double couple component. In the principal axes coordinate system it consists of three orthogonal force dipoles with moments in the ratio 2: -1: -1. Geller (1976) noted that the CLVD body-force system can be obtained from the sum of two double couples.

A CLVD source is represented by a moment tensor

$$M = \begin{matrix} 2 & 0 & 0 \\ 0 & -1 & 0 \\ 0 & 0 & -1 \end{matrix} \qquad \text{(B.2)}$$

in the principal axes system $\underline{x}$, $\underline{y}$, and $\underline{z}$. The tensional force dipole is parallel to the $\underline{x}$-axis and the two implosive force dipoles are parallel to the $\underline{y}$ and $\underline{z}$ axes. The CLVD moment tensor can be decomposed into the summation of two moment tensors, each representing a double couple force system.

$$\begin{matrix} 2 & 0 & 0 \\ 0 & -1 & 0 \\ 0 & 0 & -1 \end{matrix} = \begin{matrix} 1 & 0 & 0 \\ 0 & -1 & 0 \\ 0 & 0 & 0 \end{matrix} + \begin{matrix} 1 & 0 & 0 \\ 0 & 0 & 0 \\ 0 & 0 & -1 \end{matrix} \qquad \text{(B.3)}$$

Aki & Richards (1980) showed that the Cartesian components of a moment tensor for a shear dislocation source can be expressed in terms of the fault parameters - strike, dip, and rake. They are

$$\begin{aligned}
Mxx &= -Mo\,(\sin\delta\cos\lambda\sin 2\phi_s + \sin 2\delta\sin\lambda\sin^2\phi_s) \\
Mxy &= Mo\,(\sin\delta\cos\lambda\cos 2\phi_s + 1/2\sin 2\delta\sin\lambda\sin 2\phi_s) = Myx \\
Mxz &= -Mo\,(\cos\delta\cos\lambda\cos\phi_s + \cos 2\delta\sin\lambda\sin\phi_s) = Mzx \\
Myy &= Mo\,(\sin\delta\cos\lambda\sin 2\phi_s - \sin 2\delta\sin\lambda\cos^2\phi_s) \\
Myz &= -Mo\,(\cos\delta\cos\lambda\sin\phi_s - \cos 2\delta\sin\lambda\cos\phi_s) = Mzy \\
Mzz &= Mo\,(\sin 2\delta\sin\lambda)
\end{aligned} \qquad \text{(B.4)}$$

from Aki & Richards (1980). From these equations it is possible to determine the fault parameters represented by the above double couple moment tensors. These give

$$\begin{matrix} 1 & 0 & 0 \\ 0 & 1 & 0 \\ 0 & 0 & 0 \end{matrix} \begin{matrix} \phi_s = 45^o \\ \delta = 90^o \\ \lambda = 180^o \end{matrix} \qquad \begin{matrix} 1 & 0 & 0 \\ 0 & 0 & 0 \\ 0 & 0 & -1 \end{matrix} \begin{matrix} \phi_s = 90^o \\ \delta = 45^o \\ \lambda = -90^o \end{matrix} \qquad \text{(B.5)}$$

Therefore the far-field body-wave radiation pattern for a pure CLVD source is computed by determining the far-field body-wave radiation for each of the above double couple force systems using equations B.1, and adding them, following equation B.3.

APPENDIX C

THE SENSITIVITY OF SHEAR-WAVE RECONSTRUCTION TO THE ANISOTROPIC VIBRATION DIRECTIONS

Note: Appendix C includes some work which did not fit within the framework of the dissertation, but is included for its insights into the interpretation of shear-wave particle motion.

C.1 Introduction

In studies of upper mantle anisotropy attempts have been made (Ando & Ishikawa 1982; Fukao 1984) to reconstruct the particle motion of the shear-waveform prior to its entry into an anisotropic zone. Such reconstruction is usually carried out to compare pre-split shear-wave polarizations with predicted polarizations from the P-wave focal mechanisms, but it has also been used as a guide to the orientation of the anisotropic vibration directions (the polarizations of the split shear-waves). Using synthetic seismograms we show that shear-waveform reconstruction is not particularly sensitive to the orientation of the anisotropic vibration directions. The motivation for this study derives from the results of a shear-wave reconstruction carried out for a hydrofracture-induced event at the HDR site in Cornwall.

The procedure of shear-wave reconstruction is as follows for seismograms recorded on vertical, north-south, and east-west components. The north-south and east-west components are rotated into components orientated parallel to the horizontal projection of the fast and slow anisotropic vibration directions (the polarizations of the split shear-waves). The appropriate rotation resolves the shear-wave into two orthogonally-polarized, or nearly orthogonally-polarized, phases whose waveforms are similar to each other (Fukao 1984).

The slow vibration direction component is then advanced relative to the fast vibration direction component until the two waveforms are in phase, when their addition recreates the original waveform before shear-wave splitting. Cross correlation of pulse shapes or the degree of linearity of the reconstructed particle motion are used to estimate the rotation angles and time shifts.

The seismogram which prompted this work is shown in Figure C.1a. The shear-wave particle motion is interpretated as the arrival of split shear-waves with the faster shear-wave polarized at N 127°E, and separated from the slower phase by a time delay of 7/400 seconds. The reconstruction of the shear-wavefom prior to splitting (by rotation of the N-S and E-W components through 127° clockwise from north and shifting the slow component forward 7/400 seconds) produces linear particle motion as expected (see Figures C.1b and C.1c). However linear particle motion also results for rotations ranging from 87° to 167°. The seismograms and polarization diagrams are shown in Figures C.1d to C.1i. This raised some doubt over the sensitivity of shear-wave reconstruction to the orientation of anisotropic vibration directions because linear particle motion is only expected when the components align parallel to the vibration directions.

In this study we are interested in the reconstructed shear-waveform when the rotated components do not align parallel to the anisotropic vibration directions. To facilitate this, shear-wave reconstruction is carried out on some simple synthetic seismograms which model shear-wave propagation through an anisotropic region.

C.2 **Synthetic seismogram generation**

With reference to Figure C.2 we will illustrate how the synthetic seismograms are generated. A plan and sectional view of a vertical ray

Figure C1

Reconstructed seismograms and polarization diagrams of the shear-wave onset at CRA for the event of 5 November. The seismograms are rotated with components orientated vertical (Z), fast anisotropic vibration direction (FS), slow anisotropic vibration direction (SL). The upper polarization diagrams show particle motion in the vertical/FS plane, the middle row of polarization diagrams show particle motion in the vertical/SL plane, and the lower polarization diagrams show particle motion in the horizontal plane. The reconstruction parameters are:

	rotation angle	time shift (1/400 second)
(a)	0°	0
(b)	N 127°E	0
(c)	N 127°E	7
(d)	N 87°E	7
(e)	N 107°E	7
(f)	N 117°E	7
(g)	N 137°E	7
(h)	N 147°E	7
(i)	N 167°E	7

The rotation angle gives the +ve direction of the FS-component, and (90° + rotation angle) is the +ve direction of the SL-component.

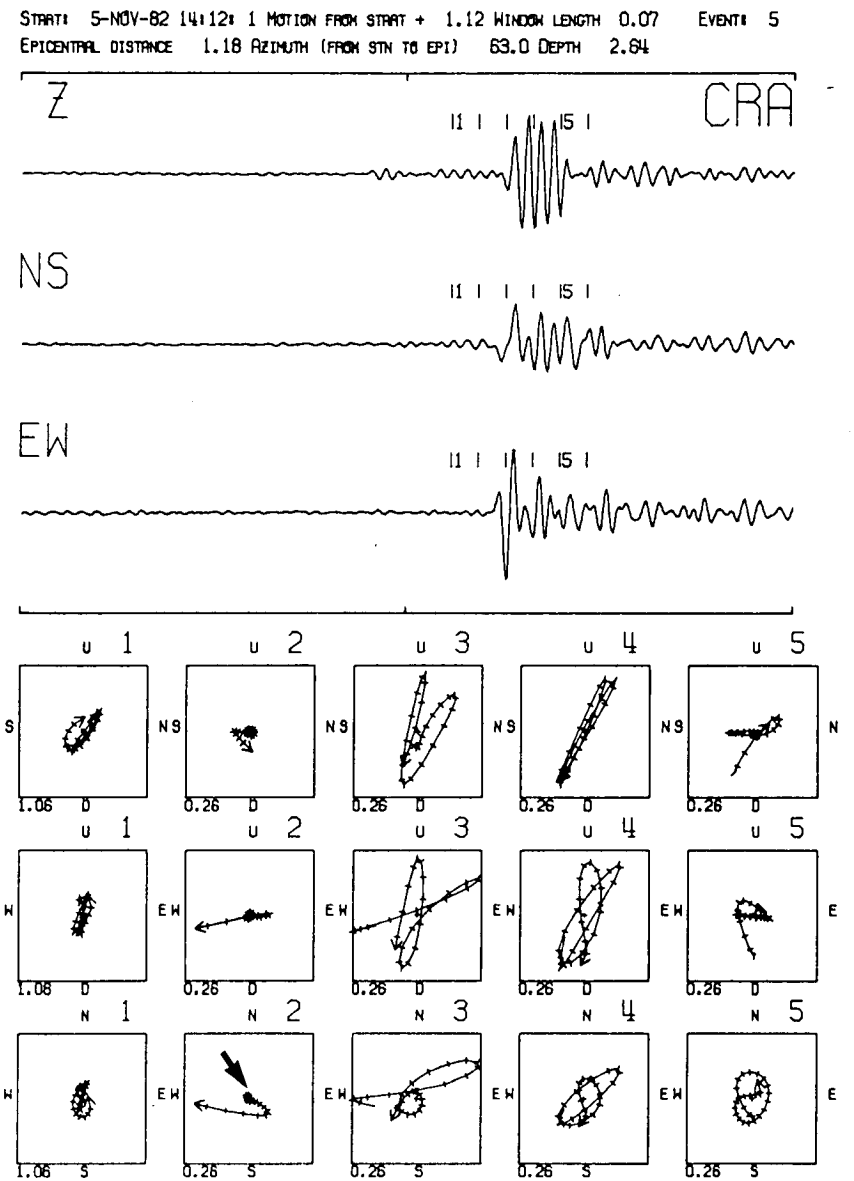
START: 5-NOV-82 14:12: 1 MOTION FROM START + 1.12 WINDOW LENGTH 0.07 EVENT: 5
EPICENTRAL DISTANCE 1.18 AZIMUTH (FROM STN TO EPI) 63.0 DEPTH 2.64
Z
CRA
NS
EW
U 1
U 2
U 3
U 4
U 5
S
NS
N
E
W
1.06
0.26
D
S

Figure C.1a

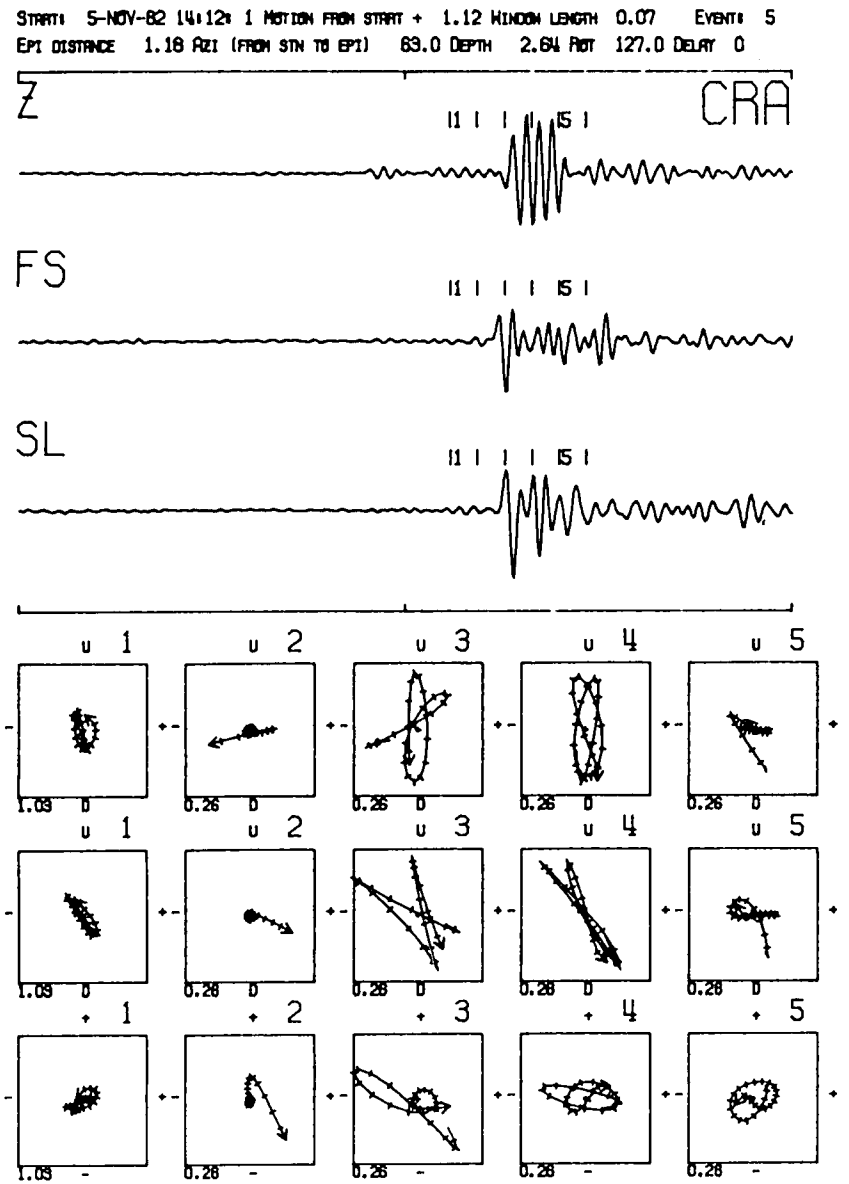

Figure C.1b

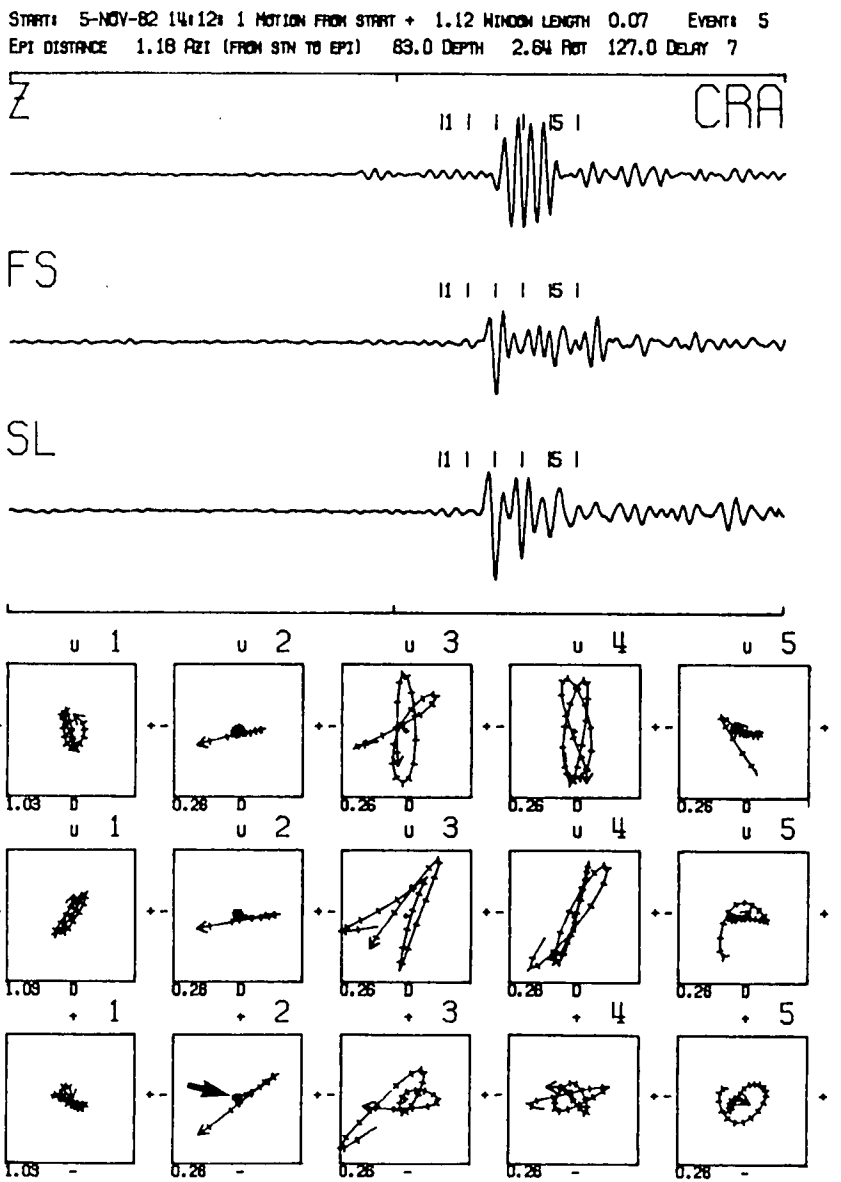

Figure C.1c

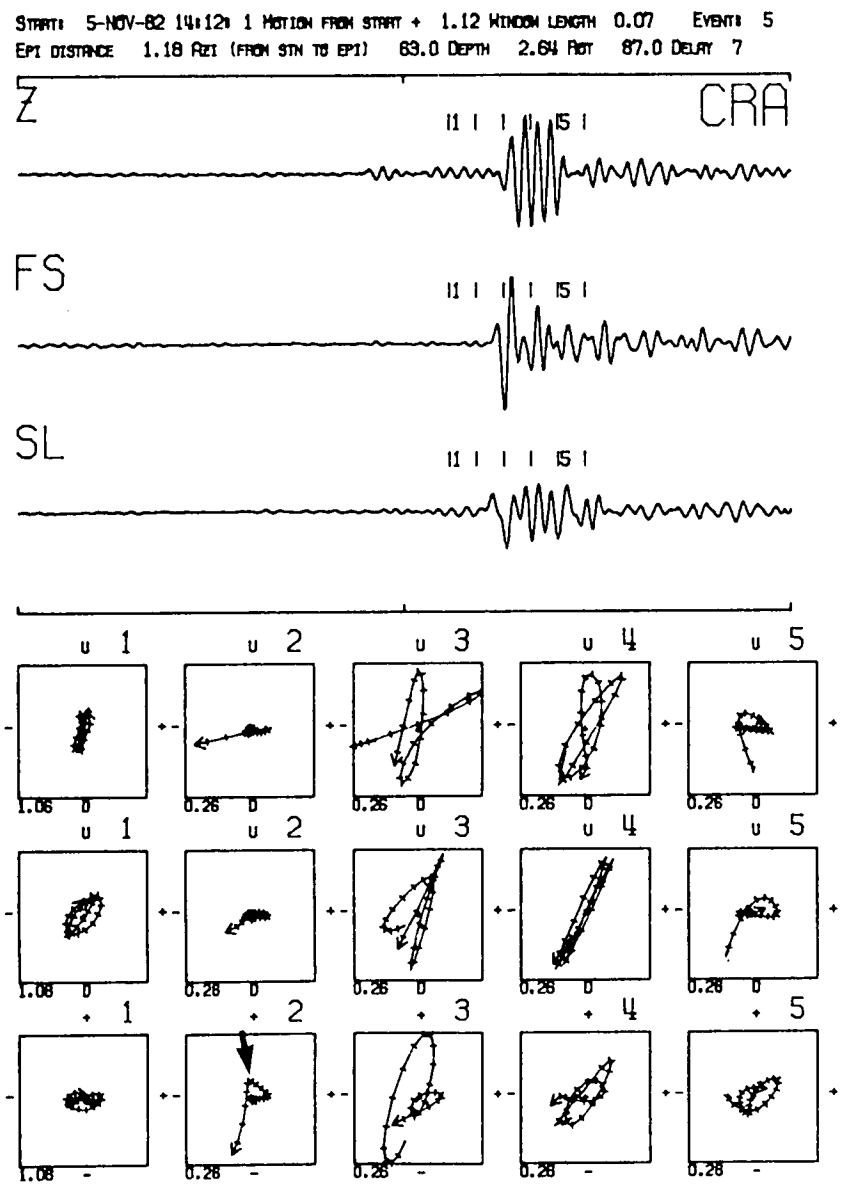

Figure C.1d

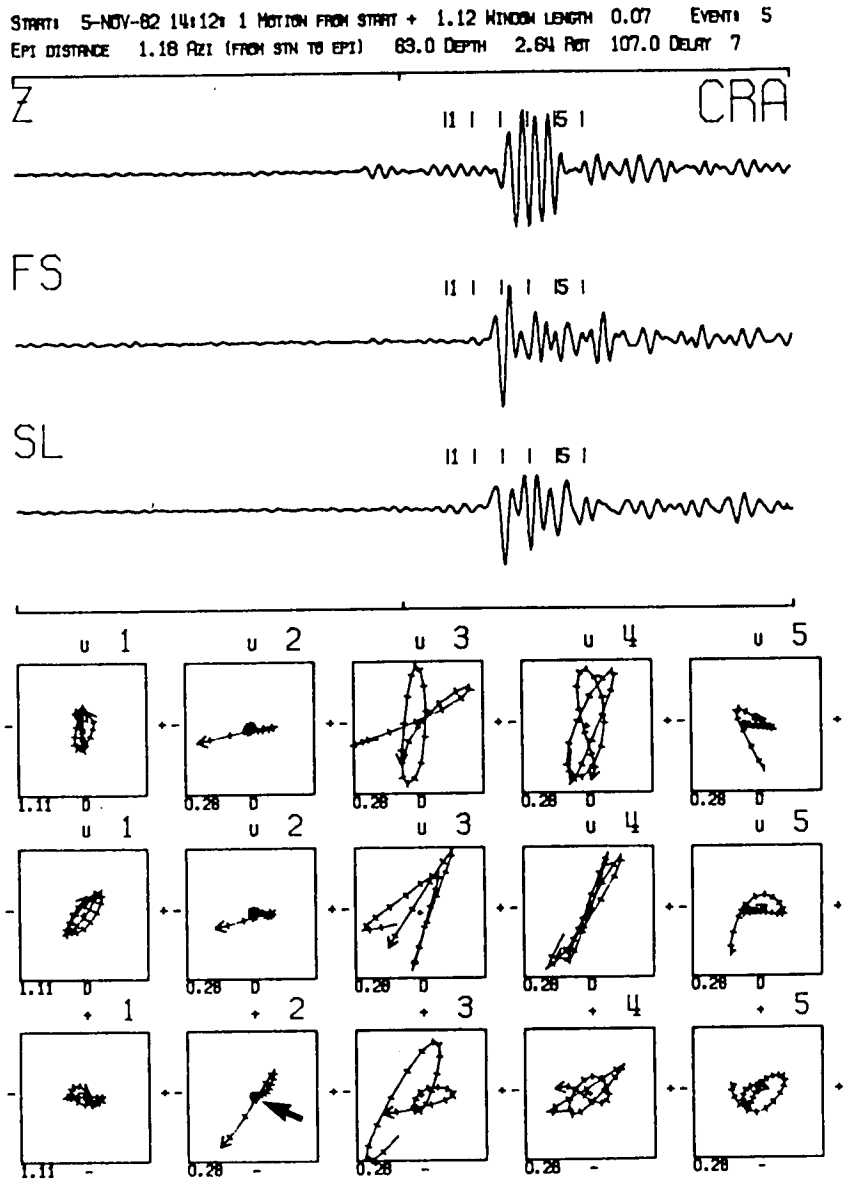

Figure C.1e

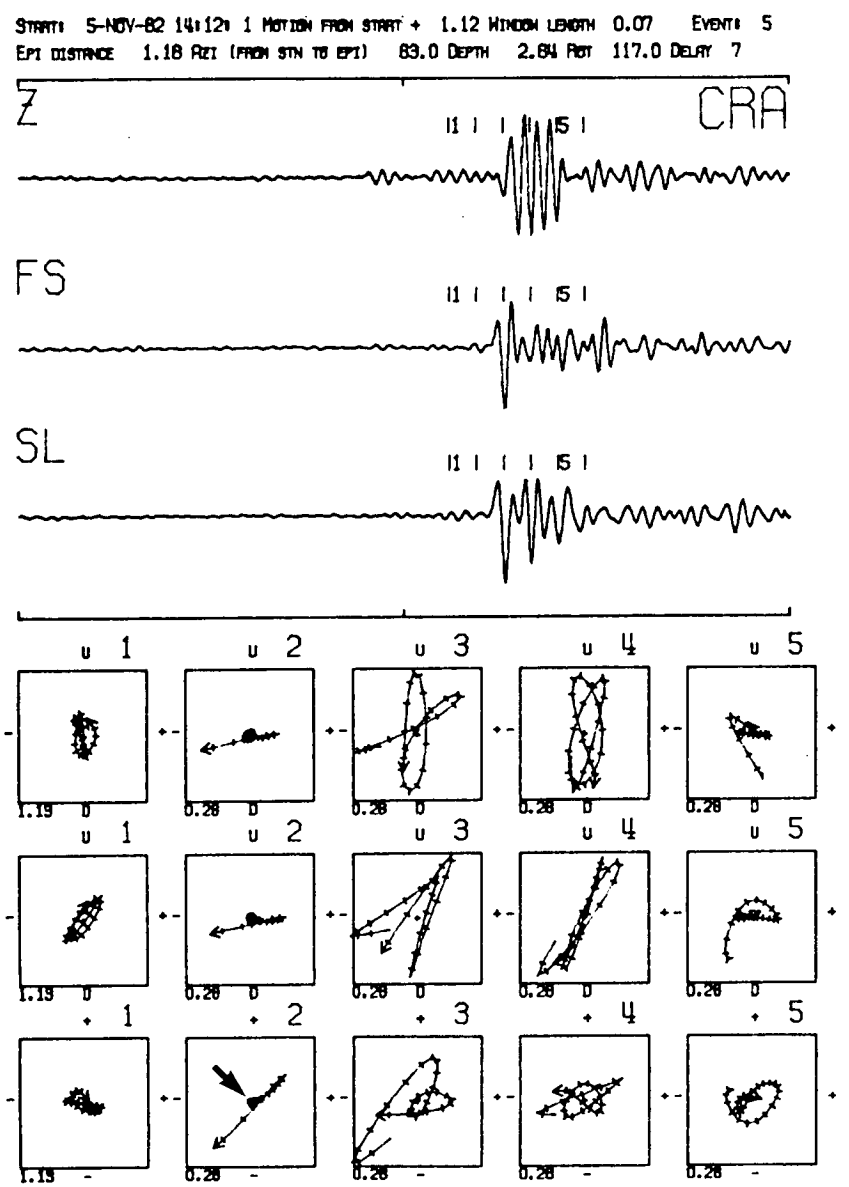

Figure C.1f

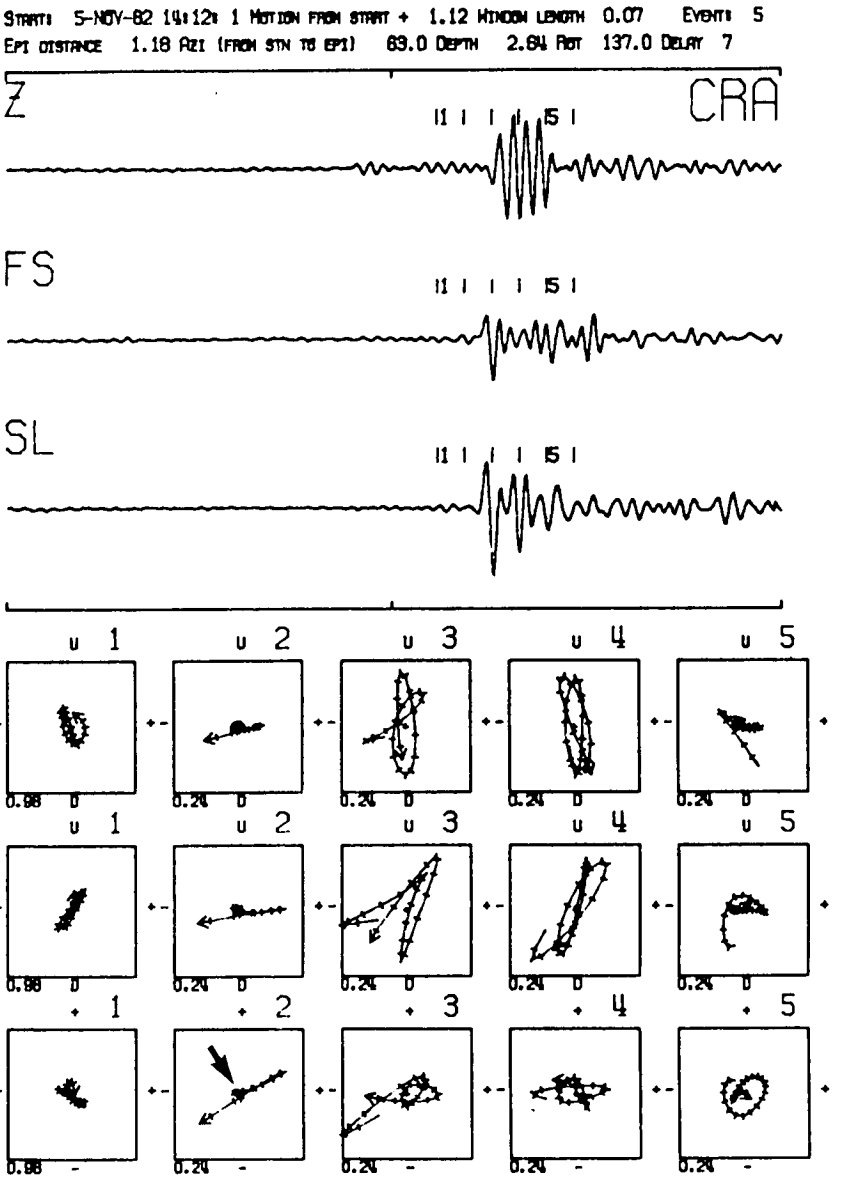

Figure C.1g

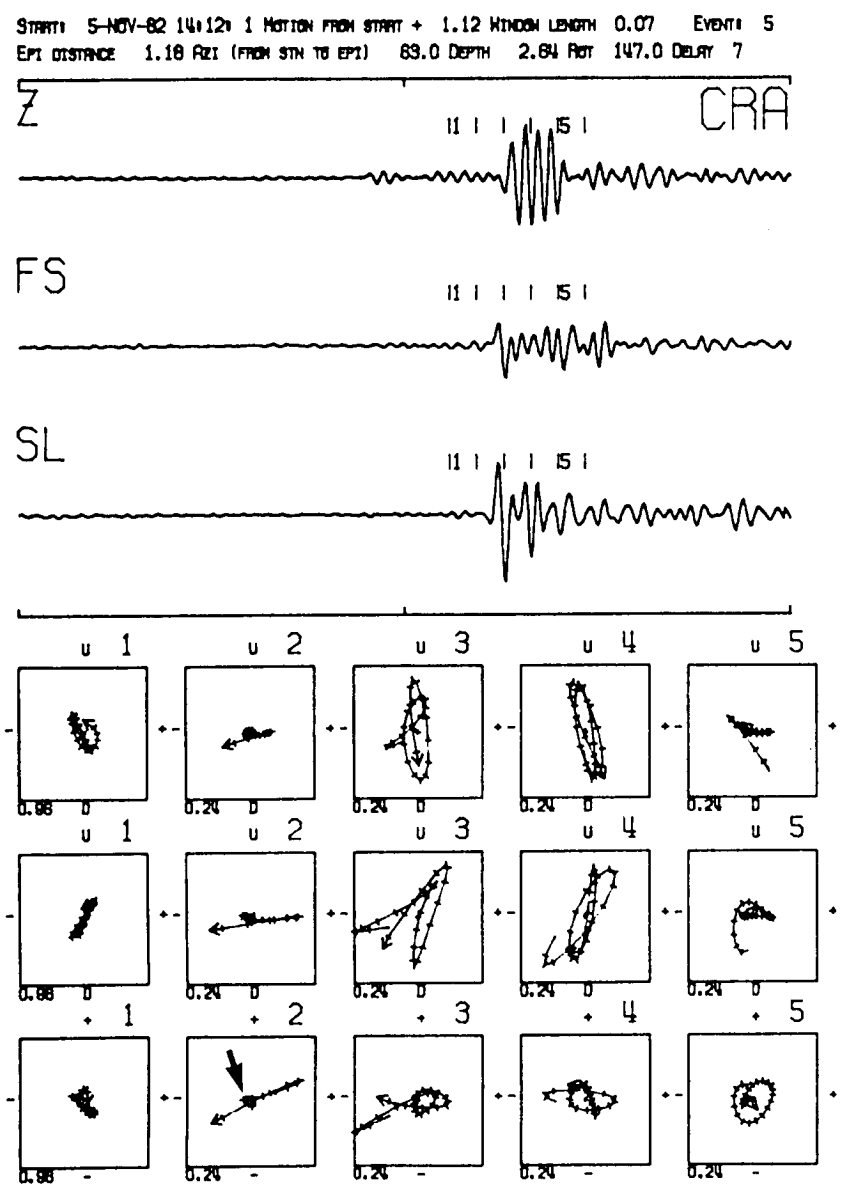

Figure C.1h

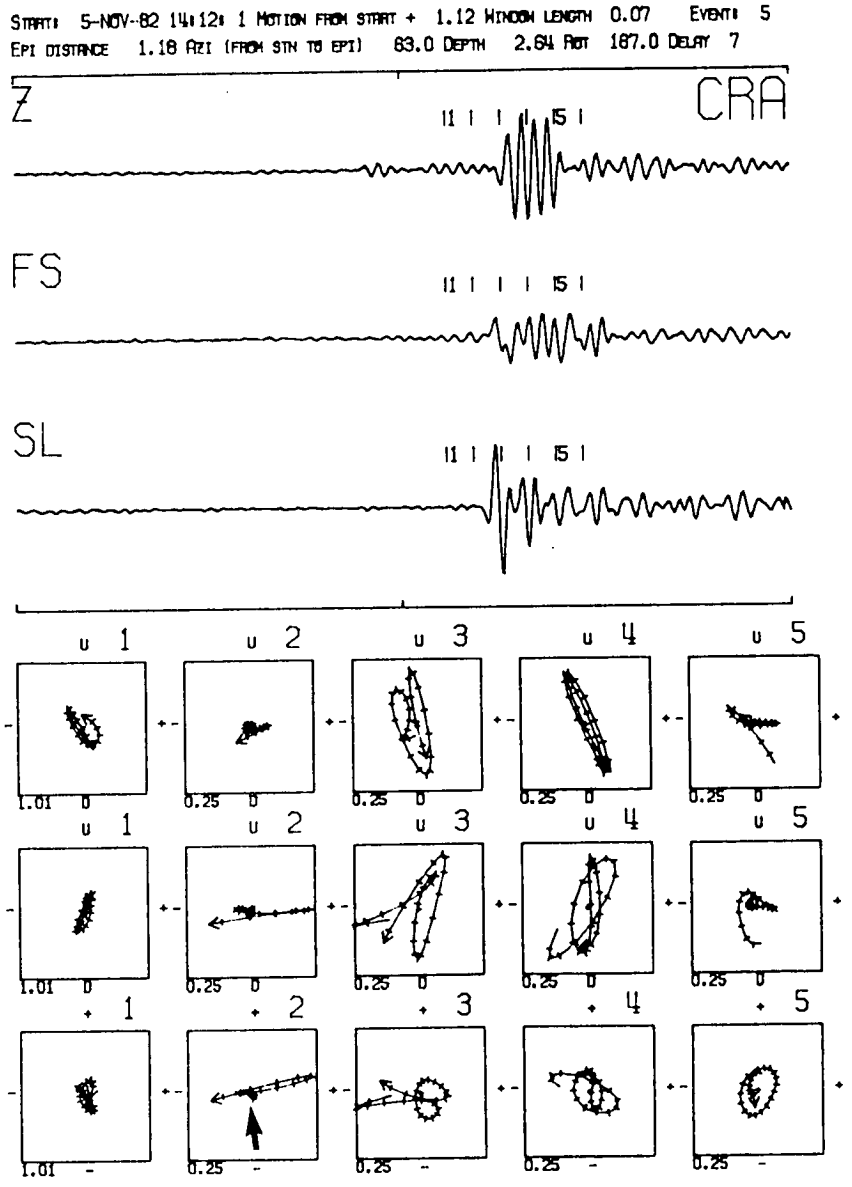

Figure C.1i

travelling through anisotropic and isotropic media are shown in Figure C.2. Below this there are four three-component seismograms of the shear-wave at various stages in the ray path. These stages - A, B, C, and D - are illustrated in the sectional view of the ray path. The plan view shows the orientation of the shear-wave polarization at stages A, B, C, and D with respect to the recording axes, R1 and R2. To clearly show the effects on the shear-waveform from incorrect reconstruction the propagation of shear-waves through anisotropic media is highly simplified. An outline is given below.

A vertically propagating plane shear-wave, with a sinusoidal waveform, passes through the anisotropic region. Upon entry the shear-wave splits into two orthogonally polarized phases each parallel to the anisotropic vibration directions. In the anisotropic zone the two phases travel with different velocities and become separated. To model surface recordings of shear-waves the split shear-waves are synthesised at a receiver, with components orientated non-parallel to the anisotropic vibration directions.

Following stages A to D and with reference to Figure C.2 the synthetic seismograms are generated.

Stage A: The shear-wave is in isotropic media, with polarization orientated at 75°. The horizontal components of the seismograms are orientated at 75° and 165°.

Stage B: The shear-wave enters the anisotropic zone and the shear-wave is split into two orthogonal phases with polarizations orientated 30° and 120°. No time delay is present, and the horizontal components of the seismograms are orientated at 30° and 165°.

Stage C: The shear-wave leaves the anisotropic zone. The shear-waves are polarized at 30° and 120°, as before, but a time delay of 10 samples is introduced. The horizontal components of the seismograms are orientated at 30° and 120°.

Stage D: The split shear-waves are recorded along components R1 and R2 orientated 0° and 90° respectively. No displacement occurs on the vertical-component and the horizontal components consist of phase shifted and rotated sinusoidal waveforms.

The procedure of shear-wave reconstruction is essentially the reverse of the above. The horizontal components, R1 and R2 (stage D), are rotated (through 30°) until two identical waveforms appear on each rotated component (stage C). The slower phase is shifted forward until the two waveforms are in phase (stage B). A shift of 10 samples is required, and linear particle motion polarized at 75° is produced. Here, the 'rotation angle' is defined as the angle (+ve clockwise) through which the recording axes, R1 and R2, are rotated in the process of reconstruction.

C.3 **Shear-wave reconstructions**

In this section the shear-wave particle motion is reconstructed for a range of rotation angles. The geometry of the recording axes and anisotropic vibration directions in Figure C.2 is retained throughout. Hence the shear-waveform and its polarization are known prior to reconstruction. This enables the comparison of the polarization angle of the reconstructed shear-wave, measured at each rotation angle, to the actual incident shear-wave polarization angle of 75°. Three-component seismograms and polarization diagrams of the horizontal particle motion of both 'recorded' (along R1 and R2) and reconstructed shear-waveforms are shown in Figures C.3 to C.5. Note that the number adjacent to each polarization diagram indicates the difference between the rotation angle used and the correct rotation angle of 30°.

In Figure C.3a the 'recorded' seismogram, with components orientated along R1 and R2 (stage D), consists of shear-waves separated by a time delay of 10

Figure C2

(a) Plan view of the shear-wave polarizations arising from a vertical ray passing through an anisotropic zone. Dashed line S-S is the shear-wave polarization prior to entry into the anisotropic zone. Dashed lines FS-FS and SL-SL are the polarizations of the split shear-waves in the anisotropic zone. A shear-wave polarized along FS-FS, the fast vibration direction, travels faster than a shear-wave polarized parallel to SL-SL, the slow vibration direction. Solid lines R1-R1 and R2-R2 give the orientation of the recording axes. (b) Sectional view of ray path through anisotropic zone. Below are three-component seismograms of the shear-wave at various stages along the ray path (A to D). The horizontal components are rotated clockwise with respect to the R1-R1 recording axis at the angles shown above each trace. (A) Before shear-wave splitting. (B) At base of anisotropic zone. (C) At top of anisotropic zone. (D) At the recorder.

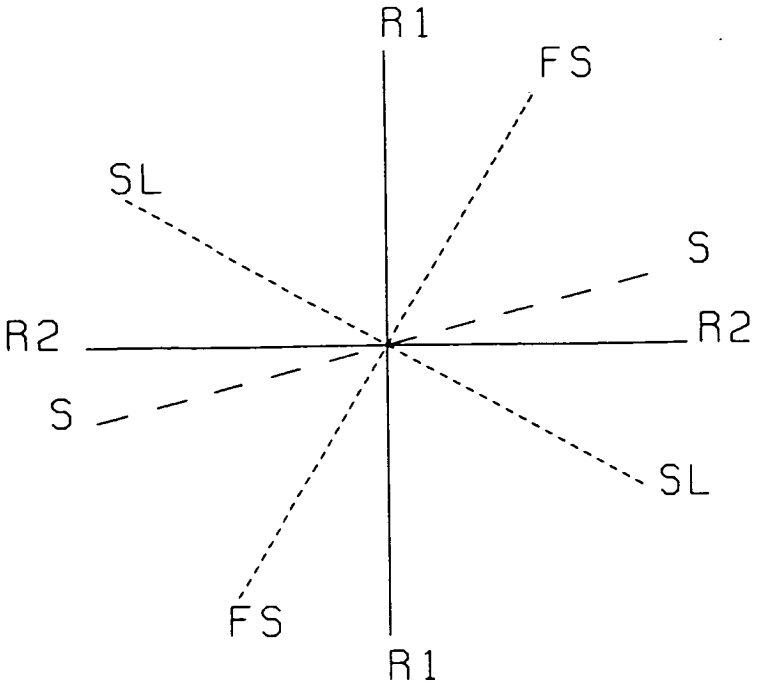
R1
FS
SL
S
R2
R2
S
SL
FS
R1

a

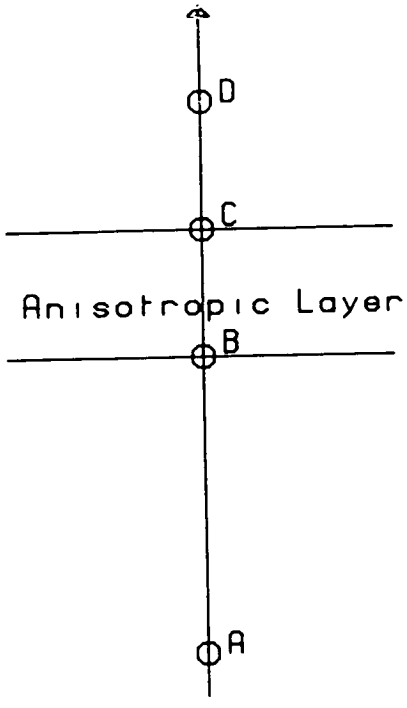
D
C
Anisotropic Layer
B
A

b

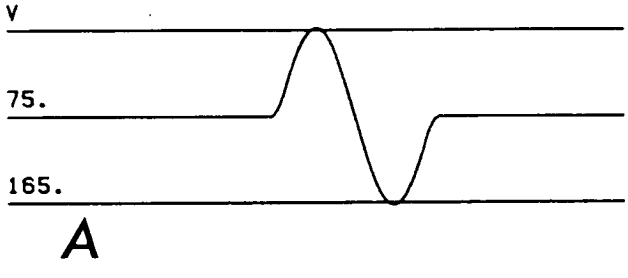
V
75.
165.
A

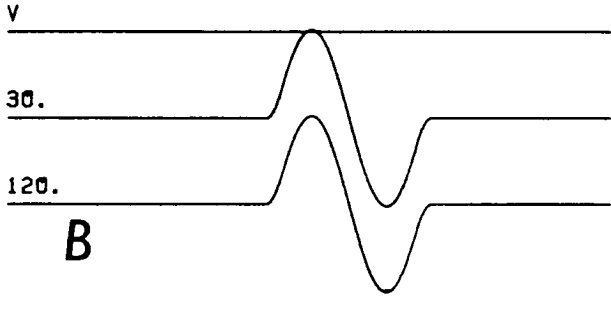
V
30.
120.
B

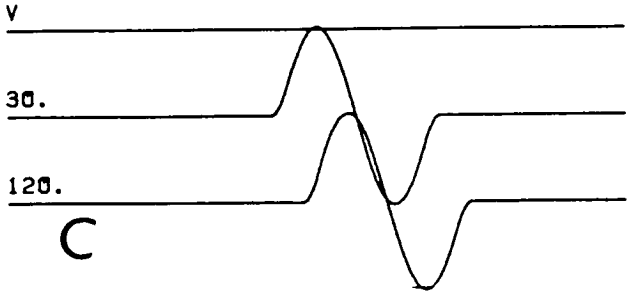
V
30.
120.
C

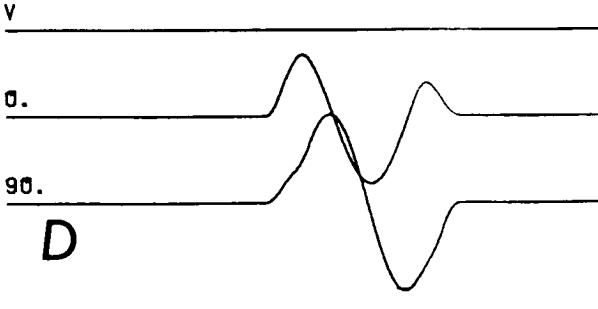
V
0.
90.
D

Figure C.2

Figure C3

Reconstructed shear-wave particle motion. A three-component seismogram and polarization diagram of the reconstructed shear-wave. Details of the technique are given in the text. The horizontal components have been rotated +ve clockwise from the R1-R1 axis by the angles shown above each trace. The polarization diagram shows particle motion in the horizontal plane. The number adjacent gives the difference between the rotation angle and that for correct reconstruction. The configuration of the shear-wave polarizations is given in Figure C2a, with a time delay of 10 samples between the split shear-waves.

(a) recorded seismogram along R1-R1 and R2-R2.
(b) rotation angle 30°
(c) rotation angle 40°
(d) rotation angle 50°
(e) rotation angle 60°
(f) rotation angle 70°
(g) rotation angle 80°
(h) rotation angle 90°

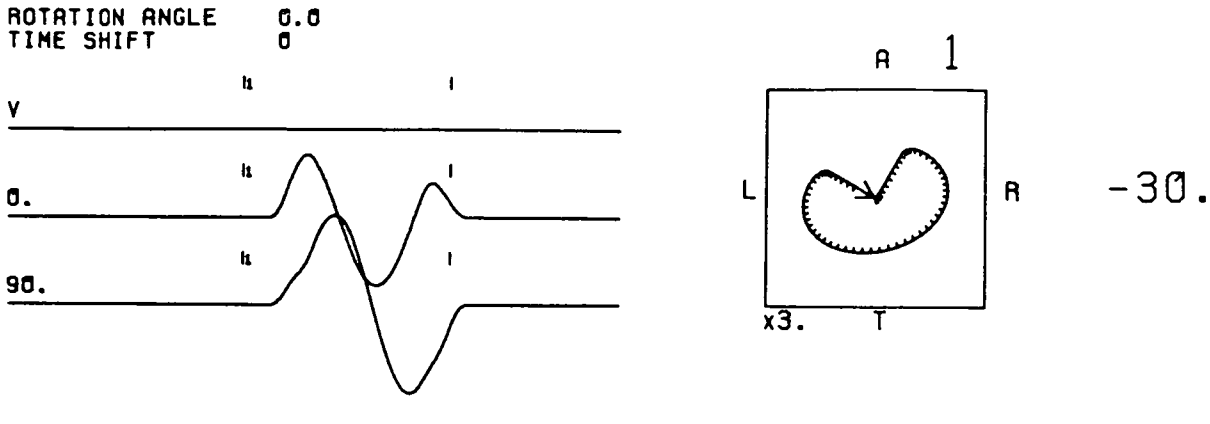

Figure C.3a

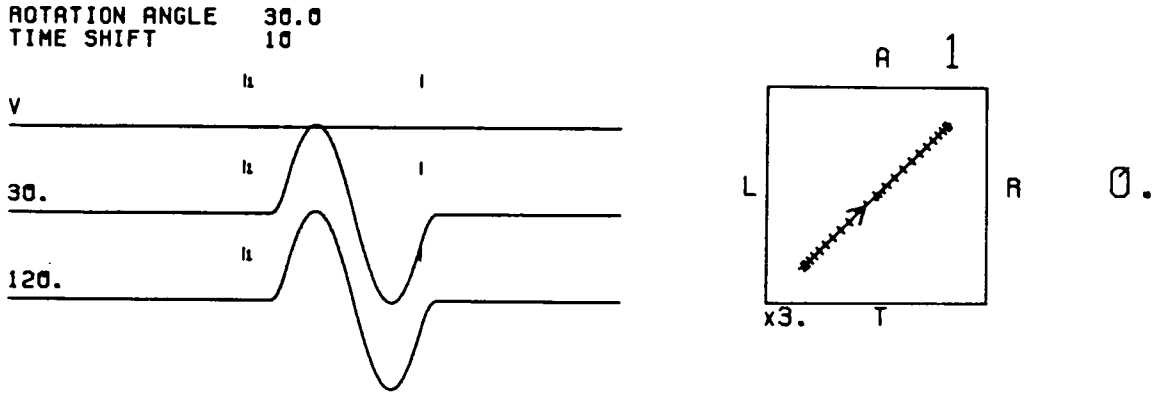

Figure C.3b

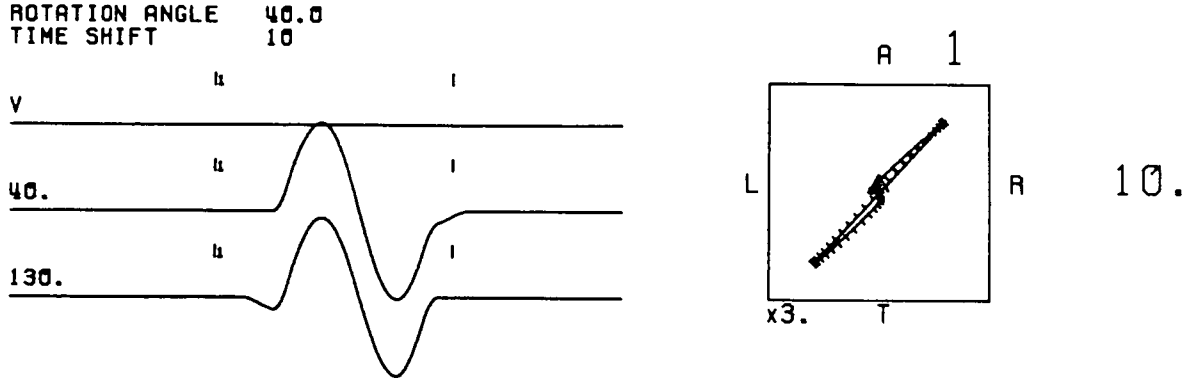

Figure C.3c

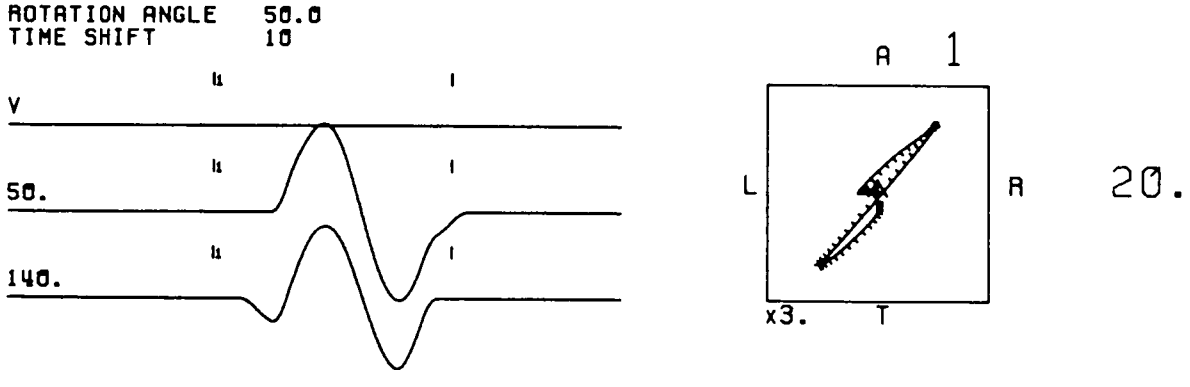

Figure C.3d

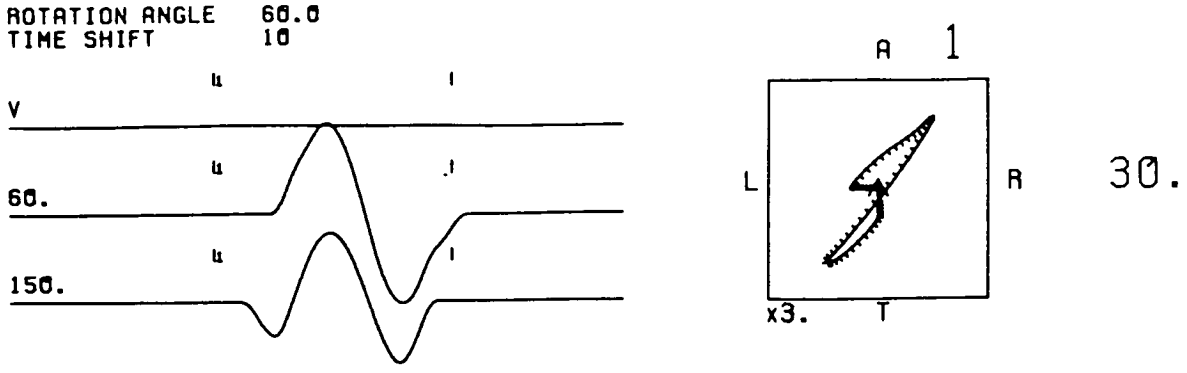

Figure C.3e

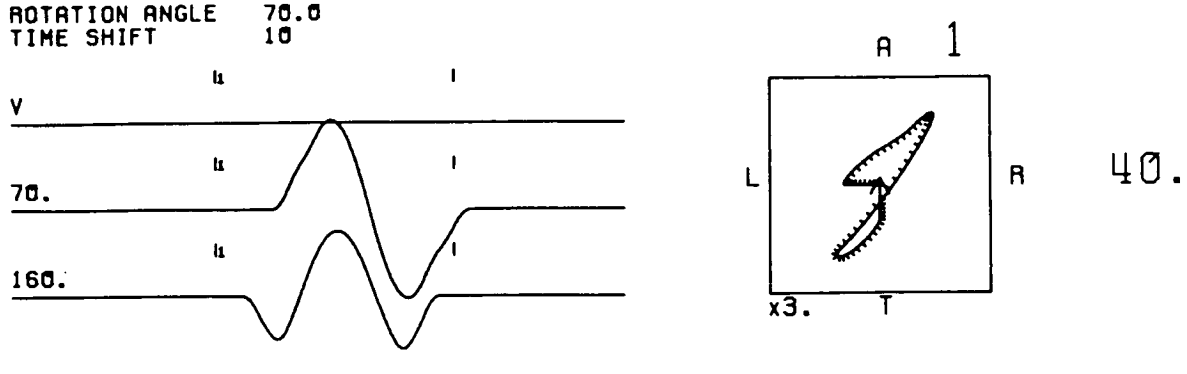

Figure C.3f

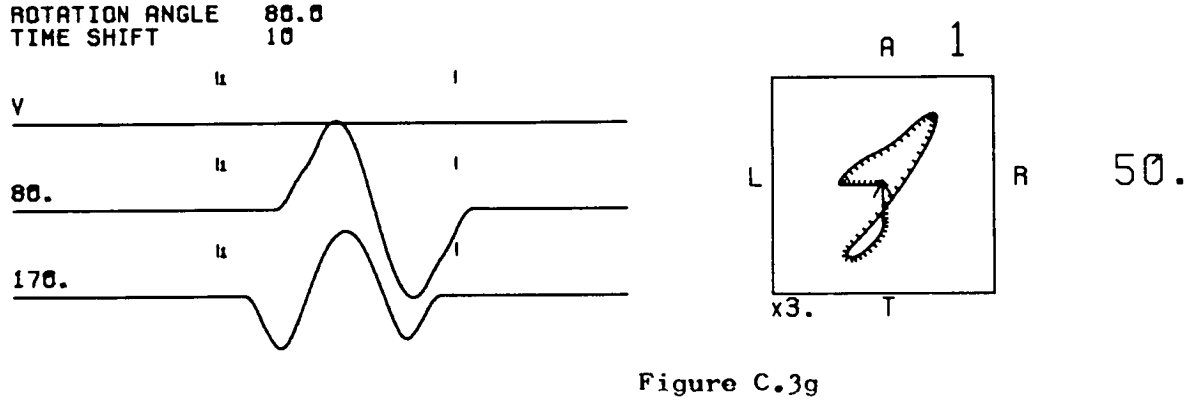

Figure C.3g

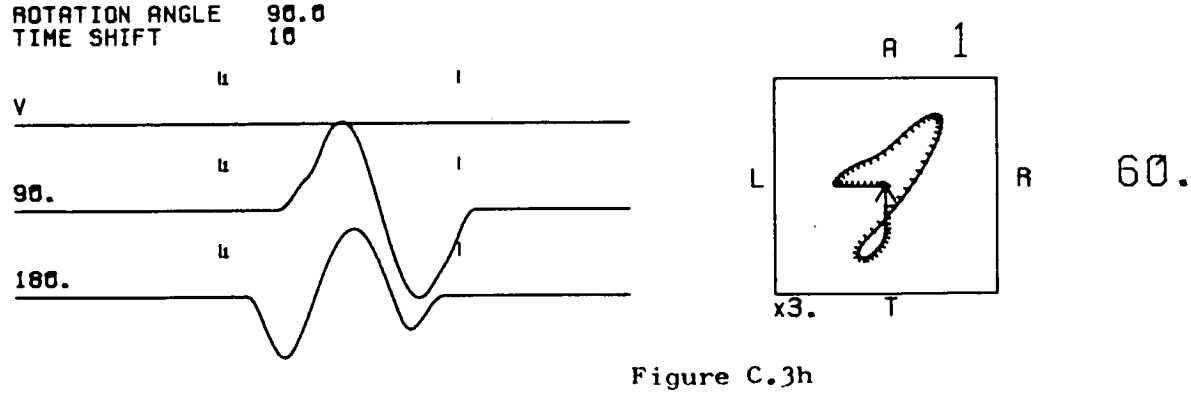

Figure C.3h

samples - 1/5 of the pulse period. To reconstruct the shear-waveform the slow-component is shifted 10 samples forward at rotation angles from 30° to 90° (stage B). When the reconstruction is carried out correctly (the recording components are rotated through 30° and align parallel to the vibration directions) linear shear-wave particle motion is generated with a polarization angle of 75° (see Figure C.3b). The seismograms in Figures C.3c to C.3h indicate what happens when the horizontal components do not align parallel to the vibration directions. When the rotation angle increases from 40° to 90° shear-wave particle motion becomes more elliptical and a precursor on the slow-component becomes larger. The synthetic seismograms show that for differences of up to 30° the reconstructed particle motion is approximately linear and the amplitude of the precursor is small. Therefore apparently correct reconstructed waveforms can be generated when the rotated components deviate by up to 30° from the orientation of the anisotropic vibration directions.

A list of shear-wave polarization angles for all the rotation angles is given in Table C.1. The polarization angle of the incident shear-wave prior to splitting is 75° (see Figure C.2) and occurs upon a rotation of 30°. As the rotation angle increases from 30° the polarization angle increases. However a rotation angle of 60° gives a polarization angle of 98° which only differs from the true value of 75° by 23°. This suggests that reasonable agreement with predicted shear-wave polarizations from source mechanisms can be attained even when the orientation of the anisotropic vibration directions are in error by 30°.

The effect of increasing the time delay to 25 samples, 1/2 the pulse period, is illustrated in Figure C.4 and Table C.2. The main points to note here is that the precursor on the slow vibration direction component has a larger time duration and that the particle motion is linear after the precursor. Also, the

Table C.1 A comparison of reconstructed shear-wave polarization angles for a range of rotation angles. DELTA ROTATION gives the difference in the rotation angle from the rotation required to align the horizontal components parallel to the anisotropic vibration directions. Similarly DELTA POLARIZATION gives the difference in the reconstructed polarization angle to the known value of 75^{o}. A rotation angle of 30^{o} aligns the horizontal components parallel to the anisotropic vibration directions. Other rotation angles illustrate the error of the polarization angle upon incorrect reconstruction.

TIME DELAY	ROTATION ANGLE	DELTA ROTATION	POLARIZATION ANGLE	DELTA POLARIZATION
0	0^{o}	-30^{o}	30^{o}	-45^{o}
10	30^{o}	0^{o}	75^{o}	0^{o}
10	40^{o}	10^{o}	82^{o}	7^{o}
10	50^{o}	20^{o}	90^{o}	15^{o}
10	60^{o}	30^{o}	98^{o}	23^{o}
10	70^{o}	40^{o}	106^{o}	31^{o}
10	80^{o}	50^{o}	114^{o}	39^{o}
10	90^{o}	60^{o}	123^{o}	48^{o}

deviation of the reconstructed polarization angle is larger than for the time delay of 10 samples. For example the polarization angle for a rotation angle of 60° is 120°, a difference of 45° from the true polarization angle.

Probably the most notable result is that the orientation of the fast vibration direction and the time delay is best estimated directly from the polarization diagram, without recourse to rotations and reconstructions. For example, in Figure C.3a the first motion of the shear-wave is orientated parallel to the fast anisotropic vibration direction, and a time delay of 10 samples elapses before elliptical particle motion. This suggests that interpretation of the shear-wave particle motion in the polarization diagram is the best way to determine the orientation of the anisotropic vibration directions, and that the main use of the shear wave reconstructions is for checking the interpretation by comparison with predicted source polarizations.

In the more general case, when a shear-wave enters an anisotropic region the incident energy will usually be distributed unequally between the anisotropic vibration directions. As an example, consider shear-wave propagation through the anisotropic zone with energy distributed in the fast and slow vibration directions in the ratio 0.3:1. The configuration is the same as before except that the incident shear-wave is now polarized at 103°. The particle motion before reconstruction is shown in Figure C.5a. It is elliptical with the major axis of the ellipse trending at 113°. There is no obvious sign of shear-wave splitting, and an interpretation of unsplit shear-waves with a polarization of 113° taken from the major axis of the ellipse seems reasonable. However when the shear-wave polarization is estimated from the first motion as 30°, with a time delay of 10 samples we know that an accurate reconstruction of the shear-wave is produced (see Figure C.5b). This shows that on recorded seismograms it may prove difficult to detect shear-wave splitting when the time delay is small and most of the seismic energy

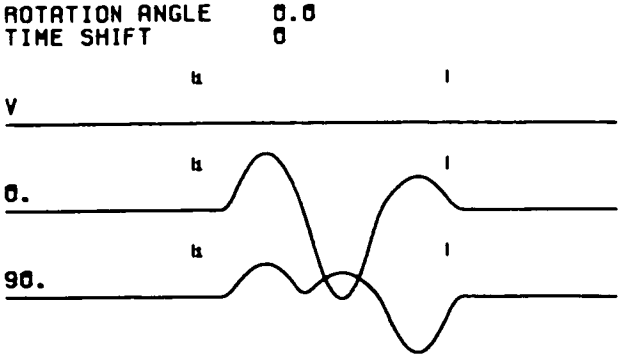

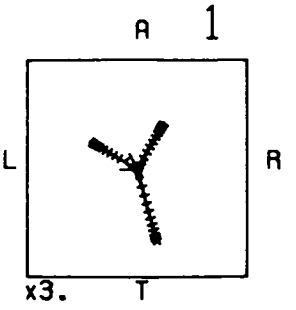

-30.

Figure C.4a

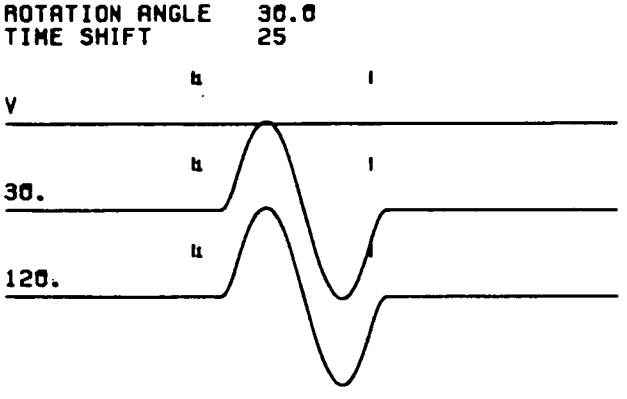

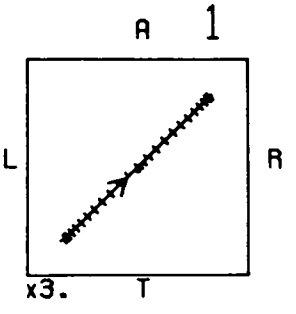

0.

Figure C.4b

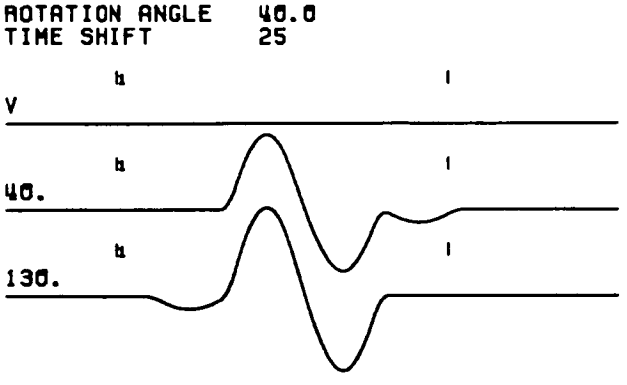

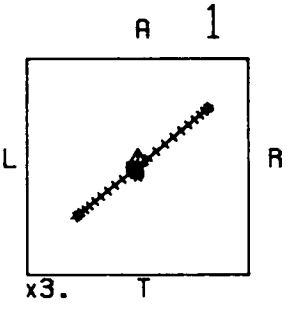

10.

Figure C.4c

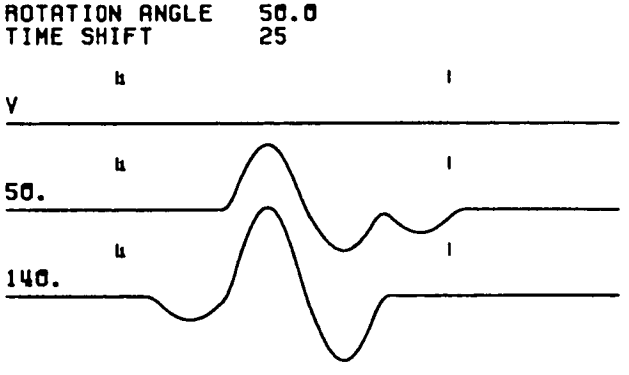

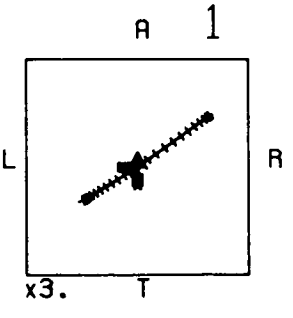

20.

Figure C.4d

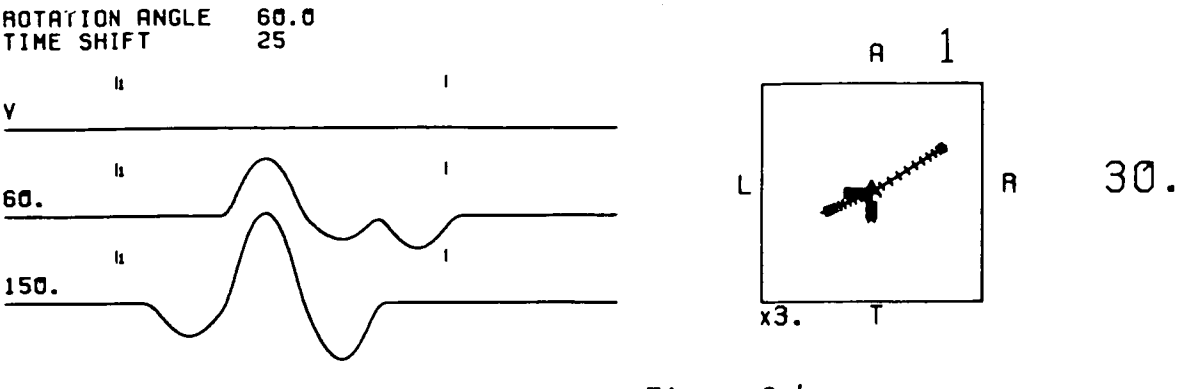

Figure C.4e

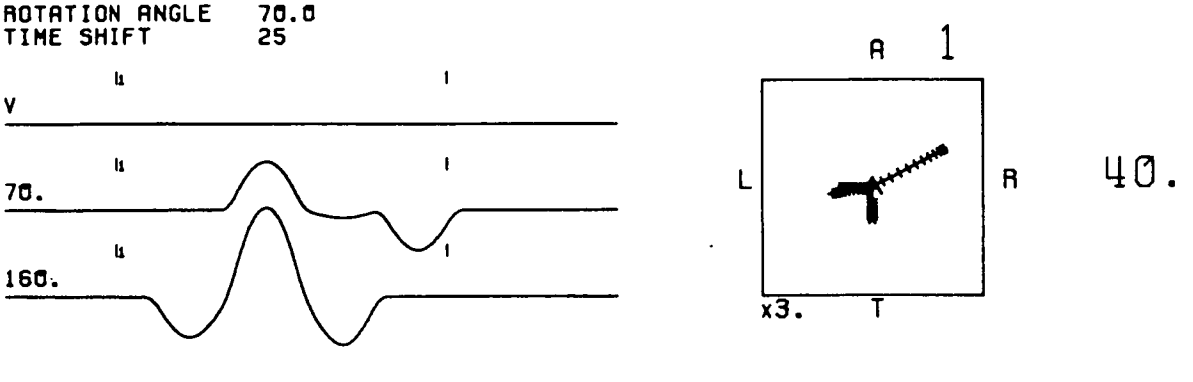

Figure C.4f

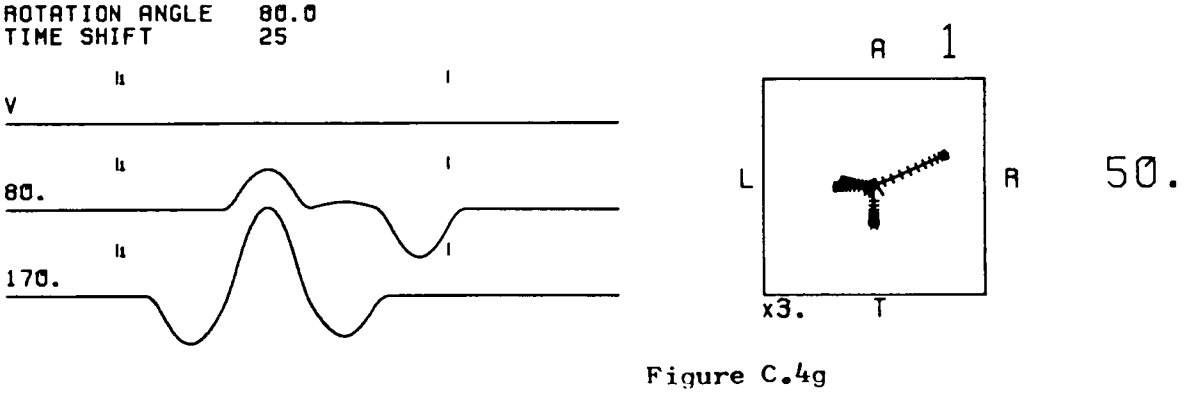

Figure C.4g

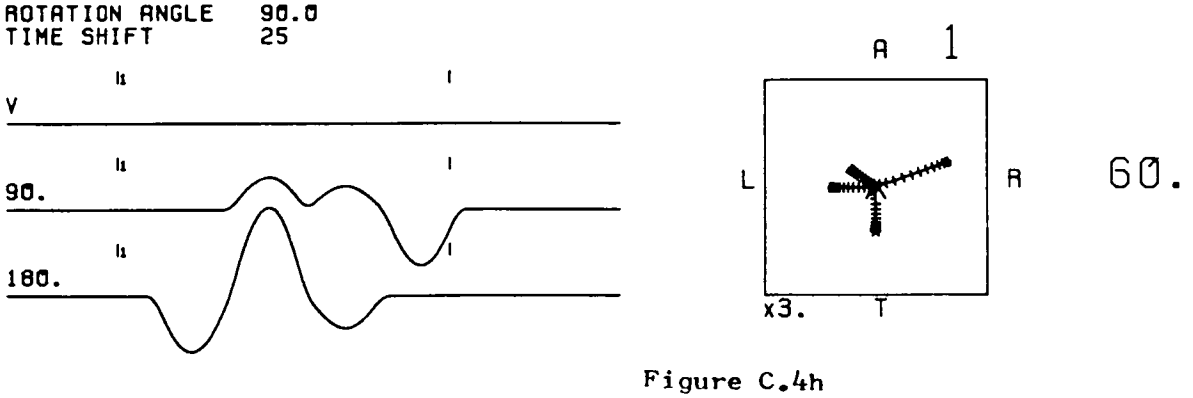

Figure C.4h

Table C.2 Same as Table C.1 above, except time delay is 25 samples.

TIME DELAY	ROTATION ANGLE	DELTA ROTATION	POLARIZATION ANGLE	DELTA POLARIZATION
0	0°	-30°	30°	-45°
25	30°	0°	75°	0°
25	40°	10°	90°	15°
25	50°	20°	104°	29°
25	60°	30°	120°	45°
25	70°	40°	133°	58°
25	80°	50°	145°	70°
25	90°	60°	165°	90°

Figure C5

Reconstructed shear-wave particle motion. The configuration of shear-wave polarizations is given in Figure C1a. Time delay is 10 samples. Energy ratio in fast and slow vibration directions FS:SL is 0.3:1.

(a) recorded seismogram along R1-R1 and R2-R2.

(b) rotation angle 30°

(c) rotation angle 50°

(d) rotation angle 70°

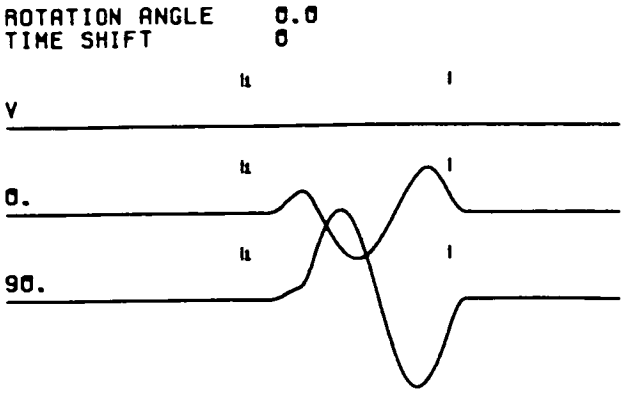

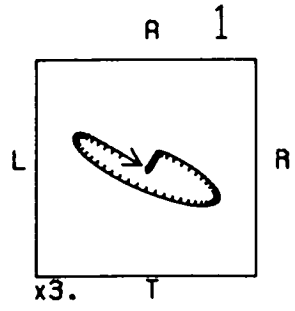

-30.

Figure C.5a

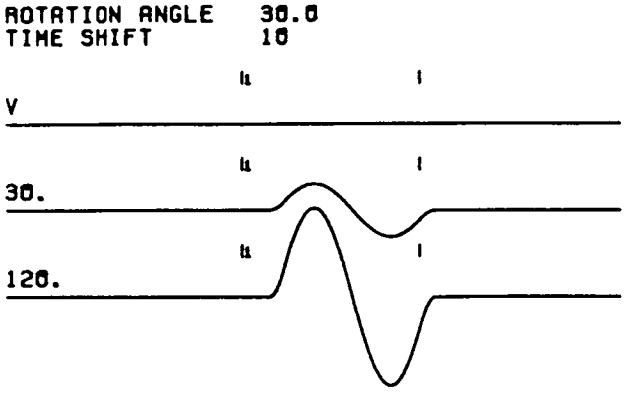

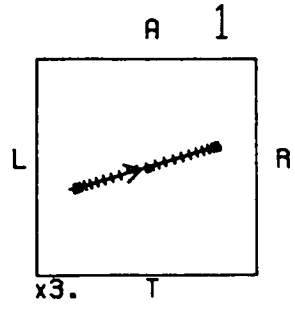

0.

Figure C.5b

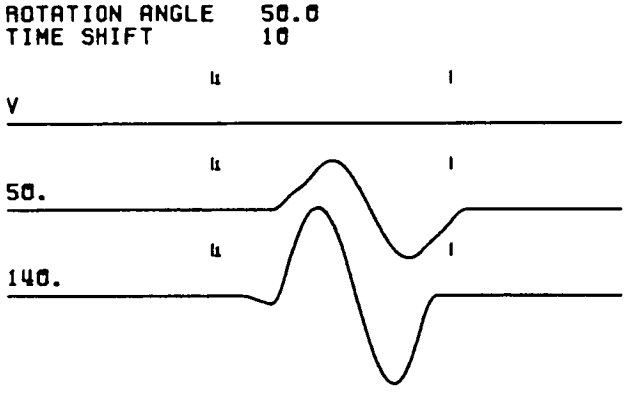

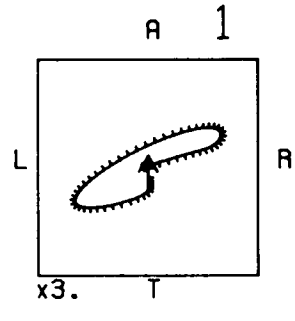

20.

Figure C.5c

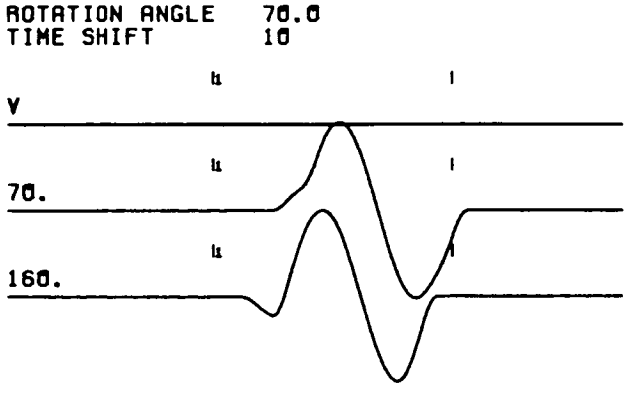

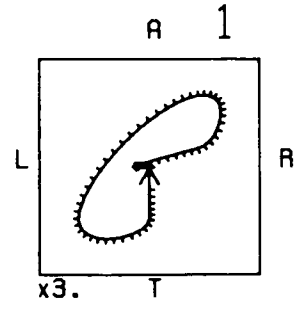

40.

Figure C.5d

propagates along one of the vibration directions. It also emphasises the importance of estimating the polarization from the first motion of the shear-wave in anisotropic studies.

C.4 Conclusions

A sensitivity of about $\pm 30^{o}$ is achieved when using the degree of linearity of the reconstructed shear-wave particle motion to determine the orientation of the anisotropic vibration directions. Correlation of similar waveforms is probably slightly more sensitive since identification of a precursor on the slow vibration direction component offers a useful guide to accurate rotation. No precursor is present when the recording components are rotated into the anisotropic vibration directions, but with increasing deviation a precursor develops with increasing amplitude.

Interpretation of the shear-wave particle motion in polarization diagrams is probably the easiest and most reliable technique for the determination of the orientation of the anisotropic vibration directions. The first motion of the shear-wave defines the fast vibration direction, and the introduction of ellipticity, or a sharp change in the direction of the particle motion marks the onset of the slower phase. The time delay is the number of samples between the shear-wave onset and the change in particle motion. Also it is important to note that, under certain conditions, it is the first motion of the shear-wave which defines the orientation of the faster shear-wave polarization, and not the average orientation direction defined by the first cycle. The main purpose of the shear-wave reconstruction should be for comparison with predicted shear-wave polarizations from P-wave fault plane solutions.